Stress-Based Topology Optimization Considering Uncertainties or Partial Damage

Vom Promotionsausschuss der
Technischen Universität Hamburg

zur Erlangung des akademischen Grades

Doktor-Ingenieur (Dr.-Ing.)

genehmigte Dissertation (Monografie)

von
Micah Kranz

aus
Mettingen

2025

Erster Gutachter: Prof. Dr.-Ing. Benedikt Kriegesmann
Zweiter Gutachter: Prof. Dr.-Ing. Alexander Düster

Tag der mündlichen Prüfung: 24. September 2025

DOI: 10.15480/882.16061
ORCiD: 0000-0003-3880-3151

Abstract

Today, topology optimization is a widely recognized tool in the field of structural optimization. It is not only implemented in scientific finite element solvers, but also in computer-aided design (CAD) programs, highlighting its broad applicability across different engineering disciplines. However, optimizing without taking possible uncertainties into account, may lead to catastrophic consequences. Uncertainties are inherently present in every practical application and should hence be properly considered during optimization.

Although the research field of topology optimization is considered as mature, most approaches are only demonstrated on structural stiffness examples, especially when uncertainties are incorporated. Nevertheless, stresses are much more relevant for strength aspects or damage tolerance. Additionally, stresses are still a challenging topic due to their localized characteristics. Hence, a main focus of this thesis is to incorporate stress measures into the optimization framework, while uncertainties are present.

The first regarded type of uncertainty is local structural damage. Damages occur for various reasons, e.g. because of fatigue, manufacturing defects, human error, accidents and many more. Consequently, it might be necessary to address the topic of damage robustness, for which different strategies exist. One is, for instance, to generate multiple load path designs. For optimization, mainly two approaches are followed to generate multiple load path designs. One approach explicitly takes generic damage patches into account, while others follow the idea of limiting the maximum feature size and hence, implicitly create multiple load paths. The explicit approach is also known as the damage patch approach, which comes at a very high computational cost, since a finite element model has to be solved for each damage patch. In the context of stress, it is demonstrated that it is beneficial to only consider as many damage patches as needed to cover the design domain without gap and overlap. This resulted in a significant decrease in computational cost compared to the original approach. Furthermore, a load path-based evaluation scheme is proposed, which is of much more practical relevance than the common evaluation based on generic damage patches. Following this evaluation philosophy, different patch configurations are investigated, showing no further benefits. Regarding the implicit approach, a lot of heuristic parameter tuning is required, while obtained results show poor damage robustness. In addition, the explicit approach is combined with feature size constraints, yielding improved designs and convergence behavior.

To incorporate uncertainties in material properties and geometry into the robust topology optimization framework, a generalized first-order second-moment method is derived. It allows any structural response function, such as displacement, volume, compliance or stresses, to be applied as robust constraint or objective. Compared to the deterministic case, the presented approach requires the solution of at most three additional adjoint systems per uncertain response. Hence, the number of adjoint systems to be solved is independent of the number of random variables. This comes at the expense of accuracy, since the objective functions are assumed to be linear with respect to random parameters. However, verification with contour models and using Monte Carlo simulations for post-processing show, that the approach is still able to find robust designs. While the proposed formulation works acceptably well for uncertainties in material properties considering displacements and stress as objective and constraint respectively, it fails in the case of geometry perturbations. Nonetheless, the benefits of considering uncertainties during optimization is emphasized. Compared to a worst-case formulation, which is current engineering practice, lighter designs are obtained.

Keywords: damage robustness; stress-based and robust topology optimization; optimization under uncertainties

Contents

Abbreviations

CAD	Computer aided design
CDF	Cumulative distribution function
CPU	Central processing unit
EOLE	Expansion optimal linear estimator
FE	Finite element
FEM	Finite element method
FORM	First-order reliability method
FOSM	First-order second-moment method
FSO	Fail-safe optimization
GCMMA	Globally converging method of moving asymptotes
KS	Kreisselmeier-Steinhauser
LPE	Load path-based evaluation
LVC	Local volume constraint
MCS	Monte Carlo simulation
MLD	Multiple load path design
MMA	Method of moving asymptotes
MPP	Most probable point
PDE	Partial differential equation
PMA	Performance measure approach
RAMP	Rational approximation of material properties
RBDO	Reliability-based design optimization
RBTO	Reliability-based topology optimization
PCA	Principal component analysis
RDO	Robust design optimization
RIA	Reliability index approach
RTO	Robust topology optimization
SIMP	Solid isotropic material penalization
SOFM	Second-order fourth-moment method
SORA	Sequential optimization and reliability assessment
SROM	Stochastic reduced-order models
WCF	Worst-case formulation

Mathematical Symbols

a, b	Parameter for uniform distribution
A_C, A_E	Area of a circle and an ellipse
$\mathcal{A}_\circ$	Aggregation function
$\mathcal{A}_{\circ,\mathcal{D}}$	Aggregation function for all damage scenarios
$\mathcal{A}_{\circ,\mathcal{E}}$	Aggregation function for all elements
$\mathcal{A}_\circ$	Aggregation function
$\mathbf{B}_{e,g}$	Strain-displacement matrix of element e at Gaussian point g
c	Constraint function
c_q	Stress constraint
c_{robust}	Robust constraint function
c_L	Local volume constraint
c_V	Volume constraint
$\mathbf{C}_0$	Material stiffness matrix for unit Young's modulus
$\mathbf{C}_e$	Penalized material stiffness matrix
CoV	Coefficient of variation
CoV_v	Coefficient of variation for vertical displacements
CoV_E	Coefficient of variation for Young's modulus
d	Hole diameter
d_{min}	Minimum feature size
d_{max}	Maximum feature size
$\mathbf{d}$	Matrix containing distances between two points
E_0	Young's modulus
E_e	Penalized Young's modulus of element e
E_{min}	Minimum Young's modulus
f	Objective or cost function
f^k	Objective at iteration k
$\mathbf{f}$	Load vector
F	Load amplitude
F_{in}	Load amplitude on input node
F_U	Cumulative distribution function of uniform distribution
$F_{\mathcal{G}}$	Cumulative distribution function of $\mathcal{G}$
$F_{\mathcal{G}}^{-1}$	Inverse cumulative distribution function of $\mathcal{G}$

$\mathcal{F}$	Arbitrary design response
$\mathcal{F}_0$	Extreme values of an arbitrary design response
$\mathcal{F}_A$	Approximated values of an arbitrary design response
$\mathcal{F}_e$	Design response of element e
FSF	Fail-safe factor
g	Design response subjected to variations
$\mathcal{G}_g$	Robust objective function of design response g
$\mathcal{G}_u$	Robust objective function for displacements
h, w	Major and minor axis of an ellipse
H	Plate height
k	Damage scenario
k	Iteration number
k	Random realization
k_{fin}, k_{inf}	Stress concentration factor
k_{in}, k_{out}	Input and output spring stiffness
$\mathbf{k}_e$	Effective local stiffness matrix of element e
$\mathbf{k}_e^0$	Local stiffness matrix of element e for unit Young's modulus
$\mathbf{K}$	Global stiffness matrix
l_c	Correlation length
l_e	Element size
L	Length
$\mathcal{L}_e$	Local domain of element e
n	Number of random samples
n_c	Number of constraints
$n_{\mathcal{D}}$	Number of damage scenarios
n_e	Number of elements
n_i	Number of last iterations
n_{opt}	Number of samples used for optimization
n_u	Number of nodal displacements
n_v	Number of design variables
n_ρ	Number of densities
$\mathcal{N}$	Normal distribution
$\mathcal{N}^(k)$	Element set of damage scenario k
$\mathcal{N}_e$	Neighborhood of element e
M_{nd}	Measure of non-discreteness
$\mathbf{M}$	Constant matrix
p	Aggregation parameter
$p_{\mathcal{D}}$	Aggregation parameter for damage scenarios
$p_{\mathcal{E}}$	Aggregation parameter for elements
$p_{\mathcal{W}}$	Aggregation parameter for worst-case
p^{RAMP}	RAMP interpolation parameter
p^{SIMP}	SIMP exponent

P	Probability
P_0	Failure probability
q_0	Allowable stress or material strength
q_0^*	Reduced material strength
$q_{0,e}$	Material strength of element e
q_e	Equivalent von Mises stress of element e
q_{max}	Maximum von Mises stress
q_{nom}	Nominal von Mises stress
Q	Quantile values
r	Radius
r_{filt}	Filter radius
r_{loc}	Radius of local volume domain
$\mathbf{R}$	Residuum
s_0	Applied stress
s_{max}	Maximum stress
SF, SF_e	Strength factor
SF_{robust}	Robust strength factor
u_h	Horizontal displacements
u_v	Vertical displacements
$\mathcal{U}$	Uniform distribution
$\mathbf{u}$	Nodal displacements
$\mathbf{u}_e$	Nodal displacements of element e
v_e, v_i	Volume of element e and i
v_{mac}	Maximum elemental volume
$\mathbf{v}$	General design variables
V	Global volume
V_0	Maximum volume of the design domain
w	Weighting function
$\mathbf{x}_e$, $\mathbf{x}_i$	Center coordinates of element e and i
α_F	Load angle
$\boldsymbol{\alpha}$	Vector of random variables
β	Projection parameter
β_{lim}	Limited projection parameter
β_{max}	Maximum projection parameter
γ	Scaling factor
$\Delta\mathbf{x}$	Perturbation range
$\Delta\eta$	Range for the projection threshold
$\Delta\rho_{max}$	Maximum change in densities
ϵ	Perturbation step size
ϵ_0	Normalization factor
$\boldsymbol{\epsilon}_{e,g}$	Strain vector of element e at Gaussian point g
η, η_e	Projection threshold of element e

η^d, η^i, η^e	Dilated, intermediate and eroded projection threshold
κ	Weighting factor
κ_{init}	Initial weighting factor
κ^*	Weighting factor related to normal distribution
$\boldsymbol{\lambda}$	Lagrange or adjoint vector
μ	Arithmetic mean
μ_E	Mean of Young's modulus
μ_g	Mean of design response g
μ_h	Mean of horizontal displacements
μ_q	Mean of von Mises stresses
μ_{q0}	Mean of material strength
μ_{SF}	Mean of the strength factor
μ_η	Mean of projection threshold
ν	Poisson's ratio
ξ_e	General penalization term
ξ_e^{RAMP}	RAMP penalization
ξ_e^{SIMP}	SIMP penalization
ρ_e, ρ_i	Density of element e and i
ρ_i^k	Density of element i and at iteration k
$\boldsymbol{\rho}$	Vector containing all densities
$\boldsymbol{\rho}^d$, $\boldsymbol{\rho}^i$, $\boldsymbol{\rho}^e$,	Dilated, intermediate and eroded density fields
$\tilde{\rho}_e$	Filtered density of element e
$\bar{\rho}_e$	Projected density of element e
σ	Standard deviation
σ_E	Standard deviation of Young's modulus
σ_g	Standard deviation of design response g
σ_h	Standard deviation of horizontal displacements
σ_v	Standard deviation of vertical displacements
σ_q	Standard deviation of von Mises stresses
σ_{q0}	Standard deviation of material strength
σ_{SF}	Standard deviation of the strength factor
σ^2	Variance
σ_g^2	Variance of design response g
σ_η^2	Variance of uniform distributed projection threshold
σ_α^2	Variance of random parameter α
Σ	Symmetric covariance matrix for normalized variance
$\Sigma^{1/2}$	Square root of the covariance matrix
Σ_α	Symmetric covariance matrix of random parameter α
$\boldsymbol{\sigma}_e^g$	Stress vector of element e at Gaussian point g
φ_e	Volume fraction of element e
φ_L	Local volume fraction
φ_V	Global volume fraction

φ_V^*	Achieved global volume fraction
Φ	Cumulative distribution function of normal distribution
Ω_e	Local domain of element e at Gaussian point g

Chapter 1

Introduction

Finding solutions to reduce material consumption and hence contribute to more sustainability is a current engineering challenge. Since the last decade, new possibilities for product design and development are opening up due to advancements in the field of additive manufacturing processes. The latter are gaining increased attention from both, industry and academia. Additive manufacturing is not only applied in rapid prototype development but also for production of structural components, which may benefit from an increased design freedom resulting in reduced weight, lower cost and higher durability. To make use of this potential, new optimization methods are needed in the field of structural mechanics. A powerful and versatile tool, which offers the biggest design freedom, is topology optimization [1]. It can for example be adapted to different physical problems and constrained by a diverse variety of limitations, e.g. related to manufacturing processes [2]. Hence, topology optimization is taken as the fundamental tool for this thesis. At this point it shall be noted, that topology optimization is strongly linked to the numerical finite element method, as will be discussed later.

In real-world applications, structural components are affected by uncertainties. They cannot be avoided, since everything in nature is inherently exposed to variations or fluctuations. Those uncertainties arise at different stages of the product life-cycle, e.g. during manufacturing due to tolerances, during service due to load variations and later due to material degradation. But also during the design process, uncertainty about the input parameters and modeling or numerical errors can lead to deviations. Especially in the context of optimization, neglecting the influence of uncertainties may lead to very sensitive and thus non-robust designs, which may fail if small variations occur. Regarding a single load vector with uncertain angle of attack, a design only optimized for one nominal direction performs very poorly under different angles [3, 4]. In conventional engineering it is common practice to apply so-called safety factors to compensate for known or unknown uncertainties which are "[...] mainly determined by corresponding design codes or by relative importance of the structural components of structural systems, rather than by a scientific consideration of the nature behind the design

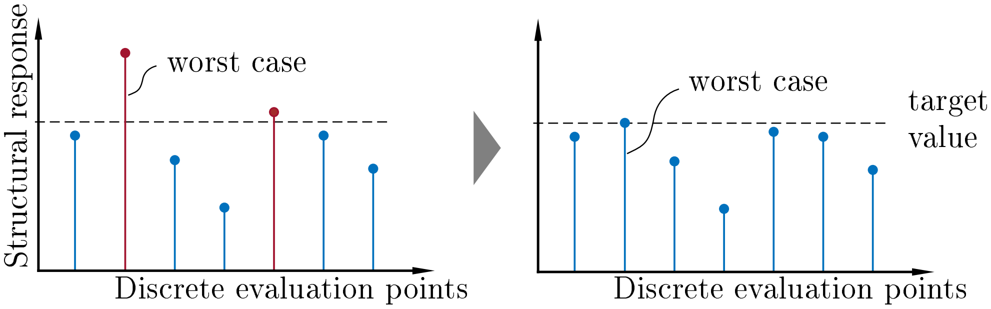

Figure 1.1: Worst-case optimization strategy.

problem" [5]. This results in safety factors which are known to be too conservative in most cases. This is contrary to the increased demand for structural efficiency, and hence new optimization methods taking uncertainties into account are required.

While different approaches exist to incorporate uncertainties into the optimization framework, the non-probabilistic or deterministic worst-case formulation is probably the most conventional and intuitive approach. Regarding the single load vector example from above considering an uncertain angle of attack, it is common engineering practice to verify a structural component by for example applying the load for the most extreme directions. Some probability considerations might be included, but the structure is basically just evaluated for a few discrete load angles. This can directly be used for optimization, which aims at the reduction of extreme values (cf Figure 1.1). Note, during optimization, the focus is solely on the worst case. Since extreme values of the input parameters are considered, it cannot be ensured, that the actual worst-case output is covered nor that a targeted reliability is fulfilled. Again, considering the load angle example, the worst direction is not necessarily represented by the minimum or maximum angle [6]. Nevertheless, this strategy may lead to a robust design but without control of the actual variability or failure probability.

Consequently, probabilistic considerations are essential to obtain a truly robust design. For that, stochastic information about the uncertain input parameters is required. The term "robust design" is very general in this case and interpreted differently in different contexts (cf. Figure 1.2). Pioneer work in the field of quality engineering was done by Taguchi [7] who stated that a robust design is insensitive or less sensitive to variations. This leads to the general category of robust design optimization (RDO), where the main goal is to reduce the variability of the system output related to uncertain input parameters (cf. Figure 1.2b). Another perspective is to focus on the failure probability and rather constrain a defined limit state. This is then regarded as reliability-based design optimization (RBDO) (cf. Figure 1.2c). For comprehensive reviews the following references are given [8–10] or more recently [11].

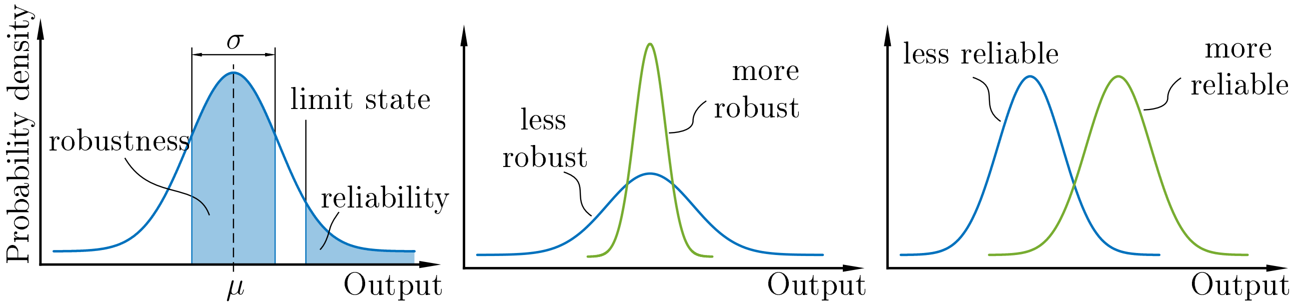

(a) RDO vs. RBDO (b) RDO (c) RBDO

Figure 1.2: Different strategies to obtain robust vs. reliable designs.

In the following the state of the art is summarized, followed by the objective and outline of this thesis.

1.1 State of the Art and Motivation

Structural optimization can be categorized into: size, shape and topology optimization. With respect to the first two categories, the latter is a method to find the best material distribution. Since regions with or without material can change in size, vanish or develop during the optimization process, topology optimization offers the highest degree of design freedom. The most prominent approach in this field is the solid isotropic material penalization (SIMP) method [1] or density-based topology optimization. Despite limitations related to the manufacturing process, topology optimization is used in a growing field of applications [2].

In this thesis, the focus is on the density-based topology optimization, which is applied to structural mechanics problems. The SIMP method is strongly linked to the finite element method (FEM) by associating one design variable to each finite element (FE). The design variables are interpreted as relative densities ranging from zero to one, which corresponds to void and solid material, respectively. By the help of an interpolation or penalization scheme, the elemental stiffness is scaled according to the design variables and penalization parameter. This is the initial and basic formulation of the SIMP method [12]. The design variables are continuous in the given range, so that gradient-based mathematical algorithms can be employed to solve a constrained optimization problem [13]. For this plain formulation, checkerboard patterns often occurred, and the solutions are mesh-dependent. Many solutions have been developed to remedy this shortcoming, but the most established solution is the variable filter [14, 15]. Since this resulted in unwanted regions with intermediate densities, a second process is established, which projects the filtered variables to nearly binary valued densities [16]. Projected variables are finally interpreted as physical densities, scaling

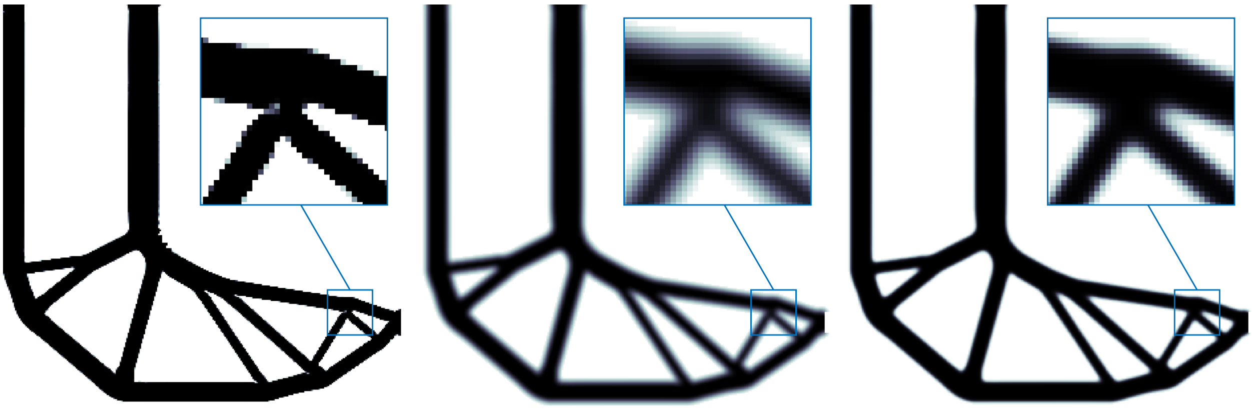

(a) Design variables $\boldsymbol{\rho}$. (b) Filtered density field $\tilde{\boldsymbol{\rho}}$. (c) Projected density field $\bar{\boldsymbol{\rho}}$.

Figure 1.3: Illustration of the three density fields.

the aforementioned elemental stiffness. An example for all three density fields is depicted in Figure 1.3. Consequently, this approach is denoted as the three field topology optimization framework, which is widely accepted and represents the current state of the art density-based topology optimization [17]. This framework forms the basis for all approaches proposed within this thesis.

1.1.1 Stress-Based Topology Optimization

Many structural components are designed with respect to their load carrying capability, especially in the automotive and aerospace sector. Consequently, stresses must be considered during the design process. This poses additional challenges to the density-based topology optimization approach mainly developed for examples of stiffness maximization, i.e. minimization of the compliance. Stress-related publications broadly agree on mentioning the singularity phenomenon and the local nature of stresses as major challenges. In the past three decades, several solutions have been proposed to overcome these difficulties.

The singularity phenomenon was first observed by Sved et al. [18] in the context of truss optimization and later discussed by others [19–21]. Consider a system of trusses where the cross-section of each truss is a continuous design variable. Decreasing the cross-section leads to increasing stress, while the optimal solution might be to remove a truss completely. This is identified as a degenerated design space where the singular optimum cannot be reached by gradient-based optimization algorithms. Senhora et al. [22] showed the same behavior for two-dimensional continuum elements. A common approach is to increase accessibility to the optimum by relaxing the design space with for example the ϵ-relation approach [23]. This is first applied to continuum problems by Duysinx et al. [24]. Inspired by the idea of stress relaxation, several other common approaches were developed, such as the *qp*-approach [25], the rational approximation of material properties (RAMP) approach [26, 27] or the power law used for SIMP.

By definition, stresses are defined locally on element level. Thus, constraining each elemental stress results in a very inefficient optimization problem, if not impractical. Additionally, optimizing for stresses is at hand not very meaningful. It is rather reasonable to consider the worst-case or maximum stress, which is then referred to as global strategy. Since topology optimization problems are usually solved with gradient-based algorithms [13], the maximum stress function needs to be differentiable. This and other circumstances lead to many approaches utilizing and suggesting different aggregation functions to approximate the maximum (for a comprehensive review and discussion see [28–33]). Regarding stress-based optimization, the majority of the literature adopted this global strategy by aggregating all stress values into a single one. However, the global measure is frequently found to be too inaccurate. To increase the approximation accuracy, some researchers proposed to split the high amount of stress constraints into smaller clusters and aggregate over each individually [33–36]. This can increase the quality of the result for low aggregation parameters but comes with an increased numerical effort. Nevertheless, by employing the adjoint sensitivity analysis [37, 38], the optimization becomes very efficient in sense of numerical cost.

Despite its efficiency, the application of this global strategy seems to be limited regarding models with millions of stress constraints [30]. The augmented Lagrangian method avoids aggregation techniques and is referred to as local strategy. It was first proposed by Fancello et al. [39] and Pereira et al. [40]. Since then, a growing number of publications related to this approach and density-based topology optimization emerged [6, 22, 41–48], showcasing examples with more than half a billion stress constraints [49, 50]. Silva et al. [30] compared global and local strategies for stress-constrained topology optimization problems and concluded, that the global approach is competitive, but requires higher aggregation parameters and more iterations for bigger models. Assis Pereira et al. [51] compared the augmented Lagrangian method to a single aggregation function, but only found minor benefits in following the local approach.

The major difficulty for stress-based optimization is probably the high nonlinearity related to stresses. Although topology optimization is usually a nonlinear optimization problem, the above-mentioned aspects may lead to a poor convergence or even divergence. Especially, the aggregation parameter plays a big role for convergence control. A lower aggregation parameter generally leads to a smoother objective and constraint history, but also reduces the approximation quality. While this is of minor importance in stress minimization problems, an accurate approximation is essential for stress-constrained problems. Consequently, a good compromise has to be found [21, 24, 33, 34]. Furthermore, the approximated stress can efficiently be scaled to fit the actual maximum stress or clustered while maintaining a good convergence [34].

Another convergence influencing aspect is the projection function. Traditionally, a 0-1 design is targeted, avoiding intermediate densities. Yet, this leads to an increased oscillation of the stress response. In the context of uniform boundary variations, Silva et al. [52] suggested limiting the sharpness of the projection function to create a gradual transition between the void and material phases. This approach smooths the stress response and enhances accuracy at the boundary. Additionally, it helps to reduce non-linearity and improve convergence behavior.

Despite some specific drawbacks of using aggregation functions described above, they are still very efficient and thus used in this thesis. Furthermore, the models shown herein are rather small-scale compared to current achievements and when it comes to robust topology optimization, it is of advantage having a single-valued function for which uncertainties can be predicted. To relax the design space, the RAMP interpolations scheme will be used throughout this work, which can be equivalently transformed to ϵ-relaxation approach. Both approaches are most often applied in stress-based optimization.

1.1.2 Topology Optimization to Increase Damage Robustness

As stated in [53] an airplane has to fulfill certain certification requirements related to fatigue or damage tolerance. One possibility of making a structure robust against a certain amount of damage is to design “multiple-load-path” or “fail-safe” structures. In the case of a localized damage, the structure must stay intact, and it has to be ensured that “catastrophic failure” will be avoided. The damage may be caused due to different circumstances, i.e. over-loading, fatigue, corrosion, manufacturing defects or accidental damage. In any case, it is important to distinguish between “damage” and “failure”. While the latter describes a global event, the first is related to local and partial effects. Optimization often results in statically determinate, truss-like and single-load-path structures. Removing one part causes it to collapse, to become unstable, or to fail completely. On the other hand, a fail-safe structure remains intact. As stated in Niu [54]: “Fail-safe structures must support 80-100% limit loads without catastrophic failure.” It is further mentioned that this requires multiple structural members with the capability of transferring loads in case a single member fails. This is similarly noted in Braga et al. [55]. In other words, redundant load paths are essential to increase damage robustness.

Earliest works related to fail-safe optimization (FSO) were published in the field of truss design [56]. Each truss is interpreted as load path and thus as possible local damage (cf. Figure 1.4a). By removing each member in a worst-case formulation, the robustness against partial damage could be increased. Later, Arora et al. [57] studied a similar problem, compared it with a nominal design optimized without failure constraints and concluded, that nominal designs fail catastrophically in case of partial damage. Feng et al. [58] introduced the term “residual strength index”, to quantify the load carrying capability of a damaged

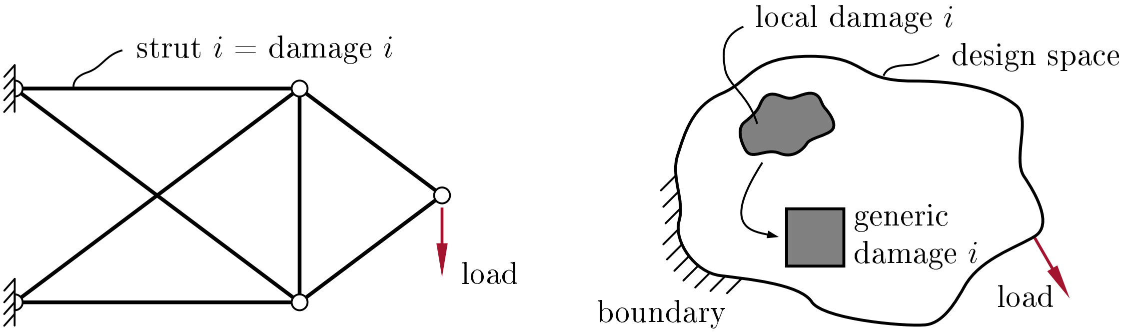

(a) Truss design (b) Continuum

Figure 1.4: Interpretation of load paths in different domains.

structure related to the nominal scenario. Since then, several authors refined, extended and proposed alternative approaches related to truss or beam optimization accounting for increased damage robustness [59–65]. A comprehensive literature review of this field can be found in [66] and [67].

While clearly distinguishable load paths are discrete members in truss designs, it requires interpretation in a continuum setting (cf. Figure 1.4). Furthermore, design features, which can be considered as load paths, do not exist at the initial phase of a density-based topology optimization. Thus, Jansen et al. [68] proposed a systematic approach, known as the damage patch method. During optimization, material is removed by a rectangular shaped area (cf. Figure 1.4b). This local damage is applied to every possible location within the design domain. As a result, in each iteration, a FE-model must be assembled and solved for each damage patch, leading to a very high computational cost. Even though several possible improvements are mentioned by Jansen et al. [68], other authors tried to cut down computing time even more. Zhou et al. [69] suggested a pragmatic approach of only considering a fraction of the generic generated damages, while Wang et al. [70] selected critical patches based on a stress criterion, reducing the numerical cost even further. Ambrozkiewicz et al. [71] evaluated fail-safe designs based on all possible damage patches and concluded that simply reducing the number of patches for optimization may cause worse failure scenarios in the final design. Thus, stepping away from the generic approach, they considered actual load path as damage patches, i.e. structural parts such as struts and nodes, which slightly increased the number of failure models. Hederberg et al. [72] employed a similar approach by projecting moving damage patches onto the design space. An inner optimization loop was implemented to determine the worst-case position and size of the patch. This method reduced the number of damage cases by half. However, the inner optimization required additional finite element calculations. Another work on geometry projection or feature mapping showed good numerical efficiency in generating fail-safe designs. In this case, the number of damage patches is equal to the number of features, since no interpretation is required [73]. Although stresses are considered in [70] and stated to be of more practical relevance than compliance [69], they are hardly considered as optimization constraint or objective in a continuum setting so far.[1] Recently, Silva et al. [74] published a work on stress-constrained FSO by utilizing the augmented Lagrangian strategy in a continuum setting. The author of this thesis presented an approach considering a stress minimization formulation, while actually removing material in accordance to the damage patch approach [75]. Since stress concentrations at sharp edges represent singularities and are assumed to influence the optimization process, different damage shapes are investigated. Evaluating the obtained fail-safe designs based on fixed shapes and positions turned out to be unpractical in the context of stresses. Inspired by [71, 76] a general load-path-based evaluation (LPE) scheme is proposed enabling good comparability. Later, Wang et al. [77] compared the worst-case and mean-performance formulations for stresses, but used generic damage shapes for post-processing. Also, Silva et al. [74] mentioned the LPE, but since this resulted in higher stresses, they did not use it for evaluation in the context of stress-constrained optimization. A fatigue stress measure is optimized by Zhao et al. [78] to generate fail-safe designs.

Prior mentioned works all considered explicit damage cases during optimization, which despite practical improvements still increased the numerical cost by at least an order of magnitude compared to the nominal case. On the other hand, damage robustness is increased by an equal amount [75]. Nonetheless, different approaches exist to create redundant load-path designs at approximately the cost of a nominal optimization. They follow the idea of controlling the maximum and minimum size of both the material and the void phase, or only one of these aspects. A very efficient and simple to implement method is known as the local volume constraint (LVC) approach [79]. It constrains the maximum size of the material phase by defining small subsets of the design domain, for which the volume is constrained. Further works dealing with maximum feature size control are [31, 80–83]. Ambrozkiewicz et al. [84] proposed a two-step optimization scheme. Here, a redundant design is generated utilizing the efficient LVC, followed by a density-based shape optimization considering actual load paths as possible damage locations. Although explicit damage patches are considered in the second step, only few iterations are required. This resulted in a very efficient framework. The author of this work also investigated LVC results for a stress-based formulation [75]. It is found that damage robustness is improved through redundant load paths, but much less than for the damage patch approach.

To this end, damage is considered in a deterministic manner, i.e. all damage scenarios are assumed to occur with an equal probability, which may lead to an unnecessary high conservatism. Thus, Cid et al. [85] proposed a reliability-based

---

[1] Verbart et al. [21] achieved damage tolerant and stress constrained designs, where material properties are degenerated if stress limits are exceeded. Nonetheless, only single-load-path designs are obtained, since they did not remove the material complete.

topology optimization framework considering the probability of each damage. A few other researchers combined uncertainties in loading and material stiffness [86] or load magnitude and direction [87] with the fixed damage approach proposed by Zhou et al. [69]. While Cid Bengoa et al. [86] and Cui et al. [88] followed a reliability-based formulation, Long et al. [87] formulated a robust topology optimization problem where uncertainties, i.e. mean value and standard deviation, are quantified by an efficient Monte Carlo simulation (MCS). This approach simply superimposes unit load cases. In the field of level-set topology optimization, Martínez-Frutos et al. [89] developed a robust formulation for a compliance-based objective function, taking into account damage probability and size.

1.1.3 Robust and Reliability-Based Topology Optimization

As mentioned at the beginning of this chapter, the least amount of stochastic information is needed for a worst-case formulation. In any case, some input has to be defined for the numerical model. This is mostly based on engineering judgment. If a force is found to be acting in a certain angular-range, one could, for example, consider the outermost angles. However, the most critical angle might be somewhere in the middle of those bounds. Consequently, all possible cases would have to be considered to capture the actual worst case. To avoid that and to save computational time, Elishakoff et al. [90] included an anti-optimization into the optimization framework. This results in a rather simple formulation for load uncertainty, but required an inner optimization loop to determine the worst-case scenario, which is then used for the actual optimization. Senhora et al. [48] proposed an efficient analytic derivation to account for continuous varying load angles. Recently, Silva et al. [6] compared a similar non-probabilistic approach to probabilistic RDO and RBDO approaches and found that this actually resulted in more conservative results.

For RDO and RBDO more stochastic information is required about the uncertain input parameters. In general, those uncertainties are then applied to the numerical model and propagated to evaluate the structural response, as depicted in Figure 1.5. This is usually very demanding from a computational standpoint, even for today's high-performance computers. Thus, computationally more efficient algorithms are required for RDO and RBDO. Note, even though those two approaches are fundamentally different from a mathematical and conceptual perspective (cf. Figure 1.2), the optimization problem can be formulated similarly, which results in comparable results [6].

Assuming enough information about the uncertain input parameters, a variety of approaches exists for the uncertainty propagation both for RDO and RBDO. A simple, but most computationally costly, is the MCS. For MCS, a number of random realizations or samples are generated and applied to the numerical model, which is then evaluated. This process can easily be parallelized, but usually

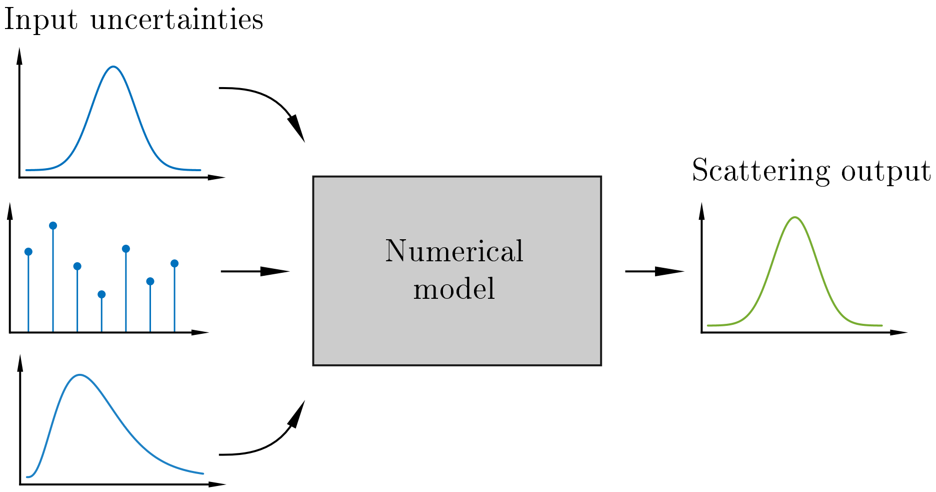

Figure 1.5: Concept of uncertainty propagation.

requires thousands of realizations to converge, which may further increase if a high reliability is targeted [91]. These realizations are then used to determine stochastic parameters needed for the probabilistic analysis. Due to the high computational cost, MCS are mostly used for post-processing or in formulations of a linear model and load uncertainty. Here, unit load cases can be calculated and efficiently superimposed with MCS (cf. to [92, 93] for instance). However, this is not possible if spatially scattering material properties or variations in geometry are considered, which led to the development of different approaches improving the computational efficiency with surrogate models [94–99]. Chatterjee et al. [100] compared different surrogate strategies and ranked them according to their reliability and usefulness. Still, the computational cost of such approaches is significantly higher than a deterministic optimization based on nominal values.

Hence, for RBDO problems, the limit stat function is usually approximated by a linear Taylor series. This is known as first-order reliability method (FORM) or Hashofer–Lind method, which is more efficient and comes with an acceptable accuracy. Still, determining the relevant limit state requires an inner optimization loop, which increases the computational cost. Earliest related works in the field of topology optimization are presented in [101–104]. To avoid the costly double-loop formulation, a more efficient strategy is to decouple the reliability assessment from the actual optimization process [105–107]. Regarding stress constraints, few works applied the decoupled approach to reliability-based topology optimization (RBTO) problems [108, 109]. Both considered uncertainties in loading and material properties. Luo et al. [110] utilized the first-order approach FORM to a stress-constrained RBTO problem, considering the allowable stress limit as a random variable. Later, uncertainties in loads are investigated in the same context [6, 111]. However, RBTO always includes an additional optimization to find the critical limit state. Another drawback of RBTO formulations is that slight variations of input uncertainties can lead to significantly different results [112]. This effect is even amplified by the fact that stochastic information about input parameters is usually very sparse and thus may exhibit strong variations.

For RDO, commonly the first and second stochastic moments, i.e. mean value and variance, are calculated and combined into a multi-objective optimization. This formulation ideally results in a lower variability of the output function, but at the cost of a higher mean or nominal value (cf. Figure 1.2). Consequently, RDO leads to a more robust and reliable design. By applying a corresponding weighting factor to the variance and combining it with the mean value (cf. Equation (5.2)), it may represent a specific limit state for a defined failure probability and can thus be equivalent to a reliability-based formulation [6]. Obviously, this is only meaningful if the constraint is subjected to variations. The advantage of RDO over RBDO is that it does not require an additional optimization. Nonetheless, even supposedly efficient approaches based on Taylor series can lead to a high computational cost. For instance, the perturbation approach expands the state equilibrium, which is very efficient for a low dimensional random space, but may become costlier than the brute force MCS for higher dimensions [113]. Hence, Silva et al. [42] suggested to only consider first-order terms, which yields designs with a lower probability of failure. Still, gradient determining can become computational expensive.

Instead of expanding the state equilibrium, the structural response function can directly be estimated by a Taylor series to calculate relevant stochastic moments. This may also be considered as a perturbation approach, as denoted by Jansen et al. [114]. Actually, no unique term has established yet, since the second-order approach is referred also to as “mean-variance” approach [9], “method of moments” [115], “second-order fourth-moment method” (SOFM) [116] or “quadratic approximation” [117]. If only linear terms are considered, this approach is more consistently denoted as “first-order second-moment” (FOSM) method [118–120]. Regarding the computational effort required to determine gradients, both first- and second-order approaches are more efficient than their counterparts, which are based on the expansion of the state equilibrium. Even though first-order approaches are deemed too inaccurate in the field of RDO and mostly second-order approaches are suggested and employed, the accuracy might still be sufficient to obtain robust designs from a practical view point. Additionally, the FOSM method promises the most potential in terms of computational cost and is thus further pursued in this work.

First works in the field of gradient-based RDO are published by Kang [5] and Doltsinis et al. [121] demonstrating the proposed formulation on truss examples. Publications in the field of robust topology optimization (RTO) are referenced in Table 1.1. Here, RTO refers to formulations where the structural response function is composed of a weighted sum of mean value and standard deviation. Usually, compliance, displacements or stresses are subjected to variations due to input perturbations. As can be noted, the majority is related to the classical compliance optimization, while only a few works are related to stresses. This fact motivated the development of a stress-based, efficient and generalized formulation of the author [122], which is recapitulated in Chapter 5. Regarding different approaches for uncertainty propagation, the latest achievements on sample-based approaches are quite remarkably. Luo et al. [123] implemented a stochastic reduced-order models (SROM) method for random load examples, which only required five model solves per iteration. However, the proposed FOSM approach required only two additional adjoint systems, which is equivalent to two model solves [122]. For gradient calculation, Krüger et al. [124] suggested a principal sensitivity formulation, which even allowed to reduce the computational cost to one additional model solve compared to a basic deterministic analysis. Additionally, the cost is independent of the amount of random variables and applicable to all combinations of response functions and random parameters. Regarding the investigated random parameter, uncertainties in load, material stiffness and geometry are well and equally covered in the literature (cf. Table 1.1). One exception being the material strength, which has not yet been considered within an RTO framework, but should be of comparable importance as a scattering geometry or material stiffness. Variations in the loading cause the most significant differences in optimized designs, as observed by several researchers. In RTO, variations in geometry are mostly modeled by considering uncertainties in the projection threshold parameter η (cf. Equation (2.14)), but also a few other variants exist. Not listed in Table 1.1 are non-probabilistic worst-case approaches such as the manufacturing tolerant three field approach suggested by Sigmund [125], where η is uniformly varied. In this case, only two additional model solves are required. Later, Wang et al. [126] improved this approach, which has recently been applied to stress-constrained problems [43, 44, 52].

Table 1.1: Publications in the field of RTO, where the robust response function is represented by a weighted average of the mean value and the standard deviation.

Publication	Year	Objective	Constr.	Random Parameter	Uncertainty Propagation
Chen et al. [127]	2010	compl.	vol.	load	QM
Asadpoure et al. [128]	2011	compl.	vol.	mat.	PA2
Lazarov et al. [94]	2011	displ.	vol.	geom.*	boosted MCS
Schevenels et al. [129]	2011	compl. displ.	vol.	geom.	basic MCS
Lazarov et al. [113]	2012	compl. displ.	vol.	geom.	PA2

Table 1.1: Publications in the field of RTO, where the robust response function is represented by a weighted average of the mean value and the standard deviation.

Publication	Year	Objective	Constr.	Random Parameter	Uncertainty Propagation
Lazarov et al. [95]	2012	displ.	vol.	geom. mat.	boosted MCS
Tootkaboni et al. [96]	2012	vol.	compl. displ.	mat.	boosted MCS
Jansen et al. [130]	2013	compl. displ.	vol.	geom.$^{+}$	basic MCS
Zhao et al. [131]	2014	compl.	vol.	load	QM
Jansen et al. [114]	2015	end-compl.	vol.	geom.*	PA2
Silva et al. [132]	2016	compl.	vol.	mat.	PA2
Martínez-F. et al. [133]	2016	compl.	vol.	mat.	boosted MCS
Silva et al. [42]	2017	vol.	stress	mat.	PA1
Keshavarzzadeh et al. [97]	2017	vol.	compl.	geom. load	boosted MCS
Silva et al. [3]	2018	vol.	stress	load	PA1
Martínez-F. et al. [134]	2018	compl.	vol.	load. mat.	boosted MCS
Rostami et al. [135]	2018	compl.	vol.	geom. mat.	boosted MCS
Zheng et al. [136]	2018	compl.	vol.	load. mat.	boosted MCS
Kriegesmann et al. [4]	2019	compl.	vol.	geom. load mat.	FOSM
Keshavarzzadeh et al. [98]	2019	compl.	vol.	mat.	boosted MCS
Silva et al. [6]	2020	vol.	stress	load	PA1
Kriegesmann [137]	2020	compl.	vol.	load. mat.	FOSM
Nishino et al. [117]	2021	end-compl.	vol.	load	SOFM
Torres et al. [138]	2021	compl.	vol.	load	boosted MCS
Thillaithevan et al. [99]	2022	compl.	vol.	geom.	boosted MCS
Steltner et al. [139]	2022	vol. compl.	stress vol.	load bound.	FOSM

Table 1.1: Publications in the field of RTO, where the robust response function is represented by a weighted average of the mean value and the standard deviation.

Publication	Year	Objective	Constr.	Random Parameter	Uncertainty Propagation
Kranz et al. [122]	2023	displ. stress	vol.	geom. mat.	FOSM
Krüger et al. [124]	2023	compl. stress	vol.	geom. cont.	FOSM
Luo et al. [123]	2024	compl.	vol.	load	boosted MCS
Krüger et al. [140]	2024	end-compl.	vol.	geom.	SOFM
Schmidt et al. [141]	2024	compl.	vol.	cont.	FOSM

bound.: boundary stiffness
cont.: contact geometry
geom.: geometry by spatially varied η cf. Equation (2.14)
geom.*: geometry by uniformly varied η cf. Equation (2.14)
geom.$^{+}$: geometry by spatially varied center for the filter kernel cf. Equation (2.13)
geom.*: node position
mat.: material stiffness (Young's modulus)
PA1: first order perturbation approach (expansion of the state equilibrium)
PA2: second order perturbation approach (expansion of the state equilibrium)
QM: quadrature method (see also Sudret et al. [142])

1.2 Objective of this Thesis

The main focus of this thesis is to develop efficient methods for topology optimization subjected to uncertainties. While the latter can be of different kind, two main topics are covered. First, robustness against local damage and secondly, robustness with respect to other uncertainties in material properties, geometry, and loading. This distinction is justified based on the type of uncertainty and the problem formulation. While local damage is considered as a binary variable, it exists or not, material properties, for example, are considered to be spatially correlated and continuous. Hence, it is reasonable to formulate a worst-case problem when damages are taken into account, while other uncertainties are incorporated into an RTO formulation.

The number of publications related to stresses increased over the past few years, yet it remains a challenging topic with open questions. As can be seen in Table 1.1, stresses are scarcely considered in RTO approaches, and shall hence be a main focus of this thesis. The major challenge stems from the fact that stresses are defined locally on element level, in difference to the global and commonly applied compliance. In general, two efficient strategies, i.e. global and local, exist to deal with the large amount of stress constraints. Within this work, the global aggregation strategy is followed, since it can directly be applied to common constrained problem formulations and does not require a reformulation into an unconstrained problem as the local approach.

Regarding the robustness against local damages, different configurations shall be investigated. Due to the local definition of stresses, the damage shape is for instance suspected to influence convergence and hence the obtained results. The number of damage patches is the main reason for the high computational cost of the original approach. Furthermore, optimizing for different damage configuration raises the question on how to evaluate and compare optimized designs? Consequently, and from a practical perspective, a unified evaluation procedure is required.

More general considerations of robustness with respect to various uncertainties are related to the field of RTO, which is characterized by a specific formulation of the constrained or optimized response function. Within this context, the main target is to improve efficiency and to investigate stress-related issues.

1.3 Outline

In Chapter 2 the general theory on stress-based topology optimization is recapitulated. First, an introduction to the general optimization problem and the common density-based approach is given, followed by a description of the stress evaluation process. Since the aggregation strategy is applied in different situations, often used functions and their properties are discussed. The domain extension approach and a formulation to constrain the minimum feature size are introduced because they are most relevant for stress-based problems, and hence included in various examples.

Chapters 3 and 4 cover the topic of damage robustness related to multiple-load-path designs, with a focus on stresses. At the beginning, an LPE scheme is motivated, followed by a formulation which explicitly incorporates local damage patches into the optimization process. Corresponding numerical results are discussed for different damage configurations. As an alternative and less computational expensive approach, a maximum-feature-size-constrained formulation is recapitulated and applied to the same examples. Additionally, the explicit formulation is combined with a minimum feature size constraint showing beneficial structural performance. To verify obtained results, all designs are validated through contour models.

The second main subject is robust topology optimization in the context of stresses (see Chapter 5 and 6). A generalized first-order approach is derived, which is applicable to different uncertain parameters. Special attention is paid to the post-processing of scattering boundary perturbations, emphasizing a suitable evaluation scheme. Results are shown for uncertainties in material stiffness and strength, as well as geometry perturbations and variations in loading. Furthermore, the robust stress function is formulated as objective or as constraint. In the latter case, the robust function can be interpreted as a reliability constraint for which mentioned uncertainties are either considered individually or simultaneously during optimization.

In Chapter 7, the most important results are recapitulated and conclusions are summarized.

The Appendix is divided into three sections. The first is related to Chapter 2 and includes general supplementary material. The second part features details for damage robustness optimization, and the last part is dedicated to additional material required for the proposed RTO approach.

Chapter 2

Theory on Stress-Based Topology Optimization

This chapter is dedicated to the theoretical background of topology optimization. General and fundamental methods are summarized and discussed, forming the basis for the in depth investigated methods of Chapters 3 to 6. Since major parts of this research is stress-related, processing and calculation of such is described, and specific aspects are analyzed.

2.1 General Optimization Methodology

In structural optimization, the goal is usually to minimize a certain objective or cost function f subjected to one or more constraints c_j. Both are most often evaluated on a discrete finite element model, which approximates the solution of partial differential equations. This results in a non-linear system of equations $\mathbf{R} = \mathbf{0}$, called state equilibrium. Solving it yields the physical state variables $\mathbf{u}$, which may represent deformation, temperature, velocity, or others. A typical structural optimization problem can be formulated as follows:

$$\begin{aligned} \min_{\mathbf{v}} \quad & f\left(\mathbf{v},\mathbf{u}\right) && \mathbf{v} \in \mathbb{R}^{n_v} \\ \text{s.t.} \quad & c_j\left(\mathbf{v},\mathbf{u}\right) \leq 0 && j = 1,\ldots,n_c \\ & \mathbf{R}\left(\mathbf{v},\mathbf{u}\right) = \mathbf{0} \Rightarrow \mathbf{u}\left(\mathbf{v}\right) && \mathbf{u} \in \mathbb{R}^{n_u}\ , \end{aligned} \tag{2.1}$$

where $\mathbf{v}$ are the design variables.

Figure 2.1 summarizes the general iterative optimization process. Within this work, the focus is on methods related to processes in the top row. Update of design variables is left to a mathematical optimization algorithm, as mentioned below. The pre-processing process includes everything from setting up the finite element model to calculating all quantities which are constant throughout the optimization process. The latter is a repeated process of model evaluations followed

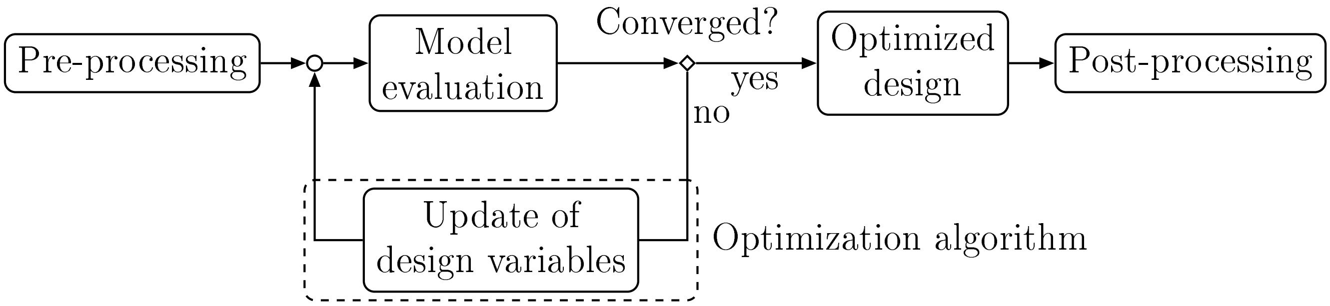

Figure 2.1: General iterative optimization process.

by design variable updates. When defined stopping criteria are met, the optimization is considered as converged and an optimized design is obtained. Finally, the optimization result is evaluated and verified in the post-processing step. Although the actual optimization is completed at this point, another run might be necessary if the obtained design turns out to be non-optimal during the post-processing step. This is for example the case if some requirements are only considered implicitly during optimization, as it is the case in Section 4.3. Hence, when comparing the computational cost of different approaches or problem formulations, this aspect has to be considered as well.

In the field of topology optimization, design variables $\mathbf{v}$ are referred to as relative densities $\boldsymbol{\rho}$, which are bound between zero and one. Thus, including box constraints for design variables, the general problem (2.1) transforms to

$$\begin{aligned} \min_{\boldsymbol{\rho}} \quad & f\left(\boldsymbol{\rho},\mathbf{u}\right) && \boldsymbol{\rho}\in\mathbb{R}^{n_\rho} \\ \text{s.t.} \quad & c_j\left(\boldsymbol{\rho},\mathbf{u}\right)\leq 0 && j=1,\dots,n_c \\ & 0\leq \rho_i\leq 1 && i=1,\dots,n_\rho \\ & \mathbf{R}\left(\boldsymbol{\rho},\mathbf{u}\right)=\mathbf{0}\Rightarrow\mathbf{u}\left(\boldsymbol{\rho}\right) && \mathbf{u}\in\mathbb{R}^{n_u}\ . \end{aligned} \tag{2.2}$$

In this general formulation, f and c_j can be any design response $\mathcal{F}\left(\boldsymbol{\rho},\mathbf{u}\right)$. Within this work, the focus is on mechanical aspects. Thus, common functions considered for topology optimization are compliance, stresses, displacements and volume. A prominent example is the minimization of compliance constrained by a given volume. In contrast to that, a classical strategy in lightweight design is to find the lowest volume, while satisfying a given allowable stress value. Nonetheless, formulation (2.2) is not limited to the mentioned design responses.

The problem in Equation (2.2) can be solved efficiently by any gradient-based optimization algorithms if derivatives are provided. Schittkowski et al. [143] compared different approaches with limited validity. While aiming at an improved convergence behavior for stress-related problems, other authors discuss existing formulations and propose extensions [47, 144]. Summarizing, only slight improvements could be achieved, but due to strong problem dependencies and made compromises, no dominating optimization algorithm could be found. In most regards, the method of moving asymptotes (MMA) [145] seemed to be versatile, adaptive, and generally applicable to several topology optimization scenarios. In stress-based formulations, the MMA is actually most often applied [146]. Hence, the MMA is utilized as an optimization algorithm within this work. Even though it comes with a procedure to control move limits for the design variables, another exterior limit is imposed to stabilize convergence. The absolute change of ρ_i is simply limited to

$$\Delta\rho_i = |\rho_i^{k-1} - \rho_i^k| \,, \tag{2.3}$$

where k is the current iteration. In most cases, design variables are limited to $\Delta\rho_{max} = 0.05$ if not stated otherwise.

The optimization process is usually terminated when the normalized change in design variables reaches a certain threshold:

$$\frac{1}{\Delta\rho_{max}\sqrt{n_\rho}}||\Delta\boldsymbol{\rho}|| \leq 0.02. \tag{2.4}$$

In addition, the constraint has to be fulfilled as well as the relative change of the objective values in Equation (2.5).

$$|f^{k-1} - f^k| \leq 0.005. \tag{2.5}$$

Furthermore, all parameters subjected to some kind of continuation scheme should have reached their predefined maximum value. Another stopping criterion considered, but hardly reached, is the relative maximum change in design variables:

$$\frac{1}{\Delta\rho_{max}} \max(\Delta\boldsymbol{\rho}) \leq 0.2. \tag{2.6}$$

Threshold values given in Equation (2.4) to (2.5) are determined empirically, and found to give good results.

All other parameters are kept constant. For the MMA only first-order derivatives are required, which are preferably calculated by the adjoint sensitivity analysis (cf. [13, 37, 38]). Differentiation of any design response $\mathcal{F}$ yields

$$\frac{D\mathcal{F}}{D\boldsymbol{\rho}} = \frac{\partial\mathcal{F}}{\partial\boldsymbol{\rho}} - \boldsymbol{\lambda}^{\mathrm{T}}\frac{\partial\mathbf{R}}{\partial\boldsymbol{\rho}} \,. \tag{2.7}$$

Note, for partial derivatives $\frac{\partial\circ}{\partial\circ}$ only directly dependent terms are differentiated (for details see Appendix A.1). The Lagrange vector $\boldsymbol{\lambda}$ is determined by solving the following system of equations, referred to as an adjoint system:

$$\frac{\partial\mathbf{R}^{\mathrm{T}}}{\partial\mathbf{u}}\boldsymbol{\lambda} = \frac{\partial\mathcal{F}}{\partial\mathbf{u}} \,. \tag{2.8}$$

This restricts the optimization algorithm to solutions $\mathbf{u}\,(\boldsymbol{\rho})$ that satisfy $\mathbf{R} = \mathbf{0}$.

2.2 Density-Based Three Field Topology Optimization

Topology optimization problems discussed within this thesis are based on a linear structural analysis. Thus, the discrete state equilibrium from (2.2) can be formulated as

$$\mathbf{R}\left(\boldsymbol{\rho}, \mathbf{u}\right) = \mathbf{K}\left(\boldsymbol{\rho}\right)\mathbf{u}\left(\boldsymbol{\rho}\right) - \mathbf{f} = \mathbf{0} \, , \tag{2.9}$$

where $\mathbf{K}$ is the global stiffness matrix and the state variable vector $\mathbf{u}$ contains nodal displacements. While, the load vector $\mathbf{f}$ may depend on design variables in self-weight problems, it is beyond the scope of this work. Hence, $\mathbf{f}$ is assumed to be constant with respect to design variables $\boldsymbol{\rho}$.

The fundamental concept of density-based topology optimization is to represent a material distribution by a field of relative densities $\boldsymbol{\rho}$ on a fixed finite element mesh with n_e elements. Normally, each density ρ_i is linked to one element $i = 1, \ldots, n_e$, scaling the elemental stiffness matrix k_e. Due to numerical aspects, the relative densities need to be regularized. The three-field approach is broadly adopted [17], including not only the initial ρ_i, but also filtered $\tilde{\rho}_e$ (see Section 2.2.1) and projected density fields $\bar{\rho}_e$ (see Section 2.2.2). For an illustration of all three density fields, see Figure 1.3. The projected densities are interpreted as physical variables, which scale the elemental stiffness matrix as follows:

$$\mathbf{k}_e\left(\bar{\rho}_e, E_0\right) = E_e\left(\bar{\rho}_e, E_0\right)\mathbf{k}_e^0 \, , \quad \text{with} \quad \mathbf{k}_e^0 = \int_{\Omega_e} \mathbf{B}_e^{\mathrm{T}}\mathbf{C}_0\mathbf{B}_e d\Omega \, , \tag{2.10}$$

where $\mathbf{C}_0$ represents the material stiffness matrix for unit Young's modulus, $\mathbf{B}_e$ is the strain-displacement matrix for element e and E_e is the penalized stiffness (see Section (2.2.3)). The domain for element e is defined as Ω_e.[1] Finally, local matrices $\mathbf{k}_e$ are assembled to form the global stiffness matrix as follows

$$\mathbf{K} = \mathop{\mathsf{A}}_{e} \mathbf{k}_e \, , \tag{2.11}$$

where A is the assembly operator.

Details on the variable filter and projection, as well as the SIMP approach, are discussed below. For further details and alternatives, the interested reader is referred to [17].

2.2.1 Variable Filter

Classical density filtering is applied to avoid numerical difficulties related to the checkerboard problem and mesh dependency. It averages densities linearly ac-

---

[1] Within this work, linear square elements are used and four Gaussian points per element are considered for numerical integration.

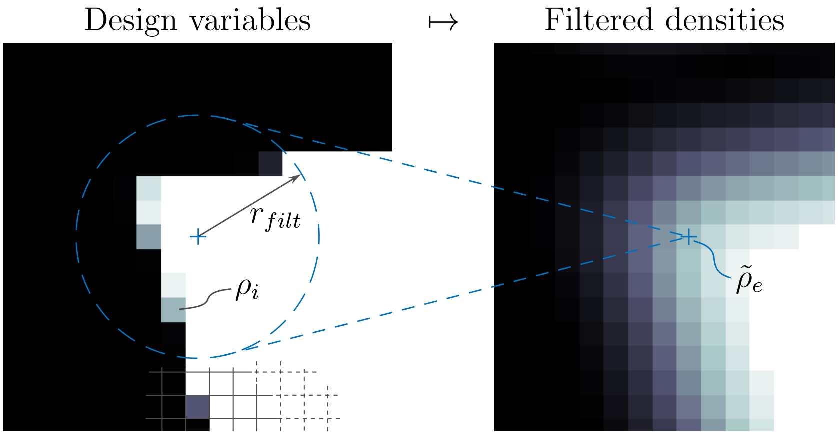

Figure 2.2: Illustration of the filtering process.

cording to weighted distance in a circular or spherical neighborhood $\mathcal{N}_e$ of element e [14, 15].

$$\mathcal{N}_e\left(r_{filt}\right)=\left\{i|r_{filt}\geq\|\mathbf{x}_i-\mathbf{x}_e\|\right\}\ , \tag{2.12}$$

where r_{filt} is the filter radius, $\mathbf{x}_i$ and $\mathbf{x}_e$ are center coordinates of element i and e, respectively. The filtered density for each element $\tilde{\rho}_e$ is then calculated as follows:

$$\tilde{\rho}_e\left(\rho_i, r_{filt}\right)=\frac{\sum_i^{\mathcal{N}_e} w\left(\mathbf{x}_i\right) v_i \rho_i}{\sum_i^{\mathcal{N}_e} w\left(\mathbf{x}_i\right) v_i}\ , \tag{2.13}$$

where $w\left(\mathbf{x}_i\right)=r_{filt}-\|\mathbf{x}_i-\mathbf{x}_e\|$ is a conic weighting function, v_i is the volume, and ρ_i is the density of the neighbor element i.

2.2.2 Projection Function

Historically, the SIMP method penalizes intermediate densities, driving the solution towards a binary design. Nevertheless, results may include intermediate density values, due to the averaging effect of the filter. To further penalize intermediate densities, a common approach is to project the filtered variables by a smooth and differentiable Heaviside function. Initial research is conducted by Guest et al. [147] and Sigmund [148]. Later, Xu et al. [16] combined the two approaches to a so-called intermediate projection filter [17]. Wang et al. [126] simplified it based on tanh-functions to

$$\bar{\rho}_e\left(\tilde{\rho}_e, \eta_e, \beta\right)=\frac{\tanh\left(\beta\eta_e\right)+\tanh\left(\beta\left(\tilde{\rho}_e-\eta_e\right)\right)}{\tanh\left(\beta\eta_e\right)+\tanh\left(\beta\left(1-\eta_e\right)\right)}\ , \tag{2.14}$$

with β being the projection parameter, which controls the approximation steepness (see Figure 2.3a). An almost linear projection is achieved for $\beta=1$. For $\beta\rightarrowtail\infty$ it becomes the step function. Generally, increasing this parameter reduces intermediate density values, but it also increases the non-linearity of the problem.

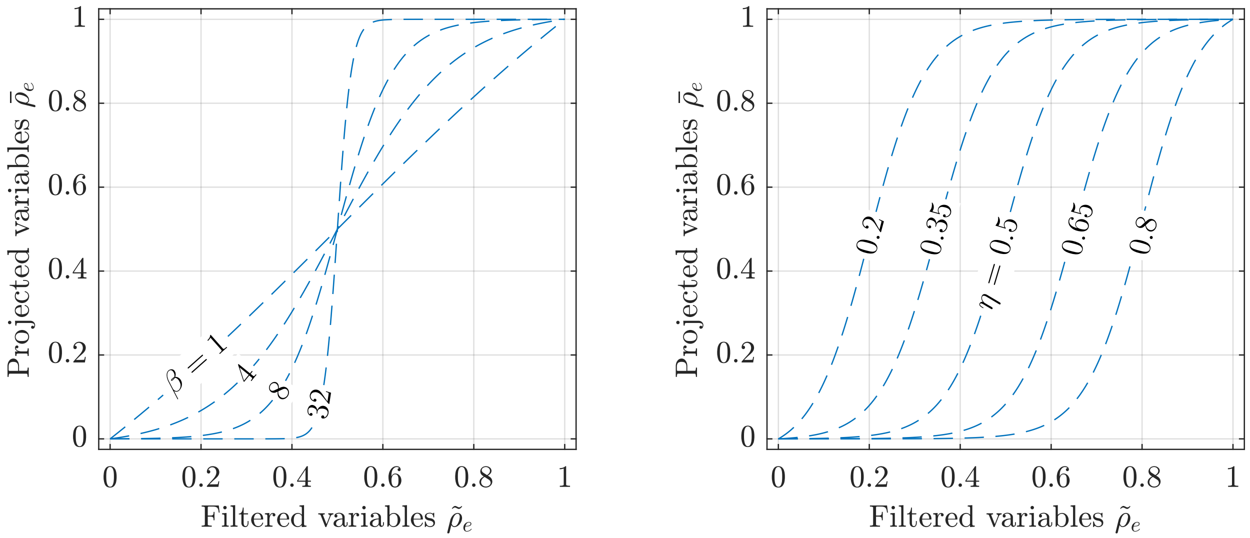

(a) Fixed projection parameter $\beta = 8$ and varied threshold parameter η.

(b) Varied projection parameter β and fixed projection threshold $\eta = 0.5$.

Figure 2.3: Projection function evaluated for different threshold and projection parameters, respectively.

Thus, β is often gradually increased during optimization. This method is known as the continuation approach and helps to avoid numerical instabilities, improving convergence behavior. Parameter $\eta_e \in [0, 1]$ controls the inflection point (see Figure 2.3b) and is denoted as projection threshold.[2] For $\eta = 0$ or $\eta = 1$ a feature size constraint is imposed on the material or void phase, respectively [126]. Wang et al. [126] concluded, that there is no explicit feature size constraint if intermediate values are used. To remedy this shortcoming, they proposed the manufacturing tolerant three-field formulation (see Section 2.6). Another important aspect in stress-based formulations is related to the choice of the projection parameter (see Section 2.3).

2.2.3 Stiffness interpolation

The modified SIMP scheme [148] is applied to interpolate the elemental stiffness E_e with respect to the physical densities $\bar{\rho}_e$ as follows:

$$E_e(\bar{\rho}_e, E_0,) = \xi_e(\bar{\rho}_e)(E_0 - E_{min}) + E_{min} \tag{2.15}$$

with $E_{min} = 1e^{-9}$ being a small number to avoid singular stiffness matrix for densities approaching zero. E_0 is the material's Young's modulus. The penalization term $\xi_e = \xi_e^{SIMP}$ yields:

$$\xi_e^{SIMP}(\bar{\rho}_e) = \bar{\rho}_e^{p^{SIMP}} , \tag{2.16}$$

---

[2] The parameter η_e is usually equal in all elements, thus $\eta_e = \eta$. If geometric perturbations shall be modeled, for instance in RTO, one possibility is to vary this parameter on element level, resulting in $\eta_e \neq \eta$.

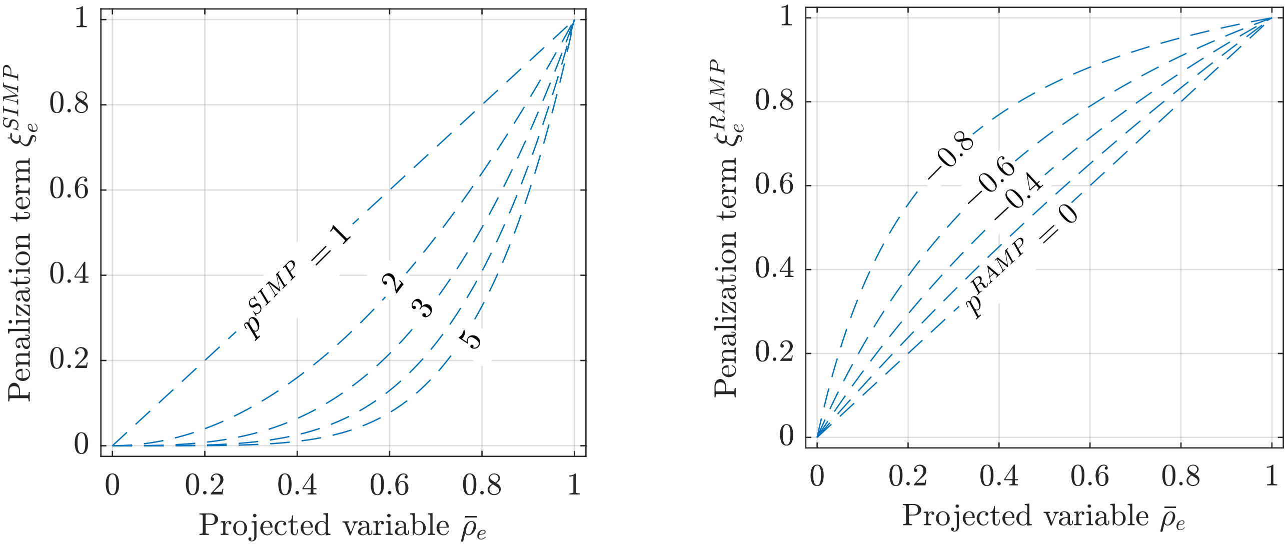

(a) Stiffness interpolation SIMP.

(b) Stress interpolation RAMP.

Figure 2.4: Interpolation functions used for stiffness and stress interpolation, respectively.

where the exponent is usually $p^{SIMP} = 3$. In Figure 2.4a Equation (2.16) is evaluated for different exponents.

2.3 Stress Evaluation

Stresses are calculated per element e and Gaussian point g. To avoid singular optima and to relax the design space, stresses are interpolated. The elemental stress tensor in Voigt notation can be calculated as follows for each Gaussian point:

$$\boldsymbol{\sigma}_e^g = \mathbf{C}_e \boldsymbol{\epsilon}_{e,g} = \mathbf{C}_e \mathbf{B}_{e,g} \mathbf{u}_e \quad \text{with} \quad \mathbf{C}_e = E_e \left(\bar{\rho}_e\right) \mathbf{C}_0 \,, \tag{2.17}$$

where $\mathbf{u}_e$ is the elemental displacement vector, $\mathbf{B}_{e,g}$ is the discretized strain-displacement matrix for element e and Gaussian point g. The constitutive matrix is $\mathbf{C}_0$. For a regular grid, $\mathbf{B}$ and $\mathbf{C}_0$ are constant across all elements, which can be used to improve efficiency of the implemented calculation. Linear elastic material behavior and plane strain condition are assumed.

For stress calculations, the material stiffness E_e is determined as defined in Equation (2.15). However, in contrast to the local stiffness matrix (cf. Equation (2.10)), the interpolation function is replaced by $\xi_e = \xi_e^{RAMP}$. Consequently, the constitutive matrix is scaled by applying the rational approximation of material properties (RAMP) scheme [26, 27]. The penalization term is defined as follows

$$\xi_e^{RAMP}(\bar{\rho}_e) = \frac{\bar{\rho}_e}{1 + p^{RAMP}(1 - \bar{\rho}_e)} \,, \tag{2.18}$$

where p^{RAMP} is the RAMP interpolation parameter. Since stresses are only evaluated at the element's center, indices e and g are equivalent.

Hence, equivalent von Mises stresses are calculated as

$$q_e = \sqrt{\boldsymbol{\sigma}_e^{\mathrm{T}} \mathbf{M} \boldsymbol{\sigma}_e} = \sqrt{\mathbf{u}_e^{\mathrm{T}} \mathbf{B}^{\mathrm{T}} \mathbf{C}_e^{\mathrm{T}} \mathbf{M} \mathbf{C}_e \mathbf{B} \mathbf{u}_e} \tag{2.19}$$

with $\mathbf{M}$ being a constant matrix for plain stress state

$$\mathbf{M} = \begin{bmatrix} 1 & -\frac{1}{2} & 0 \\ -\frac{1}{2} & 1 & 0 \\ 0 & 0 & 3 \end{bmatrix} . \tag{2.20}$$

The equivalent stress in Equation (2.19) can directly be aggregated and used for a minimum stress optimization. When stresses are considered as constraint, a strength factor SF is defined together with an allowable stress q_0. The latter is usually set by the designer and depends on the application and material. The following constraint definition is obtained:

$$c_q = \max_e \left(SF_e\right) - 1 \leq 0 \quad \text{with} \quad SF_e = \frac{q_e}{q_0} \tag{2.21}$$

Depending on the problem formulation, the projection parameter β (2.14) is often increased until a close to binary design is obtained. However, especially for stress-based problems, a value that is too high results in a diverging optimization. Furthermore, when approaching a discrete design, boundaries appear jagged and hence stresses are distorted. To increase the accuracy of stress at the boundary, it can be beneficial to allow a transition area with intermediate densities, which also helps smooth the optimization process. (see Section 2.7.2 for a detailed discussion).

As discussed in Section 2.4 the aggregation either under- or overestimates actual extreme values. In other words, the relative error is big for low aggregation parameters. This is practically not acceptable, especially if the constraint is aggregated. While conservative assumptions might lead to valid results, the full potential will never be exploited. Hence, one possible workaround is to normalize the aggregated value by a scaling factor γ inspired by Le et al. [34], Oest et al. [149], and Zhang et al. [150]:

$$\mathcal{F} = \gamma \mathcal{F}_A, \quad \text{with} \quad \gamma = \frac{1}{n_i} \sum_{k=1}^{n_i} \frac{\mathcal{F}_0^{(k)}}{\mathcal{F}_A^{(k)}} , \tag{2.22}$$

where $\mathcal{F}_0$ is the extreme value and $\mathcal{F}_A$ is its approximation. To avoid too strong oscillation, the scale factor is averaged over the last iterations n_i. This is found to allow a smooth convergence and yields good results (cf. Figure A.3).

2.4 Aggregation Functions

In this section, commonly used aggregation functions are presented and discussed, which are applied to approximate the extreme values of a given data set. These functions are differentiable, an essential property for gradient-based optimization problems. As an example, different data sets can be aggregated using these functions. In stress-based topology optimization, the maximum von Mises stress, derived from all elemental stresses q_e, as shown in Equation (2.19), is the quantity of interest. For a maximum feature size optimization, the maximum local volume fraction, derived from all elemental volume fractions φ_e, as defined in Equation (3.2), is considered.

In Figure 2.5 two graphs are given for two different data sets, one for an initial and another one for an optimized density distribution. Both data sets are taken from a cantilever example, which has been optimized for stresses q_e subjected to a global and local volume constraint as formulated in Equation (3.2). For both, initial an optimized state, density fields and stress fields are depicted in Figure A.5. The data sets for q_e is characterized by few high stress values, which decrease by approximately an order of magnitude during optimization. Note, that initial densities are uniformly distributed in the design domain, while densities in the domain extension are set to zero. The latter explains approximately 10% zero stress values and local volume fractions below 0.4 for the initial case. During optimization, the number of zero stress values increases due to a redistribution of material, which is then better utilized. The local volume fraction values are initially uniform but transform into a distribution similar to that of the stresses. The following section discusses the properties of common aggregation functions for these four characteristic data sets.

Kreisselmeier-Steinhauser (KS) [151, 152] and p-like, e.g. p-norm or p-mean, aggregation functions are commonly used to approximate extreme values. Both come with an *upper bound* and a *lower bound* versions (cf. Equation (2.23) to (2.26)). While extreme values are overestimated in the *upper bound* case, they are underestimated in the *lower bound* case. A shared characteristic is, that the approximation quality, or in other words the relative error between actual and approximated value, can be controlled by the aggregation parameter p. A higher value leads to better approximation, see Figure 2.6 and 2.7. This is usually desired, but raises some drawbacks for gradient-based optimization, since it increases the non-linearity of the problem and can lead to a diverging optimization. Thus, choosing a proper aggregation parameter is always a compromise between a low approximation error and a smooth convergence.

$$\mathcal{A}_{PN,ub}\left(\mathcal{F}_e, p\right) = \left(\sum_{e=1}^{n_e} \mathcal{F}_e^p\right)^{\frac{1}{p}}, \qquad \text{with} \quad \mathcal{F}_e \in \mathbb{R}^+ \tag{2.23}$$

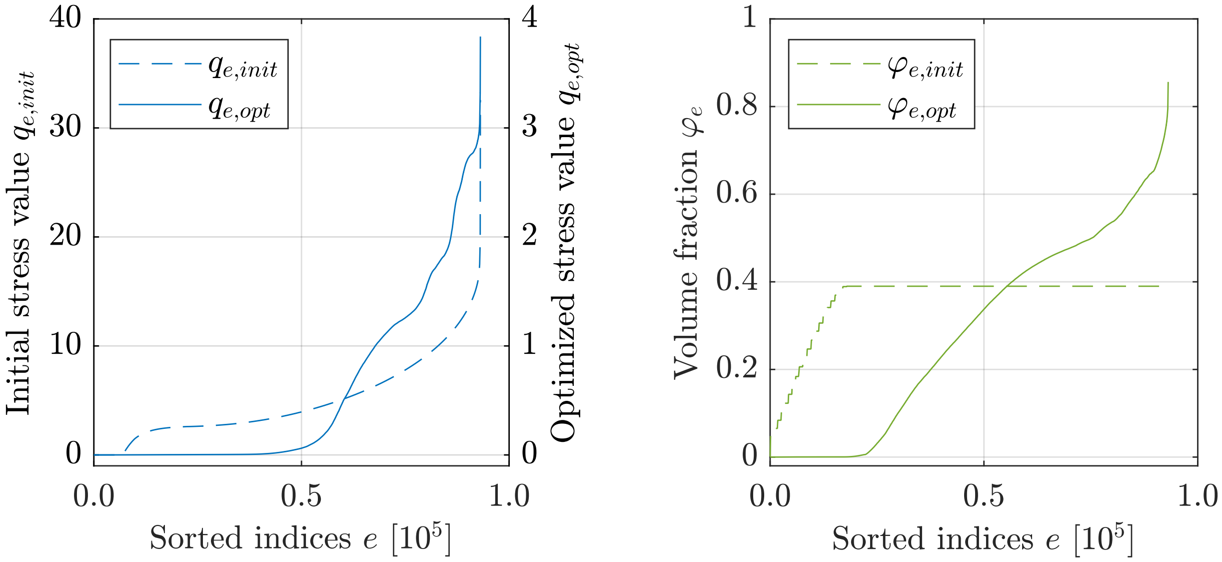

(a) Elemental von Mises Stress q_e

(b) Local volume fraction φ_e

Figure 2.5: Different data sets for initial (uniform) and optimized densities taken from an arbitrary cantilever example (cf. Figure A.5).

$$\mathcal{A}_{PM,lb}\left(\mathcal{F}_e, p\right) = \left(\frac{1}{n_e}\sum_{e=1}^{n_e} \mathcal{F}_e^p\right)^{\frac{1}{p}}, \qquad \text{with} \quad \mathcal{F}_e \in \mathbb{R}^+ \tag{2.24}$$

$$\mathcal{A}_{KS,ub}\left(\mathcal{F}_e, p\right) = \frac{1}{p}\log\left(\sum_{e=1}^{n_e} \mathrm{e}^{p\mathcal{F}_e}\right), \qquad \text{with} \quad \mathcal{F}_e \in \mathbb{R} \tag{2.25}$$

$$\mathcal{A}_{KS,lb}\left(\mathcal{F}_e, p\right) = \frac{1}{p}\log\left(\frac{1}{n_e}\sum_{e=1}^{n_e} \mathrm{e}^{p\mathcal{F}_e}\right), \quad \text{with} \quad \mathcal{F}_e \in \mathbb{R} \tag{2.26}$$

Figure 2.6 depicts the relative error of the p-norm and p-mean function for the four data sets depicted in Figure 2.6. The relative error is calculated as $|\mathcal{A}_\circ - \mathcal{F}_0|/\mathcal{F}_0$, where $\mathcal{A}_\circ$ is the approximated value and $\mathcal{F}_0$ the actual extreme value. As can be observed, the p-mean function is very accurate for any aggregation parameter for a uniformly distributed data set (cf. φ_{init}). The relative error decreases in the other cases, but slower than the p-norm function, which is worse for the uniform case. In both cases, the difference between both optimized data sets is rather small, indicating that p-like functions are independent of how the data is scaled. They depend on the data distribution only [29].

In Figure 2.7 the relative error is depicted for the upper bound KS-functions. A special aspect about KS-functions is, that the approximation accuracy is not only depending on the data distribution, but also on how the data is scaled. As can be seen in 2.7a for the initial stress case, the relative error is very low for small aggregation parameters ($p < 10$). Thus, as described in [68], the aggregation parameter is usually adapted to a predefined exponential argument ($p\mathcal{F}_0 = \text{constant}$)

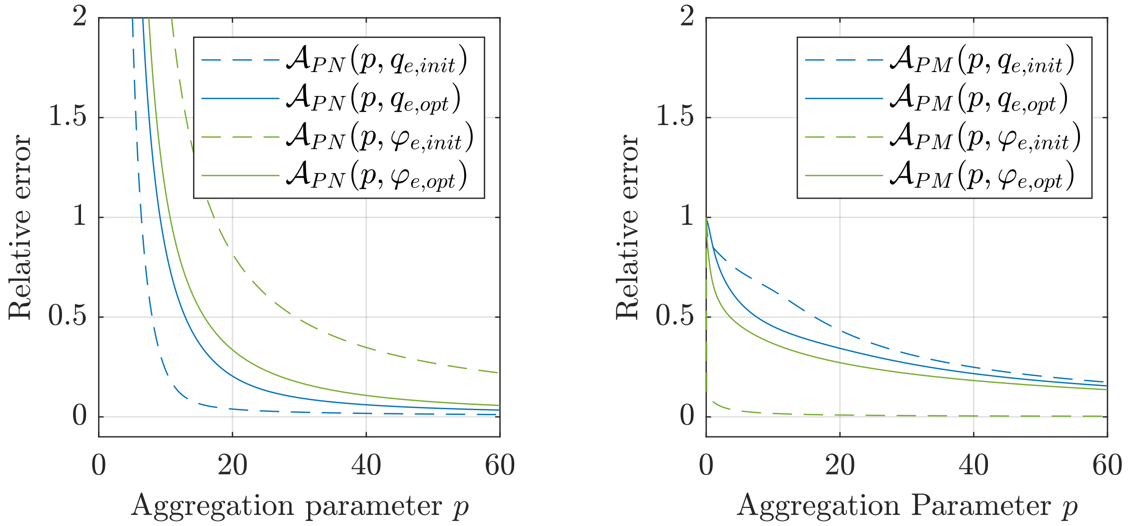

(a) p-norm (b) p-mean

Figure 2.6: Relative error of p-like functions for different data sets.

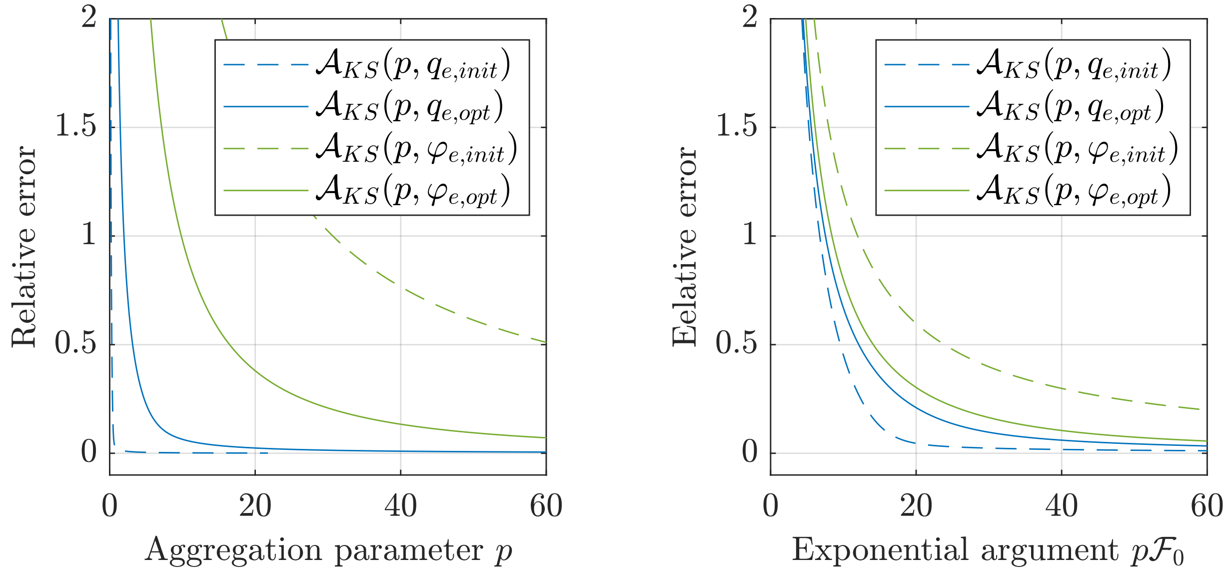

(a) p-controlled (b) p-adapted

Figure 2.7: Relative error of the upper bound KS-function for different data sets.

during optimization (cf. Figure 2.7b). Compared to the p-norm, KS-functions can process negative values, data containing mixed signs, and they can approximate minima by setting the aggregation parameter to a negative value. For the presented data sets, both upper bound functions perform very similarly if the aggregation parameter is adapted for the KS-functions (compare Figure 2.6a and 2.7b).

To avoid numerical overflow, the data set can be uniformly scaled for p-like functions. For the KS-function an alternative formulation exists [153, 154]:

$$\mathcal{A}^{*}_{KS,ub} = \mathcal{F}_0 + \frac{1}{p}\log\left(\sum_{e=1}^{n_e} \mathrm{e}^{p(\mathcal{F}_e-\mathcal{F}_0)}\right), \quad \text{with} \quad \mathcal{F}_e \in \mathbb{R} \tag{2.27}$$

where $\mathcal{F}_0 = \max\left(\mathcal{F}_e\right)$ is treated as constant. Note, that $\mathcal{F}_0$ chances in each iteration. Equation (2.28) proofs, that both formulations are equivalent and treating $\mathcal{F}_0$ as constant is a valid assumption.

$$\begin{aligned}
\mathcal{A}^{*}_{KS,ub} &= \tfrac{1}{p}\log\left(\sum_{e=1}^{n_e} \mathrm{e}^{p(\mathcal{F}_e-\mathcal{F}_0)}\right) + \mathcal{F}_0 \\
&= \tfrac{1}{p}\log\left(\sum_{e=1}^{n_e} \mathrm{e}^{p\mathcal{F}_e}\mathrm{e}^{-p\mathcal{F}_0}\right) + \mathcal{F}_0 \\
&= \tfrac{1}{p}\log\left(\sum_{e=1}^{n_e} \mathrm{e}^{p\mathcal{F}_e}\right) + \tfrac{1}{p}\log\left(\mathrm{e}^{-p\mathcal{F}_0}\right) + \mathcal{F}_0 \\
&= \tfrac{1}{p}\log\left(\sum_{e=1}^{n_e} \mathrm{e}^{p\mathcal{F}_e}\right) - \mathcal{F}_0 + \mathcal{F}_0 \\
&= \tfrac{1}{p}\log\left(\sum_{e=1}^{n_e} \mathrm{e}^{p\mathcal{F}_e}\right) \\
&= \mathcal{A}_{KS,ub}
\end{aligned} \tag{2.28}$$

As mentioned before, choosing the proper aggregation parameter is always a compromise. Exemplary, the aggregation parameter is varied for the p-norm function both for a stress-constrained and a volume-constrained formulation, respectively. Optimization is performed on the L-beam model (see Figure 4.12), which is discretized with 400 × 400 unit sized elements including domain extensions (see Section 2.5). The load is defined as $F = 10$, the Young's modulus is $E_0 = 3$ and the Poisson's ratio is $\nu = 0.3$. The filter radius is $r_{filt} = 8$ and the maximum projection parameter is $\beta = 8$. Optimized results are post-verified by contour models. For a detailed description on how contour models are generated, see Section 2.7.

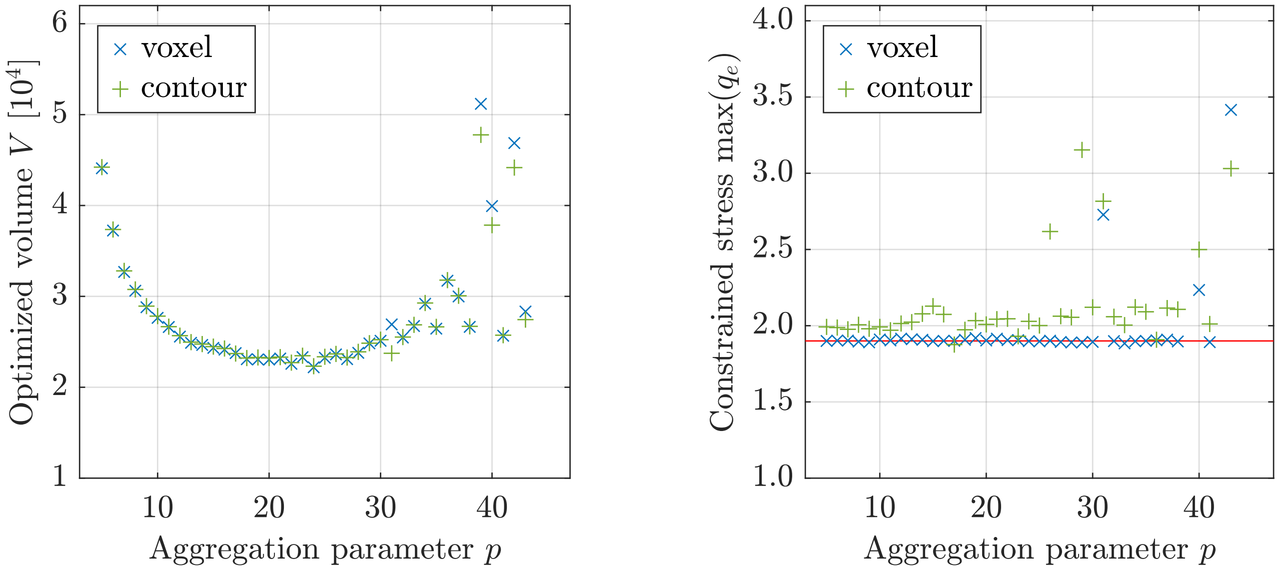

(a) Stress-constrained optimization.

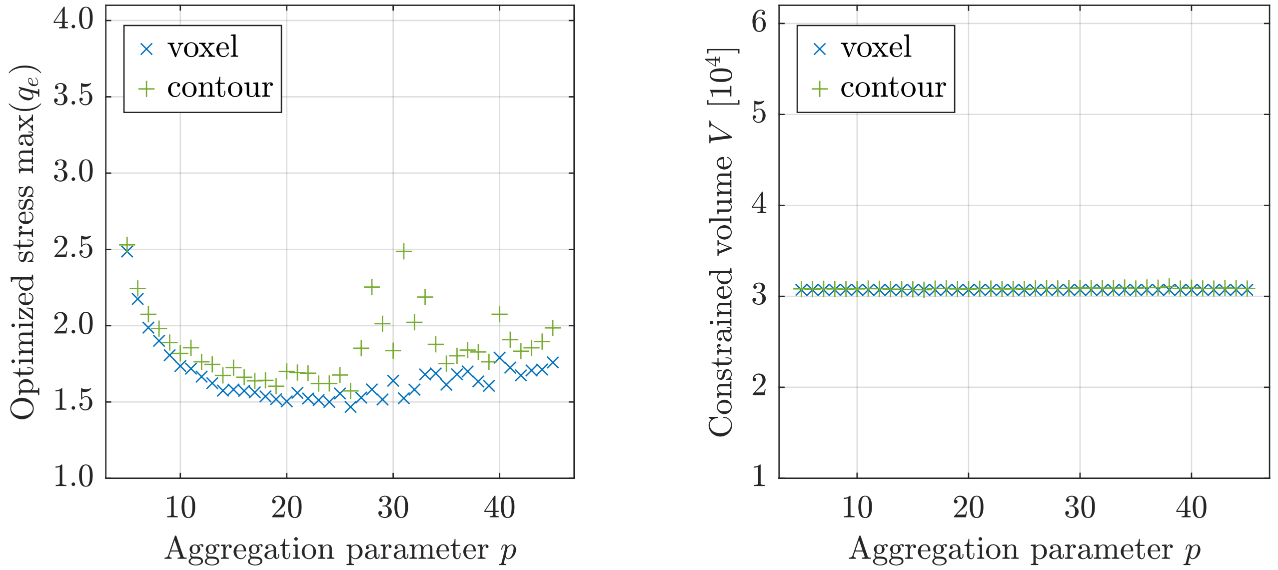

(b) Volume-constrained optimization.

Figure 2.8: Study on the p-norm aggregation parameter p for a stress-constrained, and a volume-constrained formulation.

Figure 2.8 presents the results of the parameter study investigating various aggregation parameters. The plotted data includes the objective and constraint values as functions of the aggregation parameter p, evaluated for both stress-constrained and volume-constrained optimization. As can be observed in both cases, there is an optimal range for which the objective is lowest, i.e. between $p = [10, \ldots, 30]$ for the presented example. Note, this depends on the problem considered. For example, the number of values to be aggregated, the aggregation functions and the filter radius play a role. Nonetheless, basic characteristics are demonstrated and can be discussed. Worth observing are higher objective values for low aggregation parameters. In the limit state for $p = 1$ the aggregated value is simply the sum of all absolute values. Optimizing for it reminds of a compliance optimized design with a notch at the re-entrant corner. It is not rounded off since information about its location is no longer emphasized and consequently becomes invisible to the optimizer. Gradients with respect to each design variable are just summed up and hence not dominated by peak values in critical locations. For higher aggregation parameters, objective values increase, and results start to scatter. As shown in Figures A.4 and A.3, increasing the aggregation parameter results in more and larger kinks in the evolution of the objective, particularly for the constraint. This issue worsens until the optimizer can no longer recover, such as from constraint violations, causing the optimization to diverge. When comparing the volume-constrained to the stress-constrained formulation, it is further observed that the evolution of the objective is much smoother when the volume is constrained. In this case, the constraint is rarely violated. In contrast, in the stress-constrained case, violations are much more severe. Therefore, it can be concluded that minimizing stresses under a volume constraint is more robust than using the inverted formulation. Specifically, in the stress-constrained case, small changes in the design variables may lead to divergence. As a result, it seems natural to further reduce, for example, the change in design variables $\Delta\rho_{max}$. However, the chosen limit is already quite small, and any further reduction results in very conservative design changes, which may cause the optimization to stagnate. Consequently, it is recommended to always test different aggregation parameters to avoid non-optimal local minima. Although the optimal range for this parameter may be problem-dependent, it usually does not vary significantly. Therefore, the observed range $p = [10, \dots, 30]$ is typically a good starting point.

As motivated and discussed in Section 2.7, the obtained results need to be validated. To achieve this, contour meshes are derived from the density field of the regular voxel mesh and evaluated. Regarding the deviations between the two meshes, the volume is usually captured very precisely by the contour mesh (deviations below 1%). In the case of high aggregation parameters, some differences occur due to non-converged results, e.g. non-clear geometry representation due to large areas with intermediate densities (see for instance Figure A.4d). Stress values, on the other hand, are slightly underestimated by the voxel mesh. Still, in regular cases, the deviation is below 10%, which is in good agreement with observations discussed in Section 2.7.2.

2.5 Domain Extension

As stated by Clausen et al. [155] the standard variable filter (see Section 2.2.1) introduces boundary effects if directly applied to a given design domain. Hence, a domain extension approach is proposed. It requires an extension of the design

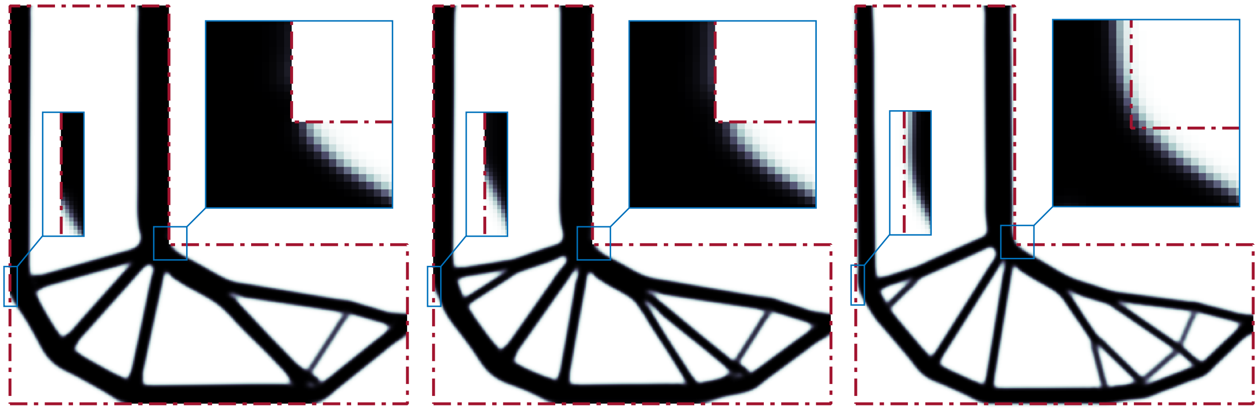

(a) No domain extension. (b) Adjusted filter kernel. (c) Added finite elements.

Figure 2.9: Effect of the domain extension for a stress constrained optimization with applied variable filter. The dash-dotted red line represents the boundary of the design domain.

space. More precisely, the finite element mesh has to be extended by multiple rows of elements. While the number of design variables stays unchanged, the amount of finite elements increases. Filtered and projected variables and gradients are calculated in the extended domain. However, for optimization, only the design variables and gradients within the design domain are considered. Since filtered and projected variables may become non-zero in the extended domain, physical material is placed outside the design domain. Nevertheless, results obtained from classical topology optimization are usually further processed, interpreted, and adapted by the designer. As a result, the final geometry will most likely adhere to the given boundary constraints.

Figure 2.9 demonstrates the effect of the domain extension on the L-beam example (see Figure 4.12). As can be observed, the design “sticks” to the boundary of the design domain if no extension is employed. At the re-entrant corner, a notch is introduced, which could not be removed by the optimizer. This is obviously disadvantages for stress-based design cases, since it results in stress peaks. If the domain extension is applied by physically adding finite elements around the design domain, the re-entrant corner is very smooth. However, a few intermediate densities are placed outside the design domain, which is a result of the filtering process. Yet, from a practical point of view, this is deemed acceptable. A post-processed contour line is hardly violating the design space. If any minimal violations exist, they can easily be smoothed by the designer.

As an alternative, a less computationally costly implementation is to modify the filter kernel by adjusting the denominator in the filter function (see Equation (2.13)). Although the resulting design appears to ’stick’ less to the boundary, similar effects occur as in the case without any modification (cf. Figure 2.9a to 2.9b). This is due to the absence of intermediate density elements outside the design domain. As noted by Clausen et al. [155], this introduces boundary effects because contributions from outside the design domain are ignored. Consequently, simply manipulating the filter kernel is not recommended, and physically present elements are preferred to extend the domain.

2.6 Formulation to Achieve Minimum Feature Size

All manufacturing techniques require a minimum feature size of both material and void phase. This motivated several researchers to incorporate different manufacturing constraints into the optimization framework [2]. One prominent approach to achieve a discrete minimum feature size is the manufacturing tolerant three-field formulation, also referred to as "robust approach" initially proposed by Sigmund [148] and later refined by Wang et al. [126].

Although a minimum feature size is imperative for manufacturability, it is also of special importance in stress-related problems. To achieve accurate stresses, a fine discretization is required. If, in such a scenario, only the filter radius (cf. Equation (2.13)) is varied to control local feature sizes, it might jeopardize convergence, since it may restrict the feasible design domain too much. Furthermore, in certain situations, small connecting features might be exposed to unexpected loads, resulting in too high stresses (cf. Section 4.3). Increasing the minimum size is believed to improve performance in such situations. Thus, the minimum feature size is constrained in several test cases. Furthermore, it ensures designs which are insensitive against uniform manufacturing errors [126].

The general idea is to apply a uniform boundary variation to the intermediate or blueprint design, represented by the projected density field $\bar{\boldsymbol{\rho}} = \bar{\boldsymbol{\rho}}^i(\boldsymbol{\rho}, \eta^i)$, where $\eta^i = 0.5$ is the nominal or intermediate threshold parameter. Boundary variations are applied by perturbing the threshold parameter, resulting in eroded $\bar{\boldsymbol{\rho}}^e(\boldsymbol{\rho}, \eta^e)$ and dilated density field $\bar{\boldsymbol{\rho}}^d(\boldsymbol{\rho}, \eta^d)$. For each density field, a separate finite element model is set up, solved and evaluated. Then, the worst-case design is optimized. Thus, the general optimization problem (2.2) is reformulated as a min/max-problem:

$$\begin{aligned}
\min_{\boldsymbol{\rho}} \quad & \max\left[f\left(\bar{\boldsymbol{\rho}}^e, \mathbf{u}^e\right), f\left(\bar{\boldsymbol{\rho}}^i, \mathbf{u}^i\right), f\left(\bar{\boldsymbol{\rho}}^d, \mathbf{u}^d\right)\right] \\
\text{s.t.} \quad & \max\left[c_j\left(\bar{\boldsymbol{\rho}}^e, \mathbf{u}^e\right), c_j\left(\bar{\boldsymbol{\rho}}^i, \mathbf{u}^i\right), c_j\left(\bar{\boldsymbol{\rho}}^d, \mathbf{u}^d\right)\right] \leq 0 \\
& \mathbf{R}\left(\bar{\boldsymbol{\rho}}^e, \mathbf{u}^e\right) = \mathbf{0} \Rightarrow \mathbf{u}^e \\
& \mathbf{R}\left(\bar{\boldsymbol{\rho}}^i, \mathbf{u}^i\right) = \mathbf{0} \Rightarrow \mathbf{u}^i \\
& \mathbf{R}\left(\bar{\boldsymbol{\rho}}^d, \mathbf{u}^d\right) = \mathbf{0} \Rightarrow \mathbf{u}^d \\
& 0 \leq \rho_i \leq 1.
\end{aligned} \tag{2.29}$$

Note, that all three density fields go through the same filtering and projection process and depend on the same set of design variables $\boldsymbol{\rho}$ (cf. Section 2.2). The

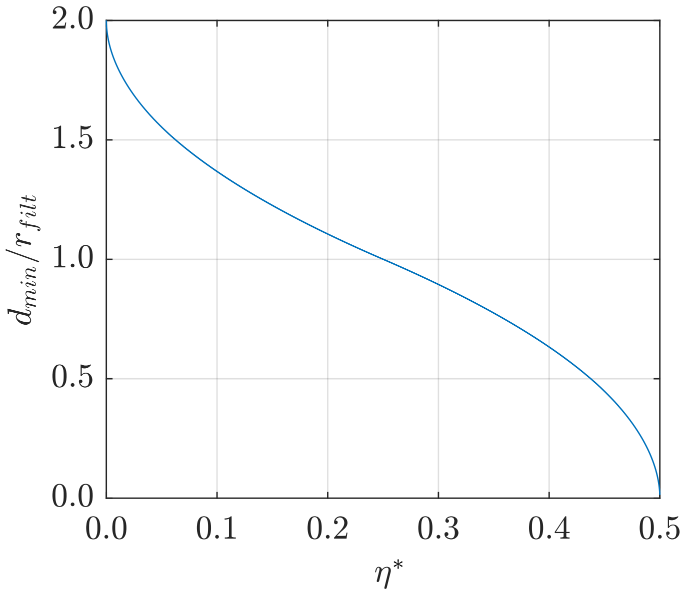

Figure 2.10: Normalized minimum feature size for the intermediate design (cf. Figure 12 derived in [126]).

only difference is a uniform variation in projection threshold η (cf. Equation (2.14)). Constraints c_j and objective f can be aggregated or handed directly to the optimization algorithm. Even though, the latter is simple to implement for the MMA, aggregation is preferred. By that, it is possible to avoid complications with, e.g. switching gradients destabilizing convergence. In the case of a predefined volume fraction, it is sufficient to constrain the intermediate design,[3] as suggested in the initial approach [148]. The remaining question is, how to choose appropriate values for the threshold parameter to obtain a defined minimum feature size d_{min}? To answer this question, Figure 12 from [126] is recreated (see Figure 2.10). Note, that the considered threshold parameter should be in the range $0 < \eta^* < 0.5$, since dilated, intermediate and eroded projection threshold parameters are determined as $[\eta^d, \eta^i, \eta^e] = [\eta^*, 0.5, 1 - \eta^*]$.

In Figure 2.11 two optimized L-beams are depicted, with and without feature size constraint. In both cases, the filter radius is $r_{filt} = 5$ for a mesh of unit-sized elements. In the feature size constrained case, the threshold parameter is defined as $\eta^* = 0.25$, resulting in an actual feature size of $d_{min} = r_{filt}$. As can be observed, the minimum feature size is much better fulfilled for the material phase in the constrained case. Violations on the void phase are also reduced. Still, a slight violation is visualized due to applied binary image operators.[4] However, the

---

[3] In the extended approach proposed by Wang et al. [126] the dilated volume is constrained without further discussion. This adds complexity, since this requires a scaling factor to obtain results for a predefined intermediate volume, which has to be updated during optimization. To avoid that and since mentioned numerical instabilities are mainly associated with the initial definition of the intermediate density field, this suggestion is not followed within this work.

[4] To visualize feature size violations morphological closing and opening operations are employed, which require the definition of a binary structuring element. Both operations are standard image operators. Since few gray elements are present inside the marked area, this results in an artificial violation of the feature size constraint.

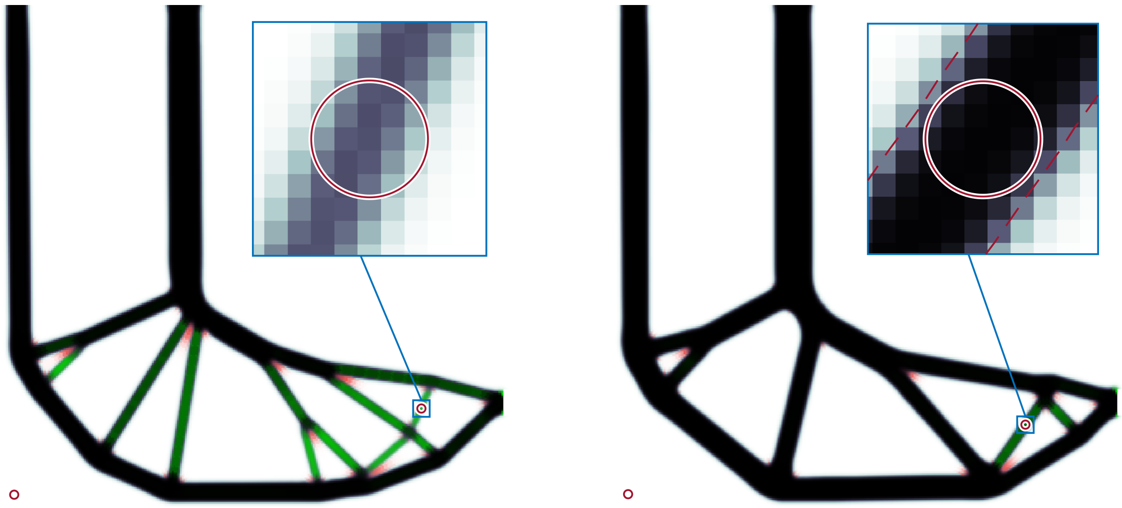

(a) Without feature size constraint.
(b) With feature size constraint.

Figure 2.11: Effect of the feature size constraint. Violations in the material and void phase are highlighted in green and red, respectively. The targeted feature size is indicated with a red circle. The red dashed line marks the nominal contour line.

nominal contour line, generated with a threshold value of 0.5, satisfies the feature size constraint. In the unconstrained case, the feature size is clearly violated.

The feature size constraint is supposed to reduce the amount of intermediate densities. To quantify the designs "grayness" the measure of non-discreteness is introduced by Sigmund [148] (see Equation (2.30)). If all densities $\bar{\rho}_e = 0.5$ then $M_{nd} = 100\%$. For a full design space ($\bar{\rho}_e = 1$), it is $M_{nd} = 0\%$. The measure of non-discreteness is calculated to 10.6% and 8.6% for the unconstrained and constrained examples. Hence, the amount of intermediate densities is reduced, while approximately the same volume is obtained. Nominal stresses differ. While the maximum stress of the unconstrained case is at the targeted stress limit, stresses of the feature size constrained example are more than 10% below the actual limit. This is due to the fact, that the worst-case stress of all three designs considered during optimization is constrained. Actually, the eroded design is utilizing the targeted stress limit and is thus robust against manufacturing errors, while the unconstrained design exceeds the stress limit in the eroded case by a factor of 20.

$$M_{nd} = \frac{\sum_{e=1}^{N_e} 4\bar{\rho}_e(1-\bar{\rho}_e)}{N_e} \cdot 100\% \tag{2.30}$$

2.7 Contour Model Evaluation

The boundary of a density-based optimized design is usually not clearly defined and non-smooth. For example, in the case of a binary or near-binary density

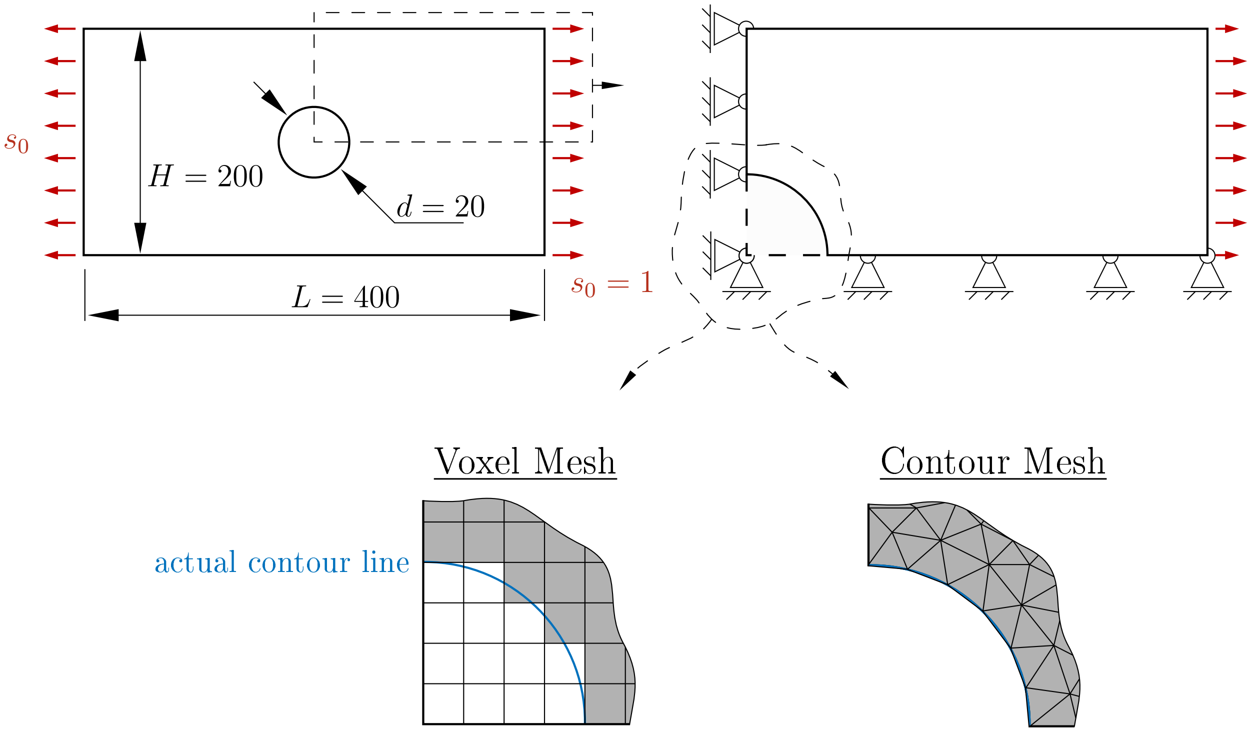

Figure 2.12: Plate with hole model, including boundary representation in voxel and contour meshes.

distribution, the boundary between the solid and void phase will be very jagged (cf. voxel mesh in Figure 2.12). Stresses evaluated at such boundaries are likely to be inaccurate. Hence, to increase accuracy of stress values at the boundary, Silva et al. [52] proposed to keep a certain amount of intermediate densities as a transition phase. This also helps to smooth the optimization process, and reduces variations in stress responses, if e.g. the geometry is varied. In this regard, different approaches exist to model boundary variations in a density-based finite element model (cf. Table 1.1). However, the most often applied technique is to perturb the projection threshold η (Equation (2.14)), which is thus also utilized within this thesis. An accurate stress representation with low variations is especially important for RTO and RBTO when uncertainties in geometry are taken into account (Chapter 5). Despite the mentioned benefits, a transition phase of intermediate densities blurs the boundary of the final design, which may require interpretation. In either case, optimized designs should always be verified with a contour mesh or a so-called body-fitted mesh [156]. Thus, within this section, the general procedure of generating a contour mesh is described. Furthermore, related issues to the topology optimized density field are discussed with respect to a structured uniform voxel mesh, as it is used for all examples within this thesis.

As depicted in Figure 2.12, the benchmark example of a plate with a hole is considered for both voxel and contour meshes. Due to symmetries, the model is reduced to a quarter of the actual plate. Based on the Kirsch equation, the stress concentration induced through a hole in a plate with infinite width is $k_{inf} = 3.0$. For plates with finite width, the stress concentration factor is given by the following empirical equation [157]:

$$k_{fin}\left(d,H\right) = 0.285 + 2.0\frac{H}{H-d} - 0.6\left(1-\frac{d}{H}\right) + 1.32\left(1-\frac{d}{H}\right)^2 . \qquad (2.31)$$

Considering dimensions given in Figure 2.12 the actual maximum stress is $s_{max} = s_0 * k_{fin} = 3.035$, which severs as reference for the following investigations. First a convergence study for the contour mesh is documented and then voxel related issues in the context of density-based topology optimization are discussed.

2.7.1 Convergence Study on Contour Mesh

For this study, linear and quadratic triangular continuum elements are considered. The line representing the perimeter of the hole is divided into a defined number of segments n_{seg}, and then meshed using a MATLAB-based Delaunay mesh generator “MESH2D” [158, 159]. In the case of quadratic elements, the geometry is exactly represented, i.e. intermediate nodes are placed on the perimeter of the hole.

Figure 2.13 depicts the relative error of the maximum von Mises stress,[5] which is determined as the ratio between Δq and the analytical maximum stress s_{max} (see above), where $\Delta q = \max(q_e) - s_{max}$. As expected, quadratic elements are more accurate at low resolution but converge at a similar rate. Since quadratic elements come with more degrees of freedom, the computational cost is also higher compared to the same number of linear elements. Thus, if the mesh resolution is chosen adequately high, linear triangular elements are considered as sufficiently accurate.

2.7.2 Stresses Variations due to Uniform Boundary Perturbation

Regarding the voxel mesh, the maximum stress at the circular cutout is subjected to variations, depending on various parameters, i.e. projection parameters, stress interpolation function and the SIMP exponent p^{SIMP}. The latter is generally kept constant for stress-based problems. For stress interpolation, several approaches exist, and also the associated parameter is often chosen without further reasoning. The following investigation helps determine an appropriate interpolation and projection parameter. The process was initially applied to a uniformly varying geometry problem [52], but applies as well for general stress-based problems that require higher accuracy in the stress response.

---

[5] Usually the stress component in the horizontal direction is evaluated. However, in the case of uni-axial loading the difference is small and in the limit case both converge to the same value. Furthermore, the von Mises stress is of higher relevance for the later examples.

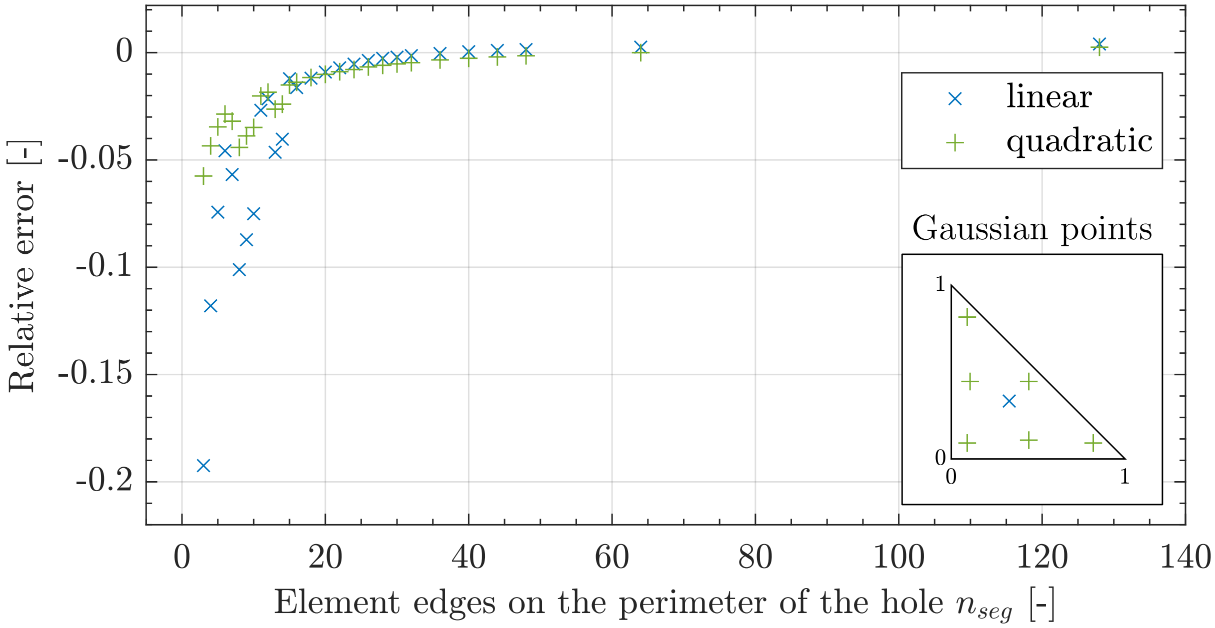

Figure 2.13: Convergence study on the plate with hole example. Relative error of the von Mises stress for an unstructured contour mesh using linear and quadratic triangular elements. Gaussian points used for stress evaluation of linear elements are marked in blue, and those for quadratic elements are marked in green on an isoparametric triangular element.

For the varying geometry problem, the projection threshold η is uniformly perturbed. In this context, Silva et al. [52] derived a limit value for the projection parameter β, as defined in Equation (2.32). This allows for a limited number of intermediate elements, acting as a transition phase between the solid and void regions. The width of the transition phase is found to be equal to one element when the maximum projection threshold is equal to the limit value, $\beta_{max} = \beta_{lim}$.

$$\beta_{lim} = \frac{2\, r_{filt}}{l_e}, \tag{2.32}$$

where l_e is the element size or edge length. Following the same process described by Silva et al. [52] yields similar results (see Figure 2.14 and compare to Figure 6 in [52]). It is found that an appropriate stress interpolation parameter is $p^{RAMP} = -0.8$, which corresponds to $\epsilon = 0.2$ and results in the most accurate stress representation in voxel meshes. Although variations across different mesh resolutions decrease with an increasing p^{RAMP}, the reference stress is increasingly underestimated.

Comparing Figures 2.13 and 2.14, it can be observed that the stress values do not converge as distinctly in the voxel model as they do for the contour mesh. For $p^{RAMP} < -0.8$ and $\beta \leq \beta_{lim}$, stress values seem to converge with more than 50 elements on the perimeter of the hole. This corresponds to a mesh resolution of 600 × 300 elements, which is not shown in Figure 2.14. However,

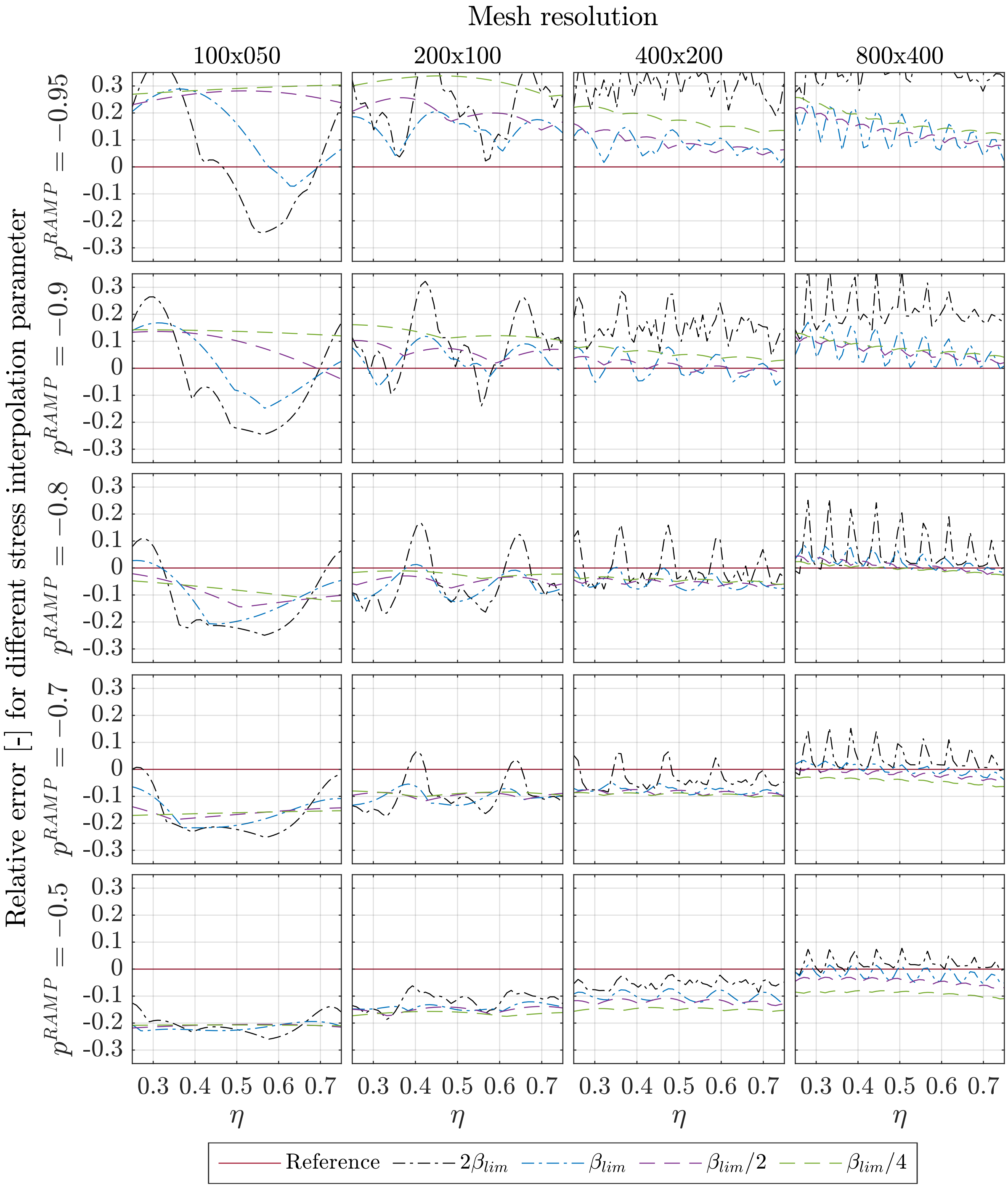

Figure 2.14: Relative error for different projection threshold values η, stress interpolation parameter p^{RAMP} and mesh resolutions.

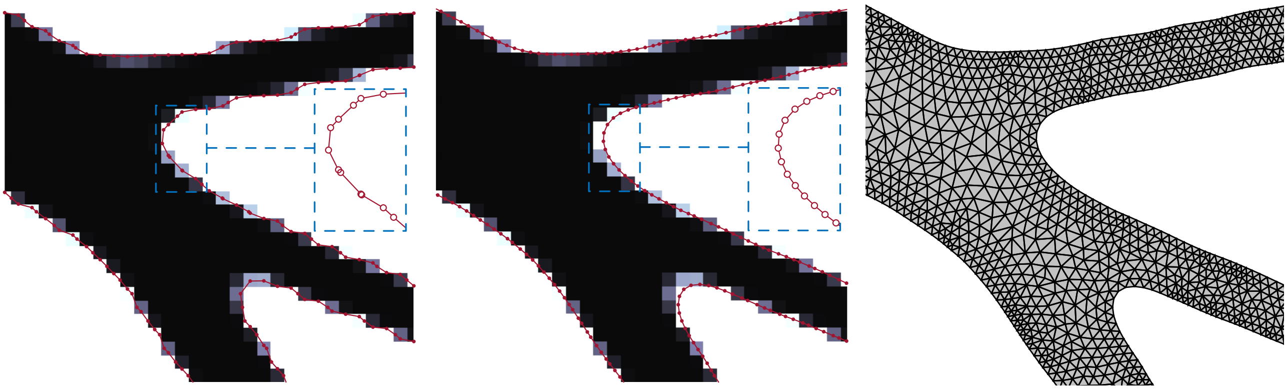

(a) Jagged and non-smooth (b) Regularized and smoothed (c) Final mesh

Figure 2.15: Contour line at three different stages to obtain a contour-fitted unstructured mesh.

this is a very high resolution that strongly depends on the obtained topology. Additionally, the latter is usually not explicitly controlled. As a possible solution, the mesh resolution could be related to the minimum feature size of the solid or void phase, while constraining it at the same time. Applying a minimum feature size constraint of $d_{min} = 5$ to the example in Figure 2.11 would require an element edge length of $l_e = 0.0785$. This again results in approximately 10 million voxel elements in a regular mesh. While technically possible, this requires iterative solvers (see for instance [49]), which have not been considered within this work. Hence, lower mesh resolutions are used, which consequently lead to a certain amount of deviation. This emphasizes the need for verification with contour models.

2.7.3 Generating Contour Meshes Based on Density Fields

Figure 2.15 illustrates the process of how a contour mesh with discrete boundary representation is created from a continuous density field. First, the raw contour line or isoline is extracted from the density field for a defined threshold value. For the extraction of the contour line, the Matlab function “contour” is used. Isolines are lines of equal value. However, in this context contour line is more appropriate, since the isoline is interpreted as the boundary between the solid and void phases. The threshold value is usually equal to the projection threshold $\eta = 0.5$ to assure volume preservation. As a second step, the contour line is smoothed and regularized to guarantee a constant element size at the boundary (for a detailed description of this step, refer to Appendix A.3). Finally, the contour line is meshed with the mesh generator “MESH2D” [158, 159]. In the end, the obtained difference in volume between the voxel and contour model is usually below 1%, and is hence assumed to be sufficiently accurate.

2.8 General Applied Optimization Techniques

The stress-based topology optimization algorithms proposed in Chapters 3 and 5 are applied to different examples in Chapters 4 and 6. Some parameters are varied, and others are kept constant across all investigations performed. The following paragraphs summarize the parameters and the applied optimization algorithm, which were used similarly across all examples.

For all cases, a linear finite element model is used with first-order quadrilateral continuum elements. Stiffness integration is performed over four Gaussian points and stresses are evaluated at the element's center. Material parameters and boundary conditions may vary and are described in the corresponding section. In all examples design variables are filtered and projected (cf. Section 2.2.1 and 2.2.2). The projection parameter is increased during optimization and initially set to $\beta = 1$. Stiffnesses are penalized using the modified SIMP scheme (cf. Section 2.2.3). Stresses are interpolated utilizing the RAMP scheme and calculated as described in Section 2.3. For optimization, they are usually aggregated with different aggregation functions listed in Section 2.4. For stress constrained optimization, aggregated stresses are normalized (see Section 2.3).

The method of moving asymptotes (MMA) is used as the gradient-based iterative optimization algorithm [145]. Therein, standard settings with external move limits are applied. Internal move limit parameters are set to `asyinit` $= 0.01$, `asyincr` $= 1.2$, and `asydecr` $= 0.7$.

Chapter 3

Topology Optimization for Damage Robustness

As stated in Section 1.1.2, different approaches can be followed to increase damage robustness. In this section, the focus is on generating multiple load path designs (MLD), for which two different methods are investigated. The first method incorporates local damage explicitly during optimization, namely the explicit damage patch formulation (see Section 3.1), and the second aims at constraining the maximum feature size to implicitly enforce MLD (see Section 3.2). The latter is computationally very cheap, but might not meet the required damage robustness. On the other hand, the explicit formulation directly considers a damage constraint, which results in a very high computational cost. Consequently, both methods are compared and evaluated regarding their potential to generate damage-robust MLD.

In Chapter 4 different damage robust designs are reported. Various problem formulations, patch configurations and optimization parameters are investigated, which raises the question on how to perform a fair comparison and assess the actual damage robustness? The most intuitive way is to consider each structural feature, such as nodes and struts, as a possible damage scenario. This is, for instance, a common approach for truss and beam models, where each strut is represented by one truss or beam element (cf. Figure 1.4). Possible damage cases are thus modeled by removing single or multiple struts from the model. This approach can be extended by adding nodes, i.e. locations where multiple struts connect, to the list of possible damage cases. Although this might seem like a very conservative assumption, it is actually not, as discussed in Section 4.2.2. In contrast to truss models, struts and nodes are not as clearly defined in a continuum setting, especially during optimization. That raises another question: How can damages be defined if they are not known a priori? They cannot. Consequently, damage scenarios are generated in a generic manner, which do not represent the actual structural feature, as discussed so far (cf. Figure 1.4). Still, regarding the optimized designs, features can be intuitively interpreted. In the proposed approach, structural struts and nodes are identified based on image processing techniques (see Section 3.4). The employed techniques are directly applicable to two-dimensional examples, but can also be extended to three-dimensional cases. However, in three-dimensional designs, the structure should primarily consist of interconnected struts, as plate-like or wall-like regions are challenging to interpret within the multiple-load-path philosophy and could not be identified with the considered techniques.

This chapter is structured as follows. First, the existing damage patch formulation is recapitulated and transformed to a stress-based topology optimization problem (Section 3.1). Then, an alternative formulation, which constrains the maximum feature size and by that implicitly enforces MLD, is recapitulated (Section 3.2). In Section 3.3 both approaches are combined and extended by a minimum feature size constraint. Finally, the proposed load-path-based evaluation scheme (LPE) is introduced (Section 3.4). Most parts of this chapter (Sections 3.1 to 3.2) and 3.4 are recapitulated from a preceding publication of the author [75].

3.1 Explicit Damage Patch Formulation

In the following, the existing damage approach from [68] is recapitulated and applied to a stress-based topology optimization problem. In Section 4.2 the explicit approach is demonstrated on two different models and their damage robustness is analyzed.

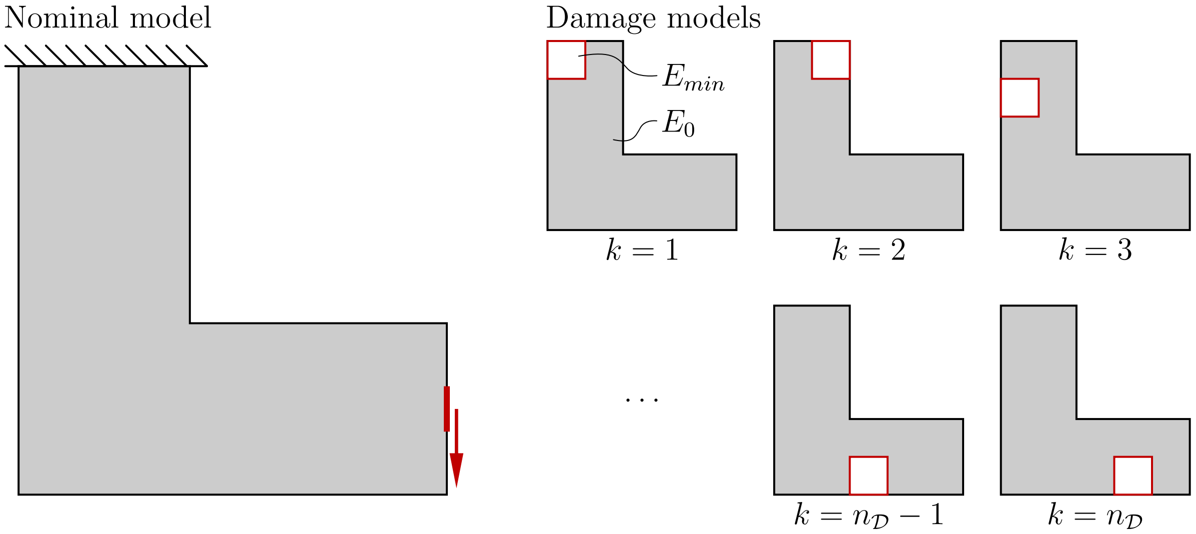

Figure 3.1: Exemplary nominal L-beam model and local damage models considered during optimization.

The basic idea of the explicit formulation is to optimize for the worst case damage. For that square shaped local damages are applied to the model, as exemplary depicted in Figure 3.1. All considered damage patches form the damage population $\mathcal{D}$. As originally proposed by Jansen et al. [68] this is referred to as patch approach. Local damages are modeled by reducing the elements Young's modulus $E_{0,e}$ in the SIMP and RAMP interpolation schemes (cf. Equation (2.16) and (2.18)). Consider a damage scenario k and let $\mathcal{N}^{(k)}$ be a set of damaged elements. If element e is affected by the damage $e \in \mathcal{N}^{(k)}$, its Young's modulus is set to the predefined minimum $E_{0,e}^{(k)} = E_{min}$. Otherwise, it is kept constant $E_{0,e}^{(k)} = E_0$. For more details on how damage scenarios are incorporated into the numerical model, see Appendix B.2.

In this study, the maximum von Mises stress is targeted for minimization. This is contrary to the original approach, but regarded as more practical relevant than compliance, as failure is primarily driven by stresses. Nonetheless, the constraint is similarly defined as the nominal volume $V\left(\bar{\boldsymbol{\rho}}\right)$. Hence, the problem formulation is defined as follows:

$$\begin{aligned} \min_{\boldsymbol{\rho}} \quad & q^{\mathcal{D}} = \max_{k}\left[\max_{e}\left(q_e^{(k)}\left(\mathbf{E}^{(k)}, \mathbf{u}^{(k)}\right)\right)\right] \approx \mathcal{A}_{\circ,\mathcal{D}}\left[p_{\mathcal{D}}, \mathcal{A}_{\circ,\mathcal{E}}^{(k)}\left(p_{\mathcal{E}}, q_e^{(k)}\right)\right] \\ \text{s.t.} \quad & c_V = \tfrac{V(\bar{\boldsymbol{\rho}})}{V_0} - \varphi_V \leq 0 \\ & 0 \leq \rho_i \leq 1 \\ & \mathbf{R}^{(k)}\left(\mathbf{E}^{(k)}, \mathbf{u}^{(k)}\right) = \mathbf{0} \Rightarrow \mathbf{u}^{(k)} \ , \end{aligned} \tag{3.1}$$

where $\mathbf{E}^{(k)}\left(\bar{\boldsymbol{\rho}}, \mathbf{E}_0^{(k)}\right)$ is a vector containing all interpolated stiffnesses and $\mathbf{E}_0^k \in \mathbb{R}^{n_e}$ are the elemental Young's moduli. The design domain's maximum volume is represented by V_0 and φ_V is a user-defined volume fraction. $\mathcal{A}_{\circ,\mathcal{E}}^{(k)}$ aggregates over all elements e and approximates the maximum elemental equivalent stress $q_e^{(k)}$ of one damage scenario k, while $\mathcal{A}_{\circ,\mathcal{D}}$ aggregates over all damage scenarios k. Both aggregation function and parameter can be chosen independently, based on which is best suited for the specific application (see Section 2.4 for details on aggregation functions). Note, the state equation $\mathbf{R}^{(k)} = \mathbf{0}$ has to be solved for each damage case, which results in a high computational cost.

3.2 Maximum Feature Size Constrained Formulation

An alternative approach to create redundant designs with multiple load path is to limit the maximum feature size. By that, bigger struts are split into two or multiple smaller ones, ensuring redundancy. In the following, an existing approach constraining maximum feature size is revisited and adapted to a stress objective. It requires only a fraction of the computational cost of the explicit formulation discussed in previous sections. But since local damages are not considered within optimization, damage robustness is expected to be worse. In Section 4.3 MLDs are obtained, and their damage robustness is investigated on two different models.

A simple and supposedly efficient method is the LVC approach proposed by Wu et al. [79], in which the volume of locally defined domains is constrained. For a stress objective, the optimization problem is formulated as follows:

$$\begin{aligned}
\min_{\boldsymbol{\rho}} \quad & \max_{e}\left(q_e\right) \approx \mathcal{A}_{\circ}\left(p, q_e\right) \\
\text{s.t.} \quad & c_V = \tfrac{V(\bar{\boldsymbol{\rho}})}{V_0} - \varphi_V \leq 0 \\
& c_L = \max_{e}\left(\tfrac{v_e(\bar{\boldsymbol{\rho}})}{v_{max}}\right) - \varphi_L \approx \mathcal{A}_{\circ,\mathcal{L}}\left(\tfrac{v_e(\bar{\boldsymbol{\rho}})}{v_{max}}\right) - \varphi_L \leq 0 \\
& 0 \leq \rho_i \leq 1 \\
& \mathbf{R}\left(\bar{\boldsymbol{\rho}}, \mathbf{u}\right) = \mathbf{0},
\end{aligned} \tag{3.2}$$

where φ_L is a predefined value and v_e is the actual volume of the local domain $\mathcal{L}_e$. The local volume of element e is determined as follows:

$$v_e\left(\bar{\boldsymbol{\rho}}\right) = \sum_{i}^{\mathcal{L}_e} v_i \bar{\rho}_i, \quad \text{with} \quad i \in \mathcal{L}_e \tag{3.3}$$

where $\mathcal{L}_e\left(r_{loc}\right)$ is the local domain of element e similar to the variable filter's neighborhood (cf. Equation (2.12)). The radius of the local domain is r_{loc}. The maximum local volume is $v_{max} = \max\left(\sum_i^{\mathcal{L}_e} v_i\right) \; \forall \; \mathcal{L}_e$. Note, the local domain $\mathcal{L}_e$ is not fixed to a circular shape. For instance, in [79] ellipses are proposed to increase interconnections between parallel struts.

To constrain the maximum feature size multiple solutions exist. Either the local volume fraction or the size of the local domain can be varied. For details on the definition of maximum feature size, see Appendix B.3.

Similar to stress normalization (cf. Equation (2.22)) the maximum value is only approximated and thus deviates from the targeted value. Fernández et al. [31] suggest an aggregation parameter of $p = 300$ to achieve an accurate approximation. Unfortunately, this often results in a non-smooth solution space and is likely to lead to divergence. Consequently, a continuation scheme may be applied, which increases complexity. As an alternative, the aggregated value can be scaled to the actual value. However, this is not done for results obtained within this section but applied in Section 3.3.

3.3 Combined Damage Patch and Feature Size Constrained Formulation

Based on numerical experience, smoothing the design response is desirable to ensure consistent convergence of the gradient-based optimization algorithm. For a stress function, the most obvious parameter to relax is the aggregation parameter

p. However, setting p too low can lead to non-redundant designs in the damage patch formulation (3.1). While increasing p can mitigate this issue, it may also cause the optimization process to become unstable. Therefore, this section introduces a combined approach (3.4), where the damage patch formulation (3.1) is extended with the local volume constraint (3.2) to better separate the redundant load paths for low values of p. Additionally, the minimum feature size is constrained by varying the projection threshold parameter, as defined in (2.29), to prevent the formation of excessively thin struts. Numerical results are summarized in Section 4.5.

$$\begin{aligned}
\min_{\boldsymbol{\rho}} \quad & q^{\mathcal{D}} = \max_{k,l}\left[\max_{e}\left(q_e^{(k,l)}\right)\right] \\
& \approx \mathcal{A}_{PN,\mathcal{D}}\left[p_{\mathcal{D}}, \mathcal{A}_{PN,\mathcal{E}}\left(p_{\mathcal{E}}, q_e^{(k,l)}\right)\right] \\
\text{s.t.} \quad & c_V = \tfrac{V(\bar{\boldsymbol{\rho}})}{V_0} - \varphi_V \leq 0 \\
& c_L = \max_{e}\left(\tfrac{v_e(\bar{\boldsymbol{\rho}})}{v_{max}}\right) - \varphi_L \\
& \approx \mathcal{A}_{PN,\mathcal{L}}\left(p_{\mathcal{L}}, \tfrac{v_e(\bar{\boldsymbol{\rho}})}{v_{max}}\right) - \varphi_L \leq 0 \\
& 0 \leq \rho_i \leq 1 \\
& \mathbf{R}^{(k,l)} = \mathbf{0} \Rightarrow \mathbf{u}^{(k,l)}
\end{aligned} \tag{3.4}$$

While the above problem (3.4) contains two aggregation parameters $p_{\mathcal{E}}$ and $p_{\mathcal{D}}$, aggregating over all damage cases and realizations required for the minimum feature size constraint $\mathcal{A}_{\mathcal{D}}$ is actually of minor importance, due to the low number of values to be aggregated. As described in Section 4.2.1 it might even be detrimental to increase $p_{\mathcal{D}}$ too much, which reduces the influence of less important damage cases. Thus, only $p_{\mathcal{E}}$ is increased in the following to increase approximation accuracy of each damage model.

3.4 Evaluation Procedure Based on Actual Load Paths

As outlined earlier, this section details the evaluation process for the optimized MLD. Structural struts and nodes are identified as potential load paths that may be damaged. The damage is modeled by severing or removing the relevant structural components.

First, the actual load paths must be identified. The proposed process builds upon image processing techniques similar to those in [76] and is inspired by [84]. While the aforementioned approaches require clustering all elements, our method only necessitates the definition of damage patches that cut through an entire feature. The following steps are performed (see Figure 3.2):

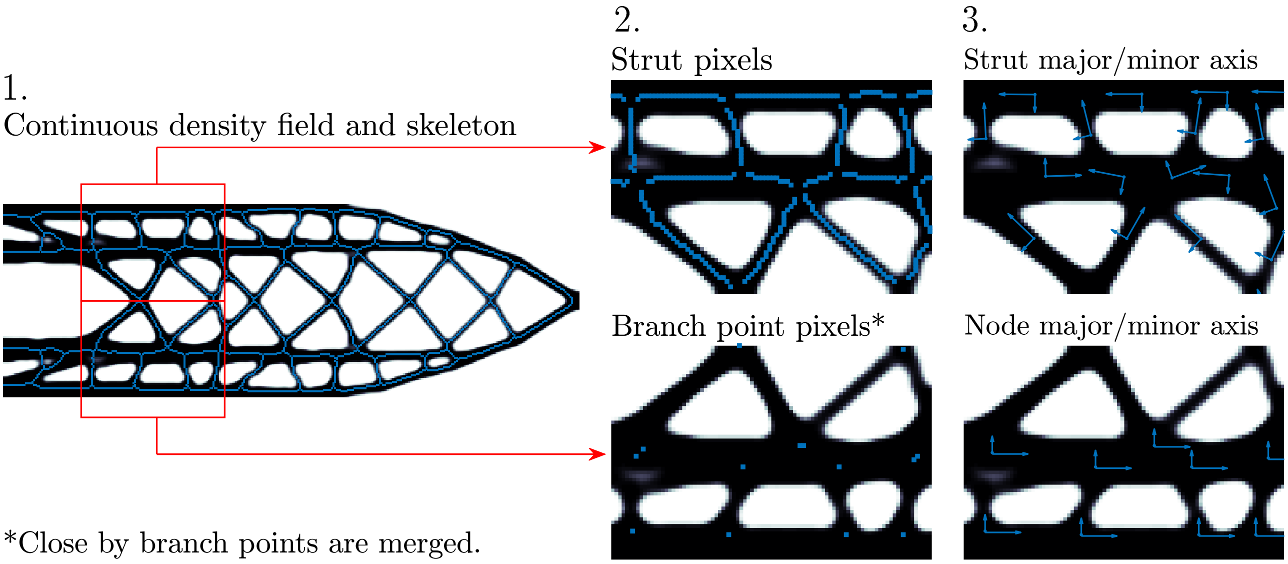

Figure 3.2: Continuous density field (left), skeleton, strut and branch point pixels (center) and corresponding major/minor axis (right) from [75].

1. Transform the continuous density field into a binary field and skeletonize it.
2. Split the skeleton into branch points and pixel clusters.
3. Calculate the corresponding midpoints for each branch point and pixel cluster. If the distance between two points is below a defined threshold, their average position is considered. The orientation of a strut is determined by calculating the major and minor axes of the corresponding pixel cluster.

Each node and strut is then treated as a potential local damage patch. To determine the size of each patch, it is incrementally enlarged until a defined number of void elements is reached in the density field. For structural nodes, the radius is increased, while for struts, the patch is enlarged along its major axis.

Figure 3.3 depicts all potential load-path-based damage patches. All struts are severed, and all nodes are completely removed. Structural features to the right of the dashed line are excluded, as they lie outside the damaged area, where no damage was considered during optimization. Additionally, to prevent the removal of excessively large areas, the maximum size of a node is limited to 10% of the maximum model dimension.

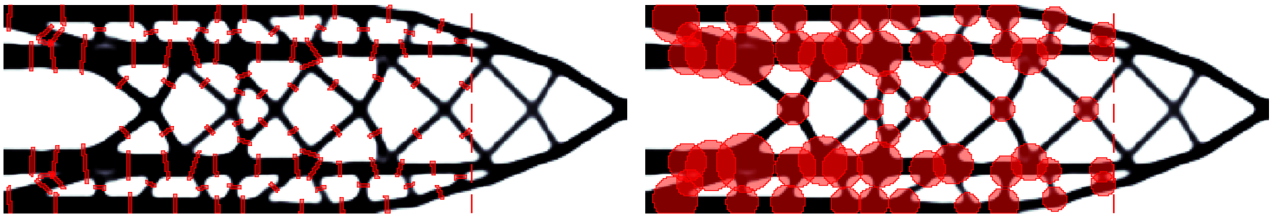
(a) Potential severed struts. (b) Potential removed nodes.

Figure 3.3: Identified load-path-based local damage patches from [75].

In a density-based finite element model, feature removal may induce high stresses in medium-density elements or very thin struts, which do not significantly contribute to the structural integrity. Removing these elements can actually reduce the maximum stress, so they should not be included in the LPE. To avoid these numerical artifacts, an extended cut procedure is developed that tests for potential stress reductions through additional minor element deletions (see Appendix B.1 for details). Additionally, the results are verified using contour models.

Chapter 4

Numerical Results for Damage-Robust Topology Optimization

In the following sections, numerical results are given and discussed for three different optimization formulations described in the previous Chapter 3.

First, the general evaluation strategy is introduced (see Section 4.1). In Section 4.2 results are given for explicit damage patch formulation. Best performing designs obtained with the implicit maximum-feature-size-constrained formulation are summarized in Section 4.3, followed by a comparison of both approaches in Section 4.4. Additionally, the explicit formulation is extended with both a minimum and a maximum feature size constraint. In summary, the last section is dedicated to the verification with contour meshes of all discussed designs (see Section 4.6). Most parts of this chapter (mainly Sections 4.1 to 4.4) are recapitulated from a preceding publication of the author [75].

4.1 General Evaluation Strategy

As described in Section 3.4 the damage robustness assessment is based on actual load patch. For all obtained designs, actual load path are identified, and worst-case stresses are determined.

Generally, damage robustness is quantified using a fail-safe factor, $FSF = \frac{q_{max}}{q_{nom}}$. It represents the ratio of the maximum worst-case von Mises stress q_{max}, determined using the proposed LPE, to the maximum von Mises stress of the undamaged or nominal design q_{nom}. Note that during optimization, the maximum von Mises stress is approximated using an aggregation function, but in the final numerical results, the actual maximum stress is considered.

In addition to the FSF, the stresses of the nominal design q_{nom} and worst-case stress q_{max} are provided for each design. The nominal density field is given,

(a) Physical densities $\bar{\rho}_e$.

(b) Normalized stresses q_e.

Figure 4.1: Color bars used to visualize optimized results.

and the worst-case damage patch is marked in red. Any elements removed by the extended cut procedure (see Appendix B.1) are marked with a red × (cf. Figure 4.4 first row). Furthermore, a stress plot of the worst-case scenario is depicted. When comparing designs from different optimizations, large differences in maximum stresses may arise. To avoid featureless stress plots, the stress scale is truncated at the lowest maximum stress of all damage cases.

When optimized results are depicted, different color scales are used (see Figure 4.1). Stresses are drawn on a rainbow scale ranging from blue to red for low and high stresses respectively, and densities are depicted on a gray scale.

4.2 Damage Patch Optimized Results

Regarding the explicit damage patch approach described in Section 3.1, patches may introduce stress singularities and are hence assumed to influence the optimization process. Consequently, different patch shapes and configurations are investigated in this section. Optimization techniques listed in Section 2.8 are applied.

Two models are considered for investigation. The cantilever model (see Figure 4.2a) is discretized using 360 × 120 unit-sized elements, while the L-beam model (see Figure 4.2b) is discretized with 300 × 300 unit-sized elements. Material properties are set to a Young's modulus of $E_0 = 1$ and a Poisson's ratio of $\nu = 0.3$. The overall volume fraction is constrained to $\varphi_V = 40\%$ and a filter radius of $r_{filt} = 6$ is applied. The load is set to $F = 1$ and distributed among several nodes to avoid stress peaks. The domain extension (see Section 2.5) is considered by modifying of the filter function (2.13). The denominator is set to the maximum value of all other elements, excluding nodes near loads or boundary conditions.

For stress aggregation, the alternative form of the upper bound KS-function (see Section 2.4) is used for both aggregation over damage scenarios $\mathcal{A}_{KS,\mathcal{D}}$ and across all elements $\mathcal{A}_{KS,\mathcal{E}}$ (cf. Equation (3.1)). In both cases, the aggregation parameter p is updated every 10 iterations, as proposed in the original approach [68]. Based on numerical studies, a proper setting is found to be $p = 10/\max(q_e^{(k)})\ \forall\ k, e$, which allows a stable convergence and is accurate enough to capture stress peaks at notches. In the following, the worst-case stress is denoted as $q_{max} = \max(q_e^{(k)})$.

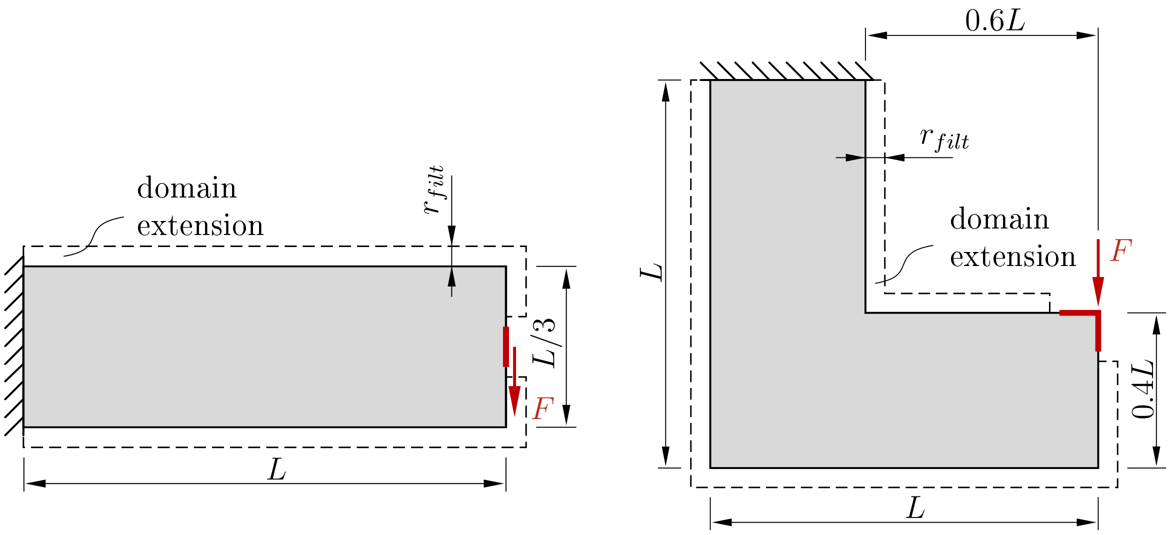

(a) Classical cantilever model.

(b) L-beam model with loads applied at the corner.

Figure 4.2: Cantilever and L-beam models.

For the MMA, parameters stated in Section 2.8 are applied. Additionally, external move limits are implemented, allowing an absolute change per design variable of $\Delta\rho_{max} = 0.1$. The iterations are limited to a maximum of 500 for the damage patch optimization. The LVC optimization required 1000 to 1500 iterations (see Section 3.2). If not stated otherwise, the projection parameter β is increased every 100 iterations. All other parameters are kept constant during the entire optimization, the objective and constraint value are both normalized at the beginning and scaled by a factor of 100.

4.2.1 Damage Patch Spacing

To achieve the best robustness with respect to occurrence of local damages, Jansen et al. [68] suggest setting the spacing between patches equal to the element size. While others proposed to use as many patches as needed to cover the design domain without gap and overlap to obtain "applicable solutions" [69]. In both cases, a compliance-based optimization is performed and evaluated with the same patch size and shape used for optimization while varying the spacing. Hence, it is reasonable that certain patch positions, which are not considered during optimization, may occur as worst-case damages [71]. Nonetheless, the effect of the number of patches on stress-based optimization is unclear and will therefore be investigated in the following.

To keep the computing time manageable, the following investigation on the number of damage patches is performed on a lower resolution (180 × 60 square elements). Furthermore, the filter radius is halved $r_{filt} = 3$. The optimization for a high number of damage patches and an aggregation parameter update of $p =$

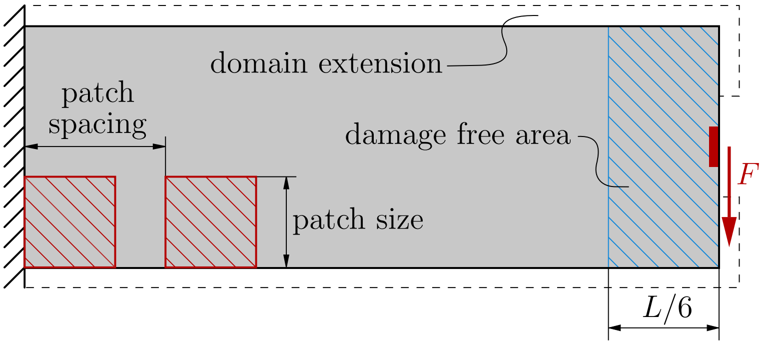

Figure 4.3: Parameters for patch configuration and damage free area of the cantilever model.

$10/q_{max}$ turned out to be unstable, supposedly due to very localized and switching stress peaks (as will be explained in the following). Thus, to further stabilize the optimization, the aggregation parameter is updated every 10 iterations to $p = 8/q_{max}$.

Different patch spacing are investigated. For a definition of the regarded damage patch parameter, refer to Figure 4.3. The patch size is chosen to ensure a clear separation of load paths (cf. Figure 4.5). Starting with a patch size of 12 and a spacing of 12, leading to a total number of 60 damage patches. The spacing is then halved by allowing overlap. Finally, placing a patch at each possible positions (spacing = element size) results in 6860 damage patches for a cantilever model discretized with 180×60 elements.

Results given in Figure 4.4 show that the worst-case stress q_{max} increases with an increasing number of damage patches. Additionally, the secondary load path is getting thinner and is even disappearing in some places for the highest number of patches. Both observations can be traced back to the local nature of stresses. Critical damage scenarios, in which just few elements are left over close to the boundary, show dominating high stresses. Decreasing patch spacing worsens this situation. Bearing in mind that aggregation can be interpreted as a weighted average, it is reasonable that for an increasing number of dominating damage scenarios, other patches' influence decreases. In the end, this results in a design more similar to the optimization without damage, rather than in an MLD. Only at the boundary, small redundant load paths are formed.

With increasing number of damage patches, unresolved spots or medium density struts emerge. Moreover, a slight asymmetry can be observed. Again, this is the result of very localized high stresses which magnify small numerical inaccuracies. In turn, this leads to an alternating stress peak location and by that to gradient switching. In the end, this results in an unstable or even diverging optimization. This effect is further amplified by an increasing aggregation parameter, which is the reason for a reduction to $p = 8/q_{max}$ for this investigation.

The FSF appears to be lowest for 216 patches (Figure 4.4 middle), even though the worst-case stress q_{max} is higher compared to the lowest number of

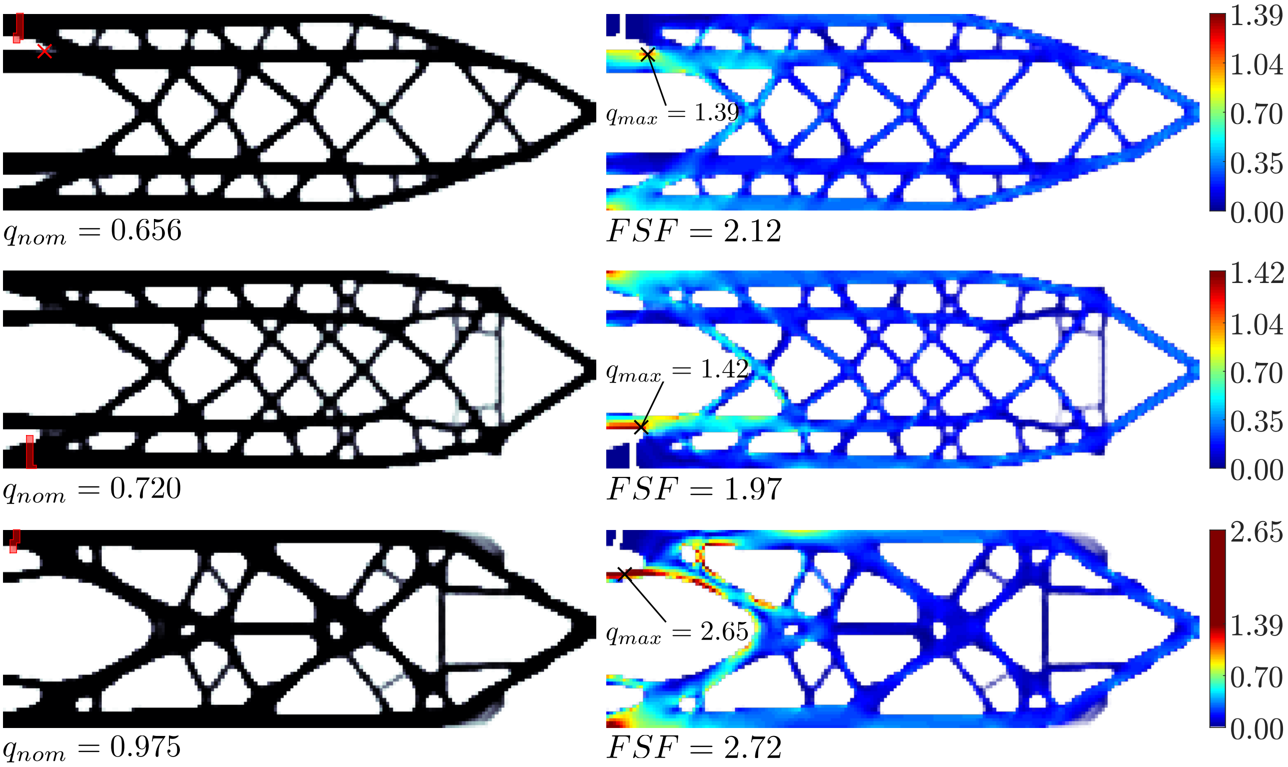

Figure 4.4: Worst-case load path damage of the cantilever model, optimized with 60 (top), 216 (middle) and 6860 (bottom) square patches, optimized design (left) and worst-case von Mises stress (right) from [75].

patches. This is due to the higher nominal stress q_{nom}. Beside the FSF, which is defined as a ratio between undamaged and worst-case stress, the actual worst-case stress q_{max} is considered to be more important. Even though the worst-case stress evaluated with square damage patches at every possible location is naturally worst for the lowest number of patches [68, 69, 71], the worst-case stress based on the proposed load path evaluation is lowest. Thus, from a practical point of view, it is sufficient to use as many damage patches as needed to cover the design domain without gap and overlap. Similarly, [69] recommended a low number of damage cases for practical applications. Thus, in the following, only a patch spacing equal to the patch size will be used.

4.2.2 Damage Patch Sizes

Figure 4.5 and 4.6 depict optimized cantilever and L-beam designs, including worst-case damages for different patch sizes. The patch configuration considered during optimization is indicated with orange squares.

As already observed by [68], the patch size can have a strong influence on the final design. Too small a patch size can lead to a low damage robustness and non-redundant load path designs (see Figure 4.5 top and 4.6 left). It can generally be said that the distance between primary and secondary load path correlates with the patch size.

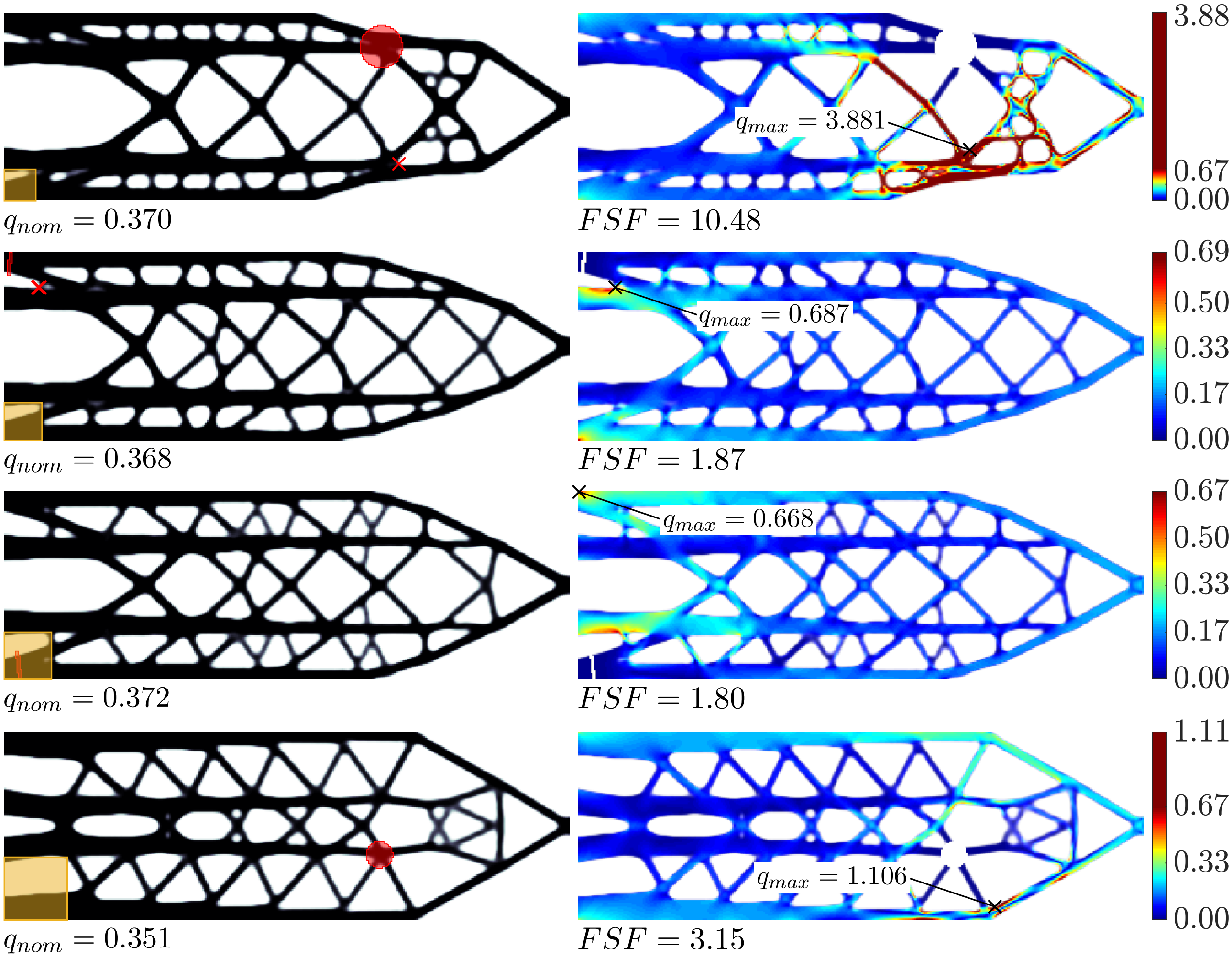

Figure 4.5: Worst-case damage for different patch size of the cantilever example, optimized with non-overlapping square patches of size 20, 24, 30 and 40 (from top to bottom), optimized design (left) and worst-case von Mises stress (right) from [75].

For the cantilever model, the lowest worst-case stress q_{max} and best FSF are both achieved by a medium patch size of 30. Interestingly, there is no big difference between size 24 and 30. Considering the biggest patch size 40, the straight struts between primary and secondary load path align with intuition. In lightweight design, most efficient designs exhibit mostly axial loads in structural features. Considering truss structures, struts are only loaded along their longitudinal axis and can thus be better utilized compared to thick bars transferring bending loads. It is also observed, that the nodes are preferably placed at the corner of damage patches, since these areas are never completely removed during optimization. By that, the design is obviously controlled by the size and placement of patches. Considering nodes as possible damage scenarios might be regarded as very conservative and can lead to bad worst-case stress, as can be observed for big patch size (40). However, considering a medium size (24 and 30) structural nodes are not always the worst-case damage scenarios.

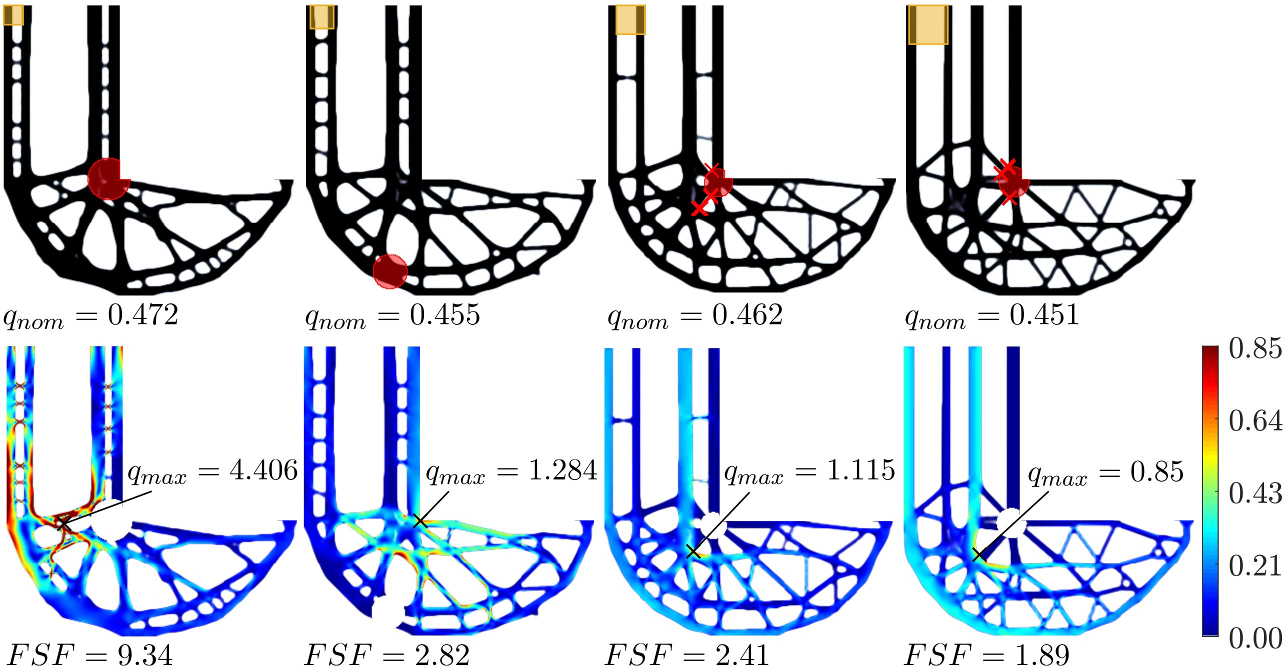

Figure 4.6: Worst-case damage for different patch sizes of the L-beam example, optimized with non-overlapping square patches of size 20, 24, 30 and 40 (from left to right), optimized design (top) and worst-case von Mises stress (bottom) from [75].

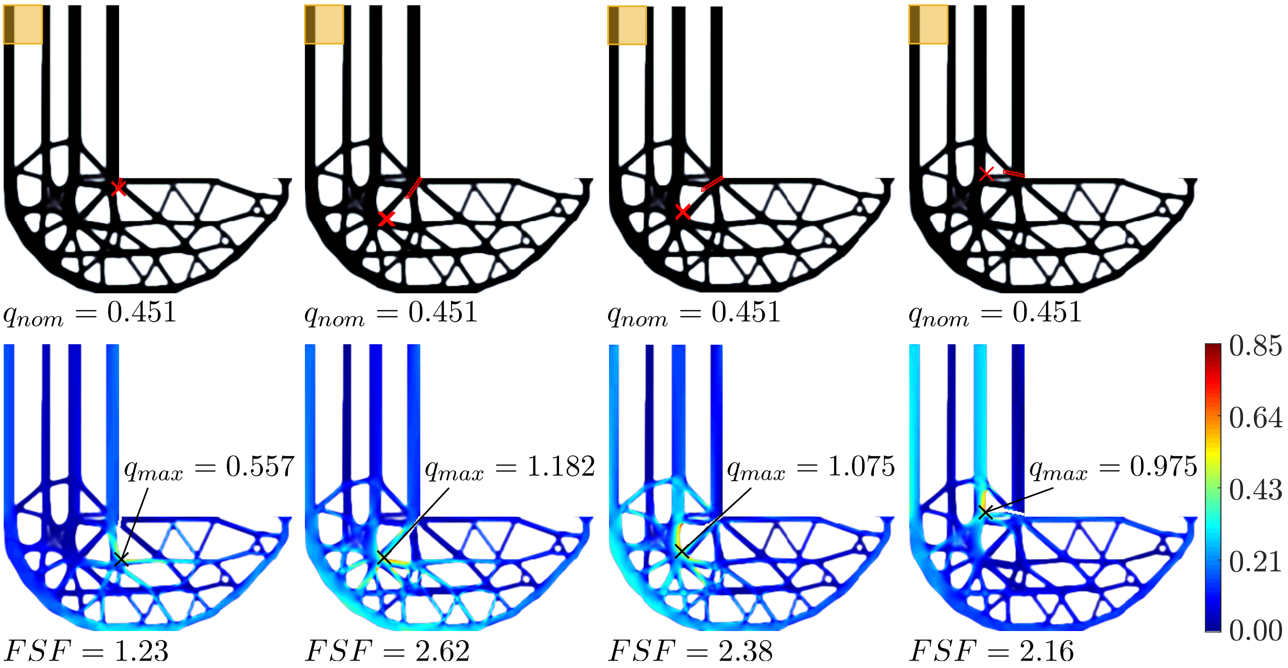

Figure 4.7: Examples of not identified load path cuts of the L-beam example optimized with a square patch shape and a size of 40, optimized design (top) and worst-case von Mises stress (bottom) from [75].

Both, the worst-case stress q_{max} and the FSF are lowest for the biggest patch size and mainly driven by the notch created by removing the patch at the re-entrant corner (compare patch size 30 and 40 in Figure 4.6). For the cantilever example, treating nodes as possible local damages seemed to be too conservative in some cases. Contrary to that, for the L-beam example, considering only nodes and struts as possible damages appears to be too optimistic. The cuts shown in Figure 4.7 starting at the re-entrant corner and running into an adjacent hole, are not identified as possible damages, even though they appear to be more realistic than a removal of the whole node. Still, the proposed approach considers more realistic damages than a patch-based evaluation.

Sharp edge | Blurred edge

Square

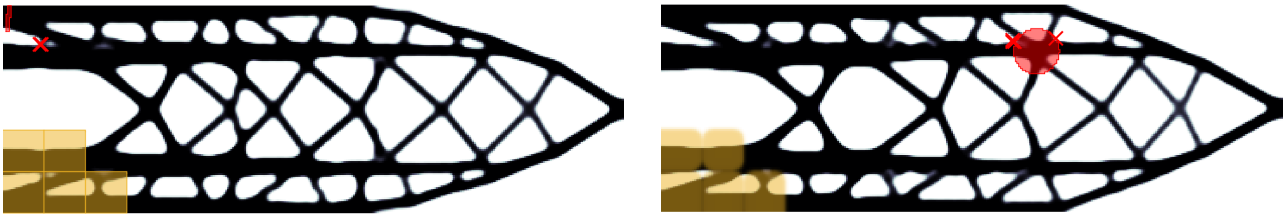

$q_{nom} = 0.368$, $q_{max} = 0.687$, $FSF = 1.87$ | $q_{nom} = 0.365$, $q_{max} = 1.101$, $FSF = 3.02$

Circle

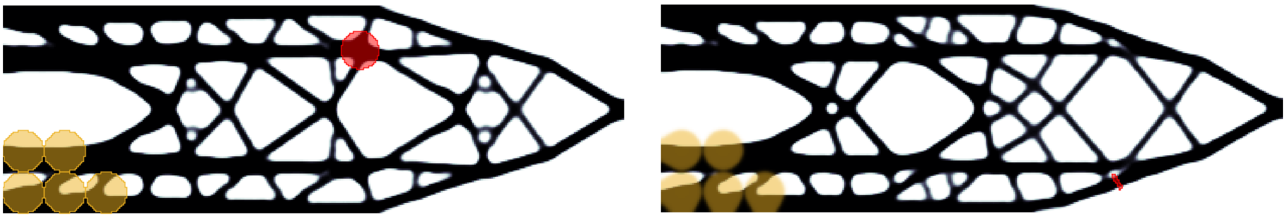

$q_{nom} = 0.370$, $q_{max} = 0.779$, $FSF = 2.11$ | $q_{nom} = 0.365$, $q_{max} = 0.750$, $FSF = 2.05$

Overlapping circle

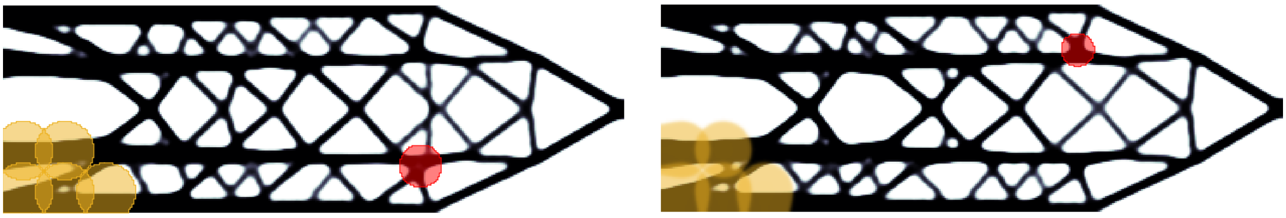

$q_{nom} = 0.384$, $q_{max} = 1.004$, $FSF = 2.61$ | $q_{nom} = 0.374$, $q_{max} = 1.057$, $FSF = 2.83$

Figure 4.8: Results for different patch shapes of the cantilever example from [75].

4.2.3 Damage Patch Shapes

Figure 4.8 and 4.9 show cantilever and L-beam designs optimized for different patch shapes. Due to stress singularities introduced by square patches, circular and blurred shapes are examined. Patch spacing is kept constant, while two different circular patch sizes are considered. Since the small circular patch contains elements which are never removed during optimization, a bigger size is incorpo-

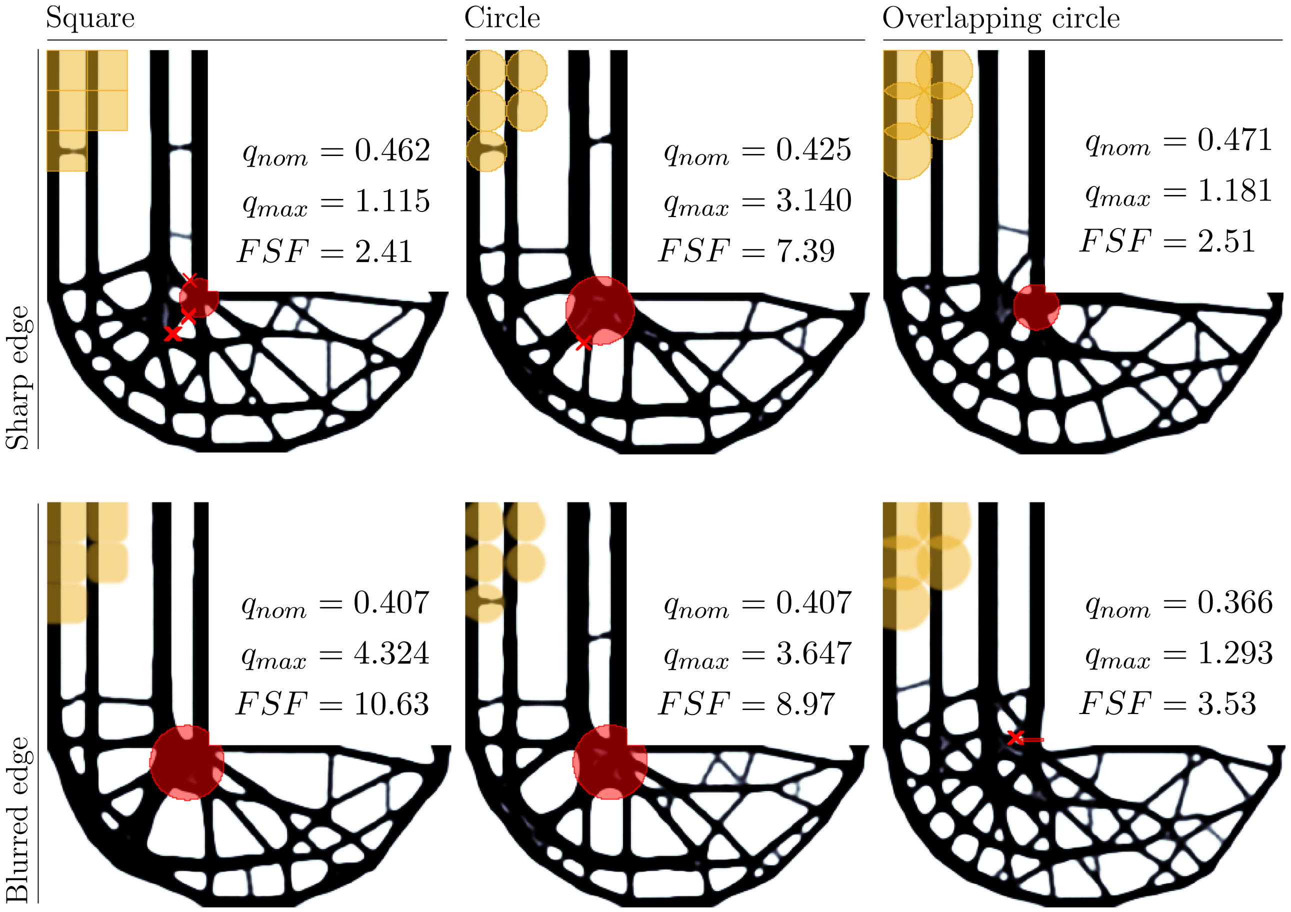

Figure 4.9: Results for different patch shapes of the L-beam example from [75].

rated. Additional to these three configurations, the patches are filtered (2.13) to blur the edges.[1]

For the cantilever designs, there is no big difference in nominal stresses q_{nom}. However, both worst-case stress q_{max} and FSF differ quite a lot, ranging from 0.687 to 1.101 and 1.87 to 3.02 respectively. Examining the worst-case damage for the blurred-square configuration, the damage location can be identified as being right between four patches where few elements are never removed completely during optimization. Such nodes also occur for square or circle patches, but are usually not the worst case. For overlapping circles, diagonal struts are preferable placed between patches and thus never removed completely during optimization. Whereas, nodes can be positioned more freely and are preferably located in regions where no overlap occurs.

In the case of the L-beam designs, all but square and overlapping patches show deficiencies in splitting up the primary load path, especially in diagonally oriented members and at the re-entrant corner. The optimized design obtained

---

[1] To generate blurred patches, a full density field ($\rho = 1$) is generated and the elemental densities of the considered sharp-edged patch are set to zero. Then, the variable filter is applied with a filter radius of 33% of the patch size. Intermediate densities (considering a threshold of 0.98) are stored and multiplied with the projected density field to scale the elemental stiffness matrix

with overlapping blurred circular patches rounds of the notch at the re-entrant corner. However, the FSF and the worst-case stress $q_{max} = 1.29$ are higher compared to a simple square patch design ($q_{max} = 1.11$ see also Figure 4.6). Both, the lowest worst-case stress q_{max} and the lowest FSF are obtained for a square shaped damage patch. The lowest nominal stress $q_{nom} = 0.366$ is naturally obtained for the design circumventing the re-entrant corner.

Looking at the re-entrant corner of all depicted L-beam designs (Figure 4.6 to 4.9), it is found that the corner is only rounded off in one case. All other designs exhibit a stress singularity at the re-entrant corner, even though the nominal design is considered during optimization by empty patches. The reason is probably related to the optimization setup. The worst-case stress q_{max}, is in the best case (patch size 40) 1.64 times higher than the nominal stress q_{nom}. Additionally, there are other patches creating higher stresses in other locations than at the re-entrant corner. Note, the aggregation function is a weighted average, which is dominated by the worst-case. With that in mind, the re-entrant corner can possibly not be detected or circumvented as long as there are other damage cases creating higher stresses. The author conducted a multi-objective optimization, additionally considering the undamaged stress field and weighting the worst-case damage (see Appendix B.4). Applying a high weighing factor to the nominal stress field yields a design in which the re-entrant corner is better avoided, while the design is less redundant and shows worse damage robustness.

Against expectations, there is no advantage in using different patch shapes. A simple square shape gives the best damage robustness by using a low number of patches. Reducing the amount of stress singularities by using circular blurred shapes did not have any advantageous effect on the optimization convergence or results for the number of patches considered.

4.3 Maximum Feature Size Optimized Results

As an alternative to the explicit damage patch approach, results obtained by employing the maximum feature size (see Section 3.2) are presented in this section. Optimization techniques listed in Section 2.8 are applied.

For comparability, similar models are used, and equal settings are applied as described in Section 4.2. Differences are mentioned below. Parameters of the local domains are chosen such that at least two redundant load paths are obtained. Different configurations are tested, and the most representative results are compared against the best performing designs of Section 4.2.2 to 4.2.3.

The projection parameter β is updated in every iteration, starting at the first iteration with $\beta = 1$, which is then multiplied by a constant factor of approximately 1.007 in order to reach a value of $\beta_{max} = 16$ after 400 iterations. From there on, β is kept constant. Hence, in the first 400 iterations, there is a small

Table 4.1: Parameters for the feature-size-constrained optimization from [75].

Model and reference		Filter radius r_{filt}	Local vol. frac. φ_L	Maximum feat. size d_{max}	Global vol. frac. φ_V	Achieved gl. vol. frac. φ_V^*
Cantilever - Fig. 4.10	a)	9	0.50	7.3	0.40	0.381
	b)	18/6	0.60	5.9		0.367
	c)	24/8	0.50	6.5		0.400
	d)	18/6	0.50	4.8		0.400
L-beam - Fig. 4.11	a)	10	0.45	7.2	0.40	0.370
	b)	24/8	0.50	6.3		0.371
	c)	27/9	0.50	7.3		0.385
	d)	30/10	0.40	6.4		0.335

error in the gradient. However, this small error is deemed acceptable and does not penalize the convergence. Updating the projection parameter in every iteration is chosen to stabilize convergence by reducing the induced design change to a minimum.

Two different local domain shapes are applied. First, the classical circular and second, the so-called anisotropic filter, which increases the cross connections in areas of high anisotropic stresses. The anisotropic filter consists of two elliptic test regions per element, one rotated by 90°. Both domains are described in the original approach [79] and are indicated with a green circle or ellipses in Figure 4.10 and 4.11. Note, that the LVC may lead to a not fully utilized global volume fraction, which was already observed by [79]. Table 4.1 summarizes the local volume parameter and lists the actual global volume fractions φ_V^* achieved after optimization.

The maximum local volume fraction φ_V is approximated by the p-mean function (2.24). An aggregation parameter of $p = 16$ was chosen, since this turned out to give good convergence and acceptable results.

Stress-optimized and feature-size-controlled designs for the cantilever example are depicted in Figure 4.10. The first design (a) is obtained with a circular test region and the remaining designs (b-d) are obtained with the anisotropic filter of different local volume fractions and ellipse radii (see Table 4.1). The stress scale is truncated at the best worst-case stress of the cantilever damage-patch-optimized designs (cf. Figure 4.5).

As can be observed from Figure 4.10 MLDs are successfully obtained with a reasonably low nominal stress. However, comparing all MLDs to the best damage patch design in Figure 4.5 and 4.8, the best alternative MLD (see Figure 4.10d) is still showing a 3.9 times higher worst-case stress q_{max}. The maximum nominal stress q_{nom} is superior to the ones obtained with the damage-patch optimization, which widens the gap between q_{max} and q_{nom} and results in a very high FSF. The FSF is approximately a factor 10 higher compared to the damage patch designs.

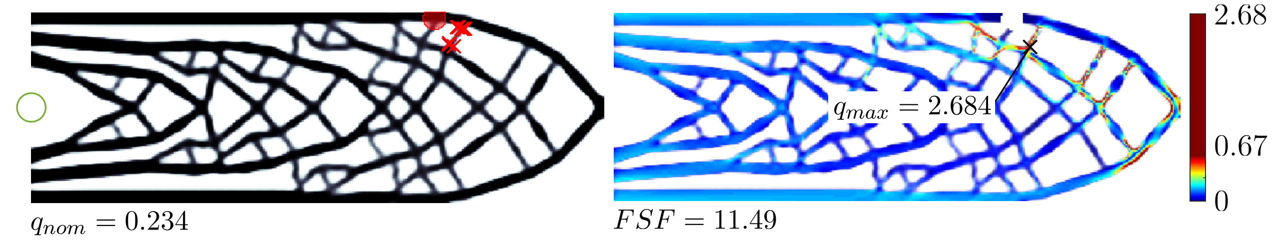

(a) Circular local domain.

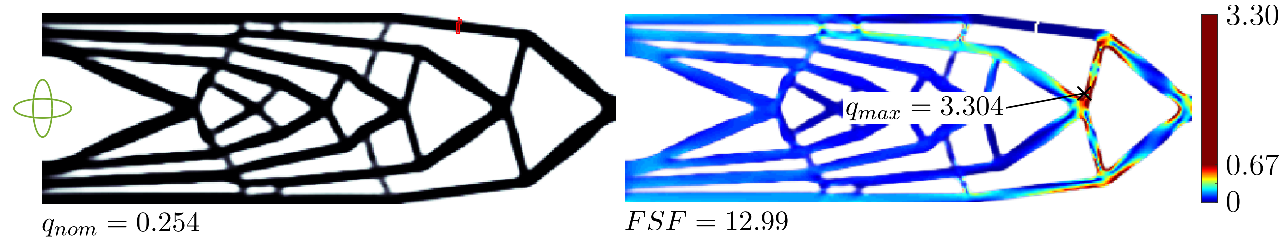

(b) Elliptical local domain.

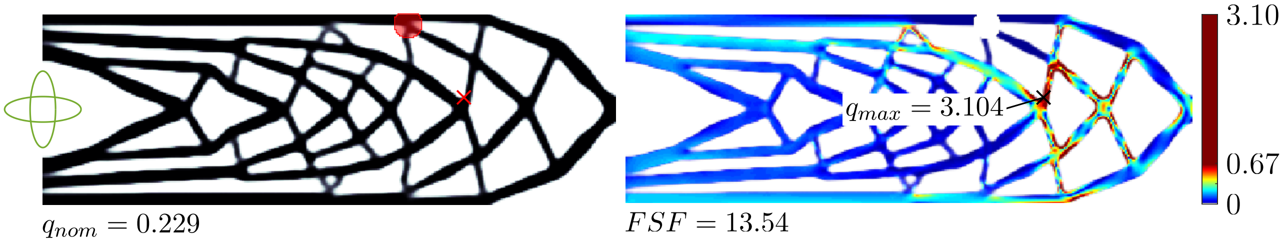

(c) Elliptical local domain.

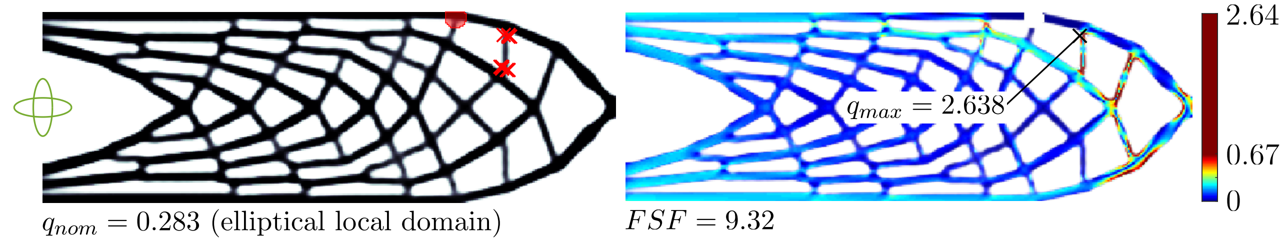

(d) Elliptical local domain.

Figure 4.10: MLDs for different maximum feature sizes and local domains of the cantilever model, optimized design (left) and worst-case von Mises stress (right) from [75].

Stress optimized and feature-size-controlled designs for the L-beam example are depicted in Figure 4.11. The first design (a) is obtained with a circular local domain, and all others (b-d) are obtained with the anisotropic filter of different local volume fractions and ellipse radii (see Table 4.1). The stress scale is truncated at the best worst-case stress of the L-beam damage-patch-optimized designs (compare to Figure 4.6).

For the following comparison, designs with redundant load paths from Figure 4.6 and 4.9 are considered only. Comparing MLDs in Figure 4.11 to the ones from

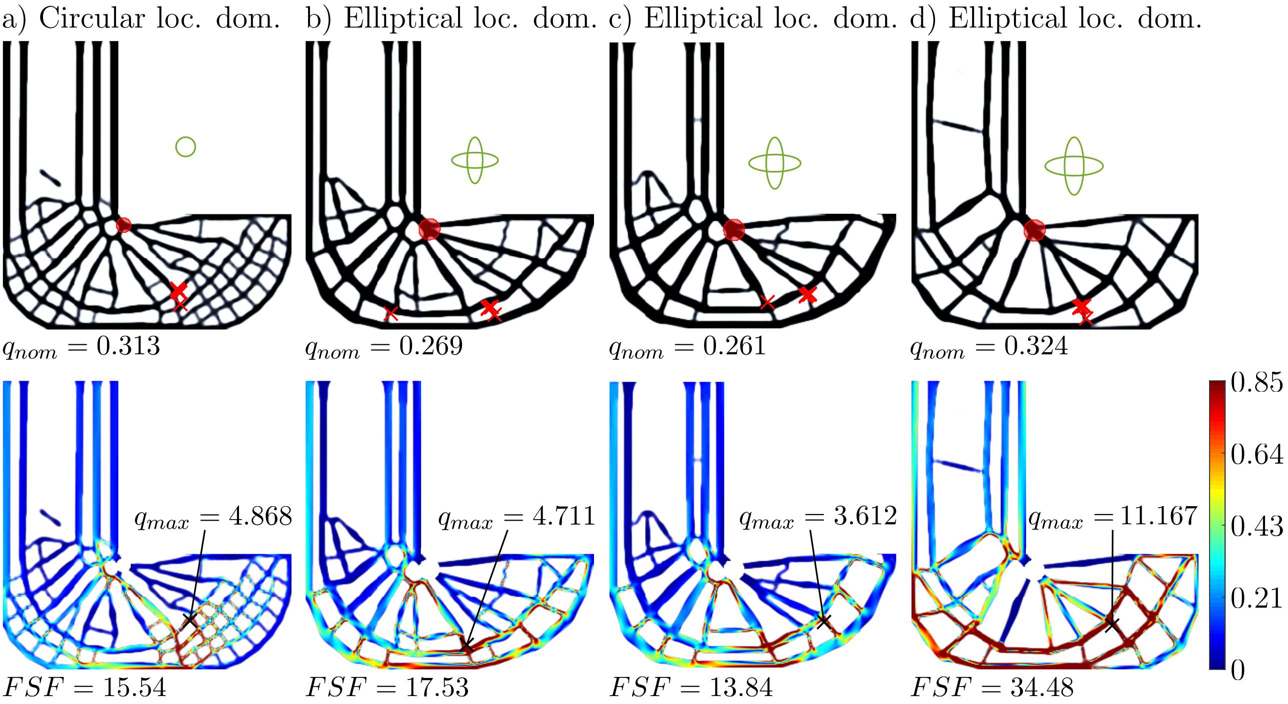

Figure 4.11: MLDs for different maximum feature sizes and local domains of the L-beam example, optimized design (top) and worst-case von Mises stress (bottom) from [75].

Figure 4.6 and 4.9, it is observed that the worst-case stress q_{max} is much lower for the damage patch optimized designs. On the other hand, the nominal stress q_{nom} is slightly lower for the feature size optimized designs, which is a result of avoiding the re-entrant corner. In conclusion, the damage robustness of the feature size optimized designs is quite detrimental due to the very high worst-case stress and FSF.

4.4 Comparison of the Explicit and Implicit Approach

Although the nominal stress of the feature size-optimized designs is lower, the high worst-case stress based on load path evaluation is detrimental for fail-safe applications for several reasons. First, damage robustness is not explicitly considered during optimization. Second, the implicit approach suppresses the formation of large members and instead divides the main load path into equally sized struts. In contrast, stress-based optimization increases the size of structural members to reduce stresses. As a result, even if a stress objective is chosen, the optimizer cannot place material where it might be most needed. Third, in stress-based explicit formulations, the secondary load path is usually thicker than the primary one because the available height or width is smaller, which increases the moment of inertia and reduces stress by thickening the structure (see Figure 4.8 and 4.9).

This option is unavailable when feature size constraints are imposed.

Regarding the implicit formulation, the computational cost is approximately 2 hours on a single CPU and the best run for the explicit approach needed approximately 12 hours on 16 CPUs. It is obvious that the explicit formulation is very computationally expensive, but there is a big difference in the worst-case stresses and damage robustness. In summary, while the computational benefits of the implicit formulation are notable, they come at the cost of significant performance losses compared to the damage patch formulation. Additionally, the implicit formulation requires extensive heuristic parameter tuning, often resulting in multiple optimization runs to find a suitable parameter setting, without guaranteeing good damage robustness. In contrast, the explicit formulation also requires a few initial runs to determine an appropriate patch size, but this process is more straightforward and can be conducted at a lower mesh resolution (see the top row in Figure 4.3 compared to the second row in Figure 4.4). Although results should ideally be mesh-independent, this is only achievable to a some extent with the implicit formulation. As the element size increases, the implicit formulation struggles to form a single strut, leading to instability in the optimization process and less reliable results.

4.5 Combined Damage Patch and Feature-Size-Constrained Approach

To better separate the redundant load paths at low aggregation parameters, the explicit damage patch formulation is extended by a minimum and maximum feature size constraint, as detailed in Section 3.3. In contrast to results from Sections 4.2 to 4.3, results obtained with the proposed combined approach, feature differences in the model configuration and variations in optimization parameters. Nonetheless, equal optimization techniques as listed in Section 2.8 are applied.

The regarded cantilever model (see Figure 4.2a) is discretized with more elements (580 × 180) and in the case of the L-beam model (see Figure 4.12) the position of the load is changed (cf. Figure 4.2b). However, the latter is again discretized with 300 × 300 elements.

The element size is 0.67 for the cantilever and 1.00 for the L-beam model, respectively. A Young's modulus of $E_0 = 3$ and a Poisson's ratio of $\nu = 0.3$ is defined. The overall volume is constrained to $\varphi_V = 40\%$ and a filter radius of $r_{filt} = 4$ is applied. The load is $F = 10$ in both cases. For stress aggregation, the p-norm function is used for both element and damage case aggregation with $p_{\mathcal{D}} = 10$ and variable $p_{\mathcal{E}}$, as described in Section 3.3. In both cases, no normalization is performed. For the β-continuation a maximum projection parameter $\beta_{max} = 6$ is considered for the cantilever and $\beta_{max} = 4$ for the L-beam model. Furthermore, starting with $\beta_{init} = 1$ it is only increased if defined stopping criteria are met

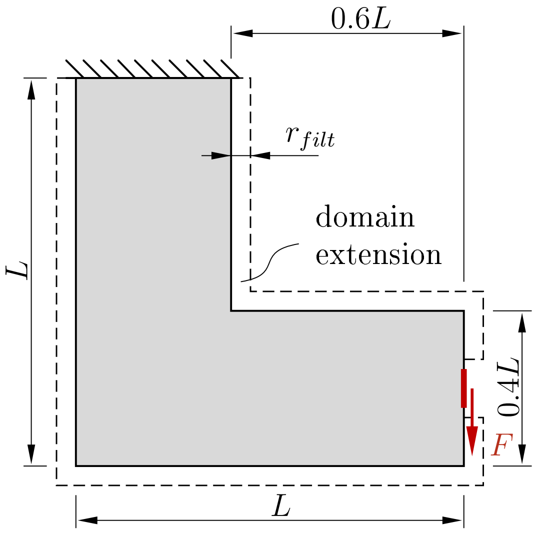

Figure 4.12: L-beam model with loads applied at the center of the vertical edge.

(see Equation (2.4) to (2.5)). The internal MMA parameters are then reset, β is increased by a constant factor, and the optimization is reinitialized. For the LVC, a circular local domain with radius $r_{loc} = 10$ is used together with a local volume fraction $\varphi_L = 0.81$ for the cantilever and 0.9 for the L-beam, respectively. This results in a targeted maximum feature size of 14 for the cantilever and 16 for the L-beam. For the approximation of the maximum local volume fraction, the p-norm is chosen with an aggregation parameter of $p_{\mathcal{L}} = 10$. Furthermore, the approximated value is normalized (cf. Equation (2.22)). Additionally, to avoid too thin struts, the minimum feature size is constrained, for which the worst-case is approximated in conjunction with all damage cases. Hence, each damage case is modeled three times for a different projection threshold, which is uniformly varied around the intermediate value of $\eta = 0.5$ by $\eta^* = 0.25$ (cf. Section 2.6) targeting a minimum feature size of $d_{min} = 4$. The minimum feature size is constrained similarly in all examples of this section.

Figure 4.13 depicts different optimized designs and worst-case stress plots. In Figure 4.13a a damage patch optimized design is given for a low aggregation parameter $p_{\mathcal{E}}$ without the LVC c_L. For Figure 4.13b the aggregation parameter is doubled and for Figure 4.13c the LVC is included as given in the combined formulation (3.4) but for a low aggregation parameter. It can be observed, that in the first case fails in generating redundant load paths. For the doubled aggregation parameter $p_{\mathcal{E}} = 20$ (see Figure 4.13b) a proper MLD is obtained, showing the lowest worst-case stress q_{max}. In Figure 4.13c a low aggregation parameter is combined with a LVC, resulting in the best FSF but a higher nominal and worst-case stress.

For the L-beam, this effect is more pronounced. Again, in Figure 4.14 results are depicted for a low aggregation parameter without the LVC, for a high aggregation parameter and for the combined formulation with a low aggregation parameter. As can be seen, even for a very high aggregation parameter of $p_{\mathcal{E}} = 100$ (see e.g. Figure 4.14b) the optimizer is not able to fully split redundant load paths. Including the LVC results in a damage robust design, even for a low aggregation parameter of $p_{\mathcal{E}} = 10$. This improved the FSF significantly compared to the two other cases.

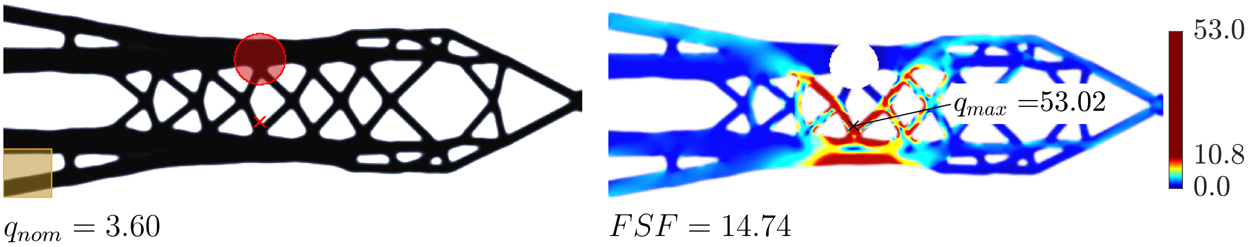

(a) Damage patch optimized non-redundant design for an aggregation parameter of $p_{\mathcal{E}} = 10$.

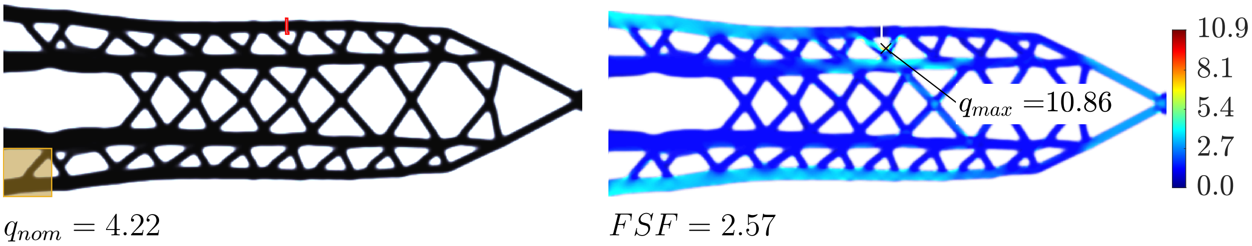

(b) Damage patch optimized redundant design for an aggregation parameter of $p_{\mathcal{E}} = 20$.

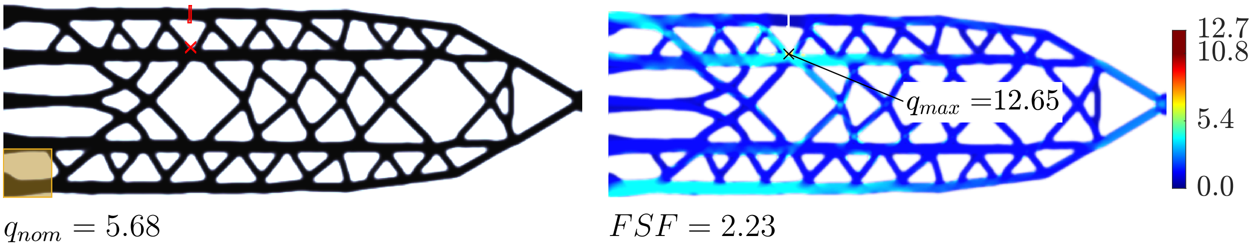

(c) Damage patch optimized redundant design obtained with an included maximum feature size constraint and an aggregation parameter of $p_{\mathcal{E}} = 10$.

Figure 4.13: Designs and worst-case stress plots of the cantilever model obtained for different aggregation parameters. Results in (c) are obtained using the combined formulation given in (3.4). Designs in (a) and (b) are obtained without the local volume constraint c_L.

Interesting to note is, that the re-entrant corner is rounded off for all L-beam designs. Unfortunately, the reason cannot be pinpointed exactly. Supposedly, the domain extension and the varied load application position (compare both L-beam configurations in Figure 4.2b and 4.12) are supposedly responsible for this outcome. But also the minimum feature size constraint, the aggregation strategy or the damage patch size play a role. Still, for slightly varied parameters results featuring a notch at the re-entrant corner have been found, but are not shown here.

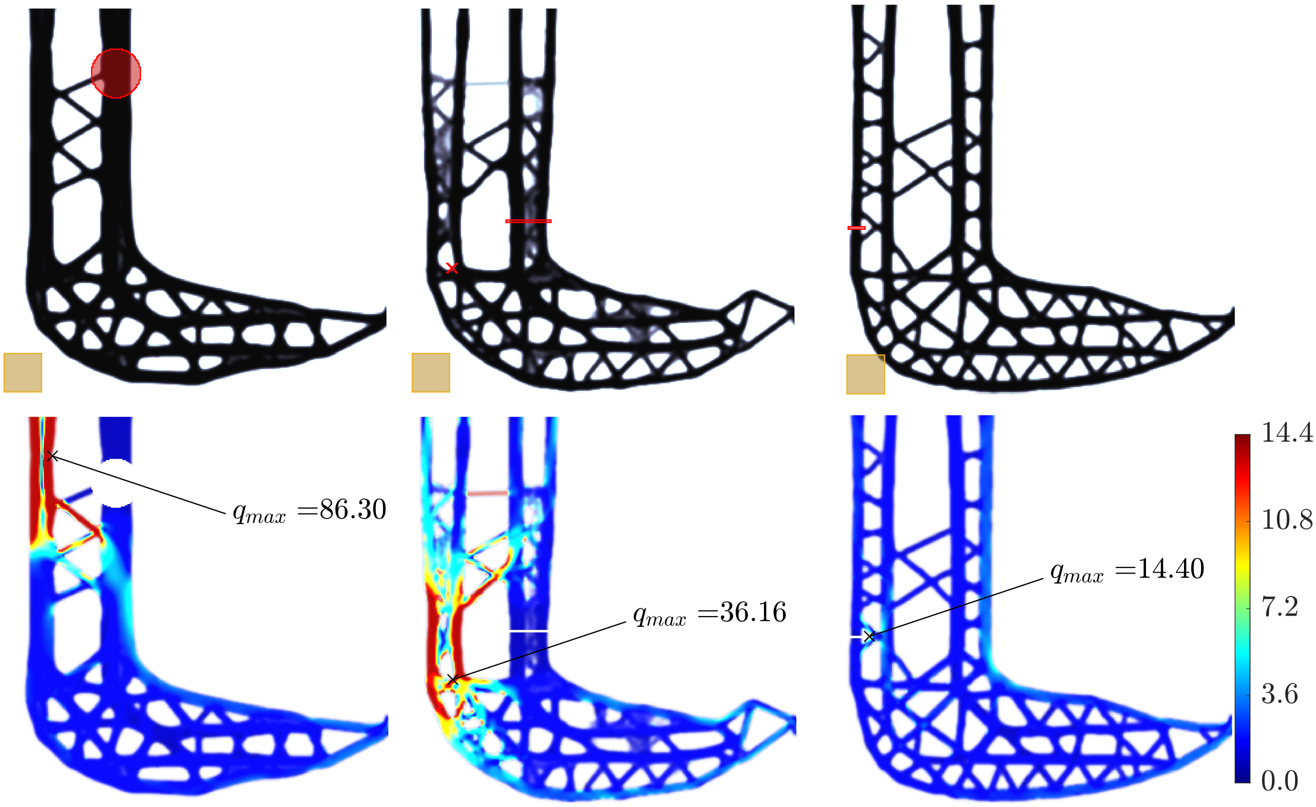

$q_{nom} = 3.56$, $FSF = 24.26$
(a) Damage patch optimized non-redundant design for an aggregation parameter of $p_{\mathcal{E}} = 10$.

$q_{nom} = 5.04$, $FSF = 7.17$
(b) Damage patch optimized non-redundant design for an aggregation parameter of $p_{\mathcal{E}} = 100$.

$q_{nom} = 4.05$, $FSF = 3.56$
(c) Damage patch optimized redundant design obtained with an included maximum feature size constraint and an aggregation parameter of $p_{\mathcal{E}} = 10$.

Figure 4.14: Designs and worst-case stress plots of the L-beam model obtained for different aggregation parameters. Results in (c) are obtained using the combined formulation given in (3.4). Designs in (a) and (b) are obtained without the local volume constraint c_L.

4.6 Contour Model Verification

Due to the non-smooth and not clearly defined boundary in the continuous density field used for optimization, a verification with a contour model is recommended, as discussed in Section 2.7. Both voxel and contour models are depicted in Figure 4.15 for an exemplary L-beam design. The L-beam design is arbitrarily selected from Figure 4.14c.

Table 4.2 to 4.4 lists performance values for all results obtained in this chapter. Column “Voxel values” contains values from Section 4.2.1 to 3.3, which are compared to “Contour values” for verification. As can be observed, both stress values q_{nom} and q_{max} differ quite significantly. Mainly due to comparably low mesh resolutions and non-optimal stress interpolation factor ($p^{RAMP} = -0.5$ for results in Table 4.2 and 4.3). But also stress concentrations at the boundary

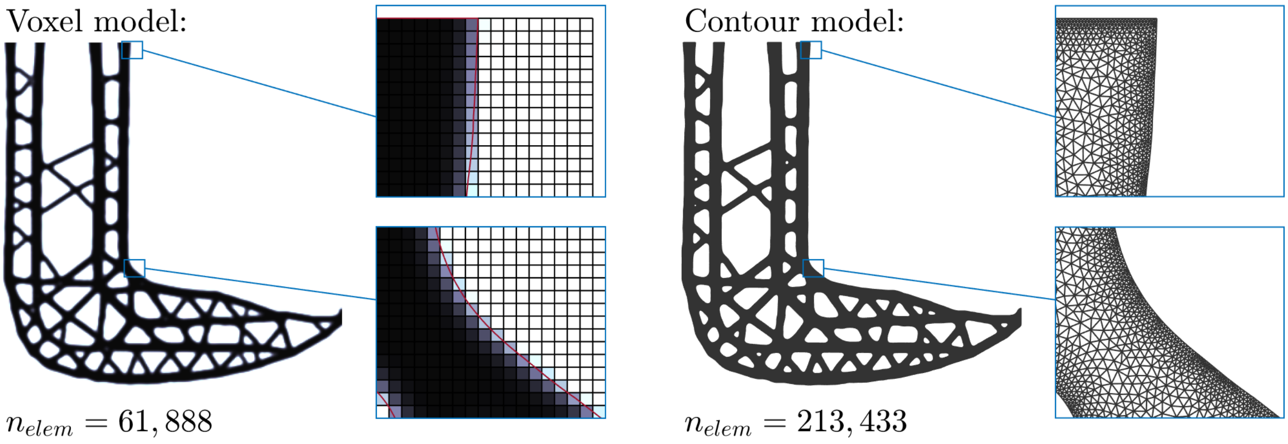

Figure 4.15: Finite element meshes of the voxel and contour model. Actual meshed contour lines are indicated with a red line.

Table 4.2: Contour verification of damage-patch-optimized results.

Model and reference (damage patch configuration)		Voxel values			Contour values		
		q_{nom}	q_{max}	FSF	q_{nom}	q_{max}	FSF
Cantilever - Fig. 4.4 (patch spacing)	low	0.66	1.39	2.1	0.52	1.91	3.6
	med.	0.72	1.42	2.0	0.54	2.29	4.3
	high	0.98	2.65	2.7	0.83	3.09	3.7
Cantilever - Fig. 4.5 (patch size)	20	0.37	3.88	10.5	0.27	4.44	16.7
	24	0.37	0.69	1.9	0.28	0.89	3.2
	30	0.37	0.67	1.8	0.27	0.85	3.1
	40	0.35	1.11	3.2	0.27	1.17	4.3
L-beam - Fig. 4.6 (patch size)	20	0.48	4.41	9.3	0.64	5.45	8.5
	24	0.46	1.28	2.8	0.62	1.71	2.8
	30	0.46	1.12	2.4	0.62	1.37	2.2
	40	0.45	0.85	1.9	0.61	0.94	1.5
Cantilever - Fig. 4.8 (patch shape)	square*	0.37	1.10	3.0	0.26	1.32	5.0
	circle	0.37	0.78	2.1	0.28	0.81	2.9
	circle*	0.37	0.75	2.1	0.29	0.87	3.0
	overl. circle	0.38	1.00	2.6	0.28	1.19	4.3
	overl. circle*	0.37	1.06	2.8	0.27	1.11	4.1
L-beam - Fig. 4.9 (patch shape)	square*	0.41	4.32	10.6	0.54	4.90	9.1
	circle	0.43	3.14	7.4	0.56	3.83	6.8
	circle*	0.41	3.65	9.0	0.54	4.02	7.4
	overl. circle	0.47	1.18	2.5	0.62	1.27	2.1
	overl. circle*	0.37	1.29	3.5	0.50	1.62	3.2

* blurred

or different worst-case damage scenarios are sources for deviations, as exemplary shown in Figure 4.16 for the L-beam results taken from Figure 4.14c. The mesh resolution of the regular voxel mesh is obliviously too coarse to capture stress concentrations in small holes as visible in Figure 4.16c. Nonetheless, tendencies[2] are almost perfectly covered for both, nominal and worst-case, stress values and the FSF. Non-fitting values are underlined (cf. Table 4.2 to 4.4). The volume fractions are not detailed here, as they are formulated as constraints that are typically satisfied with high precision. Any deviations are noted, such as in cases involving feature-size-controlled results.

The differences in volume between voxel and contour models are usually below 1%, making them negligible. However, for the results discussed in this chapter, differences of almost 4% are obtained. The reason for this deviation is the presence of too many intermediate densities. In Figure 4.17 the relative volume difference is plotted over the measure of non-discreteness (see Equation 2.30), which is a measure to quantify the amount of intermediate densities in the voxel model. As can be observed, a higher M_{nd}-value leads to more considerable differences. The worst discreteness is obtained for the cantilever design in Figure 4.10a. As is visible in Figure 4.18, some struts appear blurred or grayish. Those blurred regions are still interpreted as struts due to densities above the threshold value. Consequently, those regions count as volume in the contour model, but are only partially contributing to the volume of the voxel model, which is the reason for the observed differences.

Table 4.3: Contour verification of feature-size-constrained results.

Model and reference		Voxel values			Contour values		
		q_{nom}	q_{max}	FSF	q_{nom}	q_{max}	FSF
Cantilever - Fig. 4.10	a)	0.23	2.68	11.5	0.28	3.12	11.1
	b)	0.25	3.30	13.0	0.25	3.41	$\underline{13.6}$
	c)	0.23	3.10	13.6	0.26	3.08	12.1
	d)	0.28	2.64	9.3	0.28	2.20	7.9
L-beam - Fig. 4.11	a)	0.31	4.87	15.6	0.37	4.50	12.1
	b)	0.27	4.71	17.5	0.33	$\underline{5.11}$	15.7
	c)	0.26	3.61	13.8	0.31	3.88	12.5
	d)	0.32	11.17	34.5	0.38	12.49	32.8

---

[2] Considering a specific model type and patch configuration, the "same tendency" is considered as given, if the highest or lowest voxel value is also represented by the highest of lowest contour value respectively. Other than that, also the ranking among all values is taken into account.

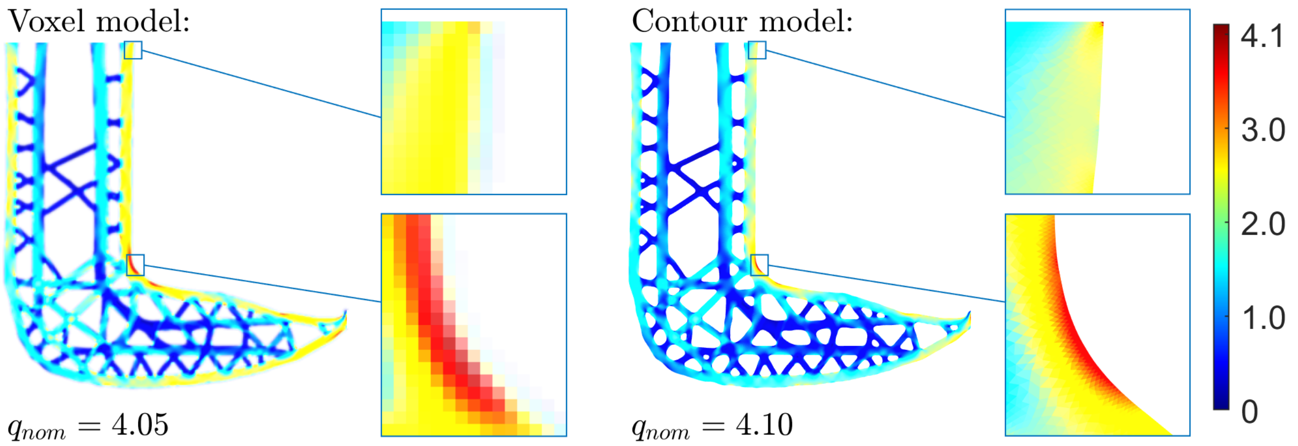

(a) Nominal stress field.

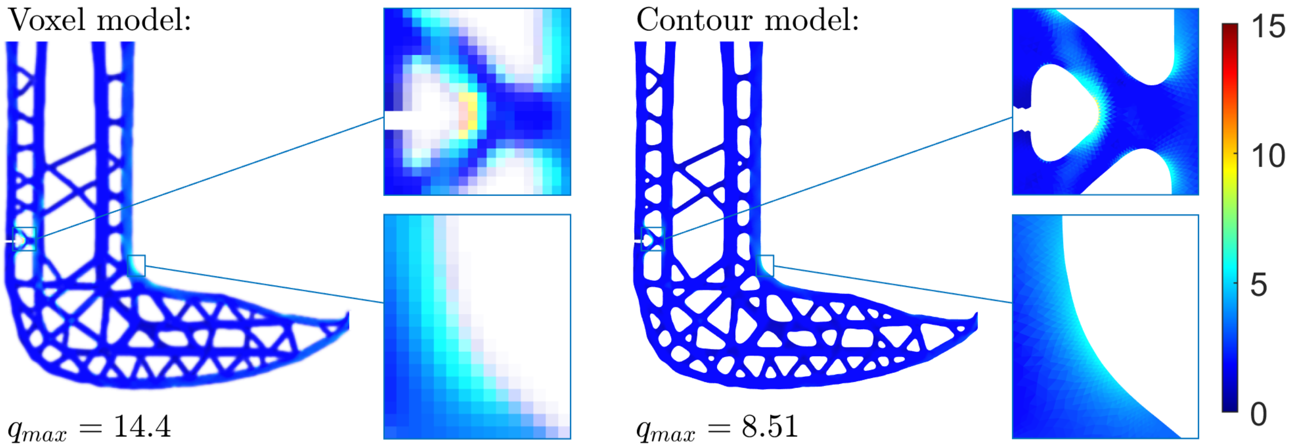

(b) Worst-case damage scenario of the voxel model.

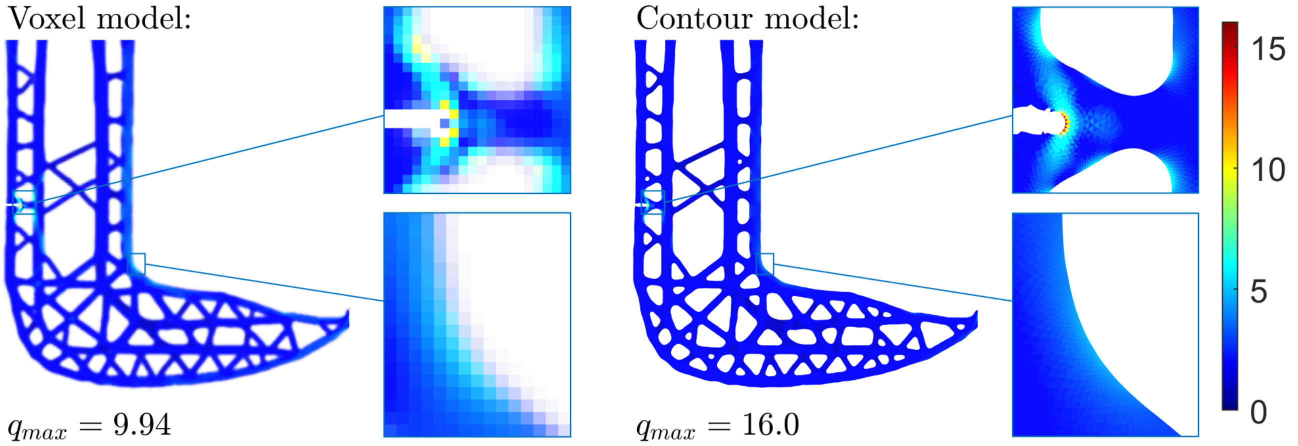

(c) Worst-case damage scenario of the contour model.

Figure 4.16: Different stress fields of the L-beam results.

Table 4.4: Contour verification of damage-patch-optimized and feature-size-constrained results.

Model and reference		Voxel values			Contour values		
		q_{nom}	q_{max}	FSF	q_{nom}	q_{max}	FSF
Cantilever - Fig. 4.13	a)	3.6	53.0	14.74	5.3	48.2	9.13
	b)	4.2	10.9	2.57	6.1	10.0	$\underline{1.63}$
	c)	5.7	12.7	2.23	7.8	13.2	1.70
L-beam - Fig. 4.14	a)	3.6	86.3	24.26	4.0	81.2	20.20
	b)	5.0	36.2	7.17	4.4	33.8	7.75
	c)	4.0	14.4	3.56	4.1	16.0	3.93

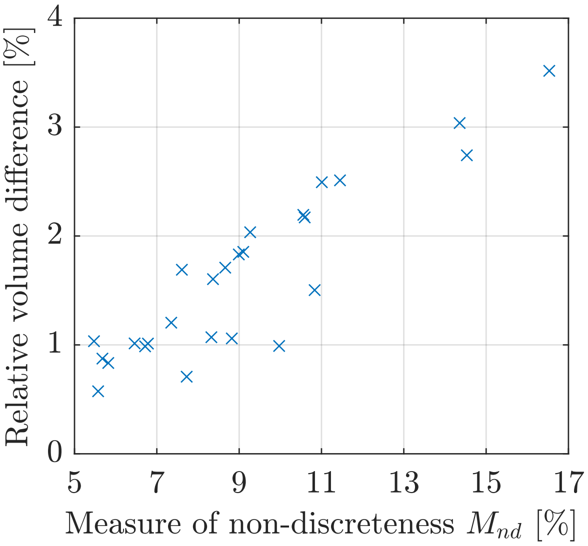

Figure 4.17: Differences in volume between voxel and contour models over the corresponding non-discreteness measure. Results from Sections 4.2.2 to 4.5 are considered.

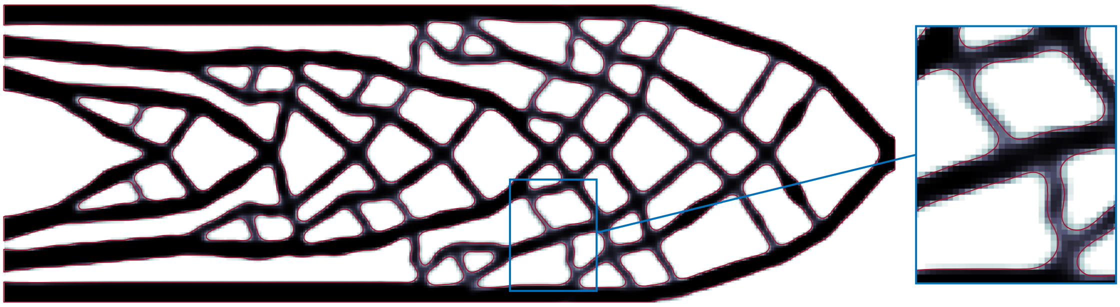

Figure 4.18: Voxel model of an optimized cantilever design and the contour line (indicated with a red line).

Chapter 5

Theory on Robust Topology Optimization

This chapter focuses on the fundamental principles and methods in the field of robust design optimization. Specifically, a generalized first-order approach is recapitulated from a preceding publication of the author [122]. In contrast to Chapter 3 other types of uncertainties shall be considered during optimization. For instance, spatially varying parameters such as material properties, parameters with uncertain direction or magnitude (e.g. the load vector), and geometry imperfections are taken into account. Furthermore, both the mean performance and the variability of the structural response are examined, rather than focusing solely on worst-case performance.

The following subsections are structured as follows. First, an overview of general problem formulations related to uncertainties in topology optimization is provided in Section 5.1. This is followed by a recapitulation of the generalized formulation for robust topology optimization (RTO), as presented in a previous publication by the author [122], along with a discussion of the improved efficiency in gradient calculation introduced in [124]. Finally, the generation of random fields is briefly described, which are required for benchmark optimizations and post-processing.

5.1 Overview of Problem Formulations

If uncertainties are present and considered during optimization, one of three primary approaches: worst-case, reliability-based, or robustness-based (see Subsections 5.1.1 to 5.1.3), can be applied in the field of topology optimization. The following discussion provides a general overview and thus does not describe the topic in depth.

5.1.1 Worst-Case Approach

Currently, the worst-case strategy is probably the most pursued approach in engineering practice [5]. It focuses solely on optimizing single extreme values and usually ignores all other cases (cf. Figure 1.1). This ensures that all considered cases are below a certain threshold or that the extreme case is as optimal as possible. Thus, the variability and consequently the robustness of the design response may also be reduced implicitly. An exemplary formulation is given in Equation (3.1). The max-operator is non-differentiable and hence requires a smooth approximation for gradient-based optimization algorithms. Since no actual probability measures are considered in this approach, is it commonly regarded as non-probabilistic or deterministic.

The computing time may only increase slightly if a few cases are considered and parallel evaluation is utilized. Naturally, this approach benefits from its simplicity and the possibility of using existing deterministic implementations. Nonetheless, this can result in very conservative results and may not fully utilize the full potential.

5.1.2 Reliability-Based Approach

Reliability-based approaches explicitly constrain the probability P of a specific event, e.g. that the highest stresses q_{max} exceed the allowable limit q_0. Assuming a failure probability of P_0 an exemplary reliability constraint can be formulated as follows

$$P(q_{max}(\boldsymbol{\rho}, \mathbf{u}, \boldsymbol{\alpha}) \geq q_0) \leq P_0, \tag{5.1}$$

where $\boldsymbol{\alpha}$ is the vector of random variables.

The probability defined in the above equation usually cannot be directly solved analytically and requires numerical approximation techniques. The most prominent is the first-order reliability method (FORM) which is based on a linear approximation at the most probable point (MPP) in the normalized space. Basically, only the distance to the MPP is required and can be determined by non-linear optimization. Different formulations have been developed,[1] which all require an inner optimization to be conducted. Hence, this results in more computational effort. Despite that, this approach suffers from other drawbacks, as discussed in Section 1.1.3.

---

[1] Namely the reliability index approach (RIA), the performance measure approach (PMA) and the sequential optimization and reliability assessment (SORA) to just mention the most frequently investigated methods. For a comprehensive review, see for instance [160].

5.1.3 Robustness-Based Approach

As illustrated in Figure 1.2a robustness is interpreted as the variability of an output function subjected to perturbations. As a result, reducing the variability increases the robustness. An often used statistical measure to quantify the variability of a design response $g\left(\boldsymbol{\rho}, \mathbf{u}, \boldsymbol{\alpha}\right)$ is the variance σ_g^2 or standard deviation σ_g. Robust approaches are characterized by including both the mean value μ_g and standard deviation in a robust design response

$$\mathcal{G}_g = \mu_g + \kappa\sigma_g, \tag{5.2}$$

where κ is a weighting factor. It can be varied to change the influence of the standard deviation and as a consequence increase robustness.

Both statistical measures μ_g and σ_g are often determined using numerical approximation techniques, which introduce additional computational costs compared to conventional deterministic optimization. To minimize these costs, first-order approaches offer high efficiency and do not require the solution of an inner optimization, as is the case with current reliability-based approaches. Although expected to be slightly less accurate, a promising first-order approach is examined in Section 6.1.

5.1.4 Interrelation Between Reliability-Based and Robustness-Based Approaches

In most cases, $\mathcal{G}_g$ from Equation (5.2) is considered as the cost function. This does not require additional assumptions, and the weighting factor is typically chosen freely to align with the practitioner's goals [89]. Since the cost function is optimized, the best possible values for μ_g and σ_g are ideally obtained. However, as the standard deviation decreases, the mean value typically increases. In other words, improving robustness often results in a trade-off with mean performance. Consequently, the absolute performance, i.e. the robust function $\mathcal{G}_g$, is most relevant for evaluation. Optimizing solely for the standard deviation can be an ill-posed problem that yields no meaningful results, and thus it is essential to consider both quantities. This also implies that an excessively high weighting factor can lead to a divergent optimization.

In the case that $\mathcal{G}_g$ is treated as a constraint, as for instance suggested by Silva et al. [42] in the context of stress constraints, the weighting factor can still be chosen somewhat arbitrarily to control the robustness of the result. However, rather than focusing solely on robustness, it is more reasonable to consider the absolute performance and interpret $\mathcal{G}_g$ as a quantile value Q, related to a given failure probability, as follows.

$$Q(1 - P_0) = F_{\mathcal{G}}^{-1}(1 - P_0), \tag{5.3}$$

where $F_{\mathcal{G}}^{-1}$ is the inverse cumulative distribution of $\mathcal{G}_g$. Per definition, the cumulative distribution function (CDF) $F_{\mathcal{G}}$ represents the probability at a certain point g as

$$F_{\mathcal{G}}(g) = P(\mathcal{G} \leq g). \tag{5.4}$$

Constraining the probability is basically a reliability constraint, similar to Equation (5.1). However, the actual quantile value is calculated as

$$Q(1 - P_0) = \mu_g + \kappa^* \sigma_g \quad \text{with} \quad \kappa^* = \Phi^{-1}(1 - P_0), \tag{5.5}$$

where κ^* is related to a standard normal CDF Φ. This assumption is likely incorrect, but considering the limit theorem, it is not arbitrarily chosen, particularly when multiple uncertainties with relatively small variations are involved. Therefore, this formulation is further examined in Section 6.3.

5.2 Theory on Robust Topology Optimization using a First-Order Approximation

As mentioned earlier, several approaches exist for probabilistic analysis. One particularly efficient approach is the FOSM method [4], for which a generalized formulation has been derived and investigated in a prior publication by the author [122]. The basic formulation is summarized below, with detailed derivations provided in Appendix C.1.

For FOSM, which should not be confused with FORM, the mean value μ_g and variance σ_g^2, also referred to as the first and second statistical moments, are approximated using a first-order Taylor series, yielding

$$\mu_g \approx g\left(\boldsymbol{\mu}_\alpha\right) \tag{5.6}$$

$$\sigma_g^2 \approx \frac{Dg}{D\boldsymbol{\alpha}}^{\mathrm{T}} \boldsymbol{\Sigma}_\alpha \frac{Dg}{D\boldsymbol{\alpha}}, \tag{5.7}$$

where $\boldsymbol{\mu}_\alpha$ is the mean vector and $\boldsymbol{\Sigma}_\alpha$ is the symmetric covariance matrix of the random parameter α.

5.2.1 Adjoint Sensitivities

Gradient-based optimization algorithms require derivatives with respect to design variables. Hence, the discrete adjoint method [37] is employed in the following to determine necessary derivatives. First, the square root of (5.7) is inserted into (5.2) and differentiated, yielding:

$$\frac{D\mathcal{G}_g}{D\boldsymbol{\rho}} = \frac{D\mu_g}{D\boldsymbol{\rho}} + \frac{\kappa}{2\sigma_g} \frac{D\sigma_g^2}{D\boldsymbol{\rho}}. \tag{5.8}$$

Consequently, total derivatives for the mean and variance with respect to design variables are needed and defined as:

$$\frac{D\mu_g}{D\boldsymbol{\rho}} \approx \frac{\partial g}{\partial \boldsymbol{\rho}} - \boldsymbol{\lambda}^{\mathrm{T}} \frac{\partial \mathbf{R}}{\partial \boldsymbol{\rho}} \tag{5.9}$$

and

$$\frac{D\sigma_g^2}{D\boldsymbol{\rho}} \approx \frac{\partial \sigma_g^2}{\partial \boldsymbol{\rho}} - \boldsymbol{\lambda}_u^{\mathrm{T}} \frac{\partial \mathbf{R}}{\partial \boldsymbol{\rho}} - \boldsymbol{\lambda}_\alpha^{\mathrm{T}} \frac{\partial \mathbf{R}_\alpha}{\partial \boldsymbol{\rho}}. \tag{5.10}$$

Additionally, following two adjoint systems have to be solved

$$\frac{\partial \mathbf{R}}{\partial \mathbf{u}}^{\mathrm{T}} \boldsymbol{\lambda} = \frac{\partial g}{\partial \mathbf{u}} \tag{5.11}$$

together with

$$\begin{bmatrix} \frac{\partial \mathbf{R}}{\partial \mathbf{u}}^{\mathrm{T}} & \frac{\partial \mathbf{R}_\alpha}{\partial \mathbf{u}}^{\mathrm{T}} \\ \mathbf{0} & \frac{\partial \mathbf{R}}{\partial \mathbf{u}} \end{bmatrix} \begin{bmatrix} \boldsymbol{\lambda}_u \\ \boldsymbol{\lambda}_\alpha \end{bmatrix} = \begin{bmatrix} \frac{\partial \sigma_g^2}{\partial \mathbf{u}} \\ \frac{\partial \sigma_g^2}{\partial \boldsymbol{\lambda}} \end{bmatrix} \tag{5.12}$$

where the first system in Equation (5.11) is similar to the deterministic case (2.8), and the second can be split into two systems, which are solved sequentially. In conclusion, compared to the deterministic case, only two additional adjoint systems of equal size have to be solved. Further required derivatives are given in Appendix C.1.

5.2.2 Principal Sensitivities

In some cases, for instance if stresses are considered, second-order derivatives occur in Equation (5.8), resulting in large, non-sparse matrices that increase the required numerical effort. For a medium mesh resolution of a few ten thousand degrees of freedom, the computational cost is already prohibitively high. Hence, a much more efficient approach based on principal sensitivities is derived by [124], which is summarized in the following.

The fundamental idea is to efficiently compute the derivative of the variance, $D\sigma_g^2/D\boldsymbol{\rho}$, as required in Equation (5.8). Basic first-order derivatives, such as $Dg/D\boldsymbol{\rho}$ or $Dg/D\boldsymbol{\alpha}$, are typically straightforward to compute and do not significantly increase the computational cost. For the derivation, basic differentiation with respect to the design variables is employed, yielding the following expression:

$$\frac{D\sigma_g^2}{D\boldsymbol{\rho}} \approx 2 \frac{D^2 g^{\mathrm{T}}}{D\boldsymbol{\alpha} D\boldsymbol{\rho}} \boldsymbol{\Sigma}_\alpha \frac{Dg}{D\boldsymbol{\alpha}} \tag{5.13}$$

To find a substitution for the product (which includes the costly second-order derivative in Equation (5.13)) the derivative of g is perturbed by a small step of the random variables $\Delta\boldsymbol{\alpha}$ and expanded by a Taylor series

$$\frac{Dg}{D\boldsymbol{\rho}}\left(\boldsymbol{\mu}_\alpha + \Delta\boldsymbol{\alpha}\right) \approx \frac{Dg}{D\boldsymbol{\rho}}\left(\boldsymbol{\mu}_\alpha\right) + \frac{D^2 g}{D\boldsymbol{\rho} D\boldsymbol{\alpha}}\left(\boldsymbol{\mu}_\alpha\right)\Delta\boldsymbol{\alpha}. \tag{5.14}$$

Higher-order terms are neglected and $\Delta\boldsymbol{\alpha}$ is chosen to be

$$\Delta\boldsymbol{\alpha} = \varepsilon\,\boldsymbol{\Sigma}_\alpha \frac{Dg}{D\boldsymbol{\alpha}}\left(\boldsymbol{\mu}_\alpha\right), \tag{5.15}$$

where ε is a scaling factor. By inserting Equation (5.15) in (5.14) and after reordering, following substitution is obtained:

$$\frac{D^2 g^{\mathrm{T}}}{D\boldsymbol{\alpha} D\boldsymbol{\rho}}\boldsymbol{\Sigma}_\alpha \frac{Dg}{D\boldsymbol{\alpha}} \approx \frac{1}{\varepsilon}\left[\frac{Dg}{D\boldsymbol{\rho}}\left(\boldsymbol{\mu}_\alpha + \varepsilon\,\boldsymbol{\Sigma}_\alpha \frac{Dg}{D\boldsymbol{\alpha}}(\boldsymbol{\mu}_\alpha)\right) - \frac{Dg}{D\boldsymbol{\rho}}(\boldsymbol{\mu}_\alpha)\right] \tag{5.16}$$

As can be observed, no second-order derivatives are required. Only the derivative ${}^{Dg}/_{D\boldsymbol{\rho}}$ needs to be reevaluated once for a perturbed function value. Finally, a normalization factor ε_0 is introduced to ensure a constant perturbation step size.

$$\varepsilon = \frac{\varepsilon_0}{\|\boldsymbol{\Sigma}_\alpha \frac{Dg}{D\boldsymbol{\alpha}}\|} \tag{5.17}$$

By inserting Equation (5.16) into Equation (5.13) and selecting an appropriate step size ε_0, the calculation of demanding second-order derivatives is circumvented, thereby reducing the numerical effort by at least an order of magnitude [124]. It is important to note that principal sensitivities exhibit behavior similar to finite differences and may become inaccurate for excessively large or small step sizes. However, numerical studies have shown that comparable results are obtained across a wide range of ε_0. FOSM results in Section 6.1 are obtained using adjoint sensitivities, while results in Section 6.3.1 are obtained using principal sensitivities.

5.2.3 Covariance Matrix

Besides required partial derivatives, the covariance matrix $\boldsymbol{\Sigma}_\alpha$ has to be set up. Given the variance σ_α^2 of the random parameter α the components of a stationary *squared exponential* or *Gaussian* covariance function are expressed as follows:

$$\Sigma_{i,j} = \sigma_\alpha^2 \exp\left(-\frac{d_{i,j}^2}{l_c^2}\right), \tag{5.18}$$

where $d_{i,j} = \|\mathbf{x}_i - \mathbf{x}_j\|$, with $\mathbf{x}_i$ and $\mathbf{x}_j$ representing the coordinates of points i and j, respectively. The correlation length is denoted as l_c and can either be defined by the user or derived from measurements. Various autocorrelation functions, such as simple *exponential* or *linear*, exist but are not further investigated in this work. A reasonable choice for the correlation length is found to be approximately 10% of the design domain dimensions.

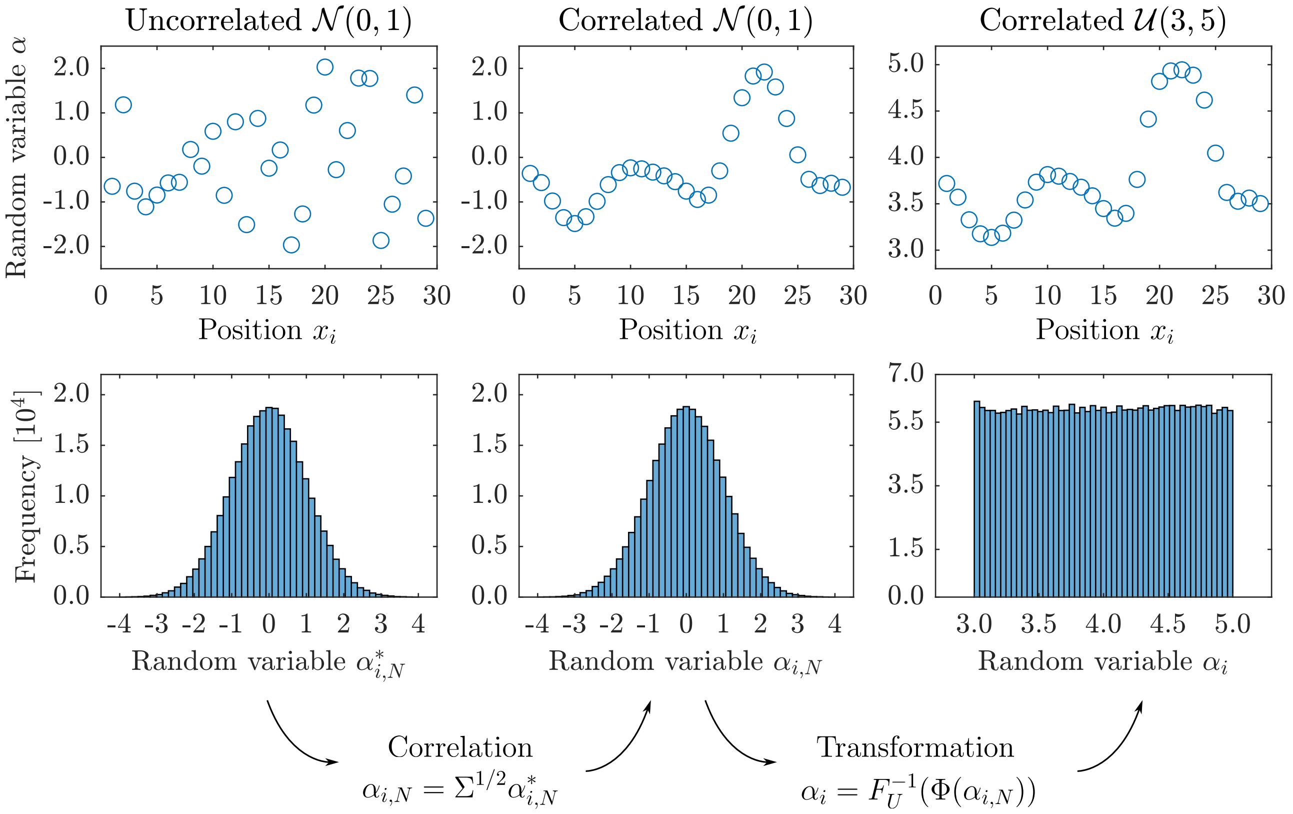

Figure 5.1: 1D example of the random field generation process. One discrete realization with 28 parameters (top row) and discrete probability distribution for 10^4 realizations.

5.3 Modeling Discrete Random Fields

While for FOSM only the covariance matrix is required (see Equation (5.18)), for MCS and post-processing, discrete realizations of the considered uncertain parameters are needed. For this purpose, scattering material properties, i.e. stiffness and strength, as well as geometry perturbations, are modeled as correlated random fields. Assuming that corresponding information is provided for the considered random parameter, the general process can be described as follows: Uncorrelated and standard normal distributed $\mathcal{N}(0,1)$ random numbers are generated, then correlated and transformed to the desired distribution type, as illustrated in Figure 5.1. In this case, the final data is uniformly distributed, with lower and upper bounds given by 3 and 5, respectively, $\mathcal{U}(3,5)$. The corresponding continuous CDFs are denoted as Φ for the standard normal distribution and F_U for the uniform distribution. The correlation matrix for normalized variance is denoted as $\mathbf{\Sigma}$ (cf. Equation (5.18)). For the considered 1D example, the correlation length is $l_c = 4$.

Since random fields are required only for the optimization of benchmark examples and post-processing, they are not the primary focus of this work. For a detailed description, refer to Appendix C.3.

Chapter 6

Numerical Results for Robust Topology Optimization

In this chapter, numerical results obtained using the theoretical methods outlined in Chapter 5 are presented and discussed. Various uncertainties are considered during optimization, i.e. scattering material properties, variable load direction or magnitude, and geometry imperfections. Different configurations are investigated. Optimizations with one single type of uncertainty are initially conducted to analyze the performance of the proposed first-order approach. In the end, multiple uncertainties are incorporated simultaneously.

This chapter consists of three main sections. Firstly, uncertainties in stiffness and geometry are addressed in the context of a robust objective function (see Section 6.1). Regarding variations in geometry, different verification approaches are examined and discussed in detail in Section 6.2. Finally, in Section 6.3, uncertainties in material strength are considered within a stress-constrained framework. Specific aspects associated with this robust constraint function are investigated, and multiple types of uncertainties are considered simultaneously.

6.1 Randomness in Geometry or Stiffness Considering a Robust Objective

In this section, the objective f is considered to be affected by variations in either material stiffness or geometry. The proposed generalized FOSM approach (see Section 5.2) is applied to a displacement objective with a spatially varying Young's modulus, as well as to an example regarding the maximum stress subjected to variations in the projection threshold η_e from Equation (2.14). Common benchmark examples are investigated, namely the well-known inverter (Figure 6.1) and the L-beam (Figure 4.2b). The inverter contains spring stiffnesses at both the input and output nodes, along with two small fixed supports. The load is applied to a single node, whereas for the L-beam, it is distributed across several nodes to

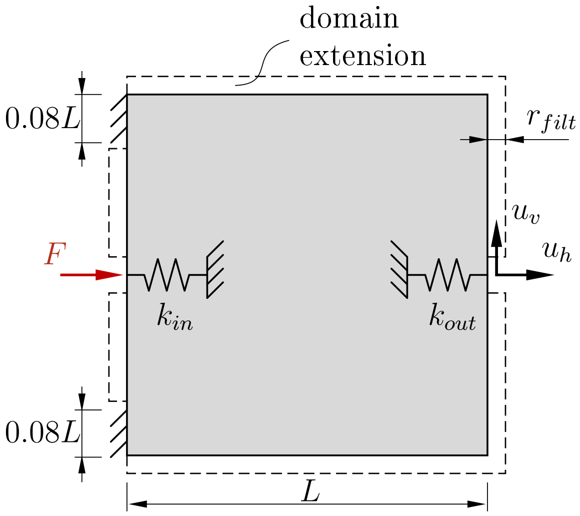

Figure 6.1: Inverter model with spring stiffnesses.

mitigate stress concentrations. The projection steepness parameter is initialized with $\beta = 1$ and gradually increased between iterations 50 and 250, reaching a maximum of 64 for the inverter and 16 for the L-beam, respectively. In both cases, a Young's modulus of $E_0 = 1.0$ and a Poisson's ratio of $\nu = 0.3$ are used as nominal material parameters. The design space is discretized into 150×150 elements ($L = 300$), with an element size of 2 and a filter radius of $r_{filt} = 16$ for both models. For all results presented, the volume is constrained to a fraction of the entire non-extended design domain. Specifically, the volume fraction is constrained to 35% for the inverter and 40% for the L-beam. For further details on the underlying numerical process, refer to Section 2.8.

6.1.1 Inverter Model with Spatially Scattering Young's Modulus

The inverter is optimized for the horizontal displacement u_h (see Figure 6.1). While the design is required to be symmetric, it must still account for an asymmetric, spatially scattering material stiffness. To achieve this, the entire model is calculated, but symmetry is enforced on the design variables during optimization. Due to the asymmetric random field, the vertical displacement u_v is non-zero ($u_v \neq 0$), and its standard deviation σ_v is therefore incorporated into the robust objective as follows:

$$\mathcal{G}_u = \mu_h + \kappa(\sigma_h + \sigma_v) \tag{6.1}$$

with μ_h and σ_h represent the mean and standard deviation of u_h, respectively (for details on the definition and derivatives of the nodal displacement, see Appendix A.2.6). The weighting factor is set to $\kappa = 10$ for all inverter examples. Typically, the horizontal displacement u_h starts with a positive value, decreases to zero,

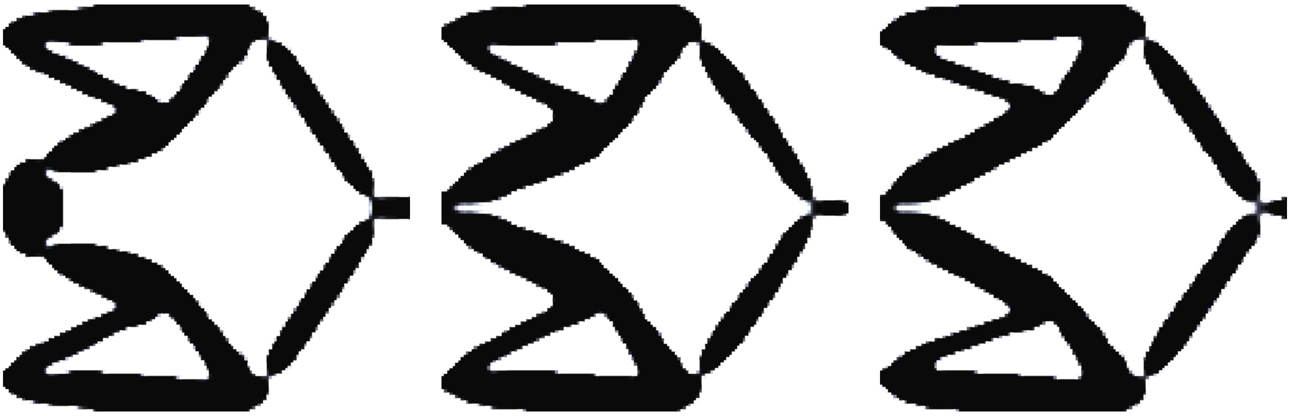
(a) Deterministic (b) FOSM (c) Monte Carlo

Figure 6.2: Deterministic and robust compliance inverter designs from [122].

and then becomes negative, eventually converging to a final value where $u_h < 0$. Numerical experiments indicate that if the initial weighting factor κ is set too high, the MMA algorithm is unable to reduce u_h below zero. Consequently, the initial value $\kappa_{init} = \kappa/1000$ is held constant for the first 10 iterations and then gradually increased in each subsequent step until it reaches its predefined value, 40 iterations later. For the deterministic case, only u_h is minimized.

The load input is defined as $F_{in} = 2$, with input and output spring stiffness values of $k_{in} = 1$ and $k_{out} = 0.01$, respectively. To ensure well-posed function values, both the objective and constraint values are scaled by a factor of 100. The spatially scattering Young's modulus is modeled as a Gaussian random field. The covariance is generated with Equation (5.18), $l_c = 30$, a mean of $\mu_E = 1.0$ and a variance of $\sigma_E^2 = 0.1^2$.

The resulting optimized designs are depicted in Figure 6.2. Figure 6.2a shows the deterministically optimized inverter with bulk material agglomerated at the input node, which is connected to the rest of the structure via two hinges. The robust designs avoid this by directly connecting the input node. Removing σ_v from the robust objective yields designs similar to the deterministic one. Thus, obviously avoiding those two hinges and directly connecting the input node helps to reduce the variation in vertical displacements. This is further proven by the reduced standard deviation of horizontal displacement σ_v (see Table 6.1). As can be observed, σ_v is reduced by 48.4% comparing deterministic and FOSM post-processing values. The MCS benchmark shows an improvement of 67.2%. Note, for each optimization iteration, 1000 samples are evaluated for MCS. For post-processing, $n = 10^4$ random samples are considered. The increased robustness comes at the expense of around 4% less mean horizontal displacement, which is to be expected in robust design optimization.

Evaluating the proposed approach, the approximation quality of FOSM is very good, if optimization and post-processing values for the horizontal displacement values μ_h and σ_h are compared. The approximation of σ_v, on the other hand, is

Table 6.1: Numerical results of the compliance inverter from [122]. Post-processing values are obtained using a Monte Carlo simulation with $n = 10^4$ random samples.

Type	Optimization			MCS using $n = 10^4$ samples		
	f, μ_h	σ_h	σ_v	μ_h	σ_h	σ_v
Determ.	-2.37	-	-	-2.36	0.0326	0.0114
FOSM	-2.25	0.0227	0.0175	-2.24	0.0226	0.0059
MCS	-2.28	0.0240	0.0037	-2.27	0.0243	0.0037

Table 6.2: Contour verification results for the compliance inverter obtained using a Monte Carlo simulation with $n = 10^4$ random samples.

Type	μ_h	σ_h	σ_v
Determ.	-1.85	0.0533	0.0317
FOSM	-1.95	0.0356	0.0162
MCS	-1.96	0.0376	0.0216

close to a factor of three worse, but still a more robust design, i.e. less variation in u_h and u_v, is obtained. Note, the coefficient of variation of the deterministic design $\text{CoV}_v = \sigma_v/\mu_h \approx 0.5\%$, which is a quite low, compared to $\text{CoV}_E = 10\%$ for the Young's modulus.

Table 6.2 contains post-processing values for the contour verification and in Figure 6.3 the considered contour lines are presented. Comparing FOSM and MCS to the deterministic values, the reduced variability in the vertical and horizontal displacement can be confirmed. Interestingly, the FOSM design shows the highest robustness. Nonetheless, absolute contour values differ significantly from the voxel values (compare Table 6.1 and 6.2), which is due to the softening effect of intermediate density elements in the voxel mesh.

6.1.2 L-beam Model with Spatially Scattering Projection Threshold

For the L-beam example, the aggregated stress $\max(q_e) \approx \mathcal{A}_{KS}(q_e)$ is employed as the objective. Stress aggregation is conducted as outlined in Section 4.2, with the aggregation parameter updated iteratively during each optimization step. A distributed force $F = 10$ is applied around the top-right corner of the beam (see Figure 4.2b) to mitigate stress concentration peaks and ensure a more uniform

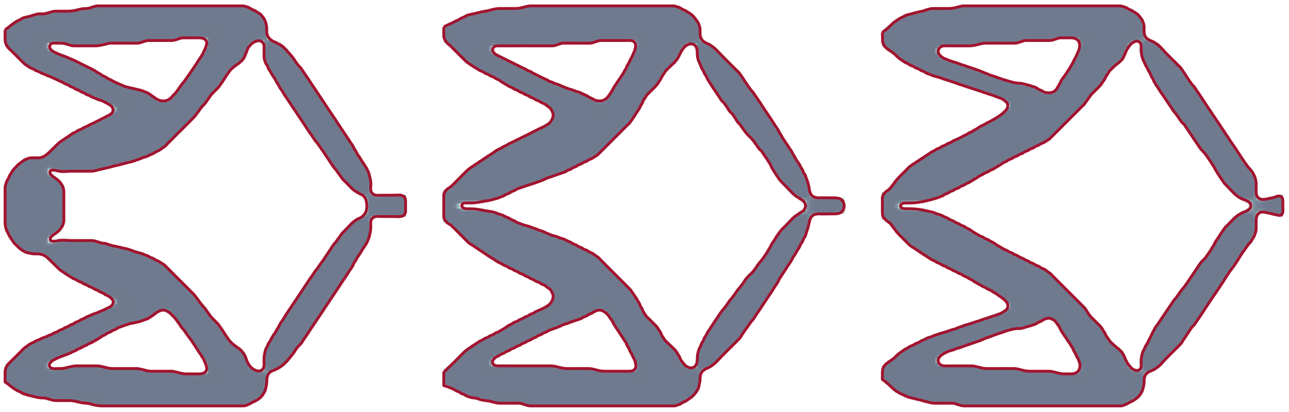

(a) Deterministic (b) FOSM (c) Monte Carlo

Figure 6.3: Density field of the three optimized inverters, superimposed with the contour line indicated in red.

stress distribution throughout the structure. The robust objective is given by

$$\mathcal{G}_q = \mu_q + \kappa\sigma_q \tag{6.2}$$

with $\kappa = 3$. To properly scale the optimization problem for the design variable update, both the objective and volume constraint function values are multiplied by a factor of 10. The spatially and uniformly scattered projection threshold $\eta_e = [0.45, \dots, 0.55]$ is modeled as a Gaussian random field and subsequently transformed to the target uniform distribution. The covariance is determined using Equation (5.18), with a correlation length of $l_c = 30$ and a mean value of $\mu_\eta = 0.5$. The variance of the continuous uniform distribution is computed as $\sigma_\eta^2 = \frac{1}{12}(0.55 - 0.45)^2 = 8.33 \cdot 10^{-4}$.

Figure 6.4 presents the obtained designs alongside the corresponding nominal von Mises stress plots. Interestingly, the FOSM result exhibits the lowest nominal stress among all cases. Apart from this observation, only minor differences are noticeable across the designs.

The obtained numerical results are summarized in Table 6.3. It is observed that the FOSM approach reduces the standard deviation of the true maximum stress, $\sigma_{\hat{q}}$, by more than 12%. Additionally, the mean value is slightly decreased. In the case of MCS, a significant reduction of $\sigma_{\hat{q}}$ by more than 84% is achieved. When comparing the standard deviation estimated by the FOSM approach with that obtained through MCS of the same design, it is evident that the linear approximation is highly inaccurate. Consequently, the RTO with the FOSM method fails to exploit the same optimization potential as the RTO using Monte Carlo sampling.

Note that the computational time is considerably high when aggregated stresses are considered for the proposed generalized FOSM approach. In fact, it even exceeds the MCS run time for models with very fine discretization. For MCS, 1000 models are solved in parallel across 24 cores, making a direct comparison some-

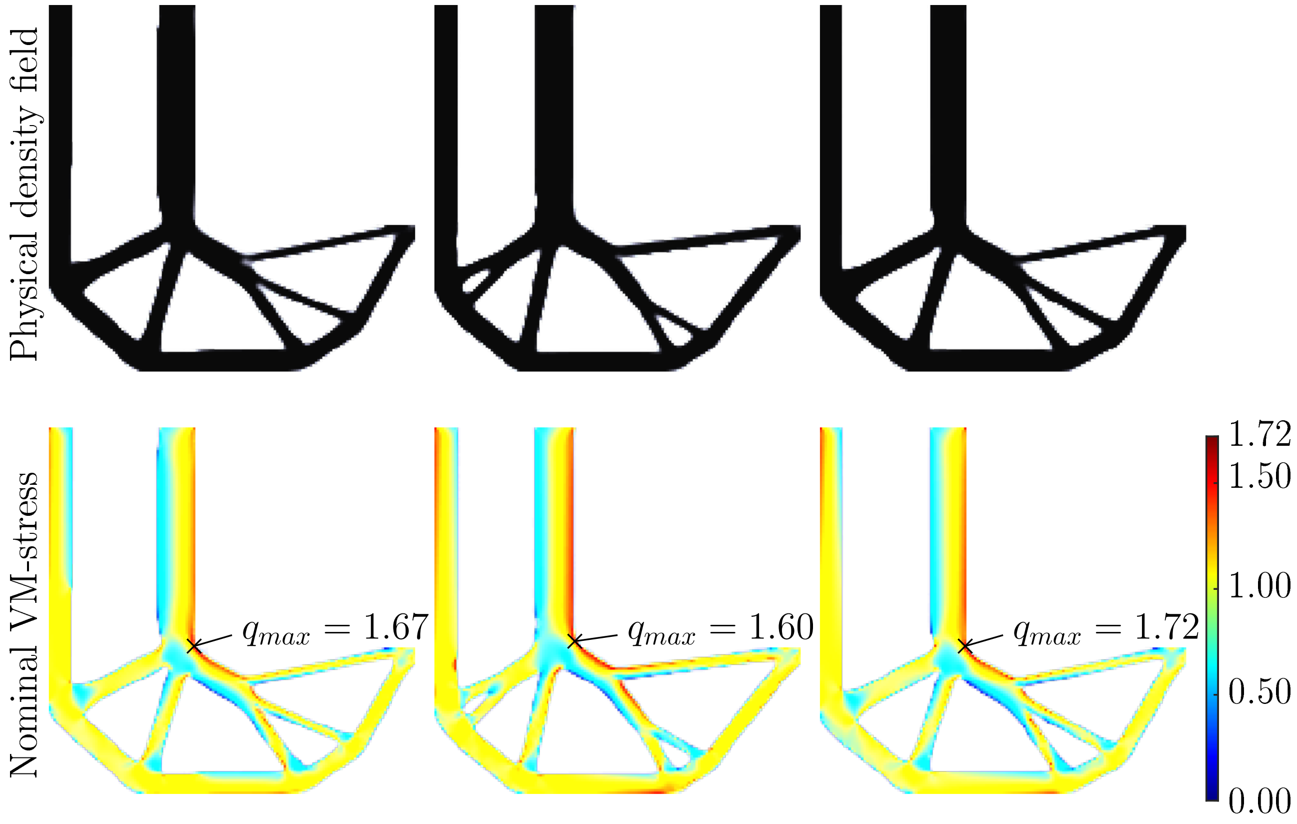

(a) Deterministic (b) FOSM (c) Monte Carlo

Figure 6.4: Deterministic and robust L-beam designs (top row) and nominal von Mises stress plots (bottom row) from [122].

what unfair. However, only three adjoint systems need to be solved per iteration for the proposed generalized FOSM approach. For coarse discretizations, FOSM is significantly faster in all cases. The increasing computational time can be attributed to the gradient calculation of aggregated stresses (cf. Appendix C.1 and C.2). Many of the required partial derivatives are non-zero, and some are non-sparse. Furthermore, performing simple matrix operations on these non-sparse, large matrices is computationally expensive. Generally, the calculation of second-order partial derivatives for aggregated stresses accounts for the majority of the computational time.

From visual inspection, all three designs appear very similar. However, small differences can be identified upon closer examination. The obtained volume is, by definition, equal across all cases. Therefore, special attention is given to the verification of the obtained L-beam designs in the following section.

6.2 Verification of Boundary Variations

The verification of boundary perturbations is non-trivial when variations are modeled on the voxel model by manipulating the projection threshold η_e. For the

Table 6.3: Numerical results of the L-beam from [122] obtained using a Monte Carlo simulation with $n = 10^4$ random samples. For each random sample, the maximum stress is calculated and approximated, from which the mean and standard deviation are subsequently determined.

Type	Optimization			MCS using $n = 10^4$ samples			
				Aggregated $\mathcal{A}(q_e)$		Maximum $\max(q_e)$	
	f, μ_q	σ_q	$M_{nd}[\%]$	μ_q	σ_q	$\mu_{\hat{q}}$	$\sigma_{\hat{q}}$
Determ.	2.08	-	3.37	2.29	0.333	2.09	0.454
FOSM	2.08	0.001	3.33	2.24	0.240	1.97	0.399
MCS	2.17	0.002	3.04	2.17	0.002	1.73	0.071

contour model, discrete nodal displacements perpendicular to the boundary must be defined. In contrast, the voxel model includes a transition phase between solid and void material, which may vary in size. Fitting a discrete line through this transition phase is straightforward by calculating the contour line for a defined threshold, typically $\bar{\rho} = 0.5$ (cf. Figure 2.15). To some extent, the contour line can be adjusted by applying perturbations to the projected density field $\bar{\boldsymbol{\rho}}$. However, the underlying filtered density field $\tilde{\boldsymbol{\rho}}$ depends on several factors, including the element size, filter function, filter radius, and the design variables $\boldsymbol{\rho}$.

In the following, an approach to relate threshold perturbations in the voxel model to actual physical boundary variations is described and discussed. Three different strategies for contour line perturbations are then presented, based on the results obtained in Section 6.1.2. To conclude the investigation and harmonize both the voxel and contour models, the voxel models are reevaluated with an adjusted density field.

6.2.1 From Threshold to Boundary Variations

Consider a one-dimensional example of design variables as depicted in Figure 6.5. The linear filter (see Equation (2.13)) is applied with a filter radius of $r_{filt} = 10$, resulting in the given filtered variable field. Additionally, a range for the projection threshold is defined as $\Delta\eta = \eta_{max} - \eta_{min}$. The basic concept is to project the filtered variables $\tilde{\rho}_e$ to actual physical positions x for different threshold values. This process is analogous to the derivation of the minimum feature size approach (compare with the derivation in [126]). For example, consider $\Delta\eta = 0.4$, assuming a nominal threshold of 0.5. The filtered variables are then projected for two different threshold values, $[0.5 - \Delta\eta/2; 0.5 + \Delta\eta/2] = [0.3; 0.7]$, and the corresponding range Δx is evaluated, as shown in Figure 6.5. By evaluating Δx over the entire range of $\Delta\eta$ and normalizing it by the filter radius, the results are

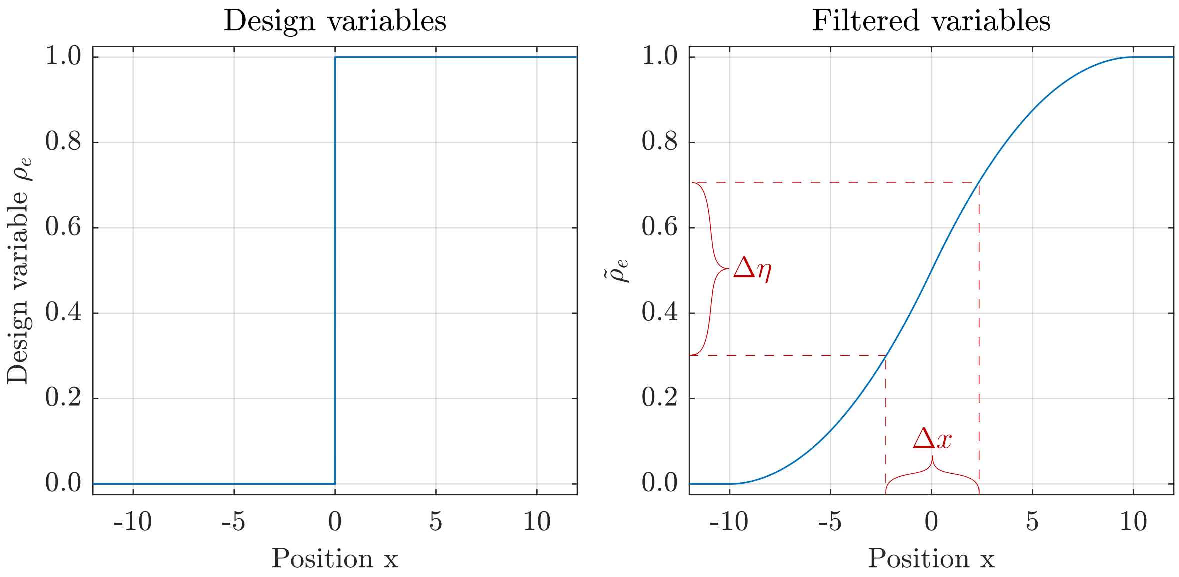

Figure 6.5: One dimensional example of design and filtered variables.

presented in Figure 6.6.

This can also be applied to higher dimensions, with Δx being the radius of a circle or sphere for two or three dimensions respectively. Still, this approach is based on some assumptions. Firstly, a perfect binary design field is assumed. This is not always the case in density-based topology optimization problems. Intermediate densities in the design variables will widen the evaluated range, leading to higher boundary perturbations, as discussed in the following subsections. Secondly, the mesh resolution should be high enough to capture variations. If the element size is smaller than the perturbation range Δx, deviations may not be captured at all.

6.2.2 Contour Variations Based on Threshold Perturbations

The first approach is based on the idea of using the perturbed physical density fields $\bar{\boldsymbol{\rho}}(\tilde{\boldsymbol{\rho}}, \boldsymbol{\eta}^k)$, e.g. applied in MCS, and to simply extract the contour line for a fixed threshold $\bar{\rho} = 0.5$ (cf. Figure 2.15). By that, boundary perturbations are applied through the projection process, with a correlated random field for $\boldsymbol{\eta}^k$ being the k-th random realization for the projection threshold. It does not require any assumptions and directly verifies geometry variations applied during optimization or post-processing of the voxel model. In the following, this approach is referred to as “filtered densities” approach, since the underlying density field is the filtered field $\tilde{\boldsymbol{\rho}}$.

Table 6.4 summarizes post-processing results for two different sample sizes denoted with “Filtered”. Comparing them to the last two columns in Table 6.3 shows that tendencies are confirmed in both case. The standard deviation is

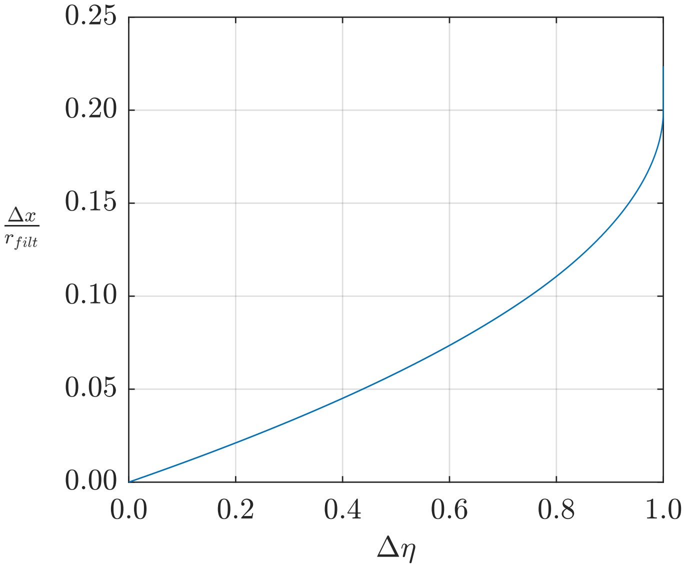

Figure 6.6: Normalized physical boundary perturbation as a function of threshold perturbations.

Table 6.4: Contour model verification based on threshold perturbations, obtained by a MCS using n random samples.

Type	Nominal stress	Filtered $\tilde{\boldsymbol{\rho}}$ ($n = 10^4$)		Filtered $\tilde{\boldsymbol{\rho}}$ ($n = 10^5$)		Regularized $\tilde{\boldsymbol{\rho}}$ ($n = 10^5$)	
	q_{max}	μ_q	σ_q	μ_q	σ_q	μ_q	σ_q
Determ.	2.13	2.40	0.69	2.50	14.28	2.23	0.08
FOSM	2.05	2.42	0.13	2.42	0.13	2.31	0.08
MCS	2.02	2.27	0.07	2.27	0.07	2.31	0.07

lower for FOSM and lowest for MCS relative to the deterministic case. The nominal stress values q_{max} (compare to Figure 6.4) deviate by approximately 20%. Nevertheless, the latter can be explained with the coarse voxel mesh. Yet, significant differences occur in the standard deviations for the deterministic case.

The deterministic optimized design is reevaluated in Figure 6.7a. The nominal unperturbed geometry for the filtered density approach is depicted, with positions where the maximum stresses occur marked and clustered. The number of maximum stress values n_i within each cluster is provided, and each cluster is assigned a different color. Additionally, the stress value distributions are plotted for the three largest clusters. As can be observed, clusters 2 and 3 exhibit much larger data ranges and significantly higher values compared to cluster 1. This is due to the relatively high amount of intermediate densities in these areas, which leads to larger boundary perturbations than in other regions. The effect is further amplified by a larger sample size, where more extreme perturbations are likely to occur, which explains the increase in σ_q from 10^4 to 10^5 samples. For the designs optimized with FOSM and MCS, this effect is less pronounced, and stress peaks do not dominate in the critical region (compare Figure 6.7a with C.2a and C.4a).

While the filtered density approach aims to verify variations in the optimized density field, it appears impractical from a pragmatic perspective. In practice, a more homogeneous boundary perturbation of the actual contour line may be of higher relevance. Hence, another approach is proposed, which aims at a more uniform perturbation along the boundary line by regularizing the underlying filtered field. To achieve that, the optimized physical densities $\bar{\boldsymbol{\rho}}$ are projected to a nearly binary values using $\beta = 100$ and an adjusted value for η to assure volume preservation. This is followed by a filtering step where the same filter radius is used as applied for optimization. Finally, the obtained regularized filtered densities are passed through the same projection process with varying threshold parameter $\boldsymbol{\eta}^k$ (as described for the filtered density approach above).

Table 6.4 summarizes post-processed results based on the regularized density field in the last two columns denoted with “Regularized”. As can be observed, differences between the considered three optimization formulations are considerably small. The highest difference is below 5%, which is interpreted as non-significant. Figure 6.7b, C.2b and C.4b show significantly low boundary variations and much less occurring maximum stresses at regarded critical locations. Still, distributions appear indistinct, even for a considerably high sample size of $n = 10^5$. Although boundary variations are more uniform, the covered range is still slightly varying along the nominal contour line. The reasons are supposedly related to the coarse mesh resolution of the voxel model and the relatively small transitions area of approximately one element (cf. Section 2.7.2). Regarding the filtered density approaches, only the MCS shows good agreement because perturbations in the critical region are not dominant. In the case of FOSM, deviations are higher, but still much better than in the deterministic case. Note, numerical studies indicated that uniform threshold perturbations can help to reduce the amount of intermediate densities (cf. Section 3.3). Consequently, a non-uniform threshold perturbation is supposedly helping to regularizing the filtered densities during optimization. For FOSM this effect is less pronounced due to the rough first-order approximation. This observation is supported by a decreasing measure of non-discreteness M_{nd} in Table 6.3 calculated according to Equation (2.30).

6.2.3 Contour Variations Based on Direct Boundary Perturbations

Thus far, boundary perturbations on the contour mesh have only been obtained indirectly. Directly moving boundary nodes along their normal vectors is the most straightforward approach but requires assumptions, as discussed in Section 6.2.1. Nevertheless, disregarding derivation issues, this approach holds the highest practical relevance. If actual boundary perturbations or related statistical information

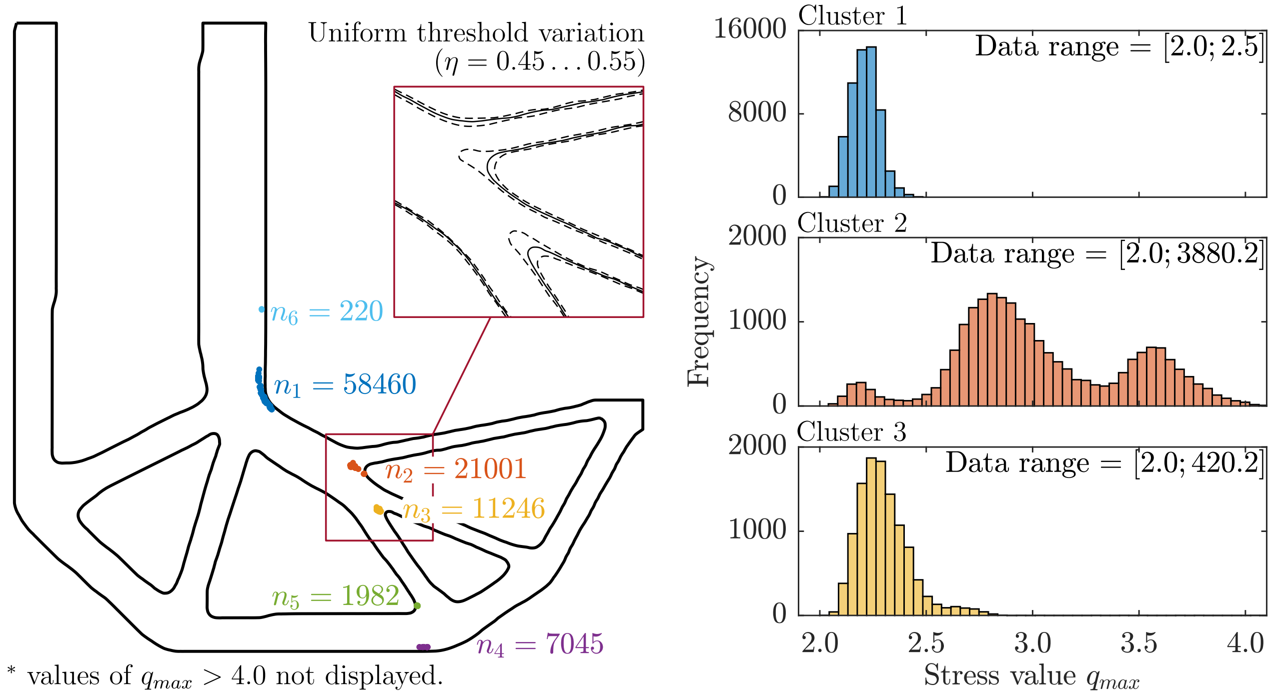

(a) Contour variations based on the filtered density field.

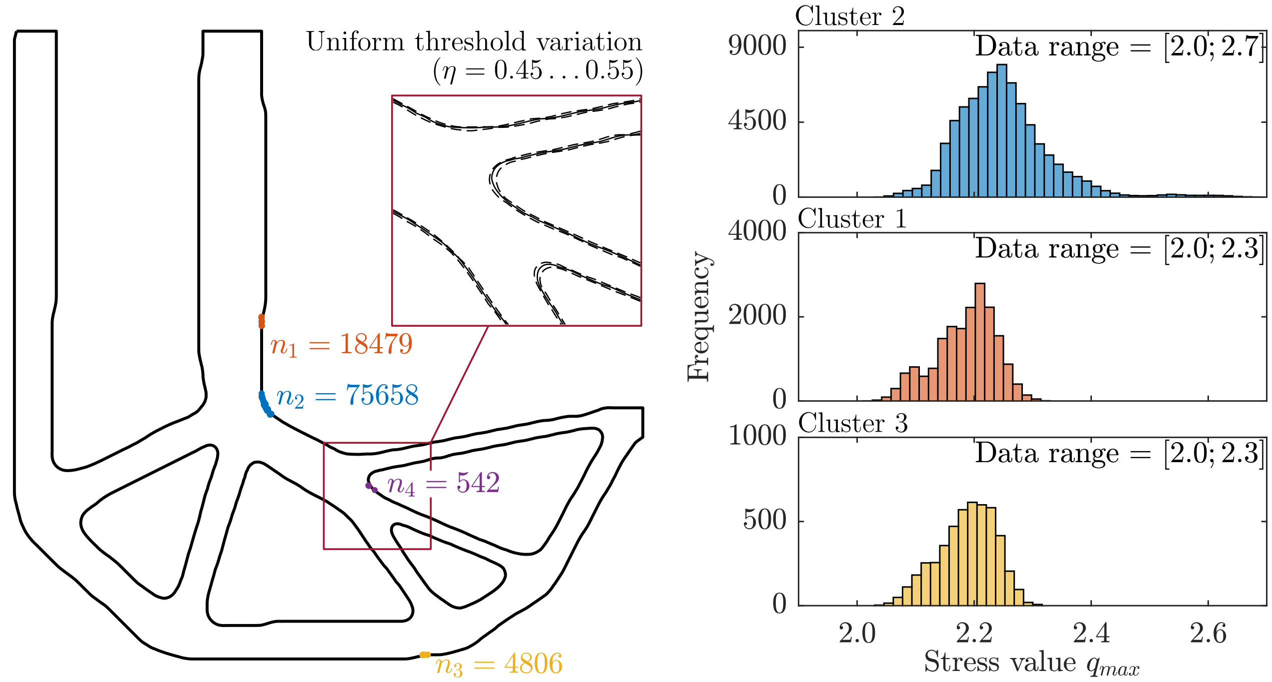

(b) Contour variations based on the regularized density field.

Figure 6.7: Worst-case stress positions and corresponding histograms based on threshold perturbations of the deterministically optimized L-beam.

are known, they can be directly applied to the model.

Two different techniques can be employed when boundary nodes are perturbed. First, the nominal contour line can be meshed, and perturbations are then applied to the boundary nodes of the finite element mesh. This approach results in a deformed mesh, which requires smoothing. The advantage of this method is that the original element definitions are preserved, with only the nodes being modified. However, due to the small element size, mesh distortions become too significant and cannot be smoothed effectively. Consequently, an alternative approach is adopted, where the contour nodes are perturbed according to the three following steps. This process generates a unique mesh for each realization and is found to be the most practical.

1. Generation of random samples: Correlated random realizations, as discussed in Section 5.3, are generated for the contour nodes. For that, a uniformly distributed boundary perturbation of $\mathcal{U}(-0.82, +0.82)$ is incorporated, corresponding to the uniform threshold perturbation of $\Delta\eta = 0.05$ under consideration. For a detailed description of the applied process on generating correlated random samples, refer to Section 6.2.1.

2. Regularization of the perturbed contour nodes: Regularization along the contour line is necessary at this stage to ensure consistent mesh quality across all realizations. As each finite element node corresponds to a contour node, the contour nodes must be equally spaced.

3. Finally, the perturbed and regularized contour line is meshed.

Results are summarized in Figure 6.8, C.1, C.3 and Table 6.5. As can be observed, distributions are much more distinct and the worst-case stress mostly occurs at the design space's re-entrant corner. Surprisingly, the deterministic results show the lowest standard deviation, but the highest mean value. Regarding the robust objective (see Equation (6.2) and the last column in Table 6.5), the best value is achieved by the MCS, though the difference is approximately 3%. Note, the mean values are much closer to the unperturbed nominal case q_{max}, which is usually expected. However, high deviations are present for both threshold approaches and in the voxel model for the deterministic and FOSM results (compare q_{max} in Figure 6.4 to $\mu_{\hat{q}}$ in Table 6.3).

6.2.4 Geometry Variations on Voxel Models

In this subsection, the voxel model is reevaluated based on a regularized density field. Following the same strategy as in Section 6.2.2 the optimized physical density field is projected to a nearly binary field and then filtered. Random samples

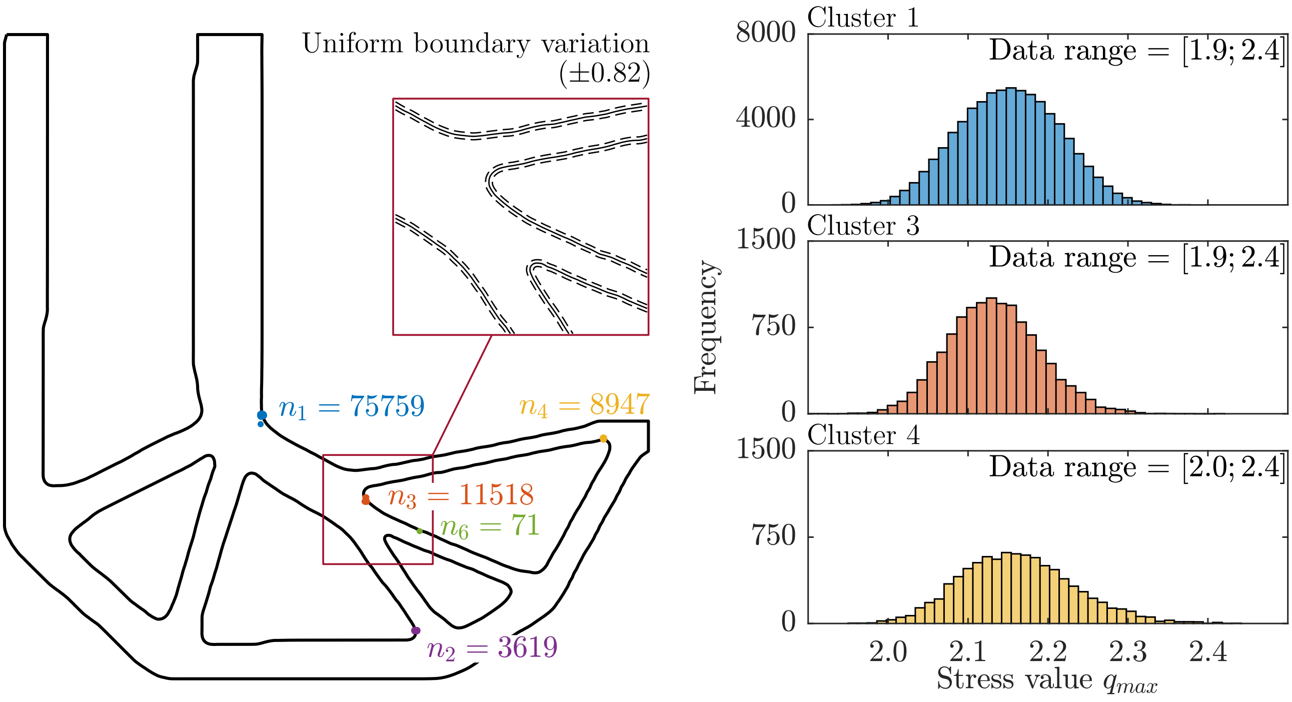

Figure 6.8: Worst-case stress positions and corresponding histograms based on direct contour line perturbations of the deterministically optimized L-beam.

Table 6.5: Contour model verification based on direct contour line perturbations, obtained by a MCS using $n = 10^5$ random samples.

Type	μ_q	σ_q	$\mathcal{G}_q(\kappa = 3)$
Determ.	2.15	0.06	2.34
FOSM	2.09	0.08	2.34
MCS	2.01	0.08	2.27

Table 6.6: Voxel model reevaluation based on a regularized density field, obtained by an MCS using $n = 10^5$ random samples.

Type	μ_q	σ_q	$\mathcal{G}_q(\kappa = 3)$
Determ.	1.97	0.05	2.12
FOSM	1.99	0.04	2.12
MCS	2.01	0.05	2.16

are generated for the threshold parameter and used to project the regularized filtered density values. Table 6.6 summarized the resulting stochastic quantities.

As can be noted, all three cases show a similar performance with only minor differences. This observation is equivalent to those drawn from Table 6.5 and the last two columns in 6.4.

6.2.5 Conclusion on Boundary Variations

Due to poorly conditioned filtered density fields obtained from the deterministic and FOSM formulation, significantly deviating post-processing values are found. While this effect is less pronounced for FOSM, fundamentally different results are obtained in the deterministic case. Regularization of the underlying filtered density field lead to the correct conclusion: All three L-beam designs do not significantly differ in terms of performance. This is most reasonable, since both the topology and volume are equivalent in all cases. However, this raises the question of why RTO is not having any influence? It is concluded, that either the influence of the considered geometric uncertainty is negligible or there is simply no better or more robust material distribution for the given volume.

Based on the threshold projection strategy, obtained distributions appeared indistinct. Directly applying boundary perturbations to the contour line resulted in better conditioned results. Revisiting the voxel model and performing an evaluation based on a regularized density field leads to comparable values and hence harmonizes both voxel and contour models.

In the case of MCS, the filtered density field obtained from optimization is well-conditioned, resulting in no significant differences in the standard deviation among the evaluation approaches considered. In conclusion, this investigation underscores the importance of employing a suitable verification process.

6.3 Randomness in Material Strength Considering a Robust Constraint

In the following, the classical volume minimization problem subjected to a robust stress constraint is investigated. This is not only of more practical relevance, but it also widens the design space. For instance, constraining the volume, the only possibility of achieving a higher robustness is by redistributing the given material (as could be demonstrated for the inverter). Regarding the volume as the optimization objective adds the possibility of changing the amount of material used.

The robust stress constraint is formulated in Equation (6.3) below. For an uncertainty-affected strength factor, refer to Equation (2.21). Note that in the following, the allowable stress or material strength parameter q_0 is defined for each element e and hence denoted as $q_{0,e}$. The p-norm ($p = 10$) is used for aggregation and stresses are interpolated using the RAMP scheme with $p^{RAMP} = -0.8$.

$$c_{robust} = SF_{robust} - 1 \quad \text{with} \quad SF_{robust} = \mu_{SF} + \kappa \sigma_{SF} \tag{6.3}$$

Although the weighted sum of mean value and standard deviation is characteristic for robust topology optimization, it can also be seen as a reliability-based formulation, as discussed in Section 5.1.4.

Uncertainty propagation is either conducted by FOSM or MCS. The latter is specifically used for post-processing, but also for optimization as benchmark. In the case of the MCS, multiple finite element models are evaluated. The obtained element-wise strength factor $SF_e^{(i)}$ (cf. Equation (2.21)) is calculated for each random sample i, aggregated and normalized in accordance with Equations (2.23) and (2.22), respectively. Stochastic moments are subsequently derived from these aggregated and normalized strength factors, as defined in Equations (6.4) to (6.5). This approach ensures the elimination of any approximation errors.

$$\mu_{SF,MCS} = \frac{1}{n} \sum_{i=1}^{n} \gamma \mathcal{A}_{PN}^{(i)} \left(p, SF_e^{(i)} \right) \tag{6.4}$$

$$\sigma_{SF,MCS}^2 = \frac{1}{n-1} \sum_{i=1}^{n} \left| \gamma \mathcal{A}_{PN}^{(i)} \left(p, SF_e^{(i)} \right) - \mu_{SF,MCS} \right|^2 \tag{6.5}$$

In contrast, for FOSM, the underlying stress function employed to evaluate the mean and standard deviation is subject to approximation errors. Consequently, the scaling factor γ is also determined in accordance to Equation (2.22) and applied to both moments as follows:

$$SF_{robust} = \gamma \left(\mu_{SF} + \kappa \sigma_{SF} \right) \tag{6.6}$$

with μ_{SF} and σ_{SF} being approximated using the FOSM method, as give in Equations (5.6) to (5.7).

6.3.1 Uncertainties in Material Strength

In this subsection, a spatially scattering material strength $q_{0,e}$ is considered. This property is usually reduced by so-called knock-down factors in common design practice. It is most relevant in lightweight design, since stresses are often dominating. Furthermore, it has yet not been applied to RTO nor RBTO problems to the author's best knowledge (cf. Table 1.1). Hence, it is investigated on the common stress benchmark example (see Figure 4.12) together with the proposed generalized FOSM approach summarized in Section 5.2. Here, the variance's derivative is determined by the principal sensitivity approach recapitulated in

Section 5.2.2 with a step size of $\varepsilon_0 = 10^{-3}$. Besides FOSM, MCS and two deterministic variants are compared. In many publications, designs obtained from RTO and RBTO are compared to deterministic results only, e.g. optimized with mean values of random parameters. However, this is far from engineering practice and thus an inappropriate and unfair comparison. Consequently, in addition to the mean valued case, also reduced strength values are considered in the deterministic optimization. In the end, results are verified with contour models.

The computational cost associated with the principal sensitivity approach is approximately double that of the deterministic case, as the state equation must be assembled and solved twice in each iteration. For MCS, the state equation is solved only once because the elemental stresses q_e are independent of the allowable strength values $q_{0,e}$. However, due to the large number of random realizations $n \geq 1000$ of $q_{0,e}$, the element-wise operations require a significant amount of computational time. This process can be parallelized in a straightforward manner, but may still result in higher computation times compared to the principal sensitivity approach. From this perspective, it remains advantageous to employ the FOSM method.

The L-beam model (see Figure 4.12) is discretized with 300 × 300 unit-sized elements. A load $F = 10$, a Young's modulus $E_0 = 3.0$ and a Poisson's ratio $\nu = 0.3$ are applied. The design domain is extended, and the filter radius is $r_{filt} = 5$. The maximum projection parameter is $\beta_{max} = 5$, which is updated when the stopping criteria are met. Starting at $\beta = 1$, this parameter is updated three times by multiplying it by a constant factor until it eventually reaches β_{max}. For further details on the underlying numerical process, refer to Section 2.8.

The material strength q_0 is assumed to be normally distributed, featuring a mean value of $\mu_{q0} = 3.0$ and a standard deviation of $\sigma_{q0} = 0.3$. For MCS and post-processing, the material strength is modeled as a Gaussian random field with a correlation length $l_c = 40$. The reduced allowable strength value $q_0^* = 2.1$ is determined by the corresponding quantile value for a given failure probability of $P_0 = 0.135\%$, which is related to a weighting factor of $\kappa = 3$. Although the distribution of the constrained strength factor is unknown, it is assumed to be normally distributed as an initial guess. This allows to relate the given failure probability P_0 and its quantile value $Q(1-P_0)$ to a corresponding weighting factor κ (cf. Section 5.1.4).

Results are summarized in Table 6.7 and obtained designs are depicted in Figure 6.9. For post-processing, $n = 10^5$ random samples are generated for the MCS, from which the mean value and the standard deviation are calculated in Table 6.8. Here, actual maximum values are considered without aggregation. The robust strength factor is calculated according to Equation (6.3) and the actual quantile value $Q(1-P_0)$ is determined from the empirical cumulative distribution of the strength factor.

While optimizing with the mean material strength shows the lowest volume,

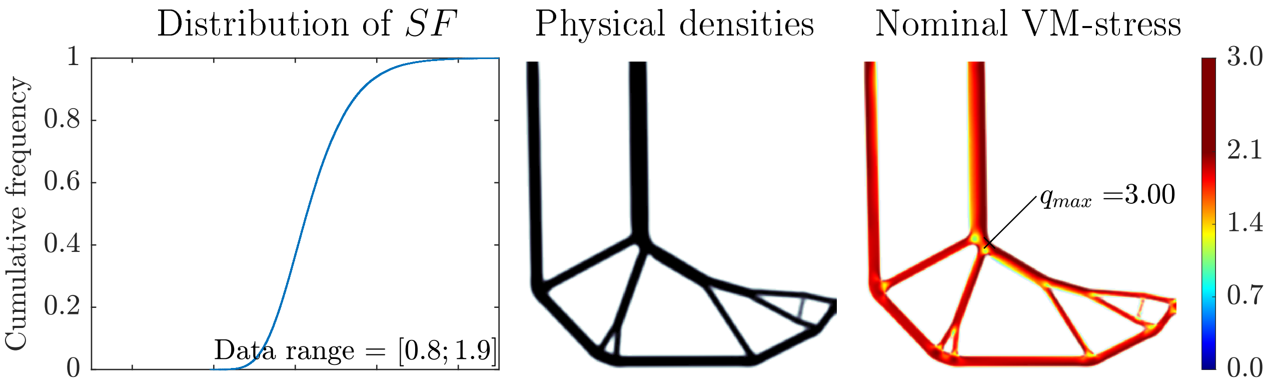

(a) Deterministic optimization with mean allowable stress $q_0 = 3.0$

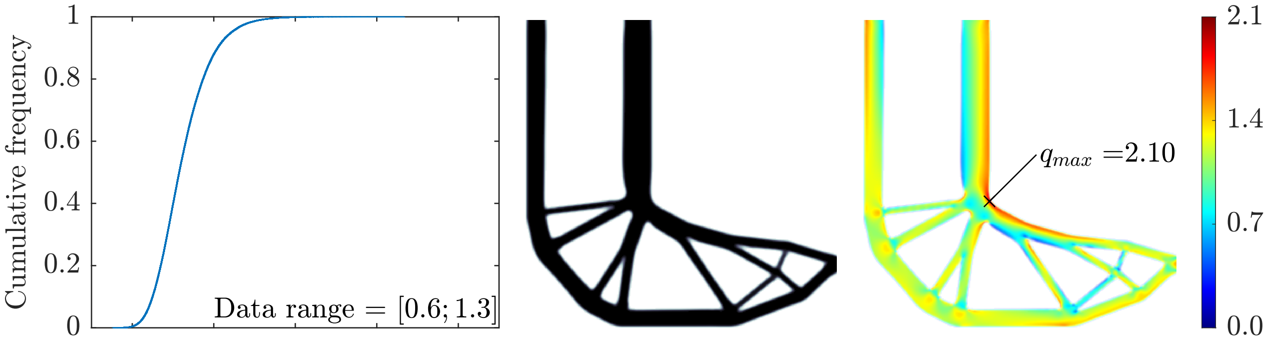

(b) Deterministic optimization with reduced allowable stress $q_0^* = 2.1$

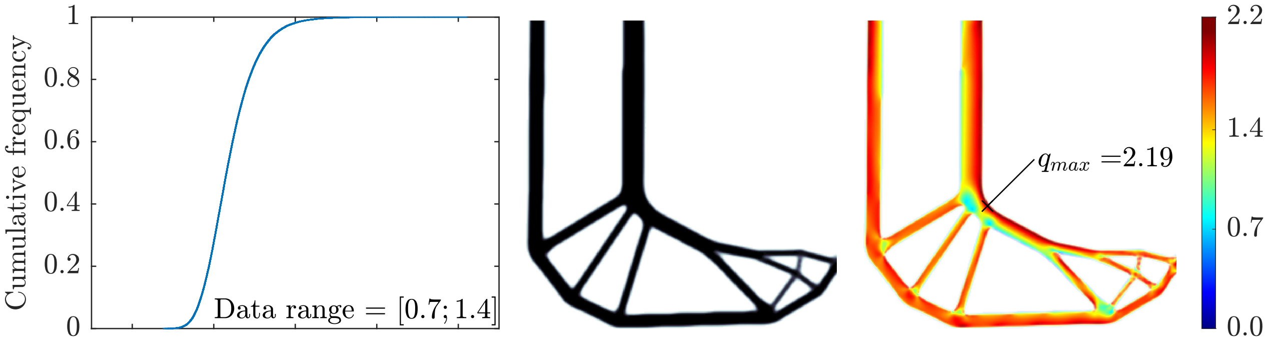

(c) Robust optimization using FOSM

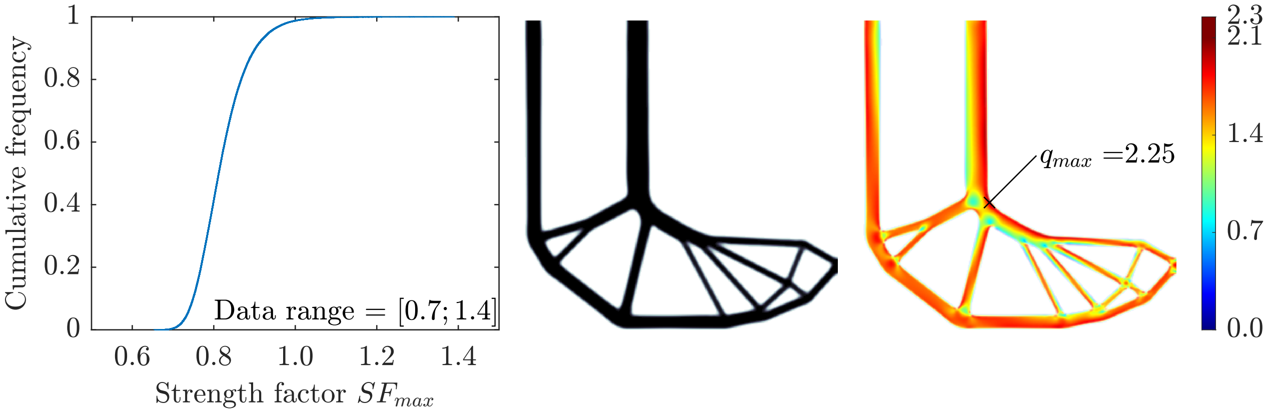

(d) Robust optimization using MCS

Figure 6.9: L-beam designs obtained from deterministic and robust topology optimization considering randomness in material strength. All data is based on post-processing of the voxel model.

Table 6.7: Objective and constraint values for obtained L-beam designs, considering uncertainties in material strength. Mean and standard deviation of the strength factor SF are determined as defined in Equations (6.4) to (6.6) including the scaling factor γ.

Type	Objective f	Constraint c		
	φ_V	μ_{SF}	σ_{SF}	SF_{robust}
Mean q_0	0.212	-	-	1.000
Red. q_0^*	0.323	-	-	1.000
FOSM	0.260	0.922	0.026	1.000
MCS	0.257	0.818	0.061	1.000

Table 6.8: Post-processed values for obtained L-beam designs, considering uncertainties in material strength. Mean and standard deviation of the strength factor are determined from the actual maximum of each Monte Carlo sample $\max_e(SF_e^{(i)})$.

Type	Voxel ($n = 10^5$)				Contour ($n = 10^5$)			
	μ_{SF}	σ_{SF}	SF_{robust}	$Q_{0.9987}$	μ_{SF}	σ_{SF}	SF_{robust}	$Q_{0.9987}$
Mean q_0	1.041	0.093	1.31	1.43	0.968	0.091	1.24	1.36
Red. q_0^*	0.724	0.065	0.92	0.99	0.731	0.071	0.95	1.03
FOSM	0.839	0.062	1.03	1.12	0.827	0.065	1.02	1.12
MCS	0.821	0.063	1.01	1.11	0.799	0.065	1.00	1.09

but also the lowest robustness (highest σ_{SF}) and worst reliability (highest Q), optimizing with a reduced strength value results in the highest volume, higher robustness and best reliability. Both FOSM and MCS designs achieve an approximately 20% lower volume fraction. Considering the given failure probability, the obtained quantile values should be $Q_{0.9987} \leq 1$. Although it is supposedly constrained in both robust formulations, the obtained quantile value is at most 12% above the targeted value. Note that, during optimization the robust constraint is fulfilled ($SF_{robust} \leq 1$) for FOSM and MCS, while the post-processed robust strength factor is exceeding the goal by less than 3% and is hence very close to the target value. Deviations in the quantile value originate from the inappropriate assumption of normally distributed strength factor. The deviations between voxel and contour values is around ±5% and hence deemed acceptable. Failure probabilities differ more, but are showing the same tendencies. Deviations in the volume fraction φ_V are below 1% in all cases and thus only given for the voxel models.

From results in Table 6.7 to 6.8, it can be concluded that the proposed FOSM approach yields similar results to the benchmark MCS. Comparable volume fractions and strength factor statistics are observed during post-processing. However, the approximated and scaled standard deviation deviates by more than 50% compared to the post-processed values.

6.3.2 Adapted Weighting Factor for Strength Uncertainties

To this point, the weighting factor κ is based on the initial assumption of a normally distributed strength factor, which turned out to underestimate the actual quantile value and hence lead to a violation of the targeted constraint value. To remedy this shortcoming, the weighting factor can be adapted to the actual data obtained during optimization. At least in the case of the MCS, the actual empirical cumulative distribution can directly be derived, from which the actual quantile value can be determined. With that, the weighting factor κ is adjusted in each iteration to match the targeted quantile value.

The weighting factor κ was initially based on the assumption of a normally distributed strength factor. However, this approach was found to underestimate the actual quantile value, resulting in a violation of the targeted constraint. To address this limitation, the weighting factor can be fitted to the actual data obtained during the optimization process. In the case of MCS, the empirical cumulative distribution and the actual quantile value can be directly derived. Consequently, the weighting factor κ is iteratively adjusted to match the targeted quantile value. Numerical studies showed no convergence issues, however results scatter due to the supposedly low sample sizes used for optimization ($n_{opt} = 1000$) and the selected aggregation parameter. Hence, a series of optimizations are run. The deterministic optimization with q_0^* and MCS are rerun for different aggregation parameters in the range of ($p = [10, \ldots, 30]$). MCS are additionally rerun for different sets of randomly generated samples and sample sizes n_{opt}. Numerical values are given in Table C.1 to C.2 and summarized in Figure 6.10.

As can be observed, results scatter significantly. In the deterministic case, low volume fractions can be obtained, but violate the targeted strength constraint. Nonetheless, competitively viable results can be obtained. The targeted quantile value is fulfilled in only one of the deterministic cases, while the obtained volume fraction is 15% higher compared to the best MCS result (compare data points at $\varphi_V = 0.281$ and 0.323). However, accounting for a 1% tolerance of the quantile value and comparing it against the heaviest MCS result yiels only a 2% difference in the obtained volume (cf. data points at $\varphi_V = 0.297$ and 0.303). In the deterministic case, clear trends are noticeable. For an increasing aggregation parameter, the volume fraction is decreasing, and the quantile value is increasing. The robustness or standard deviation of the strength factor is ap-

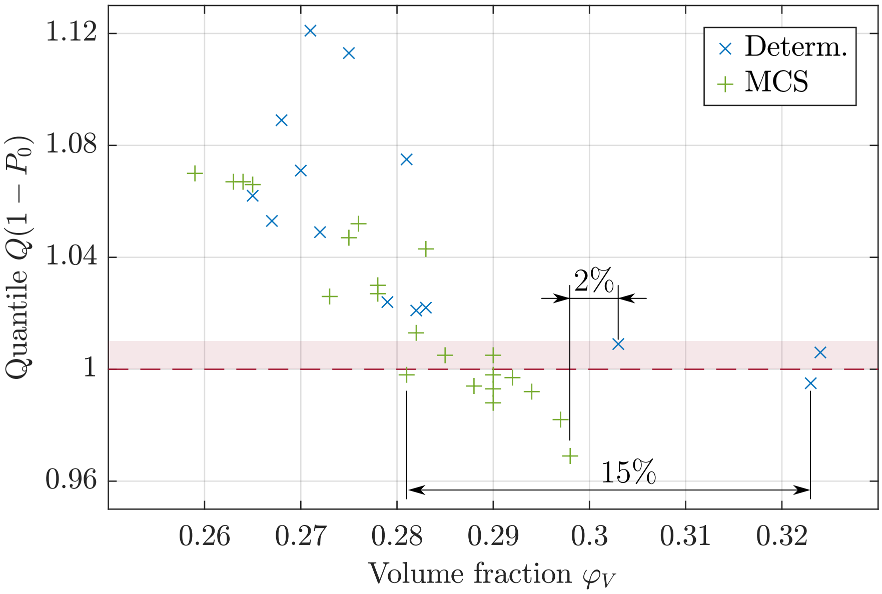

Figure 6.10: Deterministic and robust optimized performance values considering uncertainties in material strength for different aggregation parameter and varying samples sizes. Numerical values are listed in Table C.1 to C.2 and based on post-processing of the voxel models.

proximately constant for this investigation. The mean performance value, on the other hand, is increasing. Regarding MCS results, similar robustness is obtained. Nevertheless, quantile values scatter less and gather around the target value for increasing samples sizes. However, the results are subject to uncertainties and should be interpreted carefully. If no tolerance on the constraint is allowed, the robust formulation found to be superior to the deterministic case, highlighting the unexploited potential of the latter. On the other hand, if some tolerance is allowed, competitive results can be achieved at a fraction of the computational cost. The introduced κ-adaptation demonstrates that the targeted quantile value can be reached. For a sample size of $n_{opt} = 1000$ results scatter and may violate the constraint by at most 7%. For a higher amount of samples the scatter is reduced, although it does not significantly influence the approximation quality of the considered stochastic moments (compare μ_{SF} and σ_{SF} for optimization and post-processing in Table C.2). However, a higher sample size means more data points and hence a better approximation of the actual quantile value. Consequently, the weighting factor can be fitted more precisely.

For the proposed FOSM formulation, a similar adaptation of the scaling factor is not possible, since no information about the specific statistics of the constraint is available. As an alternative, the upper bound could be approximated by the one-sided Chebychev inequality, also known as Chebychev-Cantelli inequality. It is independent of the distribution and according to Silva et al. [42], the following equation can be derived for the targeted probability:

$$P(SF > 1) \leq \frac{1}{1 - \kappa^2}. \tag{6.7}$$

Regarding a failure probability of $P_0 = 0.135\%$, this results in a weighting factor of $\kappa \approx 27$. Hence, it is nine times higher than the initial value and around six times higher than the adapted weighting factor of the benchmark, which scatters roughly around five for the examples in Figure 6.10. The Chebychev inequality obliviously gives a poor approximation of the upper bound, but is independent of the distribution. Yet, applying $\kappa \approx 27$ to the same FOSM formulation leads to a diverging optimization.

Revisiting the proposed FOSM formulation and comparing corresponding results from Table 6.8 against Figure 6.10 the following can be observed. FOSM yields the best volume fraction but the worst quantile values. Especially the mean performance is worse than almost all deterministic results, which is an indication of the actual performance, since the standard deviation is hardly deviating in any example. For this reason and due to the lacking possibility of adapting the weighting factor, FOSM is regarded as impractical for stress-based optimization considering uncertainties in geometry or material strength. Although promisingly efficient, the approximation accuracy turned out to be too low, which led to worse results than in the deterministic case. Furthermore, many optimizations diverged. Either, due to too strong an influence of the standard deviation approximated by FOSM or other parameters affecting the non-linearity of the design space. However, often it was not possible or meaningful to relax the problem parameter any further. As a result, FOSM is found to be unsuitable if stresses are subjected to variations.

6.3.3 Robust Topology Optimization Considering Multiple Random Variables

In real-world applications, a structural component is exposed to various uncertainties from different sources. Hence, in this section multiple types of uncertainties in material properties, loading, and geometry are considered. A robust formulation using MCS for uncertainty quantification is compared to a worst-case formulation (WCF) based on a targeted failure probability of $P_0 = 1\%$. FOSM is not considered due to the decreasing numerical efficiency and since it is already proven to be unsuited for uncertainties in loading [4].

In the MCS, the four uncertainties are assumed to be independent and are thus varied in parallel. Specifically, for each Monte Carlo sample, a distinct correlated random field is applied to the geometry and each material property. For uncertainties in loading, the load angle is varied accordingly. During optimization, $n_{opt} = 1000$ random samples are evaluated in each iteration. For each sample,

Table 6.9: Declaration of random parameters for optimization subjected to multiple uncertainties.

Uncertain parameter	Distribution type	Distribution parameter		Parameters for worst-case formulation
Load angle α_F	Normal	$\mu = 6\frac{\pi}{4}$	$\sigma = \frac{1}{2.33}\frac{\pi}{4}$	$\alpha_F(P_0 = 1\%) = [5; 6; 7]\frac{\pi}{4}$
Proj. thresh. η_e	Uniform*	$a = 0.25$	$b = 0.75$	$\eta = [0.25; 0.5; 0.75]$
Stiffness $E_{e,0}$	Normal	$\mu = 3.0$	$\sigma = 0.3$	$E_{e,0}(P_0 = 1\%) = 2.3$
Strength $q_{e,0}$	Normal	$\mu = 4.17$	$\sigma = 0.417$	$q_{e,0}(P_0 = 1\%) = 3.2$

* The parameters for the uniform distribution are the lower bound a and the upper bound b

the maximum strength factor is approximated using the p-norm and $p_{PN,\mathcal{E}}$, as specified in Table 6.10. In the case of the WCF, the lower quantile value is used for the material strength and stiffness, as detailed in the last column of Table 6.9. For the load angle and the projection threshold parameter, three distinct states are considered respectively. As a result, nine unique combinations, corresponding to nine different FE models, are evaluated and solved during each iteration. For each model, the maximum strength factor is approximated using the p-norm and $p_{PN,\mathcal{E}}$, as specified in Table 6.10. The worst case among these models is then estimated using an additional p-norm function with a different aggregation parameter, $p_{PN,\mathcal{D}}$. This approach aligns with the damage-robust formulation presented in Equation (3.1).

The considered uncertainties, i.e. load angle, geometry,[1] material stiffness and strength, are listed in Table 6.9. Note, the mean load angle α_F corresponds to a load vector pointing down, as depicted in Figure 4.12. The L-beam example is considered for demonstration purpose, and discretized with 300×300 unit-sized finite elements. The design domain is extended, and a filter radius of $r_{filt} = 5$ and a maximum projection parameter of $\beta_{max} = 5$ is defined. The load magnitude is $F = 10$ and a Poisson's ratio of $\nu = 0.3$ is applied. Correlated random fields are modeled using the Gaussian correlation function with $l_c = 40$. All four uncertainty parameters are assumed to be uncorrelated among each other. As an initial guess, the weighting factor is set to $\kappa = 2.33$ which corresponds to a failure probability of 1% assuming a normal distributed strength factor.

Numerical results from Table 6.10 show an obtained volume fraction of about 31% for the WCF and about 27% for the MCS. The lightest designs from both formulations are depicted in Figure 6.11. In both cases, the targeted reliability could be achieved by the contour models (cf. Table 6.11). Hence, no further optimization is required, and it can be concluded that the weight-saving potential

---

[1] Variations in geometry are modeled by applying a correlated random field to the projection threshold parameter η_e.

Table 6.10: Nominal values for optimized L-beam designs considering multiple types of uncertainties. For the WCF nine models are solved and for the MCS $n_{opt} = 1000$ random samples are considered during optimization.

Type	Optimization						Nominal stress q_{max}	
	$p_{PN,\mathcal{E}}$	$p_{PN,\mathcal{W}}$	φ_V	μ_{SF}	σ_{SF}	SF_{robust}	Voxel	Contour
WCF-a	10	10	0.363	-	-	1.000	2.46	2.73
WCF-b	20	10	0.309	-	-	1.000	2.45	2.47
WCF-c		20	0.302	-	-	1.000	2.61	2.73
WCF-d	30	10	0.315	-	-	1.000	2.42	2.45
WCF-e		30	0.309	-	-	1.000	2.75	2.99
MCS-a	10	-	0.276	0.809	0.082	1.000	2.71	2.77
MCS-b	20	-	0.269	0.823	0.076	1.000	2.87	2.99
MCS-c	30	-	0.275	0.827	0.074	1.000	2.85	3.02

is not fully utilized by the worst-case formulation. This results in approximately 15% lower volume fractions for the robust optimized designs.

Adapting the weighting factor to the actual quantile value and rerunning MCS for different sample sizes yields better fitting quantile values for the voxel model but also higher volume fractions (cf. Table 6.12). Nevertheless, robust optimized results are still superior to the deterministic designs. Contour values differ by approximately the same amount and are roughly 10% below the voxel values. Although results scatter for a sample size of $n_{opt} = 1000$ a slight improvement is observed. For a higher number of realizations, deviations between optimized and post-processed standard deviations decrease and hence lead to a better approximation of the actual quantile value during optimization.

So far, designs have been evaluated with all uncertainties occurring simultaneously. In this case, the coefficient of variation is $\mathrm{CoV}_{all} = 10.2\%$ and 9.8% for the designs shown in Figure 6.11, which serves as the reference. For all uncertainties listed in Table 6.9, a $\mathrm{CoV}_{in} = 10\%$ is prescribed. Reevaluating both designs from Figure 6.11 separately for each type of uncertainty, yields the following CoV values given in Table 6.13. As can be observed, variation in material strength contributes the most to the variation in the strength factor, followed by the projection threshold and load angle variations. The least impact is observed from the material stiffness, as expected in a linear model. When different load angles or multiple load cases are considered, the designs typically feature cross-bracing, which enhances the structure's ability to withstand different loading directions. Consequently, the topologies differ significantly from the nominal case (compare, for instance, Figure 6.11 and 6.9, or see [6]). Interestingly, the load angle does not dominate the variation in the strength factor. Clearly, the optimizer was able to

Table 6.11: Post-processed performance values for optimized L-beam designs considering multiple types of uncertainties.

Type	Voxel ($n = 10^5$)				Contour ($n = 10^5$)			
	μ_{SF}	σ_{SF}	SF_{robust}	$Q_{0.99}$	μ_{SF}	σ_{SF}	SF_{robust}	$Q_{0.99}$
WCF-a	0.618	0.066	0.77	0.81	0.613	0.074	0.79	0.83
WCF-b	0.698	0.071	0.86	0.90	0.669	0.069	0.83	0.86
WCF-c	0.731	0.074	0.90	0.94	0.702	0.073	0.87	0.91
WCF-d	0.720	0.077	0.90	0.94	0.681	0.070	0.85	0.87
WCF-e	0.786	0.077	0.97	1.01	0.757	0.077	0.94	0.97
MCS-a	0.816	0.091	1.03	1.09	0.742	0.075	0.92	0.96
MCS-b	0.830	0.085	1.03	1.08	0.773	0.076	0.95	0.99
MCS-c	0.835	0.089	1.04	1.10	0.788	0.076	0.96	1.01

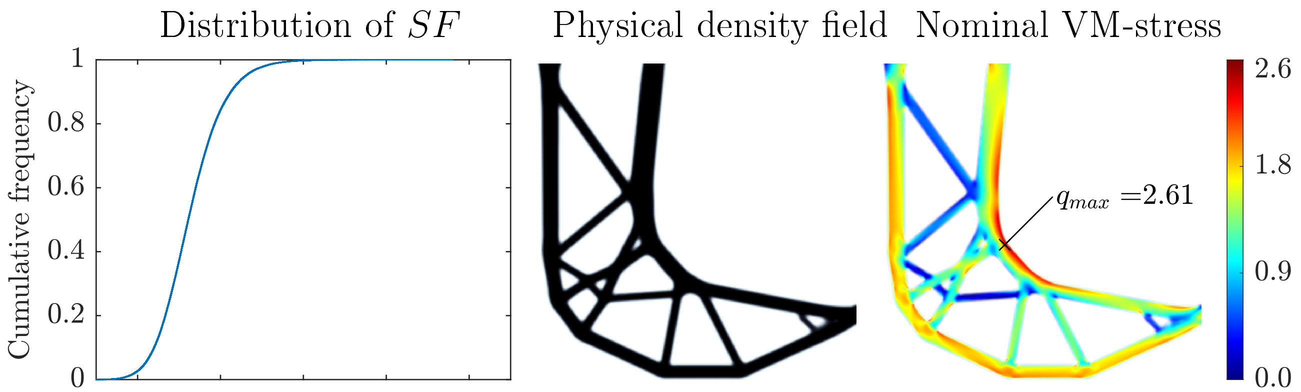

(a) Worst-case formulation (cf. WCF-c in Table 6.10 to 6.11)

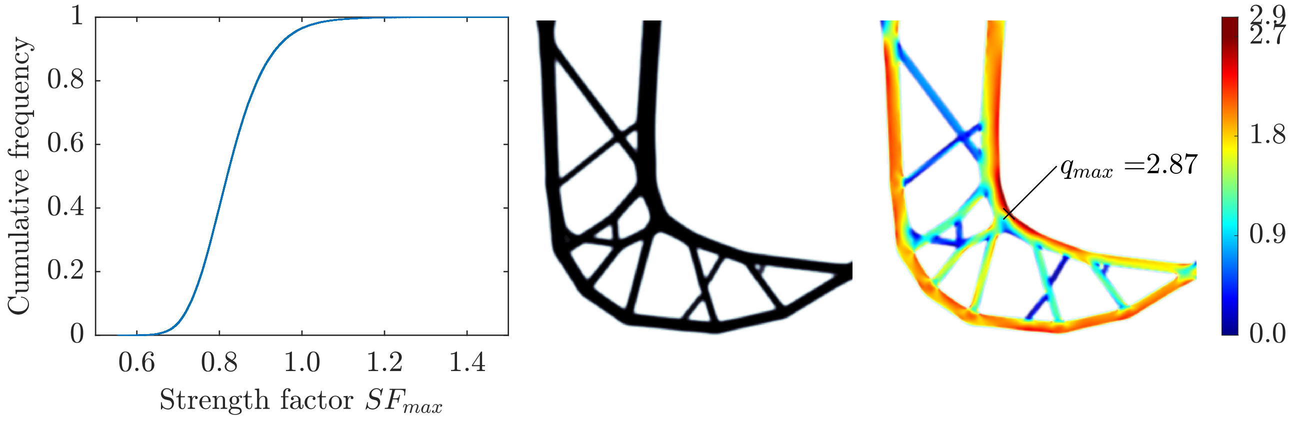

(b) RTO formulation using MCS (cf. MCS-b in Table 6.10 to 6.11)

Figure 6.11: Lightest L-beam designs that satisfy the strength-factor constraint, obtained from various optimization formulations and accounting for multiple types of uncertainties.

Table 6.12: L-beam results obtained by optimizing with an adapted weighting factor considering multiple types of uncertainties. Constraint aggregation is performed with $p_{PN,\mathcal{E}} = 10$.

Optimization				Voxel ($n = 10^5$)			Contour ($n = 10^5$)		
n_{opt}	f, φ_V	c, μ_{SF}	c, σ_{SF}	μ_{SF}	σ_{SF}	$Q_{0.99}$	μ_{SF}	σ_{SF}	$Q_{0.99}$
1000	0.280	0.784	0.076	0.793	0.086	1.06	0.727	0.074	0.94
1000	0.287	0.770	0.077	0.769	0.082	1.02	0.709	0.093	0.91
1000	0.286	0.804	0.075	0.805	0.088	1.07	0.734	0.075	0.94
1000	0.278	0.789	0.076	0.795	0.083	1.04	0.732	0.072	0.94
2000	0.280	0.789	0.077	0.790	0.082	1.03	0.731	0.074	0.94
5000	0.282	0.776	0.079	0.778	0.081	1.02	0.720	0.073	0.93
7500	0.284	0.767	0.078	0.768	0.080	1.00	0.714	0.072	0.92
10000	0.293	0.755	0.080	0.759	0.080	0.99	0.709	0.071	0.91

find an efficient material distribution that mitigates the impact of variable load angles. To demonstrate this, a design obtained for a single nominal load case only, i.e. the design from Figure 6.9d, was evaluated for a varying load angle, as in the current examples. A mean strength factor of $\mu_{SF} = 1.94$ and a standard deviation of $\sigma_{SF} = 0.96$ were obtained, corresponding to a $\mathrm{CoV}_{SF} = 49.2\%$. This indicates that this design is not robust against load angle variations. It is worth noting that even the simple WCF can generate a design with excellent robustness in this regard. In this linear stress-constrained L-beam example, other uncertainties, aside from loading, seem to primarily influence the volume rather than the overall topology.

Table 6.13: Separate evaluation with respect to each type of uncertainty for two selected designs.

Design	Uncertainty		Performance values ($n = 10^5$)		
			μ_{SF}	σ_{SF}	CoV_{SF}
WCF-c	Stiffness	$E_{e,0}$	0.627	0.018	2.9%
	Strength	$q_{e,0}$	0.675	0.056	8.3%
	Geometry	η_e	0.683	0.042	6.2%
	Load angle	α_F	0.607	0.029	4.7%
MCS-b	Stiffness	$E_{e,0}$	0.691	0.019	2.8%
	Strength	$q_{e,0}$	0.729	0.062	8.5%
	Geometry	η_e	0.748	0.038	5.1%
	Load angle	α_F	0.678	0.025	3.7%

Chapter 7

Summary and Conclusions

The overall focus of this thesis is on stress-based topology optimization subjected to various uncertainties. This topic is divided into two major parts related to the type of uncertainty considered and problem formulation. The first part covers local damages as possible uncertainty to obtain multiple-load-path designs, where the optimization problem is described as a worst-case formulation (see Chapters 3 to 4). The second part is dedicated to robust topology optimization (RTO), while different uncertainties in material properties, loading, and geometry are considered (see Chapters 5 to 6). Building upon existing approaches, more efficient methods are developed.

Within this thesis, the aggregation strategy is followed to approximate the maximum stress. To control the approximation quality, the aggregation parameter can be adjusted. However, it has to be chosen carefully. A too small parameter yields non-optimal results, while too high a parameter leads to numerical instabilities. In the worst-case, the optimization may even diverge. Yet, if stresses are considered to be constrained, the approximation quality is too low in any case and the actual maximum stress is either under- or overestimated, depending on the chosen aggregation function. To remedy this shortcoming, the approximated stress value can simply be scaled to the actual maximum value by a continuously updated factor. Although the use of aggregation functions requires heuristic parameter tuning, it is still an efficient strategy when stresses are considered during optimization.

Since stresses are inaccurately represented at the boundary in density-based finite element models, contour models are generated for verification. It is shown that the maximum stress value and hence its accuracy varies, depending on the stress interpolation parameter, the projection parameter and threshold. Limiting the maximum projection parameter and choosing an appropriate interpolation parameter resulted in less variations and the most accurate stress calculation. Still, small deviations due to the non-optimal mesh resolution are expected. Despite the observed deviations, tendencies can be verified, increasing the overall reliability of obtained numerical results.

7.1 Optimization of Damage Robustness

Different problem formulations are investigated and evaluated on their ability to efficiently generate multiple-load-path designs (MLD). Two common test models are considered, namely the cantilever and the L-beam.

To compare results obtained from different problem formulations, a uniform assessment methodology is required and motivated. For this reason, designs are evaluated based on their actual load paths. Although, this is not explicitly nor equivalently part of the optimization process, it is found to be the most reasonable and practical relevant evaluation strategy.

The first assessed approach explicitly considers local damages during optimization, and is denoted as the damage patch formulation. It turned out that reducing the number of patches is the best option in case of a stresses objective. Compared to the original approach, the numerical cost is drastically reduced, in parallel to an increased damage robustness. From a practical perspective, it is sufficient to use as many damage patches as necessary to cover the design domain without gaps. This observation is contrary to the classical stiffness optimization and can be explained by local effects, which can dominate the optimization process if stresses are considered. Due to this observation and actually occurring local stress peaks at the edge of discretely defined patches, the patch shape was expected to influence the optimization process and outcome. Although the final designs showed specific characteristics related to the used patch configuration, no other clear differences were found. Neither convergence behavior nor the damage robustness could be improved by using other patch shapes than the conventional square with sharp edges and non-smooth corners. Varying the patch size, on the other hand, clearly resulted in different designs. A moderate size is found to be most optimal in terms of damage robustness. While the computational cost is reduced for bigger patches, the damage robustness increases. However, the damage size may be constrained by design requirements. Consequently, the only patch parameter to improve the computational efficiency is the number of patches. Beyond the patch configuration, it is suggested to only modify affected entries in the global stiffness matrix to avoid reassembly for each damage model and hence save computing time. Furthermore, the calculation of each damage model can be parallelized straightforwardly. It may in case of a moderate number of damage patches and enough CPUs only require a slightly longer runtime compared to a nominal optimization.

As a supposedly efficient alternative, a maximum-feature-size-constrained formulation is implemented. Due to only one additional constraint, the computational cost is only a fraction of the damage patch formulation. However, obtaining a suitable design, requires much more heuristic parameter tuning, which in practice involves many optimization runs to find a good parameter setting. In contrast to that, the assumptions required for the damage patch approach (e.g. the patch size) are more reasonable and easier to justify. Additionally, the actual damage robustness turned out to be much worse for the feature-size-constrained formulation. Consequently, this approach is concluded to be non-competitive regarding the damage patch formulation.

In real-world applications, the patch size might be subjected to design requirements, or it must be adapted to specific geometries. In any case, the size must be big enough to split the main load path. Furthermore, in some cases, a moderate aggregation parameter might be insufficient to split the primary load paths for the damage patch formulation. Hence, higher aggregation parameters are required, leading to a badly conditioned optimization problem. To relax the latter and improve convergence behavior, the damage patch formulation is combined with a minimum and maximum feature size constraint. This resulted in improved layouts, especially for the L-beam example. However, it also increases the computational cost, especially due to the considered minimum feature size constraint.

7.2 Robust Topology Optimization

In contrast to the worst-case formulation employed to obtain damage robust designs, in RTO the robust objective or constraint is expressed as a weighted sum of the mean and standard deviation of a specific response function. Variations of the latter are caused by uncertainties in the input parameters, i.e. material stiffness, strength, loading, or geometry. As a benchmark for comparison, stochastic quantities of the response function are determined through a Monte Carlo simulation (MCS) embedded into the optimization framework. This technique is also applied for post-processing, however with a higher sample size to increase accuracy.

As an approach for uncertainty quantification in RTO, a generalized approach is derived based on a linear Taylor series expansion, namely generalized FOSM. Compared to other RTO approaches, it is supposedly very efficient, since only two additional adjoint systems have to be solved for gradient calculation, independent of the number of random variables. However, computational costly second-order derivatives are required if, for instance, stresses are considered, resulting in an increased computational effort. To avoid the calculation of those derivatives and to improve the efficiency for stresses, principal sensitivities are successfully adopted, which decreased the computing time to approximately 10% of the adjoint-based formulation.

The proposed approach is tested on two common test models, namely the inverter and L-beam. Regarding the inverter model, for which the robust displacement objective is subjected to spatially scattering material stiffness, a low sensitivity with respect to the random variable is observed. Still, a more robust design with a significant increase in robustness is obtained by the proposed FOSM formulation. The L-beam model is optimized for the robust worst-case stress subjected to geometry perturbations. It turned out that no significant improvements could be archived in this case. Neither FOSM nor the MCS benchmark design showed notable differences in topology and performance, which is verified by contour models. For post-processing, the importance of a suitable verification is highlighted. Different techniques on how to model geometry perturbations are investigated. Variations applied to the projection threshold parameter require a properly conditioned filtered density field to reliably determine the standard deviation of the stress response. In the case of a poorly conditioned filtered density field, a possible solution is to regularize the filtered field by performing a threshold projection followed by a filtering step. Then, the threshold parameter can be varied to model geometry variations and a conclusion can be drawn reliably. Nevertheless, direct perturbation of contour nodes is the most obvious choice from a practical perspective, and it results in the most trustworthy conclusions. Nonetheless, during optimization, geometry variations are directly based on the filtered density field, which can be poorly conditioned. Consequently, the investigated techniques can only be applied in the post-processing step. In this special case, no significant differences could be observed between the optimized design, supposedly since there is no better solution than the deterministic. Regarding the volume constraint, the only possibility to improve the robustness of the design is by redistributing material, as in the case of the inverter. For the L-beam example, there is probably no better topology. As a consequence, the optimization problem is reformulated in the following.

By constraining the robust stress function and optimizing for the volume, more design possibilities are available to the optimizer. In the case of an uncertain material strength, the proposed generalized FOSM approach is demonstrated on the L-beam model. The constrained strength factor showed a comparable robustness to the benchmark design. However, the targeted reliability is violated by approximately 10% in the case of FOSM and the benchmark MCS. Conversely, the obtained volume fraction is approximately 20% lower than the deterministic result, indicating potential for further improvements in the RTO approaches.

The constraint violations observed in the proposed RTO formulations result from an improperly selected weighting factor and an insufficient sample size. For the sampling-based benchmark formulation MCS, it is proposed to adapt the weighting factor during optimization to better align with the actual distribution. As demonstrated, it is possible to avoid constraint violation without added cost or numerical issues. However, a sufficient big sample size is required for accurate and reproducible results. The increasing reliability leads to an increased volume fraction, which is still lower than comparable deterministic results. Consequently, it could be shown that using knock-down factors in a deterministic formulation results in unexploited weight saving potential. Hence, the usefulness of RTO is emphasized for stress-based problems.

For FOSM, no adaptation scheme could be found. Additionally, almost all deterministic results outperformed FOSM in terms of reliability and mean performance. This indicates that the proposed FOSM approach is not suitable to be applied to stress-based problems. Furthermore, FOSM often leads to non-stable optimizations, as observed in other numerical studies not documented in this work, also if different types of uncertainties are regarded.

As a final investigation, four types of uncertainties are considered simultaneously for a robust stress constraint. Monte Carlo benchmarks are compared to a worst-case formulation. The unexploited weight saving potential in the deterministic case could be verified for this example. Evaluating obtained designs for each type of uncertainty separately showed that a scattering material strength is dominating the variation on the strength factor. Nonetheless, both approaches were able to find solutions to efficiently counteract applied variations.

7.3 Outlook

Generally, when stresses are taken into account, an appropriate mesh resolution is required. This is not only important for an accurate stress representation, but also for a smooth and reliable optimization process. Especially for a regular voxel grid, very small elements are necessary to obtain actual mesh convergence, as mentioned in Section 2.7.2. Other researchers showed that such resolutions are technically possible, but require efficient multi grid solvers. However, this is not considered in this work. As an alternative, it could be more efficient to only refine the mesh or some other domains locally at the boundary between material and void phase. This could be achieved by an adaptive procedure, which allows movement of the boundary line. To solve this issue, the extended finite element method (XFEM) [161] or the finite cell method (FCM) [162] could be employed. The use of multi grid solvers might still be necessary when it comes to three-dimensional examples. To this end, only two-dimensional academic examples are shown due to the still high computational effort.

Although the numerical cost could be cut down in several aspects, still some heuristic parameter tuning remains. Since this is usually little discussed, it is an important issue to mention. The most prominent parameter in all considered examples is the aggregation parameter. As often highlighted, the optimal value is problem-dependent. Even though, there is a big confidence about the range for an appropriate aggregation parameter, it still requires a few runs, to roughly approximate the best value. It is still an open question on how to determine the optimal aggregation parameter a prior! The approximation accuracy can easily be determined, but predicting the convergence behavior is non-trivial, as discussed in Section 2.4. Furthermore, this is influenced by the applied mathematical optimization algorithm and its related parameters. Instead of using the widely applied MMA, the globally converging versions (GCMMA) [163] might be better suited for high non-linear problems. However, this comes at the cost of additional function evaluations.

Appendix A

General Supplementary Material

In this chapter, general supplementary material is collected.

A.1 Adjoint Sensitivity Analysis

The adjoint sensitivity analysis [37] is usually preferred for determination of required derivatives in topology optimization [13, 38]. Here, the general procedure is explained in detail. Starting by defining a design response $\mathcal{F}\left(\mathbf{u}, \boldsymbol{\rho}\right)$ which depends on the state variable $\mathbf{u}\left(\boldsymbol{\rho}\right)$ and has to be differentiated with respect to design variables $\boldsymbol{\rho} = \left[\rho_i, \ldots, \rho_i\right]$ as introduced in Section 2.1. The state variable is determined by solving the state equilibrium in residuum form $\mathbf{R}\left(\mathbf{u}, \boldsymbol{\rho}\right) = \mathbf{0} \rightsquigarrow \mathbf{u}$. Both are functions of the design variables.

Direct differentiation of an arbitrary design response yields:

$$\frac{D\mathcal{F}}{D\boldsymbol{\rho}} = \frac{\partial \mathcal{F}}{\partial \mathbf{u}} \frac{D\mathbf{u}}{D\boldsymbol{\rho}} + \frac{\partial \mathcal{F}}{\partial \boldsymbol{\rho}} \tag{A.1}$$

were, ${}^{D\mathbf{u}}/_{D\boldsymbol{\rho}}$ is determined by differentiating $\mathbf{R}$ and solving the following system of equations for each design variable ρ_i.

$$\mathbf{0} = \frac{\partial \mathbf{R}}{\partial \mathbf{u}} \frac{D\mathbf{u}}{D\boldsymbol{\rho}} + \frac{\partial \mathbf{R}}{\partial \boldsymbol{\rho}} \tag{A.2}$$

In topology optimization, this is naturally very costly in terms of computation, due to the large amount of design variables.

Regarding the adjoint sensitivity analysis, a Lagrangian function is defined as follows:

$$\bar{\mathcal{F}} := \mathcal{F} - \boldsymbol{\lambda}^{\mathrm{T}} \mathbf{R} \tag{A.3}$$

were, $\boldsymbol{\lambda}$ is the Lagrangian vector. Differentiation yields

$$\begin{aligned}\frac{D\bar{\mathcal{F}}}{D\boldsymbol{\rho}} &= \frac{\partial \mathcal{F}}{\partial \mathbf{u}}\frac{D\mathbf{u}}{D\boldsymbol{\rho}} + \frac{\partial \mathcal{F}}{\partial \boldsymbol{\rho}} - \boldsymbol{\lambda}^{\mathrm{T}}\frac{\partial \mathbf{R}}{\partial \mathbf{u}}\frac{D\mathbf{u}}{D\boldsymbol{\rho}} - \boldsymbol{\lambda}^{\mathrm{T}}\frac{\partial \mathbf{R}}{\partial \boldsymbol{\rho}} \\ &= \underbrace{\frac{\partial \mathcal{F}}{\partial \boldsymbol{\rho}} - \boldsymbol{\lambda}^{\mathrm{T}}\frac{\partial \mathbf{R}}{\partial \boldsymbol{\rho}}}_{\text{explicit}} + \underbrace{\left[\frac{\partial \mathcal{F}}{\partial \mathbf{u}} - \boldsymbol{\lambda}^{\mathrm{T}}\frac{\partial \mathbf{R}}{\partial \mathbf{u}}\right]\frac{D\mathbf{u}}{D\boldsymbol{\rho}}}_{\text{implicit}}.\end{aligned} \tag{A.4}$$

Partial derivatives are already grouped into explicit and implicit terms. The term in square brackets is referred to as adjoint system (see Equation (2.8)), which is set to be zero so that the $D\mathbf{u}/D\boldsymbol{\rho}$ vanishes. Solving the adjoint system once, yields the Lagrangian vector, with which the actual derivative of the design response can be calculated efficiently. Hence, Equation (A.4) simplifies to

$$\frac{D\bar{\mathcal{F}}}{D\boldsymbol{\rho}} = \frac{\partial \mathcal{F}}{\partial \boldsymbol{\rho}} - \boldsymbol{\lambda}^{\mathrm{T}}\frac{\partial \mathbf{R}}{\partial \boldsymbol{\rho}} \tag{A.5}$$

A.2 Partial Derivatives for Basic Topology Optimization

In this section, all required partial derivatives for the basic topology optimization problem (cf. Equation (2.2)) are given, including those of applied design responses.

A.2.1 Three-Field Topology Optimization

As mentioned in Section 2.2 the three-field topology optimization is employed. Hence, design variables undergo a filtering and projection step. While the projected variables $\bar{\boldsymbol{\rho}}$ scale physical quantities, filtered $\tilde{\boldsymbol{\rho}}$ and design variables $\boldsymbol{\rho}$ are pure mathematical variables. Still, gradients with respect to design variables are required. Thus, for all dependent response functions $\mathcal{F}$, i.e. objective or constraint (cf. Equation (2.2)), the following differentiation has to be applied:

$$\frac{\partial \mathcal{F}}{\partial \boldsymbol{\rho}} = \left(\frac{\partial \mathcal{F}}{\partial \rho_1}, \dots, \frac{\partial \mathcal{F}}{\partial \rho_{n_e}}\right)^{\mathrm{T}} \quad \text{with} \quad \frac{\partial \mathcal{F}}{\partial \rho_i} = \sum_{e=1}^{\mathcal{N}_e} \frac{\partial \mathcal{F}}{\partial \bar{\rho}_e}\frac{\partial \bar{\rho}_e}{\partial \tilde{\rho}_e}\frac{\partial \tilde{\rho}_e}{\partial \rho_i}. \tag{A.6}$$

For which partial derivatives of the projection filter (2.14) are calculated as

$$\frac{\partial \bar{\rho}_e}{\partial \tilde{\rho}_e} = \frac{\beta \operatorname{sech}^2(\beta(\tilde{\rho}_e - \eta_e))}{\tanh(\beta\eta_e) + \tanh(\beta(1-\eta_e))} \tag{A.7}$$

and partial derivatives of the variable filter (2.13) are determined as follows.

$$\frac{\partial \tilde{\rho}_e}{\partial \rho_i} = \frac{w\left(\mathbf{x}_i\right) v_i}{\sum_{i=1}^{\mathcal{N}_e} w\left(\mathbf{x}_i\right) v_i} \tag{A.8}$$

A.2.2 State Equilibrium

As mentioned in Section 2.2 all calculations within this publication are based on a linear structural analysis. Hence, the discrete residuum is given in Equation (2.9). It is a function of projected and state variables. For the adjoint sensitivity analysis, the following derivatives may be required:

$$\frac{\partial \mathbf{R}}{\partial \bar{\boldsymbol{\rho}}} = \frac{\partial \mathbf{K}}{\partial \bar{\boldsymbol{\rho}}} \mathbf{u} \tag{A.9}$$

$$\frac{\partial \mathbf{R}}{\partial \mathbf{u}} = \mathbf{K} \tag{A.10}$$

A.2.3 Aggregation Functions

Aggregation functions are applied in different cases and thus required to be differentiated. Both the upper bound KS-function in its alternative formulation (2.27) and the p-norm (2.23) are used. For the KS-function, the following partial derivatives are obtained:

$$\frac{\partial \mathcal{A}_{KS}}{\partial \bar{\boldsymbol{\rho}}} = \sum_{e=1}^{n} \frac{\exp(p(\mathcal{F}_e - \mathcal{F}_0))}{\sum_{i=1}^{n} \exp(p(\mathcal{F}_i - \mathcal{F}_0))} \frac{\partial \mathcal{F}_e}{\partial \bar{\boldsymbol{\rho}}} \tag{A.11}$$

$$\frac{\partial \mathcal{A}_{KS}}{\partial \mathbf{u}} = \sum_{e=1}^{n} \frac{\exp(p(\mathcal{F}_e - \mathcal{F}_0))}{\sum_{i=1}^{n} \exp(p(\mathcal{F}_i - \mathcal{F}_0))} \frac{\partial \mathcal{F}_e}{\partial \mathbf{u}} \tag{A.12}$$

Derivatives of the p-norm functions are given below.

$$\frac{\partial \mathcal{A}_{PN}}{\partial \bar{\boldsymbol{\rho}}} = \left(\sum_{i=1}^{n} \mathcal{F}_i^p \right)^{\frac{1}{p}-1} \sum_{e=1}^{n} \mathcal{F}_e^{p-1} \frac{\partial \mathcal{F}_e}{\partial \bar{\boldsymbol{\rho}}} \tag{A.13}$$

$$\frac{\partial \mathcal{A}_{PN}}{\partial \mathbf{u}} = \left(\sum_{i=1}^{n} \mathcal{F}_i^p \right)^{\frac{1}{p}-1} \sum_{e=1}^{n} \mathcal{F}_e^{p-1} \frac{\partial \mathcal{F}_e}{\partial \mathbf{u}} \tag{A.14}$$

A.2.4 Stress Constraint

When stresses are considered as constraint, the formulation in Equation (2.21) is differentiated as follows:

$$\frac{\partial SF_e}{\partial \bar{\boldsymbol{\rho}}} = \frac{1}{q_0} \frac{\partial q_e}{\partial \bar{\boldsymbol{\rho}}} \tag{A.15}$$

$$\frac{\partial SF_e}{\partial \mathbf{u}} = \frac{1}{q_0} \frac{\partial q_e}{\partial \mathbf{u}} \tag{A.16}$$

A.2.5 Equivalent Stress

Equivalent von Mises stresses are calculated as defined in Equation (2.19). Derivatives with respect to projected and state variables yield:

$$\frac{\partial q_e}{\partial \bar{\boldsymbol{\rho}}} = \frac{1}{q_e} \mathbf{u}_e^{\mathrm{T}} \mathbf{B}_e^{\mathrm{T}} \mathbf{C}_e \mathbf{M} \frac{\partial \mathbf{C}_e}{\partial \bar{\boldsymbol{\rho}}} \mathbf{B}_e \mathbf{u}_e \tag{A.17}$$

$$\frac{\partial q_e}{\partial \mathbf{u}} = \frac{1}{q_e} \mathbf{B}_e^{\mathrm{T}} \mathbf{C}_e \mathbf{M} \mathbf{C}_e \mathbf{B}_e \mathbf{u}_e \tag{A.18}$$

A.2.6 Nodal Displacements

For the inverter model (Figure 6.1) displacements at certain degrees of freedom k are required, which are defined as follows:

$$u_k = \mathbf{e}_k \mathbf{u} \tag{A.19}$$

where $\mathbf{e}_k$ is the k-th unit vector. Differentiation yields:

$$\frac{\partial u_k}{\partial \bar{\boldsymbol{\rho}}} = \mathbf{0} \tag{A.20}$$

$$\frac{\partial u_k}{\partial \mathbf{u}} = \mathbf{e}_k \tag{A.21}$$

A.2.7 Volume

The volume is considered in all examples, either as constraint or cost function. It is calculated according to following equation

$$V = \bar{\boldsymbol{\rho}}^{\mathrm{T}} \mathbf{V}_0 \tag{A.22}$$

where $\mathbf{V}_0$ is the vector containing the volume of each element. Differentiation yields:

$$\frac{\partial V}{\partial \bar{\boldsymbol{\rho}}} = \mathbf{V}_0 \tag{A.23}$$

$$\frac{\partial V}{\partial \mathbf{u}} = \mathbf{0} \tag{A.24}$$

A.2.8 Compliance

Although not used for any numerical example within this thesis, compliance is often used in topology optimization examples due to its efficient gradient calculation. The global compliance is calculated as:

$$c = \mathbf{f}^{\mathrm{T}} \mathbf{u} \tag{A.25}$$

Differentiation yields:

$$\frac{\partial u_k}{\partial \bar{\boldsymbol{\rho}}} = \mathbf{0} \tag{A.26}$$

$$\frac{\partial u_k}{\partial \mathbf{u}} = \mathbf{f} \tag{A.27}$$

Hence, the adjoint system (cf. Equation (2.8)) can be written as

$$\mathbf{K}\boldsymbol{\lambda} = \mathbf{f} \tag{A.28}$$

where $\boldsymbol{\lambda}$ is equal to $\mathbf{u}$. Consequently, the gradient can efficiently be calculated, since no additional adjoint system has to be solved. This property is also referred to as self-adjoint and is one reason why compliance is so popular.

A.2.9 Stiffness Interpolation

Both, elemental stiffness matrix $\mathbf{k}_e$ (2.10) and material stiffness matrix $\mathbf{C}_e$ (2.19) are scaled by the interpolated elemental stiffness $E_e(\bar{\rho}_e, E_{0,e})$ (cf. Equation (2.15) together with (2.16) or (2.18)). Usually, they depend on their own related properties or parameters only. Hence, differentiation yields:

$$\frac{\partial \mathbf{k}_e}{\partial \bar{\boldsymbol{\rho}}} = \frac{\partial E_e}{\partial \bar{\rho}_e}\mathbf{k}_e^0 \tag{A.29}$$

$$\frac{\partial \mathbf{C}_e}{\partial \bar{\boldsymbol{\rho}}} = \frac{\partial E_e}{\partial \bar{\rho}_e}\mathbf{C}_0 \tag{A.30}$$

Hence, the interpolated elemental stiffness is differentiated as follows:

$$\frac{\partial E_e}{\partial \bar{\rho}_e} = \frac{\partial \xi_e}{\partial \bar{\rho}_e}\left(E_0 - E_{min}\right) \tag{A.31}$$

Which requires the derivatives for the SIMP (2.16) and RAMP (2.18) scheme with respect to projected variables.

$$\frac{\partial \xi_e^{SIMP}}{\partial \bar{\rho}_e} = p^{SIMP} \bar{\rho}_e^{p^{SIMP}-1} \tag{A.32}$$

$$\frac{\partial \xi_e^{RAMP}}{\partial \bar{\rho}_e} = \frac{1+q}{\left(1 + p^{RAMP}\left(1 - \bar{\rho}_e\right)\right)^2}. \tag{A.33}$$

A.3 Regularization of the Contour Line

As discussed in Section 2.7.3 and shown in Figure 2.15a, the contour line extracted from the density field must be regularized and refined to ensure a smooth boundary and a uniform element size, as depicted in Figures 2.15b and 2.15c. This process is described in detail here, using the L-beam example shown in Figure A.1. A detailed close-up of the regular voxel discretization is provided along with the corresponding contour mesh.

Figure A.2 illustrates the distinct steps carried out to obtain a regularized and refined contour line, which are summarized below:

(a) The contour line extracted with the Matlab function “contour” (see Figure A.2a) is roughly regularized by removing points that are too close and by splitting lines that are too large. If two points are too close, one of them is removed. Conversely, if the distance between two points is too large, a new point is inserted in between. For this, an upper and a lower threshold are defined. Since the resolution of the initial contour line depends on the voxel element size, those values are set to $1.0 \ldots 1.6$ times the voxel size. As a result, contour points that lie within this range are obtained (see Figure A.2b).

(b) In the next step, the roughly regularized line is smoothed by applying the Laplacian smoothing technique. Specifically, if the angle between two lines is below a certain threshold (in all cases 175°), the middle point is relocated. By calculating the weighted average of the three considered points, a new position is found. Equal weights are used, and this step is repeated a second time (see Figure A.2c). Note that further smoothing cycles are possible, but may result in excessive distortions or shrinkage.

(c) The final step is to refine and regularize the contour line. For this, a targeted element size is defined. In the considered case, it is chosen to be half the voxel size. With respect to the global model dimensions, this corresponds to 1/300 for demonstration purposes. In contrast, in the usual case, an element size of 0.25/300 is targeted. For refinement and regularization, all points along the smoothed contour line are considered sequentially (see Figure A.2c). Starting at an arbitrary point, the closest three points are used for a second-degree polynomial interpolation. New points are placed on the interpolation line at a defined distance. This process is iteratively repeated until all points have been processed. Finally, another smoothing step, as in the previous step (b), is applied to the refined contour line.

In case the tarted element size is much smaller than the voxel size, step (c) is repeated several times. Limiting the refinement steps to half the initial size is found to give smooth contour lines independent of the voxel mesh.

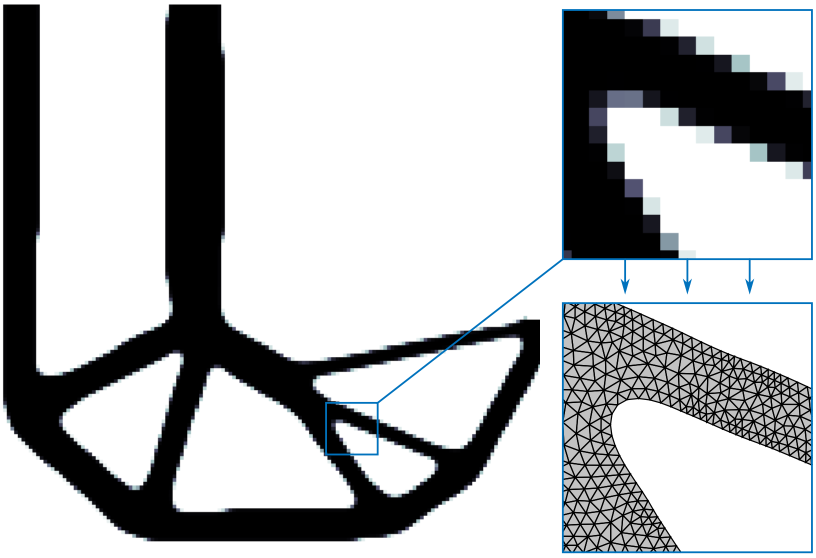

Figure A.1: Considered L-beam example with detailed cutouts for the voxel and contour mesh.

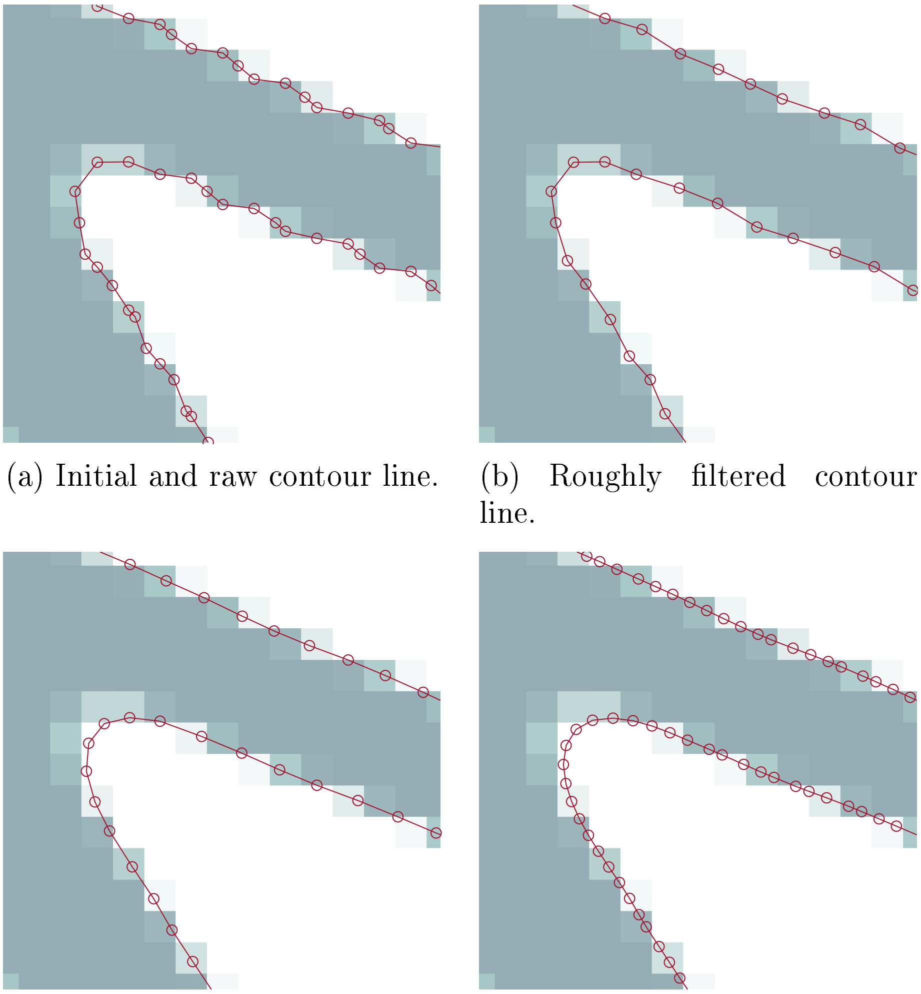

(a) Initial and raw contour line.

(b) Roughly filtered contour line.

(c) Smoothed contour line.

(d) Regularized and refined contour line.

Figure A.2: Detailed steps for contour line refinement, regularization, and smoothing.

A.4 Supplementary Material Associate to Stress Aggregation

In Figure 2.8 results of a parameter study investigating various aggregation parameters for an applied p-norm aggregation function are presented. With respect to those results, Figure A.3 and A.4 show the obtained density fields and the evolution of the objective and constraint value for four selected aggregation parameters p.

In Section 2.4 the properties of different aggregation functions are demonstrated on four exemplary data sets, which are visualized as two-dimensional fields in Figure A.5.

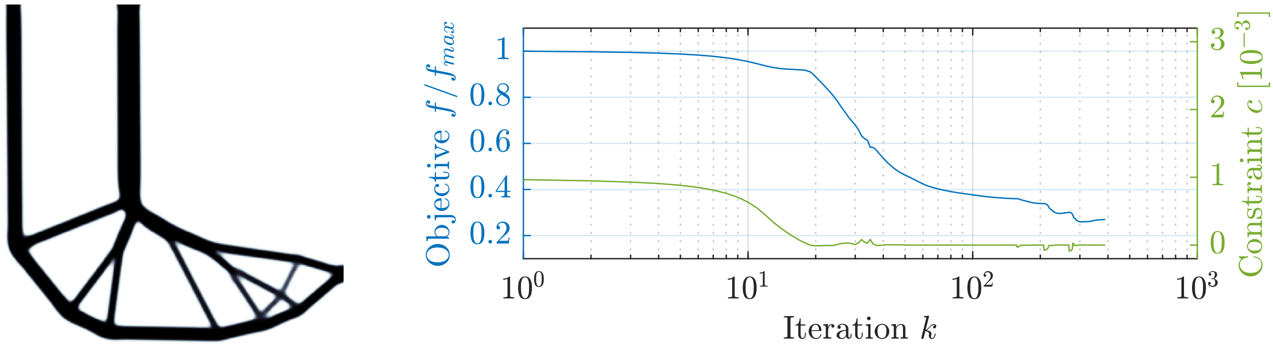

(a) Optimized with $p = 10$.

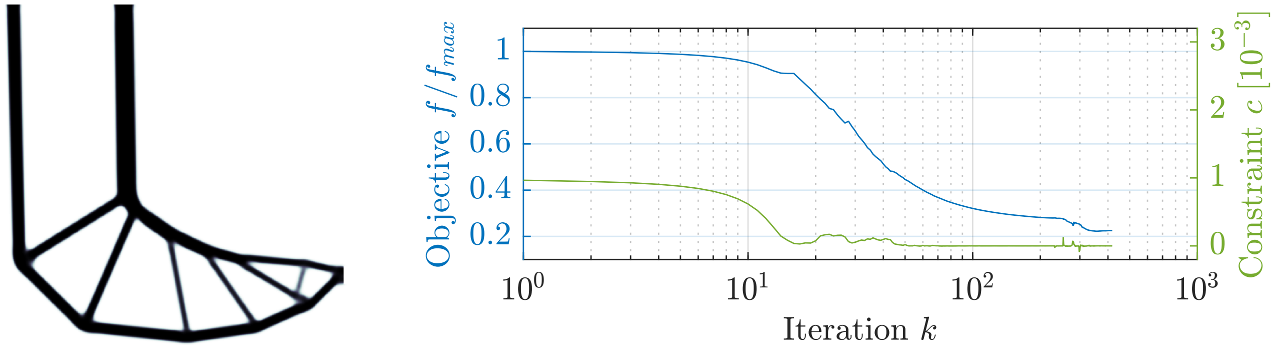

(b) Optimized with $p = 20$.

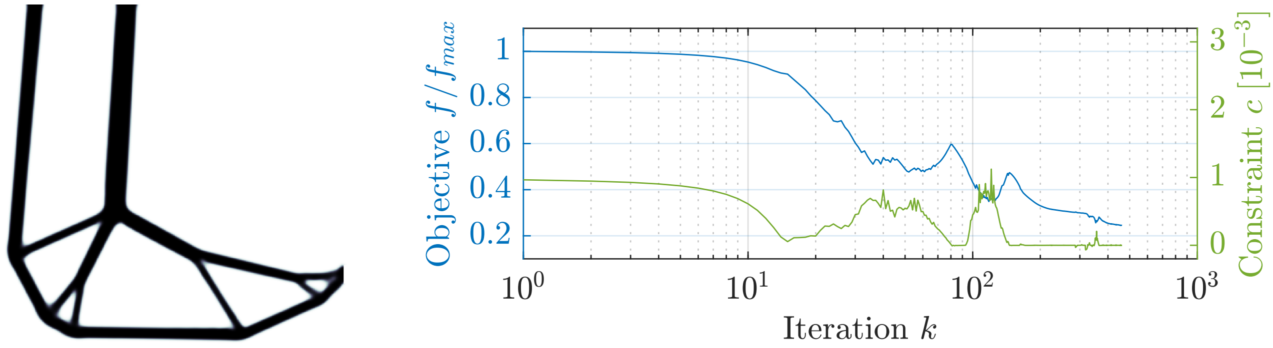

(c) Optimized with $p = 30$.

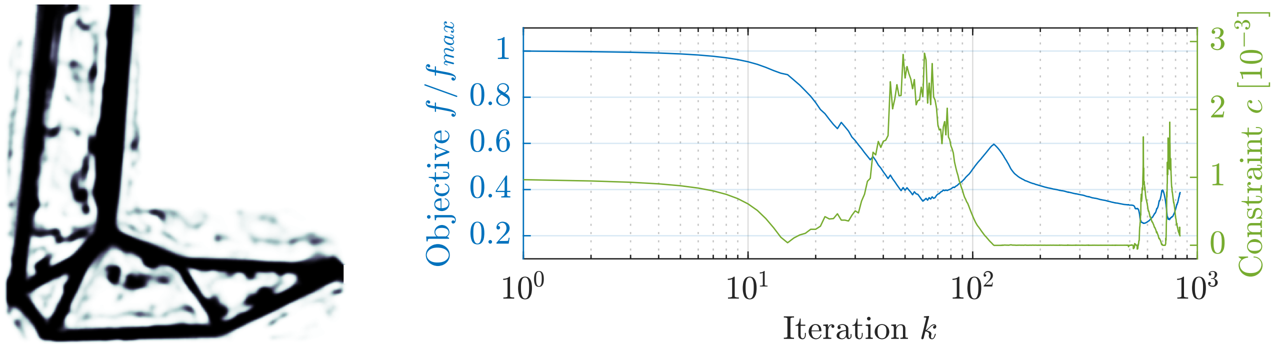

(d) Optimized with $p = 40$.

Figure A.3: Obtained density distribution and convergence plots of stress-constrained optimizations. Aggregation is performed by means of the p-norm function.

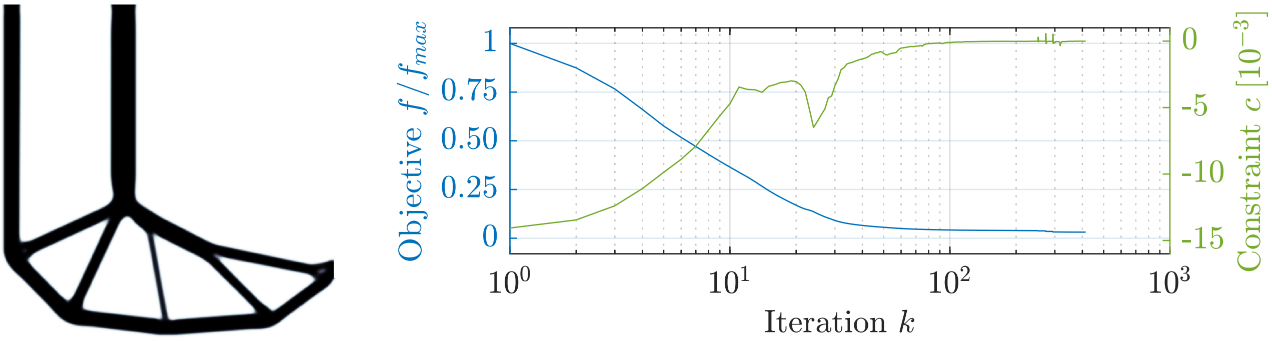

(a) Optimized with $p = 10$.

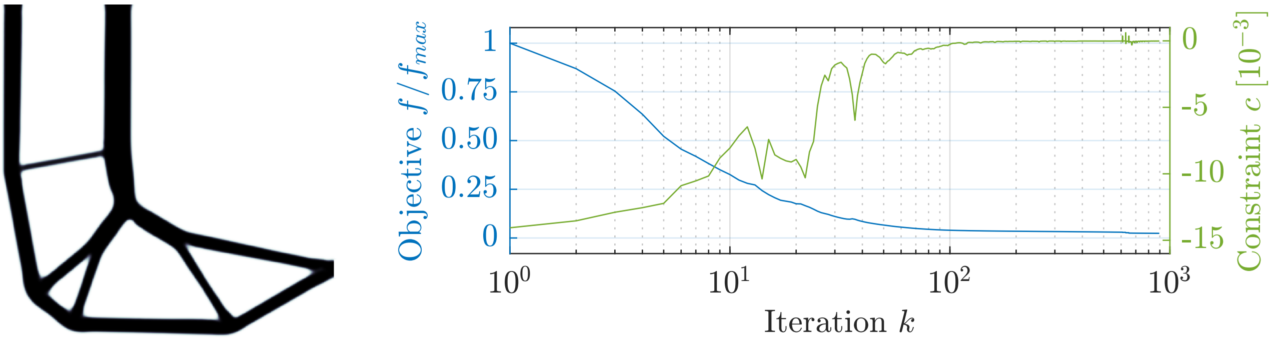

(b) Optimized with $p = 20$.

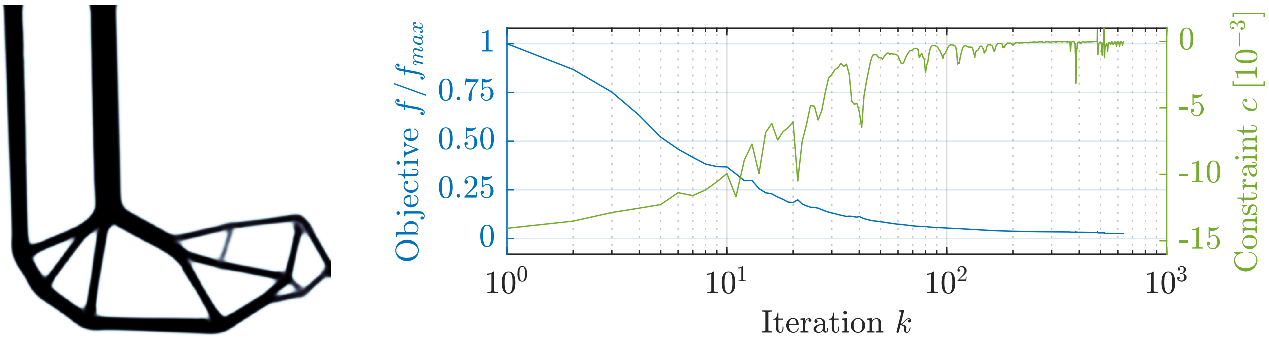

(c) Optimized with $p = 30$.

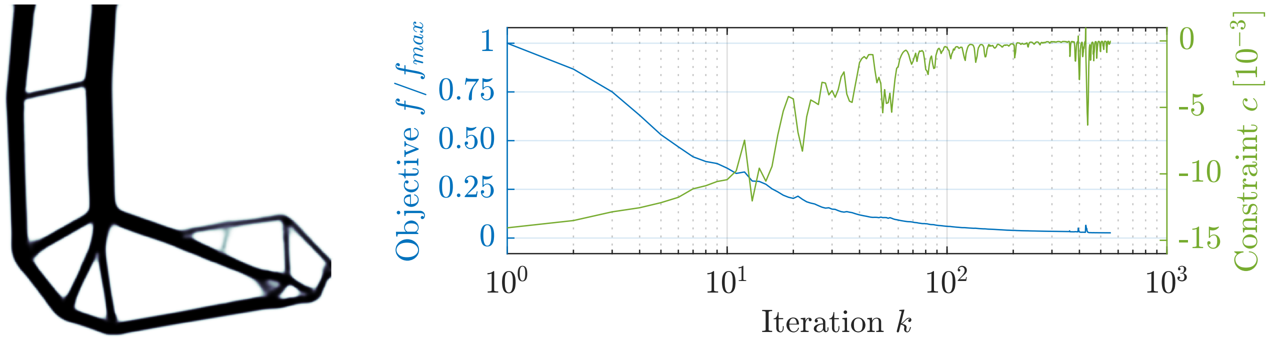

(d) Optimized with $p = 40$.

Figure A.4: Obtained density distribution and convergence plots of volume-constrained optimizations. Aggregation is performed by means of the p-norm function.

(a) Initial density field $\bar{\rho}_{e,init}$.

(b) Initial stress field $q_{e,init}$

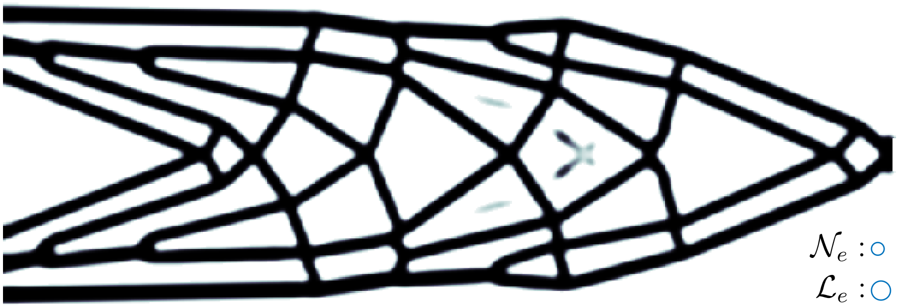

(c) Optimized density field $\bar{\rho}_{e,opt}$ and indicated filter domain $\mathcal{N}_e$ and local volume constraint domain $\mathcal{L}_e$.

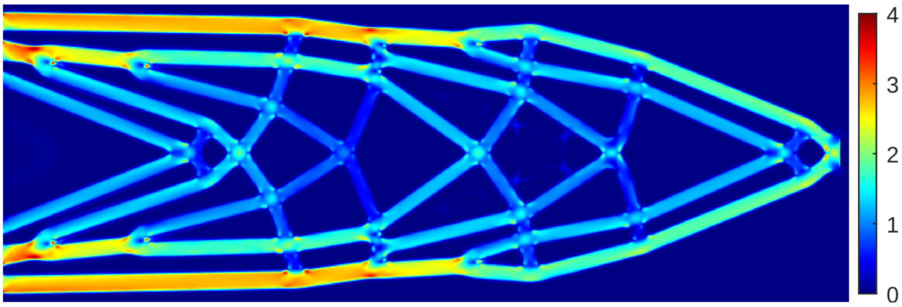

(d) Optimized stress field $q_{e,opt}$

Figure A.5: Two-dimensional representation of the initial and optimized data sets given in Figure 2.5.

Appendix B

Supplementary Material on Damage Robustness Optimization

In this chapter details related to damage robust optimization are given.

B.1 Extended Cut Procedure for the Load Path-Based Evaluation on Voxel Models

Figure B.1 shows how the extended cut procedure is implemented. The maximum stressed element is removed iteratively by setting its stiffness to the defined minimum E_{min} as long as it reduces the maximum stress. To assure, that only very small dispensable struts or elements are cut, the process is stopped after a predefined maximum number of element deletions, or if three element deletions in a row lead to a stress increase. In both cases, the configuration with the lowest stress is chosen as final worst-case stress. Note, to avoid that unloaded struts vanish in stress plots, transparency has been applied to each element according to its physical density. Due to the very low density of elements E19211 and E23891 they appear very opaque, but still, they exhibit the highest stress and are thus removed during this procedure.

B.2 Stiffness Interpolation and Fast Model Assembly

The stiffness is interpolated by utilizing the SIMP scheme. It interpolates the Young's modulus of each element $E_{0,e}$ according to the element's physical density (see Equation (2.15)). The interpolated Young's modulus is then used to scale the

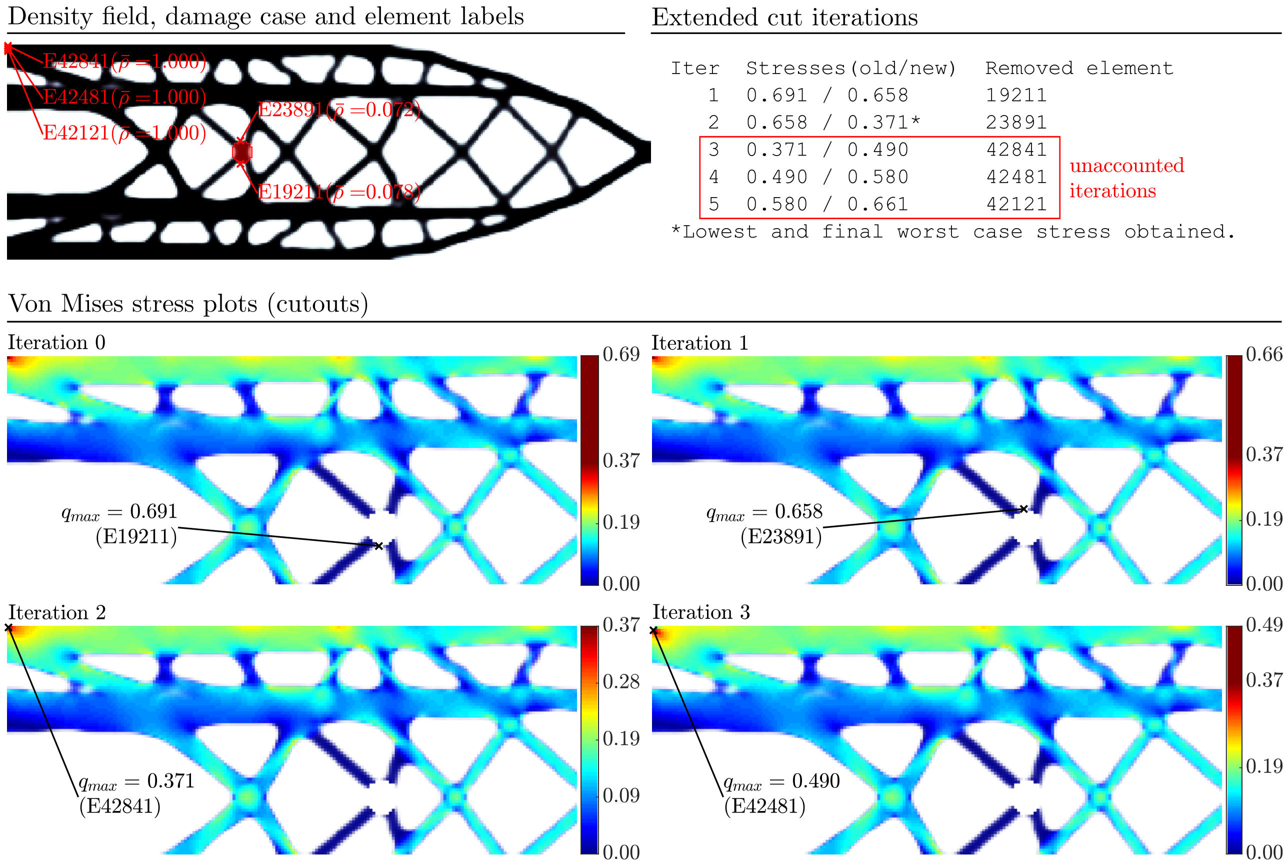

Iter	Stresses(old/new)	Removed element
1	0.691 / 0.658	19211
2	0.658 / 0.371*	23891
3	0.371 / 0.490	42841
4	0.490 / 0.580	42481
5	0.580 / 0.661	42121

*Lowest and final worst case stress obtained.

Figure B.1: Extended cut procedure for incomplete local cuts: Dispensable low density elements are removed, resulting in a lower worst-case stress from [75].

elemental stiffness matrix $\mathbf{k}_e^0$ as shown in Equation (2.10). The scaled elemental stiffness matrix $\mathbf{k}_e$ is then used to assemble the global stiffness matrix $\mathbf{K}$. This is done once per iteration. Note, $\mathbf{K}$ represents the global stiffness matrix of the undamaged density field. To avoid an entire assembly of $\mathbf{K}^{(k)}$ for each damage case, only affected entries are modified. The stiffness matrix of damage case k becomes

$$\mathbf{K}^{(i)}(\boldsymbol{\rho}) = \mathbf{K}(\boldsymbol{\rho}) - \mathbf{k}_e \left(E_e^{(i)}(\boldsymbol{\rho}) - E_{min} \right). \tag{B.1}$$

Still, the explicit damage patch optimization requires the solution of one state equation (3.1) per case, which makes this approach so computational expensive. But since these state equations are independent of each other, assembling and solving can be parallelized straightforwardly (cf. Figure B.2).

B.3 Aspects of the Maximum Feature Size Constraint

For a maximum-feature-size-constrained optimization, the local domain applied to each element has to be defined. Commonly implemented shapes are depicted in Figure B.3.

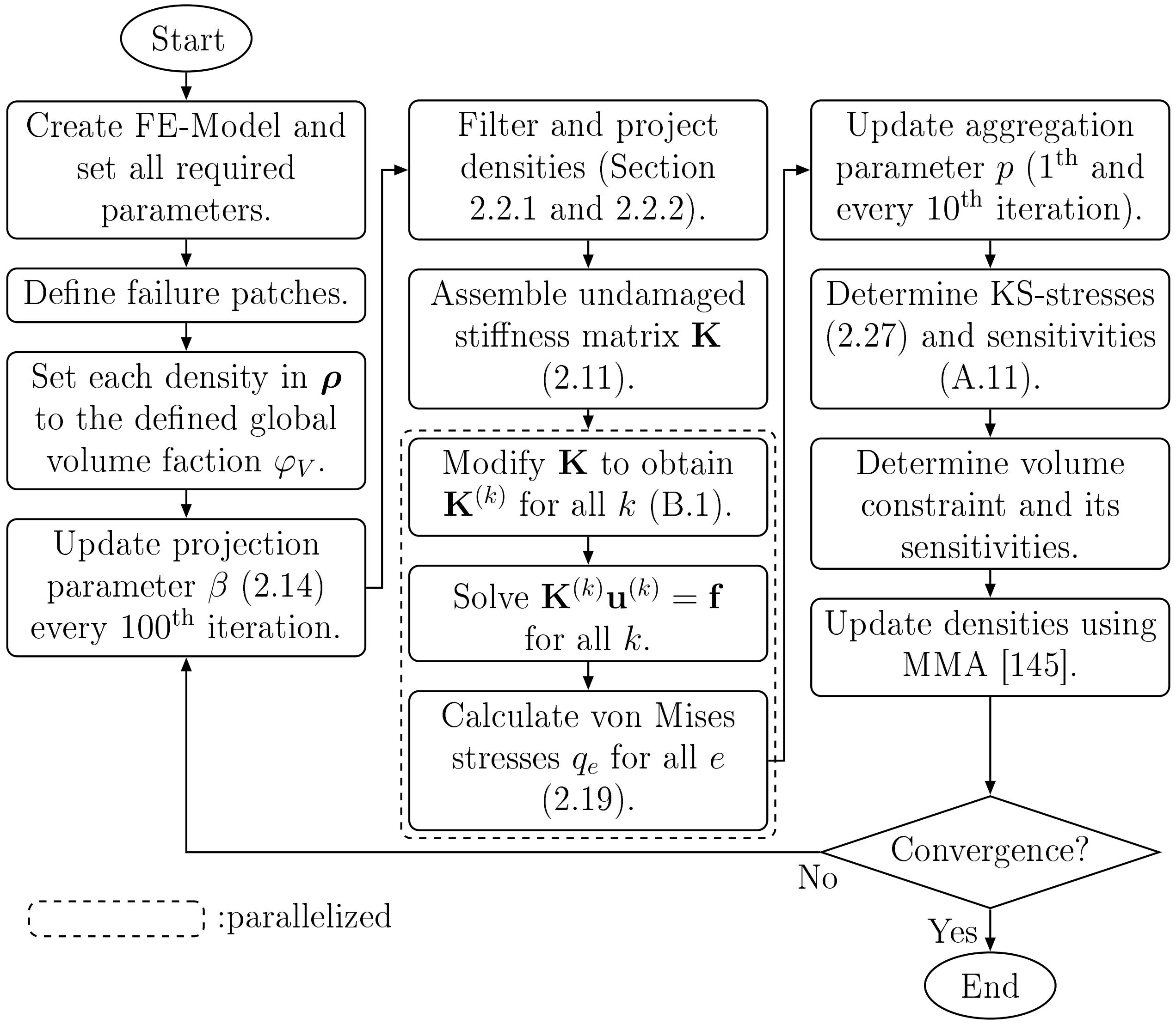

Figure B.2: Flow chart of the damage patch optimization process from [75].

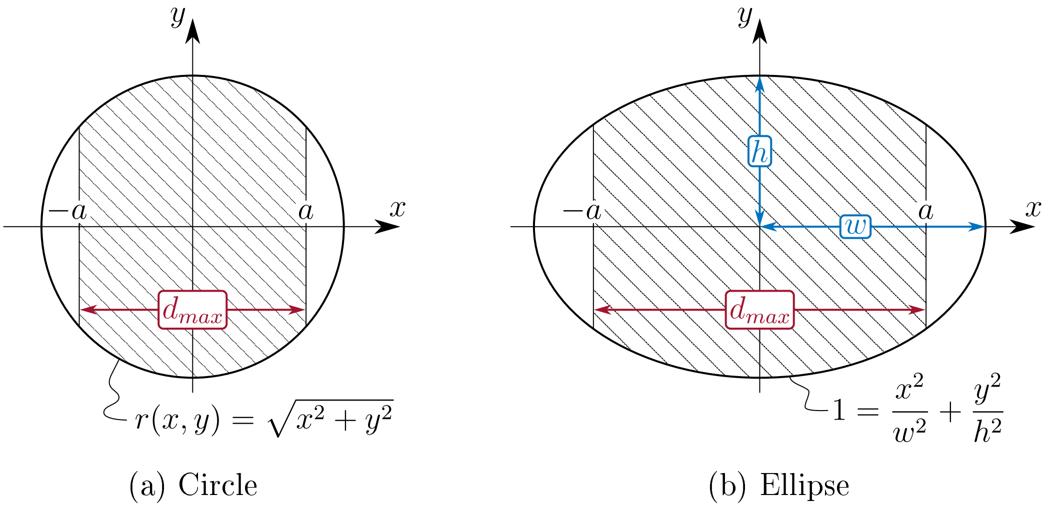

(a) Circle (b) Ellipse

Figure B.3: Geometric parameters used to calculate the local volume fraction φ_L of a circular and an elliptic local domain.

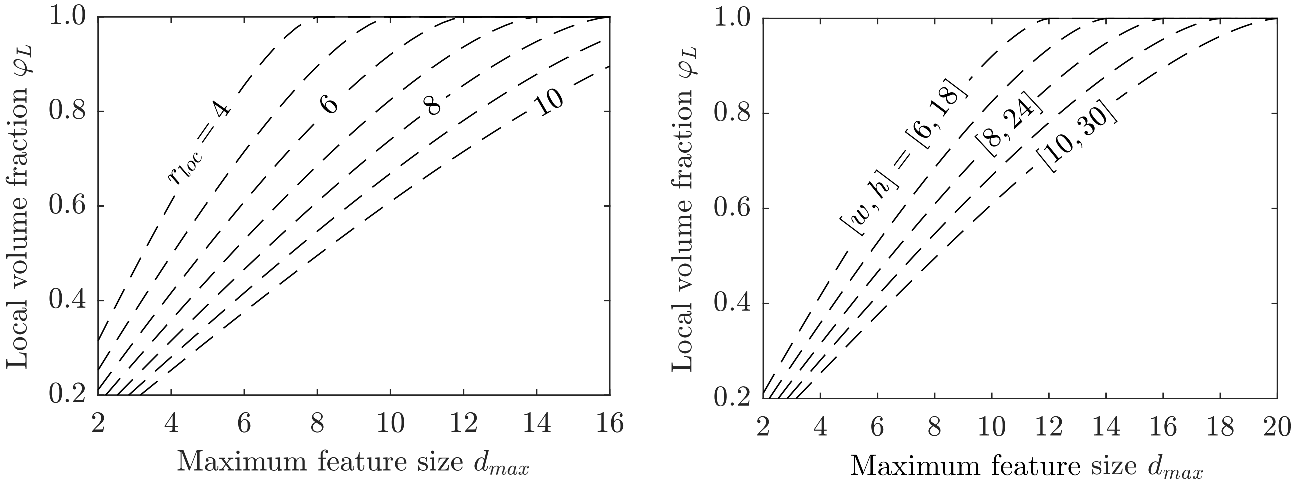

(a) Circular local domain. (b) Elliptic local domain.

Figure B.4: Local volume fraction for different maximum feature sizes and radii of two different domain shapes.

Regarding a circular test region, the maximum feature size d_{max} can be controlled by either changing the radius r or by varying the bounds $\pm a$, which directly affects the local volume fraction φ_L. For $\varphi_L \approx 1$ the local domain's size is equal to the maximum feature size ($2r = d_{max}$). This correlation is for example utilized in the maximum-feature-size-constrained approach by Fernández et al. [31]. Contrary to that, with a given $r = r_{loc}$ and a user defined $d_{max} < 2r$, it is possible to calculate the required volume fraction analytically by simple geometric evaluation according to Figure B.3. For that, $r(x, y)$ can be solved for $y(x, r) = \sqrt{r^2 - x^2}$. The integral can then be evaluated over the bounds $\pm a$ and divided by the circle's area $A^* = \pi\, r^2$:

$$\varphi_L = \frac{1}{A^*}\int\limits_{A} \mathrm{d}A = \frac{1}{A^*}\int_{-a}^{+a}\int_{-y}^{+y} \mathrm{d}\bar{y}\,\mathrm{d}\bar{x} = \frac{2}{A^*}\int_{-a}^{+a} y(x, \circ)\,\mathrm{d}\bar{x} \tag{B.2}$$

By evaluating Equation (B.2) over the interval $[-a, +a] = [-d_{max}/2, +d_{max}/2]$ for different r and d_{max}, the graph in Figure B.4a is obtained. It shows the local volume fraction for different maximum feature size and radii.

For an elliptically shaped domain the same process can be followed using the analytical expression for an ellipse $y(x, w, h) = \frac{h}{w}\sqrt{w^2 - x^2}$ and the ellipse's area $A^* = \pi\, a\, b$. Here, the major axis w of the ellipse is assumed to be oriented along the x-axis, and the minor axis h along the y-axis. By evaluating Equation (B.2) over the same interval as above and for different major and minor axis, the graph in Figure B.4b is obtained. Note, contrary to Figure B.3 the ellipse is considered to be stretched along the y-axis ($h = 3 * w$). For the depicted case $w > h$ much lower volume fractions φ_L are obtained for the same range of the maximum feature size. Obviously, if a shape without rotational symmetry is considered, the maximum feature size depends on the orientation of the domain and the material phase.

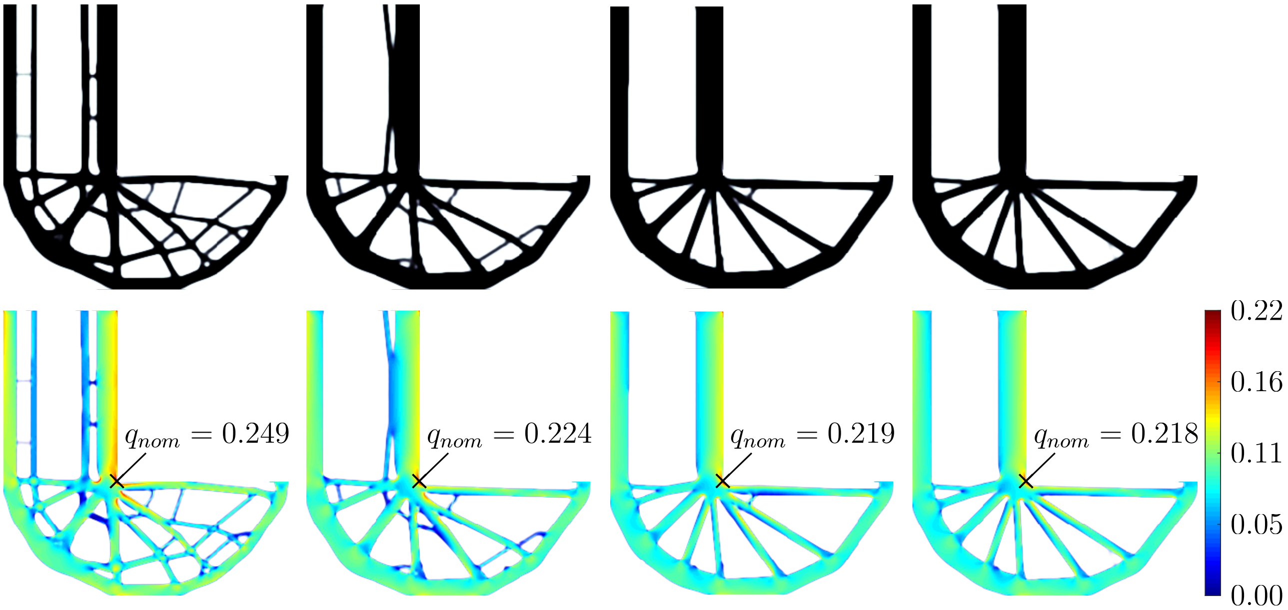

Figure B.5: Results of a multi-objective optimization for different factors κ of 1, 10, 100, 1000 (from left to right), von Mises stress plots (bottom) from [75].

However, the elliptic shape is usually applied twice in different orientations, one is rotated by 90° with respect to the other. Since the maximum volume fraction is constrained, the maximum feature size is actually assured in both directions along the minor axis, as given in B.4b.

B.4 Multi-Objective Damage Analysis

Since the L-beam designs obtained by the explicit formulation do not avoid the stress singularity at the re-entrant corner, a multi-objective optimization is carried out. The objective function in Equation (3.1) is replaced by:

$$q^{MO} = \frac{1}{\kappa^*} q^{\mathcal{D}}(p_{\mathcal{D}}, p_{\mathcal{E}}) + q^{\mathcal{N}}(p_{\mathcal{N}}), \tag{B.3}$$

where $q^{\mathcal{N}}$ is the aggregated stress of the nominal design, which is independently aggregated with a different aggregation parameter $p_{\mathcal{N}}$. By that an equal approximation quality between the damaged and nominal stress field is assured.

For aggregation, the alternative KS-function is employed and the aggregation parameter of the undamaged stress field $p_{\mathcal{N}}$ is updated to $p_{\mathcal{N}} = 10/max(q_e^{\mathcal{N}})$. The update is performed simultaneously to $p_{\mathcal{D}}$ and $p_{\mathcal{E}}$. The weighting factor $\kappa^* = \kappa\, q^{\mathcal{D}}/q^{\mathcal{N}}$ takes into account a constant factor κ and the ratio of the aggregated damaged stress and the nominal stress. This results in a normalization with respect to the nominal stress field. The weighting factor is updated in every iteration to assure a constant ratio.

Results for different weighting factors κ are depicted in Figure B.5. It is observed that the nominal stress field is dominating the optimization for increasing κ, showing a convergence towards an optimization without damage patches.

Appendix C

Supplementary Material on Robust Topology Optimization

In the following, the proposed generalized FOSM method for RTO is derived and required partial derivatives are given. Furthermore, the process of modeling random fields is described and supplementary figures and tables are collected.

C.1 Sensitivity Analysis for First-Order Approximations

In this section, the sensitivity analysis required for RTO using FOSM (see Section 5.2) is explained in more detail. Differentiation of μ_g is performed similar to the deterministic case (cf. Equation (2.7), (2.8) and for details see Appendix A.1), yielding

$$\frac{D\mu_g}{D\boldsymbol{\rho}} \approx \frac{Dg}{D\boldsymbol{\rho}} = \frac{\partial g}{\partial \boldsymbol{\rho}} - \boldsymbol{\lambda}^{\mathrm{T}} \frac{\partial \mathbf{R}}{\partial \boldsymbol{\rho}} \tag{C.1}$$

with the following adjoint system

$$\frac{\partial \mathbf{R}}{\partial \mathbf{u}}^{\mathrm{T}} \boldsymbol{\lambda} = \frac{\partial g}{\partial \mathbf{u}}. \tag{C.2}$$

Now, focusing on the derivative of the variance (second term in Equation (5.8) ${}^{D\sigma_g^2}/_{D\boldsymbol{\rho}}$), which required derivatives with respect to the random variables $\boldsymbol{\alpha}$. Note, that this leads to the same adjoint system as above, hence

$$\frac{Dg}{D\boldsymbol{\alpha}} = \frac{\partial g}{\partial \boldsymbol{\alpha}} - \boldsymbol{\lambda}^{\mathrm{T}} \frac{\partial \mathbf{R}}{\partial \boldsymbol{\alpha}}. \tag{C.3}$$

This implies, that the added computation cost for calculation of the variance is close to negligible. Nonetheless, the state equilibrium $\mathbf{R}\left(\boldsymbol{\rho}, \mathbf{u}, \boldsymbol{\alpha}\right)$ and thus also the state variables $\mathbf{u}\left(\boldsymbol{\rho},\boldsymbol{\alpha}\right)$ depend on random variables. Inserting Equation (C.3) into (5.7) yields:

$$\sigma_g^2 \approx \left(\frac{\partial g}{\partial \boldsymbol{\alpha}} - \boldsymbol{\lambda}^{\mathrm{T}}\frac{\partial \mathbf{R}}{\partial \boldsymbol{\alpha}}\right)^{\mathrm{T}} \Sigma_\alpha \left(\frac{\partial g}{\partial \boldsymbol{\alpha}} - \boldsymbol{\lambda}^{\mathrm{T}}\frac{\partial \mathbf{R}}{\partial \boldsymbol{\alpha}}\right) \tag{C.4}$$

Directly differentiating the variance with respect to design variables requires the full derivative ${}^{D\boldsymbol{\lambda}}\!/\!{}_{D\boldsymbol{\rho}}$. To avoid its computation a new residuum is defined:

$$\mathbf{R}_\alpha := \frac{\partial \mathbf{R}}{\partial \mathbf{u}}^{\mathrm{T}}\boldsymbol{\lambda} - \frac{\partial g}{\partial \mathbf{u}} = \mathbf{0}. \tag{C.5}$$

Consequently, the following Lagrangian is obtained

$$\bar{\sigma}_g^2\left(\mathbf{u},\boldsymbol{\lambda}_u,\boldsymbol{\lambda}_\alpha\right) := \sigma_g^2 - \boldsymbol{\lambda}_u^{\mathrm{T}}\mathbf{R} - \boldsymbol{\lambda}_\alpha^{\mathrm{T}}\mathbf{R}_\alpha. \tag{C.6}$$

Differentiation of Equation (C.6) leads to

$$\begin{aligned}\frac{D\bar{\sigma}_g^2}{D\boldsymbol{\rho}} = {} & \frac{\partial \sigma_g^2}{\partial \boldsymbol{\rho}} - \boldsymbol{\lambda}_u^{\mathrm{T}}\frac{\partial \mathbf{R}}{\partial \boldsymbol{\rho}} - \boldsymbol{\lambda}_\alpha^{\mathrm{T}}\frac{\partial \mathbf{R}_\alpha}{\partial \boldsymbol{\rho}} \\ & + \left[\frac{\partial \sigma_g^2}{\partial \mathbf{u}} - \boldsymbol{\lambda}_u^{\mathrm{T}}\frac{\partial \mathbf{R}}{\partial \mathbf{u}} - \boldsymbol{\lambda}_\alpha^{\mathrm{T}}\frac{\partial \mathbf{R}_\alpha}{\partial \mathbf{u}}\right]\frac{D\mathbf{u}}{D\boldsymbol{\rho}} \\ & + \left[\frac{\partial \sigma_g^2}{\partial \boldsymbol{\lambda}} - \boldsymbol{\lambda}_\alpha^{\mathrm{T}}\frac{\partial \mathbf{R}_\alpha}{\partial \boldsymbol{\lambda}}\right]\frac{D\boldsymbol{\lambda}}{D\boldsymbol{\rho}}.\end{aligned} \tag{C.7}$$

Similar to the deterministic case (cf. Section 2.1) calculation of computational expensive partial derivatives, i.e. ${}^{D\mathbf{u}}\!/\!{}_{D\boldsymbol{\rho}}$ and ${}^{D\boldsymbol{\lambda}}\!/\!{}_{D\boldsymbol{\rho}}$, can also be avoided by solving following system of equations:

$$\begin{bmatrix} \dfrac{\partial \mathbf{R}}{\partial \mathbf{u}}^{\mathrm{T}} & \dfrac{\partial \mathbf{R}_\alpha}{\partial \mathbf{u}}^{\mathrm{T}} \\ \mathbf{0} & \dfrac{\partial \mathbf{R}}{\partial \mathbf{u}} \end{bmatrix} \begin{bmatrix} \boldsymbol{\lambda}_u \\ \boldsymbol{\lambda}_\alpha \end{bmatrix} = \begin{bmatrix} \dfrac{\partial \sigma_g^2}{\partial \mathbf{u}} \\ \dfrac{\partial \sigma_g^2}{\partial \boldsymbol{\lambda}} \end{bmatrix}. \tag{C.8}$$

Note, that in the second row ${}^{\partial \mathbf{R}_\alpha}\!/\!{}_{\partial \boldsymbol{\lambda}}$ is already substituted by ${}^{\partial \mathbf{R}}\!/\!{}_{\partial \mathbf{u}}$ (cf. Equation (C.11)). To determine $\boldsymbol{\lambda}_u$ and $\boldsymbol{\lambda}_\alpha$ the second row is solved first, which simplifies the first row.

C.2 Partial Derivatives for Robust Topology Optimization

In addition to Appendix A.2 this section lists all partial derivatives required for RTO using FOSM. For the proposed first-order approximation of the variance (see Equation (5.7)) second-order derivatives and derivatives with respect to the random variables $\boldsymbol{\alpha}$ are derived. The elemental projection threshold η_e, material strength $q_{0,e}$ and stiffness $E_{0,e}$ are considered as random variables. Hence, differentiation is performed with respect to those quantities.

C.2.1 Approximated Variance

General partial derivatives of $\mathbf{R}_\alpha$ from Equation (C.7) are defined as follows:

$$\frac{\partial \mathbf{R}_\alpha}{\partial \bar{\boldsymbol{\rho}}} = \frac{\partial^2 \mathbf{R}}{\partial \mathbf{u} \partial \bar{\boldsymbol{\rho}}}^{\mathrm{T}} \boldsymbol{\lambda} - \frac{\partial^2 g}{\partial \mathbf{u} \partial \bar{\boldsymbol{\rho}}} \tag{C.9}$$

$$\frac{\partial \mathbf{R}_\alpha}{\partial \mathbf{u}} = \frac{\partial^2 \mathbf{R}}{\partial^2 \mathbf{u}}^{\mathrm{T}} \boldsymbol{\lambda} - \frac{\partial^2 g}{\partial^2 \mathbf{u}} \tag{C.10}$$

$$\frac{\partial \mathbf{R}_\alpha}{\partial \boldsymbol{\lambda}} = \frac{\partial \mathbf{R}}{\partial \mathbf{u}}^{\mathrm{T}} \tag{C.11}$$

General partial derivatives of the approximated variance σ_g^2 from Equation (C.7) are defined as follows:

$$\frac{\partial \sigma_g^2}{\partial \bar{\boldsymbol{\rho}}} = 2 \left(\frac{\partial^2 g}{\partial \boldsymbol{\alpha} \partial \bar{\boldsymbol{\rho}}} - \boldsymbol{\lambda}^{\mathrm{T}} \frac{\partial^2 \mathbf{R}}{\partial \boldsymbol{\alpha} \partial \boldsymbol{\rho}} \right)^{\mathrm{T}} \Sigma_\alpha \frac{Dg}{D\boldsymbol{\alpha}} + \frac{Dg}{D\boldsymbol{\alpha}}^{\mathrm{T}} \Sigma_\alpha \frac{Dg}{D\boldsymbol{\alpha}} \tag{C.12}$$

$$\frac{\partial \sigma_g^2}{\partial \mathbf{u}} = 2 \left(\frac{\partial^2 g}{\partial \boldsymbol{\alpha} \partial \mathbf{u}} - \boldsymbol{\lambda}^{\mathrm{T}} \frac{\partial^2 \mathbf{R}}{\partial \boldsymbol{\alpha} \partial \mathbf{u}} \right)^{\mathrm{T}} \Sigma_\alpha \frac{Dg}{D\boldsymbol{\alpha}} \tag{C.13}$$

$$\frac{\partial \sigma_g^2}{\partial \boldsymbol{\lambda}} = -2 \frac{\partial \mathbf{R}}{\partial \boldsymbol{\alpha}}^{\mathrm{T}} \Sigma_\alpha \frac{Dg}{D\boldsymbol{\alpha}} \tag{C.14}$$

C.2.2 State Equilibrium

The discrete residuum given in Equation (2.9) is a function of random variables $\boldsymbol{\alpha}$. Hence, together with derivations from Appendix A.2.2 following derivatives are obtained:

$$\frac{\partial \mathbf{R}}{\partial \boldsymbol{\alpha}} = \frac{\partial \mathbf{K}}{\partial \boldsymbol{\alpha}} \mathbf{u} \quad \text{with} \quad \frac{\partial \mathbf{K}}{\partial \boldsymbol{\alpha}} = \frac{\partial \mathbf{K}}{\partial \bar{\boldsymbol{\rho}}} \frac{\partial \bar{\boldsymbol{\rho}}}{\partial \boldsymbol{\alpha}} \tag{C.15}$$

$$\frac{\partial^2 \mathbf{R}}{\partial \boldsymbol{\alpha} \partial \bar{\boldsymbol{\rho}}} = \frac{\partial^2 \mathbf{K}}{\partial \boldsymbol{\alpha} \partial \bar{\boldsymbol{\rho}}} \mathbf{u} \tag{C.16}$$

$$\frac{\partial^2 \mathbf{R}}{\partial \boldsymbol{\alpha} \partial \mathbf{u}} = \frac{\partial \mathbf{K}}{\partial \boldsymbol{\alpha}} \tag{C.17}$$

$$\frac{\partial^2 \mathbf{R}}{\partial \mathbf{u} \partial \bar{\boldsymbol{\rho}}} = \frac{\partial \mathbf{K}}{\partial \bar{\boldsymbol{\rho}}}. \tag{C.18}$$

C.2.3 Aggregation Function

In this subsection partial derivatives for any design response $\mathcal{F}_e\left(\bar{\boldsymbol{\rho}}, \boldsymbol{\alpha}, \mathbf{u}\right)$ which can be aggregated are collected. In addition to Appendix A.2.3 following first- and second-order derivatives of the KS-function from Equation (2.27) are determined.

$$\frac{\partial \mathcal{A}_{KS}}{\partial \boldsymbol{\alpha}} = \sum_{e=1}^{n} \frac{\exp}{\Sigma_{\exp}} \frac{\partial \mathcal{F}_e}{\partial \boldsymbol{\alpha}} \tag{C.19}$$

$$\frac{\partial^2 \mathcal{A}_{KS}}{\partial \boldsymbol{\alpha} \partial \bar{\boldsymbol{\rho}}} = -p \sum_{e=1}^{n} \frac{\exp}{\Sigma_{\exp}^2} \frac{\partial \mathcal{F}_e}{\partial \bar{\boldsymbol{\rho}}} \sum_{e=1}^{n} \frac{\exp}{\Sigma_{\exp}^2} \frac{\partial \mathcal{F}_e}{\partial \boldsymbol{\alpha}} + p \sum_{e=1}^{n} \frac{\exp}{\Sigma_{\exp}} \frac{\partial \mathcal{F}_e}{\partial \bar{\boldsymbol{\rho}}} \frac{\partial \mathcal{F}_e}{\partial \boldsymbol{\alpha}} + \sum_{e=1}^{n} \frac{\exp}{\Sigma_{\exp}} \frac{\partial^2 \mathcal{F}_e}{\partial \boldsymbol{\alpha} \partial \bar{\boldsymbol{\rho}}} \tag{C.20}$$

$$\frac{\partial^2 \mathcal{A}_{KS}}{\partial \boldsymbol{\alpha} \partial \mathbf{u}} = -p \sum_{e=1}^{n} \frac{\exp}{\Sigma_{\exp}^2} \frac{\partial \mathcal{F}_e}{\partial \mathbf{u}} \sum_{e=1}^{n} \frac{\exp}{\Sigma_{\exp}^2} \frac{\partial \mathcal{F}_e}{\partial \boldsymbol{\alpha}} + p \sum_{e=1}^{n} \frac{\exp}{\Sigma_{\exp}} \frac{\partial \mathcal{F}_e}{\partial \mathbf{u}} \frac{\partial \mathcal{F}_e}{\partial \boldsymbol{\alpha}} + \sum_{e=1}^{n} \frac{\exp}{\Sigma_{\exp}} \frac{\partial^2 \mathcal{F}_e}{\partial \boldsymbol{\alpha} \partial \mathbf{u}} \tag{C.21}$$

$$\frac{\partial^2 \mathcal{A}_{KS}}{\partial \mathbf{u} \partial \bar{\boldsymbol{\rho}}} = -p \sum_{e=1}^{n} \frac{\exp}{\Sigma_{\exp}^2} \frac{\partial \mathcal{F}_e}{\partial \bar{\boldsymbol{\rho}}} \sum_{e=1}^{n} \frac{\exp}{\Sigma_{\exp}^2} \frac{\partial \mathcal{F}_e}{\partial \mathbf{u}} + p \sum_{e=1}^{n} \frac{\exp}{\Sigma_{\exp}} \frac{\partial \mathcal{F}_e}{\partial \bar{\boldsymbol{\rho}}} \frac{\partial \mathcal{F}_e}{\partial \mathbf{u}} + \sum_{e=1}^{n} \frac{\exp}{\Sigma_{\exp}} \frac{\partial^2 \mathcal{F}_e}{\partial \mathbf{u} \partial \bar{\boldsymbol{\rho}}} \tag{C.22}$$

$$\frac{\partial^2 \mathcal{A}_{KS}}{\partial^2 \mathbf{u}} = -p \sum_{e=1}^{n} \frac{\exp}{\Sigma_{\exp}^2} \frac{\partial \mathcal{F}_e}{\partial \mathbf{u}} \sum_{e=1}^{n} \frac{\exp}{\Sigma_{\exp}^2} \frac{\partial \mathcal{F}_e}{\partial \mathbf{u}} + p \sum_{e=1}^{n} \frac{\exp}{\Sigma_{\exp}} \frac{\partial \mathcal{F}_e}{\partial \mathbf{u}} \frac{\partial \mathcal{F}_e}{\partial \mathbf{u}} + \sum_{e=1}^{n} \frac{\exp}{\Sigma_{\exp}} \frac{\partial^2 \mathcal{F}_e}{\partial^2 \mathbf{u}} \tag{C.23}$$

with $\frac{\exp}{\Sigma_{\exp}} = \frac{\exp(p(\mathcal{F}_e - f_0))}{\sum_{i=1}^{n} \exp(p(\mathcal{F}_i - f_0))}$ and $\frac{\exp}{\Sigma_{\exp}^2} = \frac{\exp(p(\mathcal{F}_e - f_0))}{\left[\sum_{i=1}^{n} \exp(p(\mathcal{F}_i - f_0))\right]^2}$.

Derivatives of the p-norm function from Equation (2.23) are defined as follows:

$$\frac{\partial \mathcal{A}_{PN}}{\partial \boldsymbol{\alpha}} = \Sigma_{\mathcal{F}} \sum_{e=1}^{n} \mathcal{F}_e^{p-1} \frac{\partial \mathcal{F}_e}{\partial \boldsymbol{\alpha}} \tag{C.24}$$

$$\begin{aligned} \frac{\partial^2 \mathcal{A}_{PN}}{\partial \boldsymbol{\alpha} \partial \bar{\boldsymbol{\rho}}} &= (1-p) \Sigma_{\mathcal{F}}^2 \sum_{e=1}^{n} \mathcal{F}_e^{p-1} \frac{\partial \mathcal{F}_e}{\partial \bar{\boldsymbol{\rho}}} \sum_{e=1}^{n} \mathcal{F}_e^{p-1} \frac{\partial \mathcal{F}_e}{\partial \boldsymbol{\alpha}} \\ &+ (p-1) \Sigma_{\mathcal{F}} \sum_{e=1}^{n} \mathcal{F}_e^{p-2} \frac{\partial \mathcal{F}_e}{\partial \bar{\boldsymbol{\rho}}} \frac{\partial \mathcal{F}_e}{\partial \boldsymbol{\alpha}} + \Sigma_{\mathcal{F}} \sum_{e=1}^{n} \mathcal{F}_e^{p-1} \frac{\partial^2 \mathcal{F}_e}{\partial \boldsymbol{\alpha} \partial \bar{\boldsymbol{\rho}}} \end{aligned} \tag{C.25}$$

$$\begin{aligned}\frac{\partial^2 \mathcal{A}_{PN}}{\partial \boldsymbol{\alpha} \partial \mathbf{u}} &= (1-p)\Sigma_{\mathcal{F}}^2 \sum_{e=1}^{n} \mathcal{F}_e^{p-1} \frac{\partial \mathcal{F}_e}{\partial \mathbf{u}} \sum_{e=1}^{n} \mathcal{F}_e^{p-1} \frac{\partial \mathcal{F}_e}{\partial \boldsymbol{\alpha}} \\ &+ (p-1)\Sigma_{\mathcal{F}} \sum_{e=1}^{n} \mathcal{F}_e^{p-2} \frac{\partial \mathcal{F}_e}{\partial \mathbf{u}} \frac{\partial \mathcal{F}_e}{\partial \boldsymbol{\alpha}} + \Sigma_{\mathcal{F}} \sum_{e=1}^{n} \mathcal{F}_e^{p-1} \frac{\partial^2 \mathcal{F}_e}{\partial \boldsymbol{\alpha} \partial \mathbf{u}} \end{aligned} \tag{C.26}$$

$$\begin{aligned}\frac{\partial^2 \mathcal{A}_{PN}}{\partial \mathbf{u} \partial \bar{\boldsymbol{\rho}}} &= (1-p)\Sigma_{\mathcal{F}}^2 \sum_{e=1}^{n} \mathcal{F}_e^{p-1} \frac{\partial \mathcal{F}_e}{\partial \bar{\boldsymbol{\rho}}} \sum_{e=1}^{n} \mathcal{F}_e^{p-1} \frac{\partial \mathcal{F}_e}{\partial \mathbf{u}} \\ &+ (p-1)\Sigma_{\mathcal{F}} \sum_{e=1}^{n} \mathcal{F}_e^{p-2} \frac{\partial \mathcal{F}_e}{\partial \bar{\boldsymbol{\rho}}} \frac{\partial \mathcal{F}_e}{\partial \mathbf{u}} + \Sigma_{\mathcal{F}} \sum_{e=1}^{n} \mathcal{F}_e^{p-1} \frac{\partial^2 \mathcal{F}_e}{\partial \mathbf{u} \partial \bar{\boldsymbol{\rho}}} \end{aligned} \tag{C.27}$$

$$\begin{aligned}\frac{\partial^2 \mathcal{A}_{PN}}{\partial^2 \mathbf{u}} &= (1-p)\Sigma_{\mathcal{F}}^2 \sum_{e=1}^{n} \mathcal{F}_e^{p-1} \frac{\partial \mathcal{F}_e}{\partial \mathbf{u}} \sum_{e=1}^{n} \mathcal{F}_e^{p-1} \frac{\partial \mathcal{F}_e}{\partial \mathbf{u}} \\ &+ (p-1)\Sigma_{\mathcal{F}} \sum_{e=1}^{n} \mathcal{F}_e^{p-2} \frac{\partial \mathcal{F}_e}{\partial \mathbf{u}} \frac{\partial \mathcal{F}_e}{\partial \mathbf{u}} + \Sigma_{\mathcal{F}} \sum_{e=1}^{n} \mathcal{F}_e^{p-1} \frac{\partial^2 \mathcal{F}_e}{\partial \mathbf{u}} \end{aligned} \tag{C.28}$$

with $\Sigma_{\mathcal{F}} = (\sum_{i=2}^{n} \mathcal{F}_i^p)^{\frac{1}{p}-1}$ and $\Sigma_{\mathcal{F}}^2 = (\sum_{i=2}^{n} \mathcal{F}_i^p)^{\frac{1}{p}-2}$

C.2.4 Strength Constraint

The allowable stress limit or material strength q_0 can be considered as a random parameter if stresses are constrained (cf. Equation (2.21)). Hence, $q_{0,e}$ represents the random variable in each element e. In combination with derivations in Appendix A.2.4 the following partial derivatives are determined:

$$\frac{\partial SF_e}{\partial \boldsymbol{\alpha}} = -\frac{1}{q_{0,e}^2} q_e \tag{C.29}$$

$$\frac{\partial^2 SF_e}{\partial \boldsymbol{\alpha} \partial \bar{\boldsymbol{\rho}}} = -\frac{1}{q_{0,e}^2} \frac{\partial q_e}{\partial \bar{\boldsymbol{\rho}}} \tag{C.30}$$

$$\frac{\partial^2 SF_e}{\partial \boldsymbol{\alpha} \partial \mathbf{u}} = -\frac{1}{q_{0,e}^2} \frac{\partial q_e}{\partial \mathbf{u}} \tag{C.31}$$

$$\frac{\partial^2 SF_e}{\partial \mathbf{u} \partial \bar{\boldsymbol{\rho}}} = \frac{1}{q_{0,e}} \frac{\partial^2 q_e}{\partial \mathbf{u} \partial \bar{\boldsymbol{\rho}}} \tag{C.32}$$

$$\frac{\partial^2 SF_e}{\partial^2 \mathbf{u}} = \frac{1}{q_{0,e}} \frac{\partial^2 q_e}{\partial^2 \mathbf{u}} \tag{C.33}$$

C.2.5 Equivalent Stress

A formulation for the elemental von Mises stresses $q_e\left(\bar{\boldsymbol{\rho}}, \boldsymbol{\alpha}, \mathbf{u}\right)$ is given in Equation (2.19). Together with derivations in Appendix A.2.5 following derivatives are required:

$$\frac{\partial q_e}{\partial \boldsymbol{\alpha}} = \frac{1}{q_e}\ \mathbf{u}_e^{\mathrm{T}}\mathbf{B}_e^{\mathrm{T}}\mathbf{C}_e\mathbf{M}\frac{\partial \mathbf{C}_e}{\partial \boldsymbol{\alpha}}\mathbf{B}_e\mathbf{u}_e \tag{C.34}$$

$$\frac{\partial^2 q_e}{\partial \boldsymbol{\alpha}\partial \bar{\boldsymbol{\rho}}} = u\frac{\partial v}{\partial \bar{\boldsymbol{\rho}}} + \frac{\partial u}{\partial \bar{\boldsymbol{\rho}}}v \tag{C.35}$$

$$\frac{\partial^2 q_e}{\partial \boldsymbol{\alpha}\partial \mathbf{u}} = u\frac{\partial v}{\partial \mathbf{u}} + \frac{\partial u}{\partial \mathbf{u}}v \tag{C.36}$$

$$\frac{\partial^2 q_e}{\partial \mathbf{u}\partial \bar{\boldsymbol{\rho}}} = u\frac{\partial w}{\partial \bar{\boldsymbol{\rho}}} + \frac{\partial u}{\partial \bar{\boldsymbol{\rho}}}w \tag{C.37}$$

$$\frac{\partial^2 q_e}{\partial^2 \mathbf{u}} = u\frac{\partial w}{\partial \mathbf{u}} + \frac{\partial u}{\partial \mathbf{u}}w, \tag{C.38}$$

which include following expressions:

$$u = \frac{1}{q_e} = \left(\mathbf{u}_e^{\mathrm{T}}\mathbf{B}_e^{\mathrm{T}}\mathbf{C}_e\mathbf{M}\mathbf{C}_e\mathbf{B}_e\mathbf{u}_e\right)^{-1/2} \tag{C.39}$$

$$\frac{\partial u}{\partial \bar{\boldsymbol{\rho}}} = -\frac{1}{q_e^3}\ \mathbf{u}_e^{\mathrm{T}}\mathbf{B}_e^{\mathrm{T}}\mathbf{C}_e\mathbf{M}\frac{\partial \mathbf{C}_e}{\partial \bar{\boldsymbol{\rho}}}\mathbf{B}_e\mathbf{u}_e \tag{C.40}$$

$$\frac{\partial u}{\partial \mathbf{u}} = -\frac{1}{q_e^3}\ \mathbf{B}_e^{\mathrm{T}}\mathbf{C}_e\mathbf{M}\mathbf{C}_e\mathbf{B}_e\mathbf{u}_e \tag{C.41}$$

$$v = \mathbf{u}_e^{\mathrm{T}}\mathbf{B}_e^{\mathrm{T}}\mathbf{C}_e\mathbf{M}\frac{\partial \mathbf{C}_e}{\partial \boldsymbol{\alpha}}\mathbf{B}_e\mathbf{u}_e \tag{C.42}$$

$$\frac{\partial v}{\partial \bar{\boldsymbol{\rho}}} = \mathbf{u}_e^{\mathrm{T}}\mathbf{B}_e^{\mathrm{T}}\frac{\partial \mathbf{C}_e}{\partial \bar{\boldsymbol{\rho}}}\mathbf{M}\frac{\partial \mathbf{C}_e}{\partial \boldsymbol{\alpha}}\mathbf{B}_e\mathbf{u}_e + \mathbf{u}_e^{\mathrm{T}}\mathbf{B}_e^{\mathrm{T}}\mathbf{C}_e\mathbf{M}\frac{\partial^2 \mathbf{C}_e}{\partial \boldsymbol{\alpha}\partial \bar{\boldsymbol{\rho}}}\mathbf{B}_e\mathbf{u}_e \tag{C.43}$$

$$\frac{\partial v}{\partial \mathbf{u}} = 2\ \mathbf{B}_e^{\mathrm{T}}\mathbf{C}_e\mathbf{M}\frac{\partial \mathbf{C}_e}{\partial \boldsymbol{\alpha}}\mathbf{B}_e\mathbf{u}_e \tag{C.44}$$

$$w = \mathbf{B}_e^{\mathrm{T}}\mathbf{C}_e\mathbf{M}\mathbf{C}_e\mathbf{B}_e\mathbf{u}_e \tag{C.45}$$

$$\frac{\partial w}{\partial \bar{\boldsymbol{\rho}}} = 2\ \mathbf{B}_e^{\mathrm{T}}\mathbf{C}_e\mathbf{M}\frac{\partial \mathbf{C}_e}{\partial \bar{\boldsymbol{\rho}}}\mathbf{B}_e\mathbf{u}_e \tag{C.46}$$

$$\frac{\partial w}{\partial \mathbf{u}} = \mathbf{B}_e^{\mathrm{T}}\mathbf{C}_e\mathbf{M}\mathbf{C}_e\mathbf{B}_e \tag{C.47}$$

C.2.6 Nodal Displacements

All second-order derivatives and the derivative with respect to $\boldsymbol{\alpha}$ are zero for the nodal displacement u_k. Non-zero derivatives are given in Appendix A.2.6 for the deterministic case.

C.2.7 Stiffness Interpolation

The interpolated stiffness from Equation (2.15), may depend on random variables E_0 or η_e. Note, E_0 is now defined for each element e and thus denoted as $E_{0,e}$. Hence, the following partial derivatives are necessary:

$$\frac{\partial E_e}{\partial E_{0,e}} = \xi_e \tag{C.48}$$

$$\frac{\partial^2 E_e}{\partial E_{0,e} \partial \bar{\rho}_e} = \frac{\partial \xi_e}{\partial \bar{\rho}_e} \tag{C.49}$$

$$\frac{\partial E_e}{\partial \eta_e} = \frac{\partial \xi_e}{\partial \bar{\rho}_e} \frac{\partial \bar{\rho}_e}{\partial \eta_e} (E_0 - E_{min}) \tag{C.50}$$

$$\frac{\partial^2 E_e}{\partial \eta_e \partial \bar{\rho}_e} = \left(\frac{\partial \xi_e}{\partial^2 \bar{\rho}_e} \frac{\partial \bar{\rho}_e}{\partial \eta_e} + \frac{\partial \xi_e}{\partial \bar{\rho}_e} \frac{\partial^2 \bar{\rho}_e}{\partial \eta_e \partial \tilde{\rho}_e} \frac{\partial \tilde{\rho}_e}{\partial \bar{\rho}_e} \right) (E_0 - E_{min}) \tag{C.51}$$

$$\frac{\partial^2 E_e}{\partial^2 \bar{\rho}_e} = \frac{\partial^2 \xi_e}{\partial^2 \bar{\rho}_e} \frac{\partial \bar{\rho}_e}{\partial \eta_e} (E_0 - E_{min}) \tag{C.52}$$

Determination of the second-order derivative (C.51) is non-trivial and thus explained in more detail. It cannot directly be determined by differentiating $^{\partial E_e}/_{\partial \eta_e}$ with respect to $\bar{\rho}_e$, since projected variables are just a simple substitution in terms of differentiation. Thus, E_e is differentiated with respect to filtered variables $\tilde{\rho}_e$ and rewritten as follows:

$$\begin{aligned}
\frac{\partial^2 E_e}{\partial \eta_e \partial \tilde{\rho}_e} &= \frac{\partial^2 \xi_e}{\partial^2 \bar{\rho}_e} \frac{\partial \bar{\rho}_e}{\partial \eta_e} \frac{\partial \bar{\rho}_e}{\partial \tilde{\rho}_e} + \frac{\partial \xi_e}{\partial \bar{\rho}_e} \frac{\partial^2 \bar{\rho}_e}{\partial \eta_e \partial \tilde{\rho}_e} \\
&= \left[\frac{\partial^2 \xi_e}{\partial^2 \bar{\rho}_e} \frac{\partial \bar{\rho}_e}{\partial \eta_e} + \frac{\partial \xi_e}{\partial \bar{\rho}_e} \frac{\partial^2 \bar{\rho}_e}{\partial \eta_e \partial \tilde{\rho}_e} \frac{\partial \tilde{\rho}_e}{\partial \bar{\rho}_e} \right] \frac{\partial \bar{\rho}_e}{\partial \tilde{\rho}_e} \\
&= \frac{\partial^2 \xi_e}{\partial \eta_e \partial \bar{\rho}_e} \frac{\partial \bar{\rho}_e}{\partial \tilde{\rho}_e}
\end{aligned} \tag{C.53}$$

In line two of the above equation, the partial derivative $\frac{\partial \bar{\rho}_e}{\partial \tilde{\rho}_e}$ is drawn out of the brackets, causing the inverse $\frac{\partial \tilde{\rho}_e}{\partial \bar{\rho}_e}$ for the second term to occur.

For the SIMP in Equation (2.16) and RAMP in Equation (2.18) interpolation functions second-order derivatives with respect to projected variables are:

$$\frac{\partial^2 \xi_e^{SIMP}}{\partial^2 \bar{\rho}_e} = (p^{SIMP^2} - p^{SIMP})\bar{\rho}_e^{p^{SIMP}-2} \tag{C.54}$$

$$\frac{\partial^2 \xi_e^{RAMP}}{\partial^2 \bar{\rho}_e} = -\frac{2p^{RAMP}(1+p^{RAMP})}{\left(1+p^{RAMP}\left(1-\bar{\rho}_e\right)\right)^3} \tag{C.55}$$

C.2.8 Projection Functions

In case the projection threshold η_e from Equation (2.14) is considered as random variable, following additional partial derivatives are needed.

$$\begin{aligned}\frac{\partial \bar{\rho}_e}{\partial \eta_e} = &\frac{\beta \operatorname{sech}^2(\beta\eta_e) - \beta \operatorname{sech}^2(\beta(\tilde{\rho}_e - \eta_e))}{\tanh(\beta\eta_e) + \tanh(\beta(1-\eta_e))} \\ &- \frac{(\beta \operatorname{sech}^2(\beta\eta_e) - \beta \operatorname{sech}^2(\beta(1-\eta_e)))(\tanh(\beta\eta_e) + \tanh(\beta(\tilde{\rho}_e - \eta_e)))}{(\tanh(\beta\eta_e) + \tanh(\beta(1-\eta_e)))^2}\end{aligned} \tag{C.56}$$

$$\begin{aligned}\frac{\partial^2 \bar{\rho}_e}{\partial \eta_e \partial \tilde{\rho}_e} = &\frac{2\beta^2 \operatorname{sech}^2(\beta(\tilde{\rho}_e - \eta_e)) \tanh(\beta(\tilde{\rho}_e - \eta_e))}{\tanh(\beta\eta_e) + \tanh(\beta(1-\eta_e))} \\ &- \frac{\beta(\beta \operatorname{sech}^2(\beta\eta_e) - \beta \operatorname{sech}^2(\beta(1-\eta_e))) \operatorname{sech}^2(\beta(\tilde{\rho}_e - \eta_e))}{(\tanh(\beta\eta_e) + \tanh(\beta(1-\eta_e)))^2}\end{aligned} \tag{C.57}$$

C.3 Random Fields

In this section, details and implementation aspects are described for the generation of discrete random fields. As depicted in Figure 5.1 and outlined in Section 5.3 random variables are going through a process of correlation and transformation. With this method, generally any possible probability distribution can be applied and discretized as a correlated random field. In the following, the briefly mentioned process shall be explained in more detail.

Discrete and uncorrelated standard normal distributed random variables $\boldsymbol{\alpha}_N^* = [\alpha_{1,N}^*, \ldots, \alpha_{i,N}^*]$ can easily be generated with corresponding generators available in a wide variety of applications. The first major step is thereafter to correlate the obtained variables. In image processing and statistics, the opposite is often requested, for which the so-called Mahalanobis transformation can be applied [164]:

$$\boldsymbol{\alpha}^* = \boldsymbol{\Sigma}^{-1/2}(\boldsymbol{\alpha} - \mu_\alpha), \tag{C.58}$$

where $\boldsymbol{\alpha}$ is a vector of correlated variables, μ_α is its corresponding mean, $\boldsymbol{\Sigma}^{-1/2}$ is the square root of the covariance matrix $\boldsymbol{\Sigma}$ from Equation (5.18) and $\boldsymbol{\alpha}^*$ are uncorrelated random variables. For convenience, standard normal distribution variables are considered in this first step, resulting in $\boldsymbol{\alpha}^* = \boldsymbol{\alpha}_N^*$. Hence, the mean value is $\mu_\alpha = 0$ and the standard deviation is $\sigma_\alpha = 1$. For a transformation to correlated random parameters, Equation (C.58) can be reversed and simplified to

$$\boldsymbol{\alpha}_N = \boldsymbol{\Sigma}^{1/2} \boldsymbol{\alpha}_N^*. \tag{C.59}$$

For Equation (C.59) the square root of the covariance matrix $\boldsymbol{\Sigma}$ is determined as follows. First, $\boldsymbol{\Sigma}$ is decomposed into its eigenvalues λ_i and eigenvectors $\mathbf{v}_i$. Generally, any square $n \times n$ matrix $\mathbf{A}$ with linearly independent eigenvectors can be decomposed as

$$\mathbf{A} = \mathbf{V} \boldsymbol{\Lambda} \mathbf{V}^{-1} \tag{C.60}$$

where $\mathbf{V}$ is a square $n \times n$ matrix whose ith column is the eigenvector $\mathbf{v}_i$ and $\boldsymbol{\Lambda} = \mathrm{diag}(\lambda_1, \ldots, \lambda_n)$ is a diagonal matrix with eigenvalues of $\mathbf{A}$. For a symmetric and positive definite matrix, the decomposition can be written as follows:

$$\mathbf{A} = \mathbf{V} \boldsymbol{\Lambda} \mathbf{V}^{\mathrm{T}} = \mathbf{L} \mathbf{L}^{\mathrm{T}}. \tag{C.61}$$

Defining matrix $\mathbf{L}$ to be

$$\mathbf{L} = \mathbf{V} \boldsymbol{\Lambda}^{1/2} \tag{C.62}$$

where $\boldsymbol{\Lambda}^{1/2} = \mathrm{diag}(\sqrt{\lambda_1}, \ldots, \sqrt{\lambda_i})$ is a diagonal matrix containing the square root of each eigenvalue. Consequently, the following can be stated

$$\mathbf{L} \mathbf{L}^{\mathrm{T}} = \mathbf{V} \boldsymbol{\Lambda}^{1/2} \left(\mathbf{V} \boldsymbol{\Lambda}^{1/2} \right)^{\mathrm{T}} = \mathbf{V} \boldsymbol{\Lambda}^{1/2} \boldsymbol{\Lambda}^{1/2} \mathbf{V}^{\mathrm{T}} = \mathbf{V} \boldsymbol{\Lambda} \mathbf{V}^{\mathrm{T}} = \mathbf{A}. \tag{C.63}$$

Hence, $\mathbf{L}$ is the square root of $\mathbf{A}$ resulting in

$$\mathbf{A}^{1/2} = \mathbf{V} \boldsymbol{\Lambda}^{1/2} = \boldsymbol{\Sigma}^{1/2}, \tag{C.64}$$

which can directly be applied to Equation (C.59).

The eigenvalue decomposition is related to the principal component analysis (PCA), since it can be shown that principal components are eigenvectors of the covariance matrix. This is useful, since the PCA states, that not all principal components need to be kept. Hence, the amount of random variables can be reduced by truncating the sorted eigenvalues after k terms. Stefanou [165] recommends a minimum of $k \geq 128$ eigenvalues. In this work, k is selected with respect to the error on the diagonal, i.e. the variance error, which is determined as follows

$$\max \left(\frac{|\, \mathrm{diag}(\boldsymbol{\Sigma}) - \mathrm{diag}(\mathbf{V}_r \boldsymbol{\Lambda}_r \mathbf{V}_r^{\mathrm{T}})|}{\mathrm{diag}(\boldsymbol{\Sigma})} \right) < 0.1\% \tag{C.65}$$

where $\mathbf{V}_r$ and $\boldsymbol{\Lambda}_r$ are the reduced sets of eigenvectors and eigenvalues, respectively.

To further increase the efficiency of the random process, the expansion optimal linear estimation method (EOLE) can be employed. This might be necessary in bigger models for which a decomposition becomes prohibitive costly to calculate in terms of memory requirement and computation time. The principal concept of EOLE is to perform the costly eigenvalue decomposition on a much coarser grid and linearly interpolate on the targeted finer grid. However, this was not necessary for the considered examples and is thus not employed within this work. The interested reader is referred to Sudret et al. [142] for more details.

The final step to obtain a discrete random field is to transform the correlated variables to any desired distribution type. To achieve that, the so-called Rosenblatt transformation is employed [166]. The basic idea is to utilize the property of any cumulative distribution function F. Random variables are projected onto the normalized space and back again with different F. In the particular case of normal distributed data, the transformation is formulated as

$$\boldsymbol{\alpha} = F^{-1}(\Phi(\boldsymbol{\alpha}_N)) \tag{C.66}$$

where Φ is the CDF for a standard normal distribution and F can be any invertible CDF.

C.4 Supplementary Figures and Tables

Within this section supplementary figures and tables are listed.

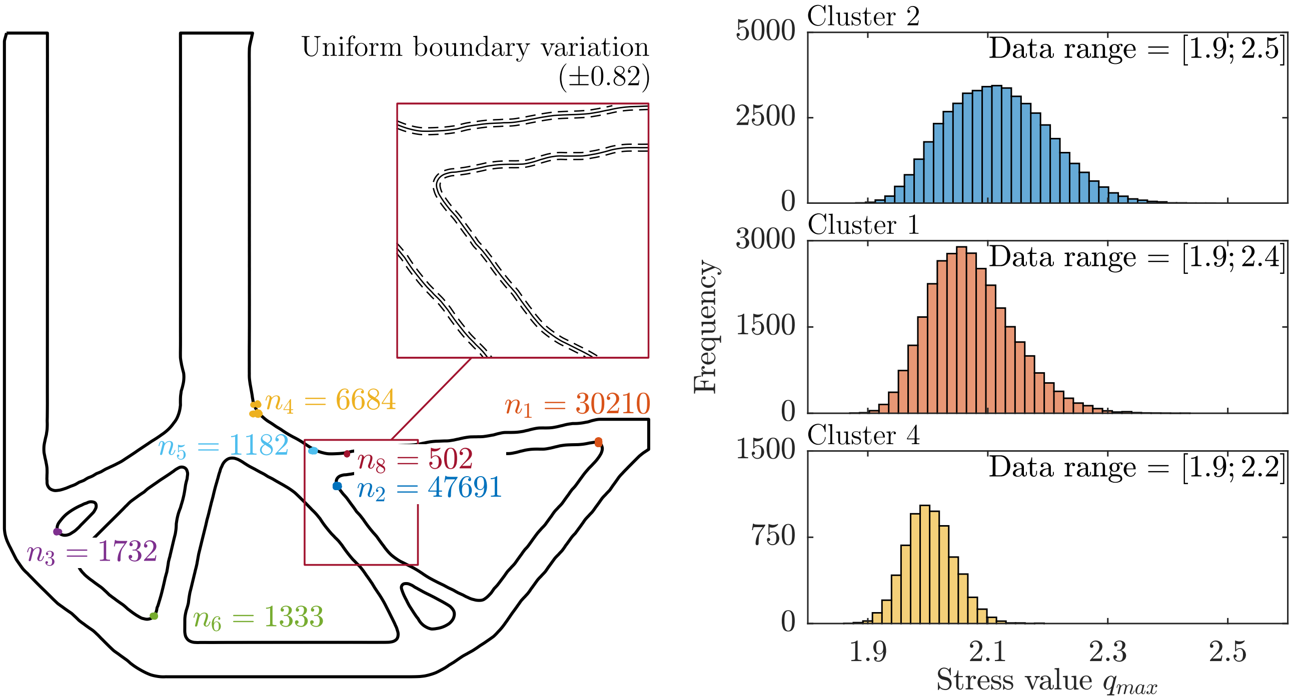

Figure C.1: Worst-case stress positions and corresponding histograms based on direct contour line perturbations of the FOSM optimized L-beam.

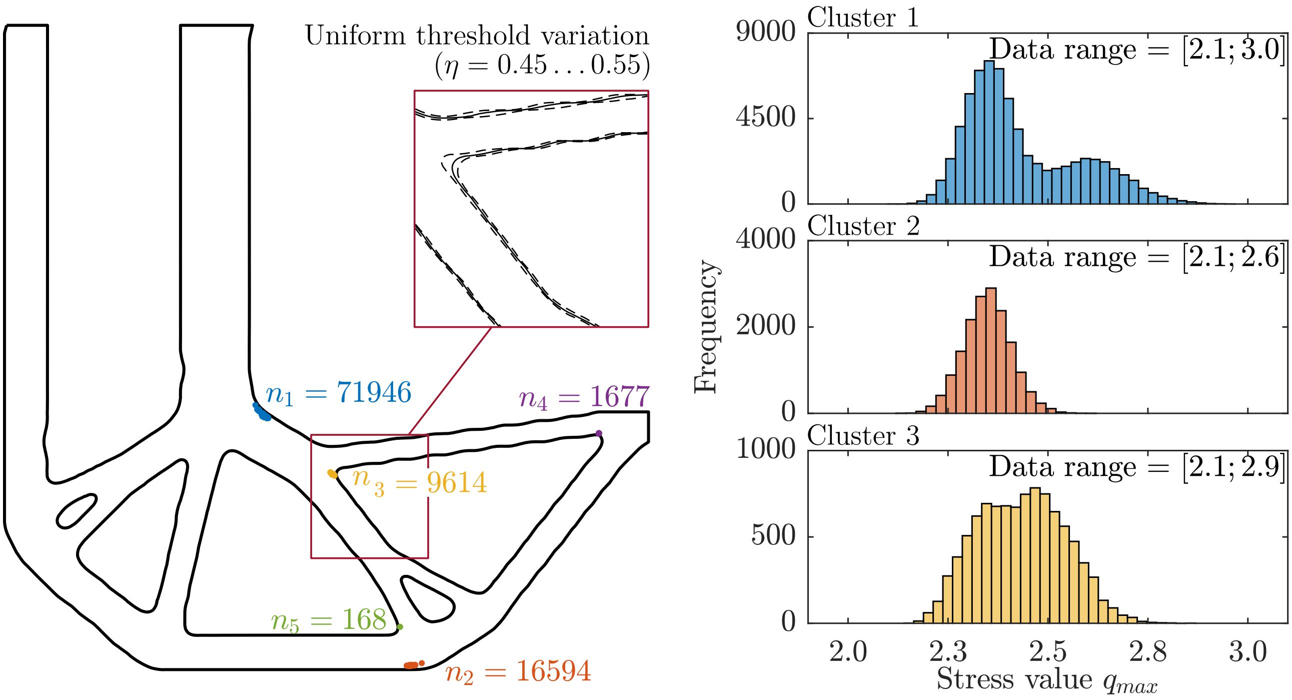

(a) Contour variations based on the filtered density field.

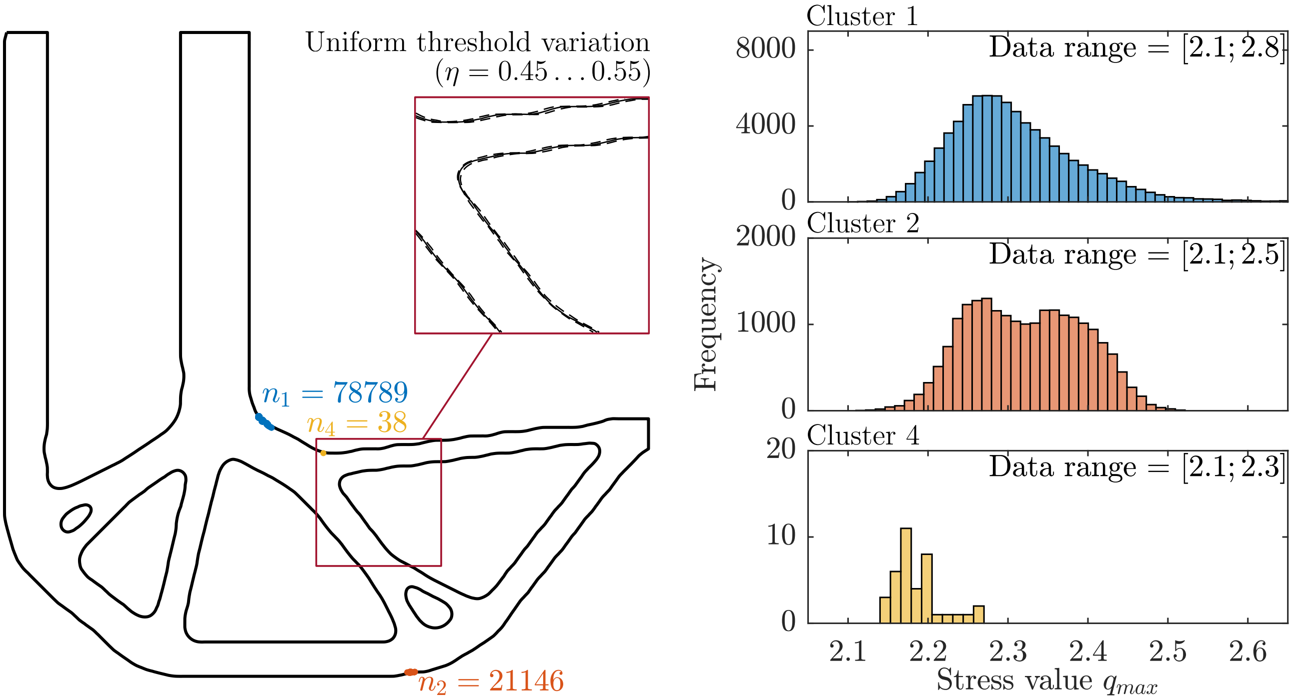

(b) Contour variations based on the regularized density field.

Figure C.2: Worst-case stress positions and corresponding histograms based on threshold perturbations of the FOSM optimized L-beam.

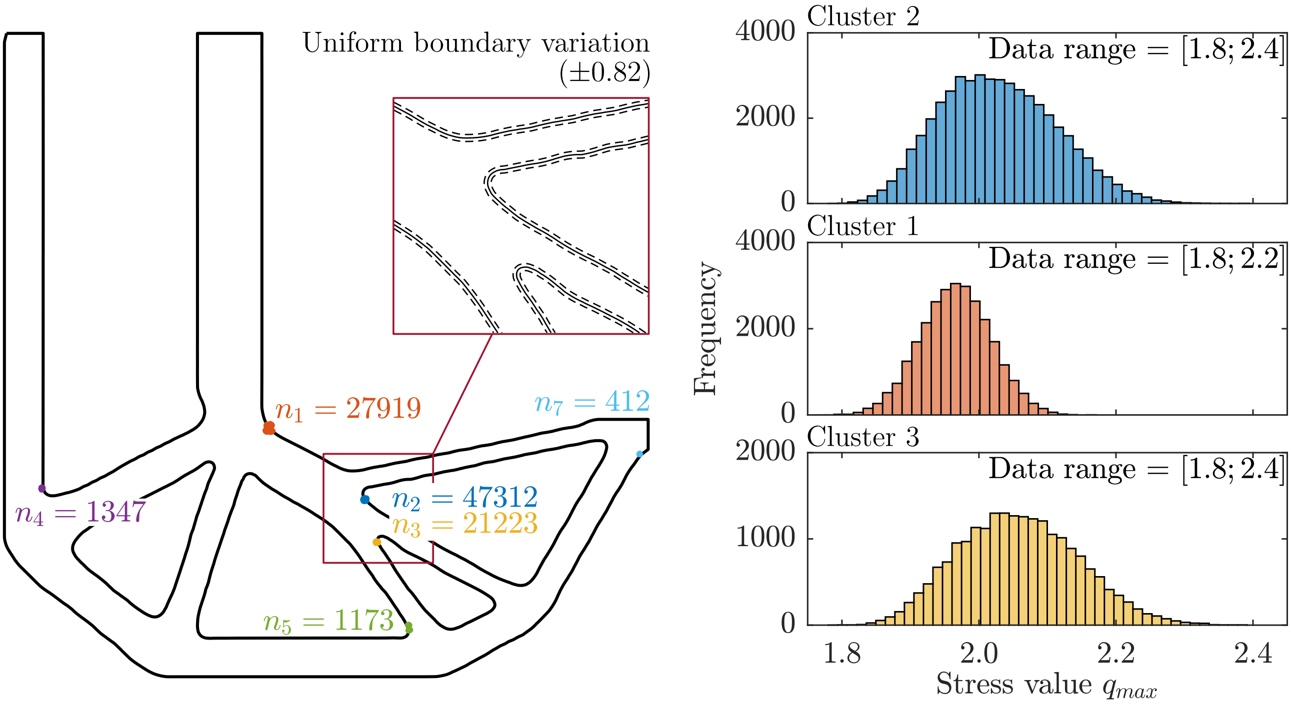

Figure C.3: Worst-case stress positions and corresponding histograms based on direct contour line perturbations of the MCS optimized L-beam.

Table C.1: Numerical data for the study on adapted weighting factor with uncertain material strength. Deterministic results optimized with reduced material strength for different aggregation parameters. Post-processing is performed for the voxel model.

Optimization			Voxel post-processing ($n = 10^5$)			
p_{PN}	f, φ_V	n_{opt}	q_{max}	μ_{SF}	σ_{SF}	$Q_{0.9987}$
10	0.323	1	2.10	0.724	0.065	1.00
10	0.324	1	2.10	0.724	0.065	1.01
12	0.303	1	2.10	0.732	0.063	1.01
14	0.283	1	2.10	0.753	0.061	1.02
15	0.282	1	2.10	0.759	0.059	1.02
16	0.279	1	2.10	0.770	0.059	1.02
18	0.272	1	2.10	0.784	0.059	1.05
20	0.267	1	2.10	0.788	0.059	1.05
22	0.265	1	2.09	0.794	0.059	1.06
24	0.268	1	2.10	0.817	0.060	1.09
25	0.281	1	2.10	0.806	0.060	1.07
26	0.270	1	2.10	0.806	0.059	1.07
28	0.275	1	2.12	0.841	0.061	1.11
30	0.271	1	2.10	0.842	0.061	1.12

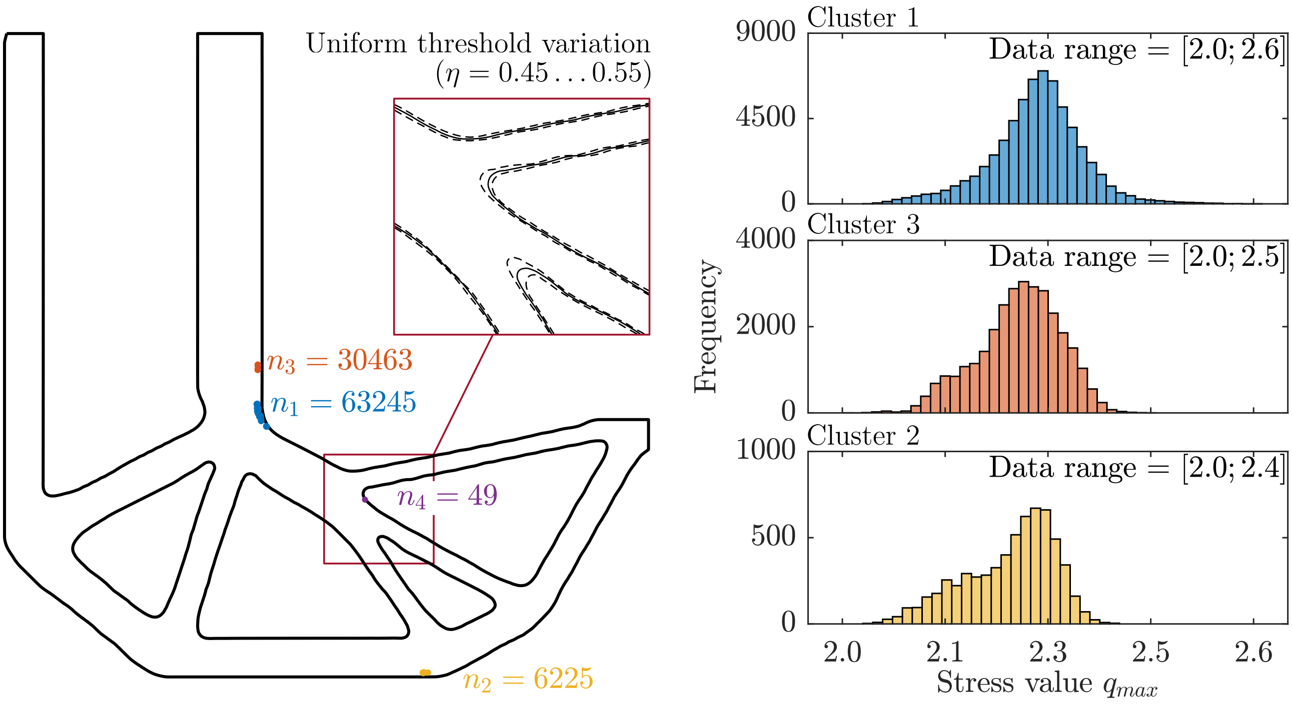

(a) Contour variations based on the filtered density field.

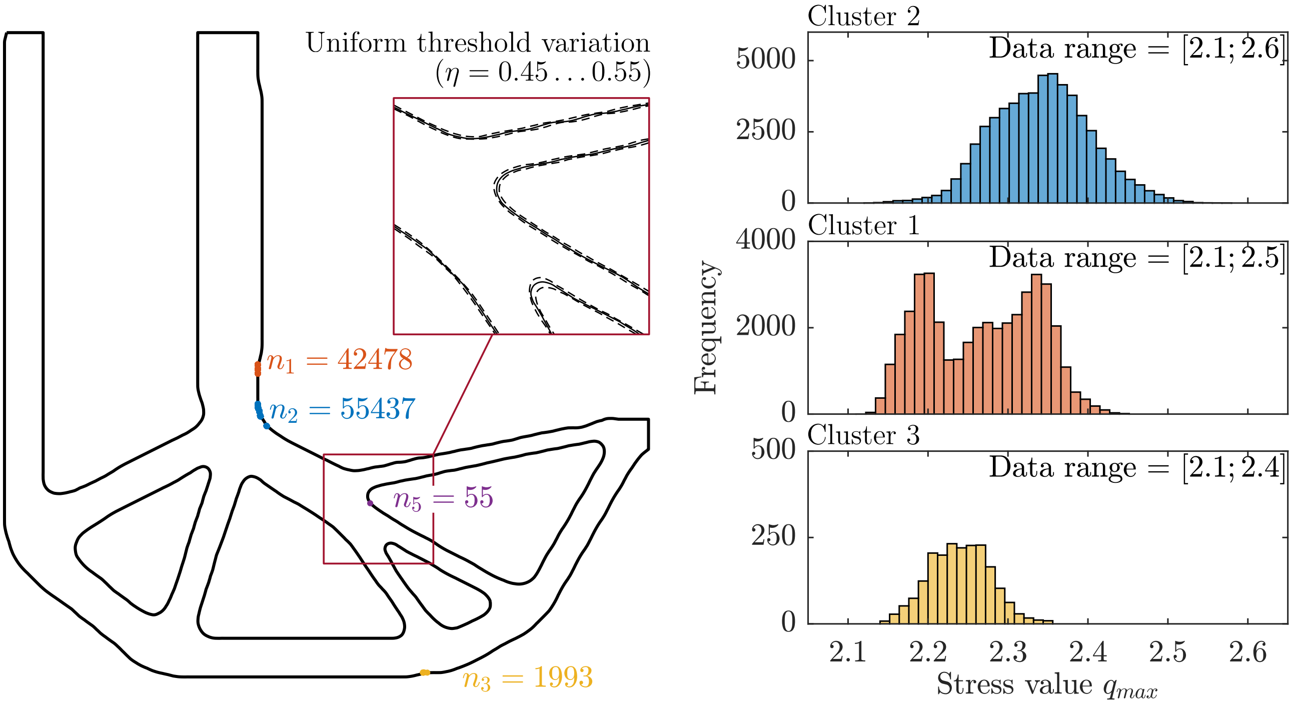

(b) Contour variations based on the regularized density field.

Figure C.4: Worst-case stress positions and corresponding histograms based on threshold perturbations of the MCS optimized L-beam.

Table C.2: Numerical data for study on adapted weighting factor with uncertain material strength. MCS results optimized for different aggregation parameters, varying sample size n_{opt} and adapted weighting factor. Post-processing is performed for the voxel model.

Optimization					Voxel post-processing ($n = 10^5$)			
p_{PN}	n_{opt}	f, φ_V	c, μ_{SF}	c, σ_{SF}	q_{max}	μ_{SF}	σ_{SF}	$Q_{0.9987}$
10	1000	0.278	0.762	0.056	2.13	0.763	0.060	1.03
10	1000	0.265	0.787	0.058	2.19	0.791	0.061	1.07
10	1000	0.290	0.742	0.057	2.08	0.747	0.059	1.00
10	1000	0.263	0.795	0.058	2.20	0.797	0.062	1.07
10	2000	0.278	0.764	0.057	2.12	0.766	0.059	1.03
10	5000	0.290	0.742	0.057	2.07	0.743	0.058	1.00
10	5000	0.285	0.753	0.057	2.06	0.752	0.058	1.01
10	5000	0.290	0.737	0.057	2.06	0.739	0.057	0.99
10	5000	0.292	0.739	0.057	2.05	0.740	0.057	1.00
10	5000	0.297	0.732	0.056	2.01	0.731	0.057	0.98
10	8000	0.282	0.755	0.057	2.09	0.756	0.058	1.01
10	10000	0.288	0.734	0.058	2.05	0.737	0.057	0.99
10	10000	0.281	0.750	0.057	2.06	0.749	0.058	1.00
10	10000	0.290	0.740	0.057	2.05	0.740	0.057	0.99
10	10000	0.294	0.736	0.057	2.04	0.737	0.057	0.99
20	1000	0.276	0.790	0.054	2.06	0.791	0.058	1.05
20	1000	0.264	0.804	0.055	2.05	0.806	0.059	1.07
20	1000	0.283	0.787	0.053	2.01	0.787	0.057	1.04
20	1000	0.259	0.801	0.054	2.09	0.804	0.059	1.07
20	1000	0.273	0.772	0.054	1.99	0.773	0.056	1.03
20	1000	0.275	0.790	0.055	2.04	0.789	0.058	1.05
20	1000	0.298	0.734	0.053	1.88	0.734	0.053	0.97

References

[1] Martin Philip Bendsøe and Ole Sigmund. *Topology Optimization Theory, Methods, and Applications*. 2nd ed. Springer-Verlag Berlin Heidelberg, 2004. ISBN: 978-3-642-07698-5.

[2] Jikai Liu, Andrew T. Gaynor, Shikui Chen, Zhan Kang, Krishnan Suresh, Akihiro Takezawa, Lei Li, Junji Kato, Jinyuan Tang, Charlie C. L. Wang, Lin Cheng, Xuan Liang, and Albert. C. To. “Current and future trends in topology optimization for additive manufacturing”. In: *Struct Multidisc Optim* 57.6 (2018), pp. 2457–2483. DOI: `10.1007/s00158-018-1994-3`.

[3] G. A. da Silva, A. T. Beck, and E. L. Cardoso. “Topology optimization of continuum structures with stress constraints and uncertainties in loading”. In: *International Journal for Numerical Methods in Engineering* 113.1 (2018), pp. 153–178. DOI: `10.1002/nme.5607`.

[4] Benedikt Kriegesmann and Julian K. Lüdeker. “Robust compliance topology optimization using the first-order second-moment method”. In: *Struct Multidisc Optim* 60.1 (2019), pp. 269–286. DOI: `10.1007/s00158-019-02216-8`.

[5] Zhan Kang. “Robust design optimization of structures under uncertainties”. doctoralThesis. 2005. DOI: `10.18419/opus-3701`.

[6] Gustavo Assis da Silva, Eduardo Lenz Cardoso, and André Teófilo Beck. “Comparison of robust, reliability-based and non-probabilistic topology optimization under uncertain loads and stress constraints”. In: *Probabilistic Engineering Mechanics* 59 (2020), p. 103039. DOI: `10.1016/j.probengmech.2020.103039`.

[7] Genichi Taguchi. *Introduction to Quality Engineering: Designing Quality into Products and Processes*. Asian Productivity Organization, 1986. ISBN: 978-92-833-1084-6.

[8] Gyung-Jin Park, Tae-Hee Lee, Kwon Hee Lee, and Kwang-Hyeon Hwang. “Robust Design: An Overview”. In: *AIAA Journal* 44.1 (2006), pp. 181–191. DOI: `10.2514/1.13639`.

[9] Hans-Georg Beyer and Bernhard Sendhoff. "Robust optimization – A comprehensive survey". In: *Computer Methods in Applied Mechanics and Engineering* 196.33 (2007), pp. 3190–3218. DOI: `10.1016/j.cma.2007.03.003`.

[10] G. I. Schuëller and H. A. Jensen. "Computational methods in optimization considering uncertainties – An overview". In: *Computer Methods in Applied Mechanics and Engineering* 198.1 (2008), pp. 2–13. DOI: `10.1016/j.cma.2008.05.004`.

[11] Yoshihiro Kanno. "On three concepts in robust design optimization: absolute robustness, relative robustness, and less variance". In: *Struct Multidisc Optim* 62.2 (2020), pp. 979–1000. DOI: `10.1007/s00158-020-02503-9`.

[12] M. P. Bendsøe. "Optimal shape design as a material distribution problem". In: *Structural Optimization* 1.4 (1989), pp. 193–202. DOI: `10.1007/BF01650949`.

[13] Ole Sigmund. "On the usefulness of non-gradient approaches in topology optimization". In: *Struct Multidisc Optim* 43.5 (2011), pp. 589–596. DOI: `10.1007/s00158-011-0638-7`.

[14] Tyler E. Bruns and Daniel A. Tortorelli. "Topology optimization of nonlinear elastic structures and compliant mechanisms". In: *Computer Methods in Applied Mechanics and Engineering* 190.26 (2001), pp. 3443–3459. DOI: `10.1016/S0045-7825(00)00278-4`.

[15] Blaise Bourdin. "Filters in topology optimization". In: *International Journal for Numerical Methods in Engineering* 50.9 (2001), pp. 2143–2158. DOI: `10.1002/nme.116`.

[16] Shengli Xu, Yuanwu Cai, and Gengdong Cheng. "Volume preserving nonlinear density filter based on heaviside functions". In: *Struct Multidisc Optim* 41.4 (2010), pp. 495–505. DOI: `10.1007/s00158-009-0452-7`.

[17] Ole Sigmund and Kurt Maute. "Topology optimization approaches: A comparative review". In: *Struct Multidisc Optim* 48.6 (2013), pp. 1031–1055. DOI: `10.1007/s00158-013-0978-6`.

[18] G. Sved and Z. Ginos. "Structural optimization under multiple loading". In: *International Journal of Mechanical Sciences* 10.10 (1968), pp. 803–805. DOI: `10.1016/0020-7403(68)90021-0`.

[19] U. Kirsch. "On singular topologies in optimum structural design". In: *Structural Optimization* 2.3 (1990), pp. 133–142. DOI: `10.1007/BF01836562`.

[20] Gengdong Cheng and Zheng Jiang. "Study on topology optimization with stress constraints". In: *Engineering Optimization* 20.2 (1992), pp. 129–148. DOI: `10.1080/03052159208941276`.

[21] Alexander Verbart, Matthijs Langelaar, and Fred van Keulen. "Damage approach: A new method for topology optimization with local stress constraints". In: *Struct Multidisc Optim* 53.5 (2016), pp. 1081–1098. DOI: `10.1007/s00158-015-1318-9`.

[22] Fernando V. Senhora, Oliver Giraldo-Londoño, Ivan F. M. Menezes, and Glaucio H. Paulino. "Topology optimization with local stress constraints: a stress aggregation-free approach". In: *Struct Multidisc Optim* 62.4 (2020), pp. 1639–1668. DOI: `10.1007/s00158-020-02573-9`.

[23] G.D. Cheng and X. Guo. "e-relaxed approach in structural topology optimization". In: *Structural Optimization* 13 (1997), pp. 258–266. DOI: `10.1007/BF01197454`.

[24] Pierre Duysinx and Ole Sigmund. "New developments in handling stress constraints in optimal material distribution". In: *American Institute of Aeronautics and Astronautics* Paper 98-4906 (1998), p. 10. DOI: `10.2514/6.1998-4906`.

[25] Matteo Bruggi. "On an alternative approach to stress constraints relaxation in topology optimization". In: *Struct Multidisc Optim* 36.2 (2008), pp. 125–141. DOI: `10.1007/s00158-007-0203-6`.

[26] M. Stolpe and K. Svanberg. "An alternative interpolation scheme for minimum compliance topology optimization". In: *Struct Multidisc Optim* 22.2 (2001), pp. 116–124. DOI: `10.1007/s001580100129`.

[27] A. Rietz. "Sufficiency of a finite exponent in SIMP (power law) methods". In: *Struct Multidisc Optim* 21.2 (2001), pp. 159–163. DOI: `10.1007/s001580050180`.

[28] A. J. Torii, J. R. de Faria, and A. A. Novotny. "Aggregation and regularization schemes: a probabilistic point of view". In: *Struct Multidisc Optim* 65.3 (2022), p. 76. DOI: `10.1007/s00158-022-03179-z`.

[29] Olaf Ambrozkiewicz. "Structural optimization of components and joints in assemblies considering fail-safety". PhD thesis. 2022. DOI: `doi.org/10.15480/882.4618`.

[30] Gustavo Assis da Silva, Niels Aage, André Teófilo Beck, and Ole Sigmund. "Local versus global stress constraint strategies in topology optimization: A comparative study". In: *International Journal for Numerical Methods in Engineering* 122.21 (2021), pp. 6003–6036. DOI: `10.1002/nme.6781`.

[31] Eduardo Fernández, Maxime Collet, Pablo Alarcón, Simon Bauduin, and Pierre Duysinx. "An aggregation strategy of maximum size constraints in density-based topology optimization". In: *Struct Multidisc Optim* 60.5 (2019), pp. 2113–2130. DOI: `10.1007/s00158-019-02313-8`.

[32] Alexander Verbart, Matthijs Langelaar, and Fred van Keulen. “A unified aggregation and relaxation approach for stress-constrained topology optimization”. In: *Struct Multidisc Optim* 55.2 (2017), pp. 663–679. DOI: `10.1007/s00158-016-1524-0`.

[33] Erik Holmberg, Bo Torstenfelt, and Anders Klarbring. “Stress constrained topology optimization”. In: *Struct Multidisc Optim* 48 (2013), pp. 33–47. DOI: `10.1007/s00158-012-0880-7`.

[34] Chau Le, Julian Norato, Tyler Bruns, Christopher Ha, and Daniel Tortorelli. “Stress-based topology optimization for continua”. In: *Struct Multidisc Optim* 41.4 (2009), pp. 605–620. DOI: `10.1007/s00158-009-0440-y`.

[35] J. París, F. Navarrina, I. Colominas, and M. Casteleiro. “Topology optimization of continuum structures with local and global stress constraints”. In: *Struct Multidisc Optim* 39 (2009), pp. 419–437. DOI: `10.1007/s00158-008-0336-2`.

[36] J. París, F. Navarrina, I. Colominas, and M. Casteleiro. “Block aggregation of stress constraints in topology optimization of structures”. In: *Advances in Engineering Software* 41 (2010), pp. 433–441. DOI: `10.1016/j.advengsoft.2009.03.006`.

[37] Panagiotis Michaleris, Daniel A. Tortorelli, and Creto A. Vidal. “Tangent operators and design sensitivity formulations for transient non-linear coupled problems with applications to elastoplasticity”. In: *Int. J. Numer. Meth. Engng.* 37.14 (1994), pp. 2471–2499. DOI: `10.1002/nme.1620371408`.

[38] F. van Keulen, R.T. Haftka, and N.H. Kim. “Review of options for structural design sensitivity analysis. Part 1: Linear systems”. In: *Computer Methods in Applied Mechanics and Engineering* 194.30-33 (2005), pp. 3213–3243. DOI: `10.1016/j.cma.2005.02.002`.

[39] Eduardo Fancello and Jucelio Pereira. “Structural topology optimization considering material failure constraints and multiple load conditions”. In: *Latin American Journal of Solids and Structures* 1 (2003).

[40] J.T. Pereira, E.A. Fancello, and C.S. Barcellos. “Topology optimization of continuum structures with material failure constraints”. In: *Struct Multidisc Optim* 26.1 (2004), pp. 50–66. DOI: `10.1007/s00158-003-0301-z`.

[41] E. A. Fancello. “Topology optimization for minimum mass design considering local failure constraints and contact boundary conditions”. In: *Struct Multidisc Optim* 32.3 (2006), pp. 229–240. DOI: `10.1007/s00158-006-0019-9`.

[42] G. A. da Silva and E. L. Cardoso. “Stress-based topology optimization of continuum structures under uncertainties”. In: *Computer Methods in Applied Mechanics and Engineering* 313 (2017), pp. 647–672. DOI: `10.1016/j.cma.2016.09.049`.

[43] Gustavo Assis da Silva, André Teófilo Beck, and Ole Sigmund. “Topology optimization of compliant mechanisms with stress constraints and manufacturing error robustness”. In: *Computer Methods in Applied Mechanics and Engineering* 354 (2019), pp. 397–421. DOI: `10.1016/j.cma.2019.05.046`.

[44] Gustavo Assis da Silva, André Teófilo Beck, and Ole Sigmund. “Topology optimization of compliant mechanisms considering stress constraints, manufacturing uncertainty and geometric nonlinearity”. In: *Computer Methods in Applied Mechanics and Engineering* 365 (2020), p. 112972. DOI: `10.1016/j.cma.2020.112972`.

[45] Oliver Giraldo-Londoño and Glaucio H. Paulino. “A unified approach for topology optimization with local stress constraints considering various failure criteria: von Mises, Drucker–Prager, Tresca, Mohr–Coulomb, Bresler–Pister and Willam–Warnke”. In: *Proceedings of the Royal Society A: Mathematical, Physical and Engineering Sciences* 476.2238 (2020), p. 20190861. DOI: `10.1098/rspa.2019.0861`.

[46] Oliver Giraldo-Londoño and Glaucio H. Paulino. “PolyStress: a Matlab implementation for local stress-constrained topology optimization using the augmented Lagrangian method”. In: *Struct Multidisc Optim* 63.4 (2021), pp. 2065–2097. DOI: `10.1007/s00158-020-02760-8`.

[47] Xiaoya Zhai, Falai Chen, and Jun Wu. “Alternating optimization of design and stress for stress-constrained topology optimization”. In: *Struct Multidisc Optim* 64.4 (2021), pp. 2323–2342. DOI: `10.1007/s00158-021-02985-1`.

[48] Fernando V. Senhora, Ivan F. M. Menezes, and Glaucio H. Paulino. “Topology optimization with local stress constraints and continuously varying load direction and magnitude: towards practical applications”. In: *Proceedings of the Royal Society A: Mathematical, Physical and Engineering Sciences* 479.2271 (2023). DOI: `10.1098/rspa.2022.0436`.

[49] Gustavo Assis da Silva, Niels Aage, André Teófilo Beck, and Ole Sigmund. “Three-dimensional manufacturing tolerant topology optimization with hundreds of millions of local stress constraints”. In: *International Journal for Numerical Methods in Engineering* 122.2 (2021), pp. 548–578. DOI: `10.1002/nme.6548`.

[50] Oliver Giraldo-Londoño, Jonathan B. Russ, Miguel A. Aguiló, and Glaucio H. Paulino. “Limiting the first principal stress in topology optimization: a local and consistent approach”. In: *Struct Multidisc Optim* 65.9 (2022), p. 254. DOI: `10.1007/s00158-022-03320-y`.

[51] Alexandre de Assis Pereira and Eduardo Lenz Cardoso. “On the influence of local and global stress constraint and filtering radius on the design of hinge-free compliant mechanisms”. In: *Struct Multidisc Optim* 58.2 (2018), pp. 641–655. DOI: `10.1007/s00158-018-1915-5`.

[52] Gustavo Assis da Silva, André Teófilo Beck, and Ole Sigmund. “Stress-constrained topology optimization considering uniform manufacturing uncertainties”. In: *Computer Methods in Applied Mechanics and Engineering* 344 (2019), pp. 512–537. DOI: `10.1016/j.cma.2018.10.020`.

[53] EASA. *Certification specifications and acceptable means of Ccompliance for large aeroplanes (CS-25)*. Vol. Amendment 27. European Union Aviation Safety Agency, 2021, pp. 265–268.

[54] MCY Niu. *Airframe structural design*. Conmilit Press Ltd., 1988. ISBN: 962-7128-04-X.

[55] Daniel F. O. Braga, S. M. O. Tavares, Lucas F. M. da Silva, P. M. G. P. Moreira, and Paulo M. S. T. de Castro. “Advanced design for lightweight structures: Review and prospects”. In: *Progress in Aerospace Sciences* 69 (2014), pp. 29–39. DOI: `10.1016/j.paerosci.2014.03.003`.

[56] P. F. Sun, J. S. Arora, and E. J. Haug Jr. “Fail-Safe Optimal Design of Structures”. In: *Engineering Optimization* 2.1 (1976), pp. 43–53. DOI: `10.1080/03052157608960596`.

[57] Jasbir S. Arora, Donald F. Haskell, and Ashok K. Govil. “Optimal design of large structures for damage tolerance”. In: *AIAA Journal* 18.5 (1980), pp. 563–570. DOI: `10.2514/3.7669`.

[58] Yuansheng (Y. S. Feng) Feng and Fred Moses. “Optimum design, redundancy and reliability of structural systems”. In: *Computers & Structures* 24.2 (1986), pp. 239–251. DOI: `10.1016/0045-7949(86)90283-X`.

[59] D. T. Nguyen and J. S. Arora. “Fail-Safe Optimal Design of Complex Structures With Substructures”. In: *J. Mech. Des* 104.4 (1982), pp. 861–868. DOI: `10.1115/1.3256449`.

[60] Kun S. Marhadi, Satchi Venkataraman, and Scott A. Wong. “Load redistribution mechanism in damage tolerant and redundant truss structure”. In: *Struct Multidisc Optim* 44.2 (2011), pp. 213–233. DOI: `10.1007/s00158-011-0623-1`.

[61] Daniel P. Mohr, Ina Stein, Thomas Matzies, and Christina A. Knapek. "Redundant robust topology optimization of truss". In: *Optim Eng* 15.4 (2014), pp. 945–972. DOI: `10.1007/s11081-013-9241-7`.

[62] Yoshihiro Kanno. "Redundancy Optimization of Finite-Dimensional Structures: A Concept and a Derivative-Free Algorithm". In: *J. Struct. Eng.* 143.1 (2017), p. 04016151. DOI: `10.1061/(ASCE)ST.1943-541X.0001630`.

[63] Julian Kajo Lüdeker and Benedikt Kriegesmann. "Fail-safe optimization of beam structures". In: *Journal of Computational Design and Engineering* 6.3 (2019), pp. 260–268. DOI: `10.1016/j.jcde.2019.01.004`.

[64] Mathias Stolpe. "Fail-safe truss topology optimization". In: *Struct Multidisc Optim* 60.4 (2019), pp. 1605–1618. DOI: `10.1007/s00158-019-02295-7`.

[65] Suguang Dou and Mathias Stolpe. "Fail-safe optimization of tubular frame structures under stress and eigenfrequency requirements". In: *Computers & Structures* 258 (2022), p. 106684. DOI: `10.1016/j.compstruc.2021.106684`.

[66] James Kirby, Shiwei Zhou, and Yi Min Xie. "Optimal fail-safe truss structures: new solutions and uncommon characteristics". In: *Acta Mech. Sin.* 38.6 (2022), p. 421564. DOI: `10.1007/s10409-022-09028-3`.

[67] Helen E. Fairclough, Linwei He, Tekle B. Asfaha, and Sam Rigby. "Adaptive topology optimization of fail-safe truss structures". In: *Struct Multidisc Optim* 66.7 (2023), p. 148. DOI: `10.1007/s00158-023-03585-x`.

[68] Miche Jansen, Geert Lombaert, Mattias Schevenels, and Ole Sigmund. "Topology optimization of fail-safe structures using a simplified local damage model". In: *Struct Multidisc Optim* 49.4 (2013), pp. 657–666. DOI: `10.1007/s00158-013-1001-y`.

[69] Ming Zhou and Raphael Fleury. "Fail-safe topology optimization". In: *Structural and Multidisciplinary Optimization* 54.5 (2016), pp. 1225–1243. DOI: `10.1007/s00158-016-1507-1`.

[70] Hongxin Wang, Jie Liu, Guilin Wen, and Yi Min Xie. "The robust fail-safe topological designs based on the von Mises stress". In: *Finite Elements in Analysis and Design* 171 (2020), p. 103376. DOI: `10.1016/j.finel.2019.103376`.

[71] Olaf Ambrozkiewicz and Benedikt Kriegesmann. "Adaptive strategies for fail-safe topology optimization". In: Springer International Publishing, 2019, pp. 200–211. ISBN: 978-3-319-97773-7. DOI: `10.1007/978-3-319-97773-7_19`.

[72] Hampus Hederberg and Carl-Johan Thore. "Topology optimization for fail-safe designs using moving morphable components as a representation of damage". In: *Struct Multidisc Optim* (2021). DOI: `10.1007/s00158-021-02984-2`.

[73] Hollis A. Smith and Julian A. Norato. "Topology Optimization of Fail-Safe Structures via Geometry Projection". In: American Institute of Aeronautics and Astronautics, 2021. DOI: `10.2514/6.2021-2026`.

[74] Gustavo Assis da Silva and Hélio Emmendoerfer. "Fail-safe stress-constrained manufacturing error tolerant topology optimization". In: *Computer Methods in Applied Mechanics and Engineering* 421 (2024), p. 116817. DOI: `10.1016/j.cma.2024.116817`.

[75] Micah Kranz, Julian K. Lüdeker, and Benedikt Kriegesmann. "An empirical study on stress-based fail-safe topology optimization and multiple load path design". In: *Struct Multidisc Optim* 64 (2021), pp. 2113–2134. DOI: `10.1007/s00158-021-02969-1`.

[76] Jean-François Gamache, Aurelian Vadean, Émeric Noirot-Nérin, Dominique Beaini, and Sofiane Achiche. "Image-based truss recognition for density-based topology optimization approach". In: *Struct Multidisc Optim* (2018), pp. 1–13. DOI: `10.1007/s00158-018-2028-x`.

[77] Hongxin Wang, Jie Liu, and Guilin Wen. "A study on fail-safe topological design of continuum structures with stress concentration alleviation". In: *Struct Multidisc Optim* 65.6 (2022), p. 174. DOI: `10.1007/s00158-022-03259-0`.

[78] Tong Zhao, Yong Zhang, Yangwei Ou, Wei Ding, and Fei Cheng. "Fail-safe topology optimization considering fatigue". In: *Struct Multidisc Optim* 66.6 (2023), p. 132. DOI: `10.1007/s00158-023-03588-8`.

[79] Jun Wu, Niels Aage, Rüdiger Westermann, and Ole Sigmund. "Infill Optimization for Additive Manufacturing – Approaching Bone-like Porous Structures". In: *IEEE Transactions on Visualization and Computer Graphics* 24.2 (2018), pp. 1127–1140. DOI: `10.1109/TVCG.2017.2655523`.

[80] James K. Guest. "Imposing maximum length scale in topology optimization". In: *Struct Multidisc Optim* 37.5 (2009), pp. 463–473. DOI: `10.1007/s00158-008-0250-7`.

[81] Boyan S. Lazarov and Fengwen Wang. "Maximum length scale in density based topology optimization". In: *Computer Methods in Applied Mechanics and Engineering* 318 (2017), pp. 826–844. DOI: `10.1016/j.cma.2017.02.018`.

[82] Josephine V. Carstensen and James K. Guest. “Projection-based two-phase minimum and maximum length scale control in topology optimization”. In: *Struct Multidisc Optim* 58.5 (2018), pp. 1845–1860. DOI: `10.1007/s00158-018-2066-4`.

[83] Eduardo Fernández, Kai-ke Yang, Stijn Koppen, Pablo Alarcón, Simon Bauduin, and Pierre Duysinx. “Imposing minimum and maximum member size, minimum cavity size, and minimum separation distance between solid members in topology optimization”. In: *Computer Methods in Applied Mechanics and Engineering* 368 (2020), p. 113157. DOI: `10.1016/j.cma.2020.113157`.

[84] Olaf Ambrozkiewicz and Benedikt Kriegesmann. “Density-based shape optimization for fail-safe design”. In: *J Comput Des Eng* 7.5 (2020), pp. 615–629. DOI: `10.1093/jcde/qwaa044`.

[85] C. Cid, A. Baldomir, and S. Hernández. “Probability-damage approach for fail-safe design optimization (PDFSO)”. In: *Struct Multidisc Optim* 62.6 (2020), pp. 3149–3163. DOI: `10.1007/s00158-020-02660-x`.

[86] Clara Cid Bengoa, Aitor Baldomir, Santiago Hernández, and Luis Romera. “Multi-model reliability-based design optimization of structures considering the intact configuration and several partial collapses”. In: *Struct Multidisc Optim* 57.3 (2018), pp. 977–994. DOI: `10.1007/s00158-017-1789-y`.

[87] Kai Long, Xuan Wang, and Yixian Du. “Robust topology optimization formulation including local failure and load uncertainty using sequential quadratic programming”. In: *Int J Mech Mater Des* 15.2 (2019), pp. 317–332. DOI: `10.1007/s10999-018-9411-z`.

[88] Yupeng Cui, Yang Yu, Shanlin Huang, Siyuan Cheng, Mingxiu Wei, Zhenmian Li, and Jianxing Yu. “Novel methodology of fail-safe reliability-based topology optimization for large-scale marine structures”. In: *Struct Multidisc Optim* 66.7 (2023), p. 168. DOI: `10.1007/s00158-023-03614-9`.

[89] Jesús Martínez-Frutos and Rogelio Ortigosa. “Robust topology optimization of continuum structures under uncertain partial collapses”. In: *Computers & Structures* 257 (2021). DOI: `10.1016/j.compstruc.2021.106677`.

[90] I. Elishakoff, R. T. Haftka, and J. Fang. “Structural design under bounded uncertainty—Optimization with anti-optimization”. In: *Computers & Structures* 53.6 (1994), pp. 1401–1405. DOI: `10.1016/0045-7949(94)90405-7`.

[91] J. Tu, K. K. Choi, and Y. H. Park. “A New Study on Reliability-Based Design Optimization”. In: *Journal of Mechanical Design* 121.4 (1999), pp. 557–564. DOI: `10.1115/1.2829499`.

[92] Peter D. Dunning, H. Alicia Kim, and Glen Mullineux. “Introducing Loading Uncertainty in Topology Optimization”. In: *AIAA Journal* 49.4 (2011), pp. 760–768. DOI: `10.2514/1.J050670`.

[93] Junpeng Zhao and Chunjie Wang. “Robust topology optimization under loading uncertainty based on linear elastic theory and orthogonal diagonalization of symmetric matrices”. In: *Computer Methods in Applied Mechanics and Engineering* 273 (2014), pp. 204–218. DOI: `10.1016/j.cma.2014.01.018`.

[94] B. S. Lazarov, M. Schevenels, and O. Sigmund. “Robust design of large-displacement compliant mechanisms”. In: *Mechanical Sciences* 2.2 (2011), pp. 175–182. DOI: `10.5194/ms-2-175-2011`.

[95] Boyan S. Lazarov, Mattias Schevenels, and Ole Sigmund. “Topology optimization considering material and geometric uncertainties using stochastic collocation methods”. In: *Struct Multidisc Optim* 46.4 (2012), pp. 597–612. DOI: `10.1007/s00158-012-0791-7`.

[96] Mazdak Tootkaboni, Alireza Asadpoure, and James K. Guest. “Topology optimization of continuum structures under uncertainty – A Polynomial Chaos approach”. In: *Computer Methods in Applied Mechanics and Engineering* 201-204 (2012), pp. 263–275. DOI: `10.1016/j.cma.2011.09.009`.

[97] Vahid Keshavarzzadeh, Felipe Fernandez, and Daniel A. Tortorelli. “Topology optimization under uncertainty via non-intrusive polynomial chaos expansion”. In: *Computer Methods in Applied Mechanics and Engineering* 318 (2017), pp. 120–147. DOI: `10.1016/j.cma.2017.01.019`.

[98] Vahid Keshavarzzadeh and Kai A. James. “Robust multiphase topology optimization accounting for manufacturing uncertainty via stochastic collocation”. In: *Struct Multidisc Optim* 60.6 (2019), pp. 2461–2476. DOI: `10.1007/s00158-019-02333-4`.

[99] Dilaksan Thillaithevan, Paul Bruce, and Matthew Santer. “Robust multiscale optimization accounting for spatially-varying material uncertainties”. In: *Struct Multidisc Optim* 65.2 (2022), p. 40. DOI: `10.1007/s00158-021-03104-w`.

[100] Tanmoy Chatterjee, Souvik Chakraborty, and Rajib Chowdhury. “A Critical Review of Surrogate Assisted Robust Design Optimization”. In: *Arch Computat Methods Eng* 26.1 (2019), pp. 245–274. DOI: `10.1007/s11831-017-9240-5`.

[101] Kyoung-ryun Bae, Semyung Wang, and Kyung K. Choi. “Reliability-based topology optimization”. In: *9th AIAA/ISSMO Symposium on Multidisciplinary Analysis and Optimization.* 2002, AIAA 2002–5542. DOI: `10.2514/6.2002-5542`.

[102] Kurt Maute and Dan M. Frangopol. “Reliability-based design of MEMS mechanisms by topology optimization”. In: *Computers & Structures* 81.8 (2003), pp. 813–824. DOI: `10.1016/S0045-7949(03)00008-7`.

[103] Hyun-Seung Jung and Seonho Cho. “Reliability-based topology optimization of geometrically nonlinear structures with loading and material uncertainties”. In: *Finite Elements in Analysis and Design* 41.3 (2004), pp. 311–331. DOI: `10.1016/j.finel.2004.06.002`.

[104] George I. N. Rozvany and Kurt Maute. “Analytical and numerical solutions for a reliability-based benchmark example”. In: *Struct Multidisc Optim* 43.6 (2011), pp. 745–753. DOI: `10.1007/s00158-011-0637-8`.

[105] Xiaoping Du and Wei Chen. “Sequential Optimization and Reliability Assessment Method for Efficient Probabilistic Design”. In: *Journal of Mechanical Design* 126.2 (2004), pp. 225–233. DOI: `10.1115/1.1649968`.

[106] Carlos López, Aitor Baldomir, and Santiago Hernández. “Deterministic versus reliability-based topology optimization of aeronautical structures”. In: *Structural and Multidisciplinary Optimization* (2015). DOI: `10.1007/s00158-015-1363-4`.

[107] Qinghai Zhao, Xiaokai Chen, Zhengdong Ma, and Yi Lin. “A Comparison of Deterministic, Reliability-Based Topology Optimization under Uncertainties”. In: *Acta Mechanica Solida Sinica* 29.1 (2016), pp. 31–45. DOI: `10.1016/S0894-9166(16)60005-8`.

[108] Carlos López, Aitor Baldomir, and Santiago Hernández. “The relevance of reliability-based topology optimization in early design stages of aircraft structures”. In: *Structural and Multidisciplinary Optimization* (2017). DOI: `10.1007/s00158-017-1740-2`.

[109] Renatha Batista dos Santos, André Jacomel Torii, and Antonio André Novotny. “Reliability-based topology optimization of structures under stress constraints”. In: *International Journal for Numerical Methods in Engineering* 114.6 (2018), pp. 660–674. DOI: `10.1002/nme.5760`.

[110] Yangjun Luo, Mingdong Zhou, Michael Yu Wang, and Zichen Deng. “Reliability based topology optimization for continuum structures with local failure constraints”. In: *Computers & Structures* 143 (2014), pp. 73–84. DOI: `10.1016/j.compstruc.2014.07.009`.

[111] Gustavo Assis da Silva and André Teófilo Beck. “Reliability-based topology optimization of continuum structures subject to local stress constraints”. In: *Struct Multidisc Optim* 57.6 (2018), pp. 2339–2355. DOI: `10.1007/s00158-017-1865-3`.

[112] Y. Ben-Haim and I. Elishakoff. *Convex Models of Uncertainty in Applied Mechanics*. Vol. 112. Elsevier, 1990.

[113] Boyan S. Lazarov, M. Schevenels, and Ole Sigmund. "Topology optimization with geometric uncertainties by perturbation techniques". In: *Int. J. Numer. Meth. Engng* 90.11 (2012), pp. 1321–1336. DOI: `10.1002/nme.3361`.

[114] M. Jansen, G. Lombaert, and M. Schevenels. "Robust topology optimization of structures with imperfect geometry based on geometric nonlinear analysis". In: *Computer Methods in Applied Mechanics and Engineering* 285 (2015), pp. 452–467. DOI: `10.1016/j.cma.2014.11.028`.

[115] Lawrence Green, Hong-Zong Lin, and M. Khalessi. "Probabilistic Methods for Uncertainty Propagation Applied to Aircraft Design". In: American Institute of Aeronautics and Astronautics, 2002. DOI: `10.2514/6.2002-3140`.

[116] Benedikt Kriegesmann, Raimund Rolfes, Christian Hühne, and Alexander Kling. "Fast Probabilistic Design Procedure for Axially Compressed Composite Cylinders". In: *Composites Structures* 93 (2011), pp. 3140–3149. DOI: `10.1016/j.compstruct.2011.06.017`.

[117] Takayuki Nishino and Junji Kato. "Robust topology optimization based on finite strain considering uncertain loading conditions". In: *Int J Numer Methods Eng* 122.6 (2021), pp. 1427–1455. DOI: `10.1002/nme.6584`.

[118] I. Elishakoff, S. van Manen, P. G. Vermeulen, and J. Arbocz. "First-Order Second-Moment Analysis of the Buckling of Shells with Random Imperfections". In: *AIAA journal* 25.8 (1987), pp. 1113–1117. DOI: `doi.org/10.2514/3.9751`.

[119] Achintya Haldar and Sankaran Mahadevan. *Probability, Reliability and Statistical Methods in Engineering Design*. 1. Auflage. John Wiley & Sons, 1999. ISBN: 978-0-471-33119-3.

[120] Armen Der Der Kiureghian. *Structural and System Reliability*. Cambridge University Press, 2022. ISBN: 978-1-108-99188-9. DOI: `10.1017/9781108991889`.

[121] Ioannis Doltsinis and Zhan Kang. "Robust design of structures using optimization methods". In: *Computer Methods in Applied Mechanics and Engineering* 193.23 (2004), pp. 2221–2237. DOI: `10.1016/j.cma.2003.12.055`.

[122] Micah Kranz, Julian Kajo Lüdeker, and Benedikt Kriegesmann. "A generalized approach for robust topology optimization using the first-order second-moment method for arbitrary response functions". In: *Struct Multidisc Optim* 66.5 (2023), p. 98. DOI: `10.1007/s00158-023-03540-w`.

[123] Kaiming Luo, Xuhui He, and Haiquan Jing. “Topology optimization of bridges under random traffic loading using stochastic reduced-order models”. In: *Probabilistic Engineering Mechanics* (2024), p. 103583. DOI: `10.1016/j.probengmech.2024.103583`.

[124] Jan Christoph Krüger, Micah Kranz, Timo Schmidt, Robert Seifried, and Benedikt Kriegesmann. “An efficient and non-intrusive approach for robust design optimization with the first-order second-moment method”. In: *Computer Methods in Applied Mechanics and Engineering* 414 (2023), p. 116136. DOI: `10.1016/j.cma.2023.116136`.

[125] Ole Sigmund. “Manufacturing tolerant topology optimization”. In: *Acta Mech Sin* 25.2 (2009), pp. 227–239. DOI: `10.1007/s10409-009-0240-z`.

[126] Fengwen Wang, Boyan Stefanov Lazarov, and Ole Sigmund. “On projection methods, convergence and robust formulations in topology optimization”. In: *Struct Multidisc Optim* 43.6 (2011), pp. 767–784. DOI: `10.1007/s00158-010-0602-y`.

[127] Shikui Chen, Wei Chen, and Sanghoon Lee. “Level set based robust shape and topology optimization under random field uncertainties”. In: *Struct Multidisc Optim* 41.4 (2010), pp. 507–524. DOI: `10.1007/s00158-009-0449-2`.

[128] Alireza Asadpoure, Mazdak Tootkaboni, and James K. Guest. “Robust topology optimization of structures with uncertainties in stiffness – Application to truss structures”. In: *Computers & Structures* 89.11 (2011), pp. 1131–1141. DOI: `10.1016/j.compstruc.2010.11.004`.

[129] M. Schevenels, B. S. Lazarov, and Ole Sigmund. “Robust topology optimization accounting for spatially varying manufacturing errors”. In: *Computer Methods in Applied Mechanics and Engineering* 200.49–52 (2011), pp. 3613–3627. DOI: `10.1016/j.cma.2011.08.006`.

[130] Miche Jansen, Geert Lombaert, Moritz Diehl, Boyan S. Lazarov, Ole Sigmund, and Mattias Schevenels. “Robust topology optimization accounting for misplacement of material”. In: *Struct Multidisc Optim* 47.3 (2013), pp. 317–333. DOI: `10.1007/s00158-012-0835-z`.

[131] Junpeng Zhao and Chunjie Wang. “Robust structural topology optimization under random field loading uncertainty”. In: *Struct Multidisc Optim* 50.3 (2014), pp. 517–522. DOI: `10.1007/s00158-014-1119-6`.

[132] G. A. da Silva and E. L. Cardoso. “Topology optimization of continuum structures subjected to uncertainties in material properties”. In: *International Journal for Numerical Methods in Engineering* 106.3 (2016), pp. 192–212. DOI: `10.1002/nme.5126`.

[133] Jesús Martínez-Frutos, David Herrero-Pérez, Mathieu Kessler, and Francisco Periago. "Robust shape optimization of continuous structures via the level set method". In: *Computer Methods in Applied Mechanics and Engineering* 305 (2016), pp. 271–291. DOI: `10.1016/j.cma.2016.03.003`.

[134] Jesús Martínez-Frutos and David Herrero-Pérez. "Evolutionary topology optimization of continuum structures under uncertainty using sensitivity analysis and smooth boundary representation". In: *Computers & Structures* 205 (2018), pp. 15–27. DOI: `10.1016/j.compstruc.2018.05.003`.

[135] Seyyed Ali Latifi Rostami and Ali Ghoddosian. "Topology optimization of continuum structures under hybrid uncertainties". In: *Struct Multidisc Optim* 57.6 (2018), pp. 2399–2409. DOI: `10.1007/s00158-017-1868-0`.

[136] Jing Zheng, Zhen Luo, Chao Jiang, and Jinglai Wu. "Level-set topology optimization for robust design of structures under hybrid uncertainties". In: *International Journal for Numerical Methods in Engineering* 0.0 (2018). DOI: `10.1002/nme.5966`.

[137] Benedikt Kriegesmann. "Robust design optimization with design-dependent random input variables". In: *Struct Multidisc Optim* 61.2 (2020), pp. 661–674. DOI: `10.1007/s00158-019-02388-3`.

[138] Alberto P. Torres, James E. Warner, Miguel A. Aguiló, and James K. Guest. "Robust topology optimization under loading uncertainties via stochastic reduced order models". In: *International Journal for Numerical Methods in Engineering* 122.20 (2021), pp. 5718–5743. DOI: `10.1002/nme.6770`.

[139] Kai Steltner, Claus B. W. Pedersen, and Benedikt Kriegesmann. "Semi-intrusive approach for stiffness and strength topology optimization under uncertainty". In: *Optim Eng* (2022). DOI: `10.1007/s11081-022-09770-z`.

[140] Jan Christoph Krüger and Benedikt Kriegesmann. "Robust design optimization using a non-intrusive second-order approximation of stochastic moments". In: *Struct Multidisc Optim* 67.7 (2024), p. 124. DOI: `10.1007/s00158-024-03843-6`.

[141] Timo Schmidt, Benedikt Kriegesmann, and Robert Seifried. "Robust contact-constrained topology optimization considering uncertainty at the contact support". In: *Struct Multidisc Optim* 67.4 (2024), p. 46. DOI: `10.1007/s00158-024-03750-w`.

[142] Bruno Sudret and Armen Der Kiureghian. *Stochastic finite element methods and reliability: a state-of-the-art report.* Tech. rep. UCB/SEMM-2000/08. 2000.

[143] K. Schittkowski, C. Zillober, and R. Zotemantel. "Numerical comparison of nonlinear programming algorithms for structural optimization". In: *Structural Optimization* 7.1 (1994), pp. 1–19. DOI: `10.1007/BF01742498`.

[144] Nam H. Kim, Ting Dong, David Weinberg, and Jonas Dalidd. "Generalized Optimality Criteria Method for Topology Optimization". In: *Applied Sciences* 11.7 (2021), p. 3175. DOI: `10.3390/app11073175`.

[145] Krister Svanberg. "The method of moving asymptotes - a new method for structural optimization". In: *Int. J. Numer. Meth. Engng.* 24.2 (1987), pp. 359–373. DOI: `10.1002/nme.1620240207`.

[146] Pedro Fernandes, Àlex Ferrer, Paulo Gonçalves, Marco Parente, Ricardo Pinto, and Nuno Correia. "Stress-Constrained Topology Optimization for Commercial Software: A Python Implementation for ABAQUS ®". In: *Applied Sciences* 13 (2023), p. 12916. DOI: `10.3390/app132312916`.

[147] J. K. Guest, J. H. Prévost, and T. Belytschko. "Achieving minimum length scale in topology optimization using nodal design variables and projection functions". In: *International Journal for Numerical Methods in Engineering* 61.2 (2004), pp. 238–254. DOI: `10.1002/nme.1064`.

[148] Ole Sigmund. "Morphology-based black and white filters for topology optimization". In: *Struct Multidisc Optim* 33.4-5 (2007), pp. 401–424. DOI: `10.1007/s00158-006-0087-x`.

[149] Jacob Oest and Erik Lund. "Topology optimization with finite-life fatigue constraints". In: *Struct Multidisc Optim* 56.5 (2017), pp. 1045–1059. DOI: `10.1007/s00158-017-1701-9`.

[150] Shanglong Zhang, Chau Le, Arun L. Gain, and Julián A. Norato. "Fatigue-based topology optimization with non-proportional loads". In: *Computer Methods in Applied Mechanics and Engineering* 345 (2019), pp. 805–825. DOI: `10.1016/j.cma.2018.11.015`.

[151] G. Kreisselmeier and R. Steinhauser. "Systematic Control Design by Optimizing a Vector Performance Index". In: *IFAC Proceedings Volumes* 12.7 (1979), pp. 113–117. DOI: `10.1016/S1474-6670(17)65584-8`.

[152] Gerhard Kreisselmeier and Reinhold Steinhauser. "Application of vector performance optimization to a robust control loop design for a fighter aircraft". In: *International Journal of Control* 37.2 (1983), pp. 251–284. DOI: `10.1080/00207179.1983.9753066`.

[153] Gregory A. Wrenn. *An Indirect Method for Numerical Optimization Using the Kreisselmeir-Steinhauser Function.* National Aeronautics, Space Administration, Office of Management, Scientific, and Technical Information Division, 1989.

[154] Nicholas M. K. Poon and Joaquim R. R. A. Martins. "An adaptive approach to constraint aggregation using adjoint sensitivity analysis". In: *Struct Multidisc Optim* 34.1 (2007), pp. 61–73. DOI: `10.1007/s00158-006-0061-7`.

[155] Anders Clausen and Erik Andreassen. “On filter boundary conditions in topology optimization”. In: *Struct Multidisc Optim* 56.5 (2017), pp. 1147–1155. DOI: `10.1007/s00158-017-1709-1`.

[156] Ole Sigmund. “On benchmarking and good scientific practise in topology optimization”. In: *Struct Multidisc Optim* 65.11 (2022), p. 315. DOI: `10.1007/s00158-022-03427-2`.

[157] Walter Pilkey and Deborah Pilkey. “Peterson’s Stress Concentration Factors, Third Edition”. In: *Peterson’s Stress Concentration Factors, Third Edition* (2008), pp. 1–522. DOI: `10.1002/9780470211106`.

[158] Darren Engwirda. “Locally optimal Delaunay-refinement and optimisation-based mesh generation”. PhD Thesis. 2014.

[159] D. Engwirda. “Unstructured mesh methods for the Navier-Stokes equations”. In: *Undergraduate Thesis, School of Engineering, University of Sidney* (2005).

[160] Rafael Holdorf Lopez and André Teófilo Beck. “Reliability-based design optimization strategies based on FORM: a review”. In: *J. Braz. Soc. Mech. Sci. & Eng.* 34 (2012), pp. 506–514. DOI: `10.1590/S1678-58782012000400012`.

[161] Carlos H. Villanueva and Kurt Maute. “Density and level set-XFEM schemes for topology optimization of 3-D structures”. In: *Comput Mech* 54.1 (2014), pp. 133–150. DOI: `10.1007/s00466-014-1027-z`.

[162] J. Parvizian, A. Düster, and E. Rank. “Topology optimization using the finite cell method”. In: *Optim Eng* 13.1 (2012), pp. 57–78. DOI: `10.1007/s11081-011-9159-x`.

[163] Krister Svanberg. *MMA and GCMMA – two methods for nonlinear optimization.* Tech. rep. 2007.

[164] W. Härdle and L. Simar. *Applied Multivariate Statistical Analysis.* Springer Verlag, 2007. ISBN: 3-540-72243-2.

[165] George Stefanou. “The stochastic finite element method: Past, present and future”. In: *Computer Methods in Applied Mechanics and Engineering* 198.9-12 (2009), pp. 1031–1051. DOI: `10.1016/j.cma.2008.11.007`.

[166] Robert E. Melchers and Andre T. Beck. *Structural Reliability Analysis and Prediction.* 3rd ed. Wiley, 2018. ISBN: 978-1-119-26599-3.